Flux Density and VLBI Measurements of the IDV Source 0917+624

Dissertation
zur
Erlangung des Doktorgrades (Dr. rer. nat.)
der
Mathematisch-Naturwissenschaftlichen Fakultät
der
Rheinischen Friedrich-Wilhelms-Universität Bonn

vorgelegt von
Simone Bernhart
aus
Ruppichteroth

Bonn 2010

Angefertigt mit Genehmigung der Mathematisch-Naturwissenschaftlichen
Fakultät der Rheinischen Friedrich-Wilhelms-Universität Bonn

1. Gutachter: Prof. Dr. Ulrich Klein
2. Gutachter: Priv.-Doz. Dr. Walter Huchtmeier

Tag der Promotion: 15.03.2010

A great pleasure in life is doing what people say you cannot do.

Walter Bagehot

Contents

CHAPTER 1

Introduction

Black holes are among the most fascinating objects in the universe - in any case intriguing enough for me so as to become an astronomer. It is today generally accepted that black holes are located in the center of most galaxies. One particular species of galaxies is that of the so-called Active Galactic Nuclei (AGN) which display energetic phenomena in their central region that are comparable to or even exceed the energy emitted by all of the galaxies' stars by orders of magnitude. The first group of AGN with high central surface brightness, that was observed in the optical in the early 1940s by Carl Seyfert, had not been considered significant until 1955 when the AGN were identified as radio sources. In the late 1950s the first radio surveys were performed which enabled an identification of the strongest radio sources with their optical counterparts which were usually galaxies, but sometimes appeared to be star-like objects. This consequently led to the term quasi-stellar radio source or quasi-stellar object which later turned into 'quasar' or 'QSO'. Only the discovery of Schmidt (1963), that the optical spectrum of the star-like object 3C273 is in fact highly redshifted and hence of cosmological origin, enabled an efficient identification of quasars.

In order to put this thesis into a larger context, I shall first give an introduction to the large variety of AGN and part of their characteristics on which this work is based.

1.1 Active Galactic Nuclei and Relativistic Jets

The radio structure of AGN can generally be referred to as either extended, i.e. spatially resolved, or compact, i.e. unresolved at the corresponding observing frequency. In the radio bands, the extended structure is usually double in nature showing two 'lobes' on either side of the central source. These structures can reach up to megaparsec dimensions. The lobes are connected to the central region via relativistic jets, i.e. plasma streams which seem to transport particles and energy to the outer lobes with relativistic speeds while emitting synchrotron radiation (e.g., Begelman et al. 1984, see also 2.3.1).

Up to the present, numerous work has been done on the structural properties of AGN and their evolution. But very important questions, such as the detailed process of jet formation, still remain unanswered. However, the knowledge about what is going on in the small central regions of those active galaxies has improved considerably during the past decades. Today we are familiar with a large variety of subclasses of AGN, one of which are **Seyfert Galaxies**, named after their above mentioned discoverer. Seyfert Galaxies are lower-luminosity AGN with a quasar-like nucleus, the host galaxy still being clearly detectable in the optical bands. They can be divided into two subclasses: **Seyfert type 1** galaxies show narrow emission lines referring to low-density ionised gas as well as broad emission lines which can be attributed to high-density gas. In **Seyfert type 2** galaxies, only the narrow lines are present. In polarised light, however, also the broad lines become visible. It is not jet fully understood what causes the difference between Seyfert type 1 and type 2 galaxies. One hypothesis says that the two types are intrinsically the same exhibiting both broad and narrow emission lines, however, Seyfert 2s are probably observed from a different viewing angle such that the broad line region is hidden by a circumnuclear torus. The radio luminosity of Seyfert Galaxies is only moderate compared to other more active AGN. **Quasars**[1], on the other hand, the most distant objects in the universe, are most luminous at every wavelength at which they have been observed, with bolometric luminosities in the range of 10^{45} to more than 10^{48} ergs s^{-1}. They display time-variable continuum flux and broad emission lines and often a large ultraviolet (UV) flux specified as UV excess. Their high redshift indicates that quasars emerged in an early phase of the universe which makes them an important cosmological probe. One distinguishes between radio-loud and radio-quiet quasars, the latter originally referred to as QSOs (quasi-stellar object). Today the terms 'quasar' and QSO are virtually equivalent.

Radio Galaxies are usually found to be giant ellipticals showing million times brighter radio luminosity than normal galaxies, although some of the brightest radio galaxies host in fact quasar-like nuclei. The bulk radio emission is concentrated in the core and the afore mentioned radio lobes. Fanaroff & Riley (1974) classified the radio galaxies according to their morphology into **FRI** sources with weaker radio flux being brightest in the center, and **FRII** sources which have well-defined jets and are more luminous and limb-brightened, i.e. they show hot spots in their radio lobes. The transition specific luminosity between the two classes is defined as $L_\nu(1.4\mathrm{GHz}) \simeq 10^{32}$ erg s^{-1} Hz^{-1} (Bridle & Perley 1984). Furthermore, we can distinguish between broad-line radio galaxies (**BLRG**) and narrow-line radio galaxies (**NLRG**) as the

---

[1] The term 'quasar' originates from their appearance as a quasi-stellar radio source.

radio-loud analogs to Seyfert galaxies of type 1 and 2.

The main target of this work, 0917+624, belongs to the class of **Blazars**, which subsume a group of radio-loud, core-dominated flat-spectrum[2] radio sources consisting of BL Lac objects, named after the prototype BL Lacertae, and the so-called optically violent variable (OVV) quasars. They have in common that they are extremely variable on all time scales and in all bands of the electromagnetic spectrum and tend to have high polarisation of up to a few percent (in contrast to <1% for most other AGN). Besides, their jet is pointing almost directly towards us enclosing only a small angle with the line of sight. Aside from that, BL Lac objects do have no or only weak spectral line emission and absorption features compared to the continuum, which often impedes a redshift detection (usually $z \leq 2$), whereas OVVs have broad emission lines as long as the continuum is not at its brightest ($z \geq 0.5$). It has become generally accepted that within the blazar class highly variable quasars are related to intrinsically powerful FRII radio galaxies, and BL Lac objects are related to lower luminosity FRI galaxies. This distinction explains the different emission line properties.

The above described types are the most common classes. Since they are partly divided into subclasses according to their overall spectral energy distribution or emission line types, it has been found a more general distinction between **type 1 AGN** (showing both broad and narrow emission lines) and **type 2 AGN** (only narrow emission lines), and **radio-quiet** and **radio-loud** objects. The term ’radio-loud’ refers to the ratio R of radio to optical emission at 6 cm and 4400 Å and is generally in the range 10–1000 for radio-loud objects (Kellermann et al. 1989).

1.1.1 Unified Scheme

One of the main achievements in AGN research is the idea about a unification of the various different types of AGN, the characteristics of which I will shortly summarise in the following. Since it is assumed that the above described properties of AGN are mainly depending on the orientation towards the observer and are less due to real physical differences like, e.g., the luminosity, it was attempted to find a kind of morphological model which is able to describe AGN with as few parameters as possible (see, e.g., Urry 2004, Peterson 1997).

The black-hole paradigm states that AGN host a ”central engine” consisting of a supermassive black hole (10^7-$10^{10}M_\odot$) encircled by an accretion disk, in which gravitational potential energy is converted into radiation (ranging from radio to X-ray). Surrounding this is the broad-line region (BLR), consisting of high velocity gas, followed by the lower density and lower velocity gas of the narrow-line region (NLR). Around the unresolved components of an AGN there lies an optically thick obscuring torus that permits the AGN radiation to escape only along the

---

[2] Source flux density S depends on observing frequency via $S_\nu \propto \nu^\alpha$ with power-law index $\alpha \geq -0.5$

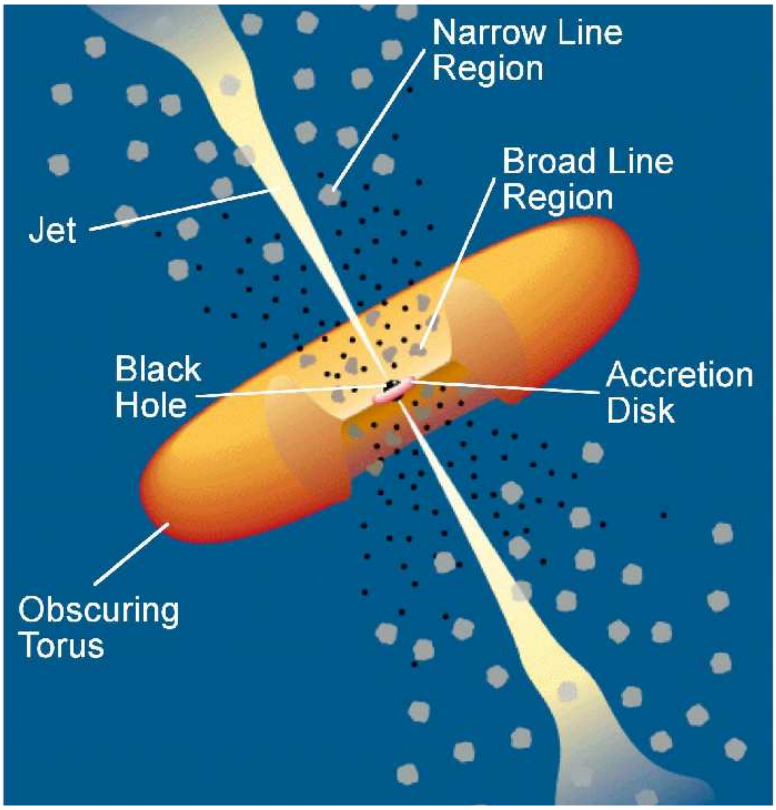

Figure 1.1: *Schematic of an AGN according to Urry & Padovani (1995); according to the orientation, this would be a radio-loud AGN.*

torus axis, which leads to observable large-scale ionisation cones. Relativistic jets, formed within $\lesssim$100 Schwarzschild radii of the black hole (most likely due to the existence of a toroidal magnetic field), extend outwards along this torus axis for tens of kpc up to Mpc in some cases (see Figure 1.1 for a schematic illustration). The alignment of the torus/jet axes seems to be independent from the rotation axis of the host galaxy (see, e.g., Schmitt et al. 2002 and references therein).

Apart from intrinsic variations in the black hole mass, size, density, luminosity, etc., the above basic description is apparently valid for all AGN - with an exception being the relativistic jets. These are found in most radio-loud AGN but with differences concerning their kinetic powers. In contrast to the powerful radio jets that expand far into the intergalactic medium, weaker jets deccelerate relatively close to the central engine, which can be even within the host galaxy. It is not yet well understood why only 5-10% of the AGN are radio-loud.

Local obscuration has been studied by Antonucci & Miller (1985), who found that the distinction between type 1 and type 2 AGN seems mainly to be due to the orientation with respect to the line of sight, at least locally. Another question is, though, why the fraction of type 2 AGN found at higher redshifts (z>2) is much less than that of type 1 AGN.

It appears that there are in fact two separate unification models by orientation, one is based mainly on optical observations describing the presence or absence of the BLR depending on the direction of the obscuring torus, the other is mainly based on radio data explaining the core-dominated (flat-spectrum) versus lobe-dominated (steep-spectrum) radio-loud AGN according to the alignment of the jet axis with respect to the line of sight.

1.1.2 Galactic Evolution

From a cosmological viewpoint, AGN belong to earlier states of cosmological galaxy formation, thus being far away but still observable due to their high nuclear activities. The observed redshifts range from z = 0.0018 for the radio galaxy Centaurus A[3] (derived from radial velocity measurements, Graham 1978) to the currently farthest known z = 6.43 for the quasar CFHQS J2329-0301 (Willott et al. 2007).

Remains the question, where these supermassive black holes (SMBH), that are supposed to constitute the central engines of AGN, stem from and how they could develop in such a – cosmologically – comparatively short time. One assumption is that SMBHs are formed during mergers of two (or more) galaxies (see, e.g., Schweizer 1986; Barnes & Hernquist 1992; Kauffmann & Haehnelt 2000). Collisions and mergers are thought to be responsible for various phenomena such as the triggering of star formation and the fueling of nuclear activity in quasars, or the formation of disk galaxies (Robertson et al. 2006). Galaxy encounters show higher activities in the UV, the near-infrared, in optical emission line strength and in radio emission; besides observations indicate that different types of AGN like Seyfert galaxies or quasars sometimes exhibit signs of past mergers (see, e.g., Sánchez et al. 2004 and references therein).

Ultraluminous infrared galaxies (ULIRGs), a class of objects with luminosities above $10^{12}L_{\odot}$ in the Far Infrared, are known to be interacting or merging systems revealing intense starburst processes (Sanders et al. 1988b; Sanders & Mirabel 1996). Furthermore, a significant fraction of the ULIRGs also shows evidence for AGN activity (Genzel et al. 1998). These ultraluminous infrared galaxies may represent an important stage in the formation of quasi-stellar objects and powerful radio galaxies: ULIRGs are thought be the progenitors of AGN. Sanders et al. (1988a) suggested a scenario for the formation of ULIRGs through the merger or strong interaction of two molecular gas-rich spirals. Molecular gas clouds are funneled towards the merger nucleus,

---

[3] which is, however, not indicative for its distance due to the proximity of Cen A and the significant superposition of the proper motion of the galaxy within its group and its cosmological velocity

which could be responsible for both nuclear starburst and AGN activity. In a transition phase the AGN might be obscured by the surrounding star forming region (see, e.g., Komossa et al. 2003), becoming visible later as an optical quasar after the starburst activities have begun to fade. Even though for QSOs the observational results are not coherent, it seems likely that at least part of the AGN developes from a preceding ULIRG which has been formed in a merger of galaxies (Canalizo & Stockton 2001).

The coalescence of SMBH binaries is supposed to be one of the primary sources of very low frequency gravitational waves (see, e.g., Volonteri et al. 2004; Wen et al. 2008), which is the main target of the new generation Laser Interferometer Space Antenna (LISA - planned to be launched around 2019-2020) and thus makes these objects perfectly suitable for future studies.

1.2 Variability in AGN

The flux density variation of compact extragalactic radio sources is known to occur on long (years to decades) as well as on short ($\lesssim$weeks) time scales over the whole frequency band not only in the continuum but also in the broad emission lines and in polarised light. Optical continuum variability was already observed before the redshifts of the identified optical counterparts were fully understood (Matthews & Sandage 1963). The variations were found to be on the order of 0.3-0.5 mag over time scales of a few months. But some sources showed even faster variations on time scales of only a few hours. Due to causality arguments that the speed of light is limited, it was concluded that much of the radiation comes from a region of the order of light hours (light travel time argument). This, however, implies that the size of the emitting region should be as small as the Solar System radiating as much energy as an entire galaxy!

A further probe of the innermost regions of the AGN accretion disc are the strong variabilities at X-ray energies on time scales of a few hundred to 10^7 seconds (see McHardy 1988). On longer time scales (days or longer), there appears to be a correlation between X-ray continuum and UV/optical variations being simultaneous to within a few days or less. The IR continuum shows the same variations as the UV/optical continuum but with a significant time delay. This indicates, that the IR emission comes from dust regions far away from the central engine, being of thermal nature.

In the 1960s two astronomers were independently looking for variability in the radio regime, when they both discovered longterm variations on a time scale of 100 days (Sholomitsky 1965) and 1000 days (Dent 1965), respectively, which suggested small source sizes. In the meantime, even faster variations have been found. One distinguishes between different types of variability (see, e.g., Wagner & Witzel 1995), among them is flickering which is a synonym for a change of the flux density with small amplitudes on a time scale of a few days to weeks (Heeschen 1984) and could be explained by Refractive Interstellar Scintillation (RISS - see Chapter 2.2, Heeschen & Rickett 1987). The variability type, which is subject of this thesis, is called **I**ntra**d**ay **V**ariability (IDV) and describes variations on time scales of hours to days. The nature of these variations is still not clear and has been controversially discussed during the years since its discovery in 1986 (Witzel et al. 1986; Heeschen et al. 1987). A more detailed description of the phenomenon of IDV and its physical interpretation is given in Chapter 2.2.

Variability in blazars is an important probe for the origin of the continuum radiation and the underlying physical processes. The strength of the continuum variability is correlated with the apparent luminosity and the degree of polarisation, which strongly favours a non-thermal origin (Edelson 1992). Moreover, the observation of variability on short time scales classifies a source as ultra-compact and most energetic. Hence, variability studies enable to find the smallest resolvable objects in our universe. This was one of the main reasons for the development of Very-Long-Baseline Interferometry (VLBI), a high-resolution observing technique which provides angular resolution down to the submilliarcsecond level. VLBI uses the principle of aperture synthesis (see Ryle & Hewish 1960) which is a type of interferometry that combines signals from multiple telescopes spread over a large area to produce images having the same angular resolution as an instrument with the size of this area. Today, numerous VLBI facilities operate worldwide such as the Very Long Baseline Array allocated across the US (see Figure 1.2), with which the larger part of the observations has been performed that are part of this thesis, the European VLBI Network (EVN) or the Global mm-VLBI Array (operating at a wavelength of 3 mm), which combines VLBA and EVN telescopes and thus can provide high angular resolution (up to 50 micro-arcseconds) and high dynamic range (of a few hundred) images of compact radio sources.

For the future, even larger instruments with increased sensitivity are planned or already under construction such as the Low Frequency Array (LOFAR), the Atacama Large Millimeter/submillimeter Array (ALMA), the VLBI Space Observatory Programme 2 (VSOP-2) or the Square Kilometer Array (SKA). This next generation of telescopes should be able to see even further back in time to probe the early Universe.

1.3 Objective and Structure of this Thesis

Working as a researcher in natural science is by and large comparable to working on a jigsaw. Each scientist tries to add a small piece of the puzzle to the big picture. The objective of this thesis is to add another portion to the understanding of the IDV phenomenon as well as having a closer look to the kinematic and polarimetric behaviour of AGNs. This is done by means of a

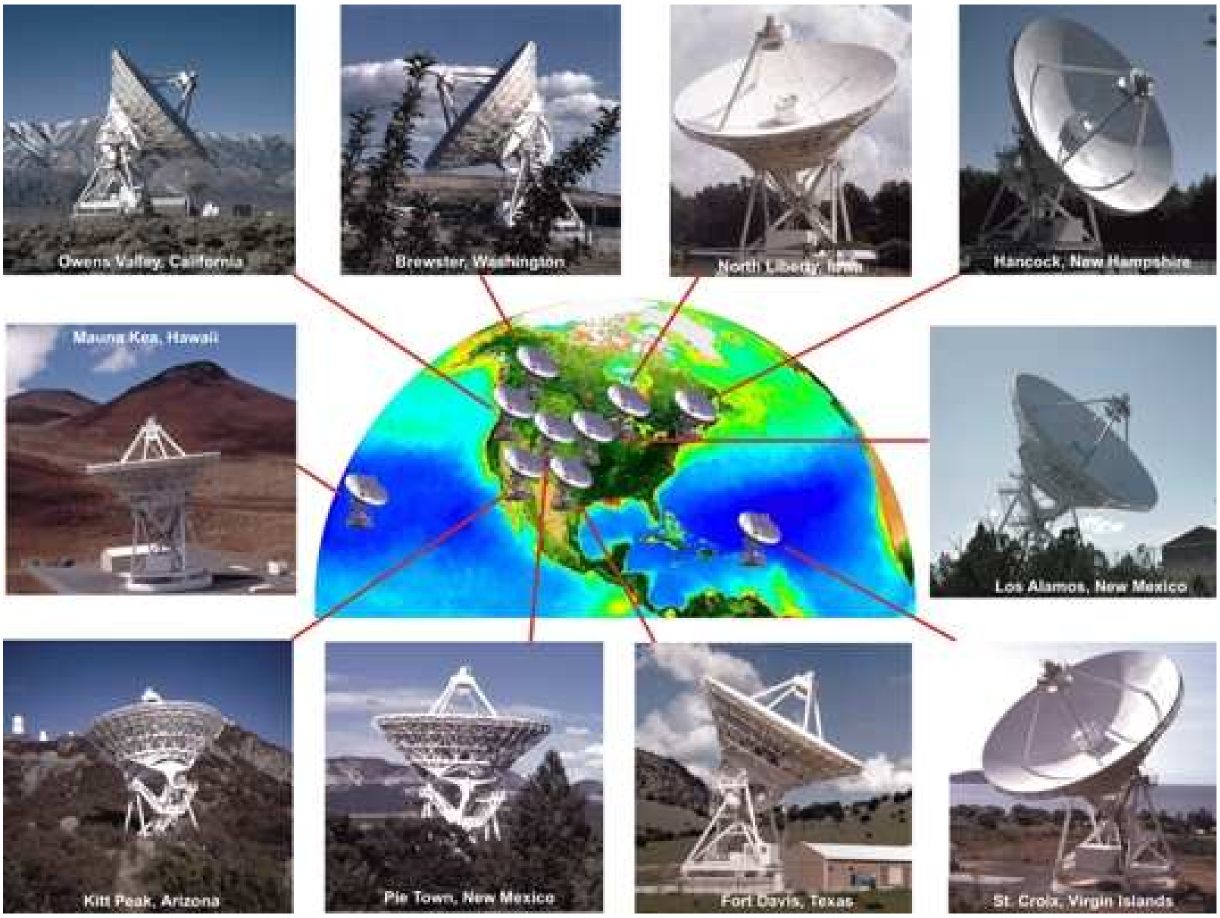

Figure 1.2: *Montage of all VLBA telescopes; Image courtesy of NRAO/AUI and Earth image courtesy of the SeaWiFS Project NASA/GSFC and ORBIMAGE.*

detailed inverstigation of the intraday variable quasar S4 0917+624 (furthermore referred to as 0917+624).

0917+624 was known to show prominent IDV behaviour from the time it was first studied as a short-time variable source by Heeschen et al. (1987). Meanwhile, however, its variability ceased and yet the reason for that is not clear (Quirrenbach et al. 1989b; Kraus et al. 1999). The working hypothesis for the observations, on which the main part of this thesis is based, was that structural changes of the variable part of the source have caused the variability decline. These changes could be revealed using high resolution observing techniques, namely VLBI. As there have been numerous explanations of VLBI principles and the required data analysis steps in the past, I will not go into detail here but refer to more precise descriptions where appropriate. Details can be found, e.g., in Thompson et al. (2001) or in the A.S.P. Conference Series Volume 180 (edited by Taylor et al. 1999), and an overview concerning the data reduction has been given in my diploma thesis (Friedrichs 2003).

The following chapters are going to give an introduction to the physical processes that are associated with IDV and describe the IDV phenomenon and its possible causes as well as the currently prevailing doctrine. In Chapter 3, I will give a more detailed introduction to the quasar 0917+624. Chapter 4 reports about flux density observations of the source with the Effelsberg 100m radio telescope. The subsequent chapters present the results of the VLBI observations of 0917+624, which were analysed in the scope of this work. I shall start with the source kinematics on VLBI scales (Chapter 5) and introduce a possible binary black hole scenario for 0917+624 based on the kinematics of one specific trajectory. In Chapter 6, the results of the polarimetry analysis are described. Each chapter contains a short introduction to the data analysis. Chapter 7 will join the results from single dish and VLBI observations and give an interpretation in terms of Intraday Variability. The thesis concludes with a final summary in Chapter 8.

Chapter 2

Theoretical Basics

2.1 Compact Radio Sources

The radio spectra of compact sources in the center of AGN are flat, i.e., the broad-band SED is defined as $S_\nu \propto \nu^\alpha$ with power-law index $\alpha \geq -0.5$. Hence, the radiation is usually expected to come from several emission regions of non-thermal synchrotron emission (see Chapter 2.3.1 for a more detailed description of the synchrotron spectrum). The spectral indices are close to flat but gradually steeper at higher frequencies with different regions becoming optically thick at different wavelengths because of radial gradients in the magnetic field and particle density within the source. Flat spectra are regarded as a superposition of several structural components (Kellermann & Pauliny-Toth 1969). In the radio unification scheme, there are many independent observational evidences for relativistic motion in the cores of flat-spectrum radio-sources because of high brightness temperatures, superluminal motion on parsec scales, predominant one-sided jets due to Doppler-boosting, or the stronger Faraday depolarisation on the counter-jet side. These points will each be briefly addressed to in the following sections.

2.1.1 Brightness Temperature

In the previous chapter, the small source sizes were already mentioned, which were derived using causality and the light travel time argument. The luminosity of these small regions is therefore extremely high. This leads to high brightness temperatures and photon densities being the main ingredients of the underlying physics.

The emissivity of a radio source at a certain frequency ν can be derived from its flux density S_ν and the angular source size θ. The blackbody equivalent temperature, i.e. the temperature the source would have if it was considered to radiate like a blackbody, is called brightness temperature T_B. In the Rayleigh-Jeans approximation, the relation between flux density and brightness temperature is given by

$$S = \frac{2k}{\lambda^2} \iint T_\mathrm{B}(\theta, \varphi) d\Omega \tag{2.1}$$

with Boltzmann constant k and wavelength λ. In convenient units and for a Gaussian brightness distribution this gives

$$T_\mathrm{B} = 1.22 \cdot 10^{12} \frac{S}{\theta^2 \nu^2} K \tag{2.2}$$

where S_ν is given in Jy, θ in mas and the frequency ν in GHz. The brightness temperature is equal to the kinetic temperature for an optically thick thermal source (T_B is less than kinetic temperature in the optically thin region). There is an upper limit for the brightness temperature of 10^{12}K, the so-called inverse-Compton (IC) limit, for the following reason: if T_B rises – i.e., the radiation energy density is increased by synchrotron radiation – until it exceeds the energy density of the magnetic field, the electrons start to inverse-Compton scatter up their own synchrotron photons (synchrotron self-Compton - SSC) to the X-ray and γ-ray regime. This runaway process is called the Compton catastrophe and it provides a fast cooling of the plasma to a point where the IC losses are of the same order as the synchrotron losses, which limits the brightness temperature to $T_\mathrm{B} \sim 10^{12}$ K (Kellermann & Pauliny-Toth 1969).

Variability studies have revealed that the IC limit appears to be violated in IDV blazar cores if one assumes a source intrinsic origin of the variability. For instance, Romero et al. (1994) refer an extreme case of brightness temperature in the strongly variable IDV source PKS 0537−411 of $\sim 10^{21}$K, the same was found for PKS 0405−385 by Kedziora-Chudczer et al. (1997). Tyul'Bashev (2005) reports about brightness temperatures in four IDV sources of the order of several 10^{12} to 10^{15}K (in the case of 0917+624). Even higher values of 10^{16} to 10^{18}K for 0917+624 were found by Quirrenbach et al. (1989b) and Kraus et al. (1999). This discloses severe problems in the theoretical interpretation of short-time variability. Considerations of how to overcome this brightness temperature problem will be explicated in the following as well as in section 2.2.

2.1.2 Superluminal Motion, Relativistic Beaming and Doppler Boosting

Since flat spectra and fast flux density variability of compact radio sources are indicative of small source sizes, these sources always have been subject to numerous VLBI observations. In order to explain the high apparent brightness temperatures which have been deduced from variability studies, Rees (1967) theoretically predicted superluminal motion where the bulk relativistic motion in a jet displays a transversal velocity $\sim \gamma c$ towards an observer[1] in excess of the speed

---

[1] $\gamma = \sqrt{1 - \beta^2}$ is the Lorentz factor.

of light. This prediction could be verified observationally later by means of VLBI (e.g., Cohen et al. 1979). Sources showing this property usually have a one-sided jet structure and the relativistic jet points towards the observer at a small angle to the line of sight (Blandford & Königl 1979). The plasma velocities within the jet typically range from 1 to 40 c (see, e.g., Zensus & Pearson 1987; Kellermann et al. 2004; Jorstad et al. 2005; Britzen et al. 2008). The spectra of many flat-spectrum sources suggest that they are composed of several components which have different turnover frequencies. If one of these components is moving down the jet with a velocity v and at an angle θ to the line of sight, it has a transversally directed velocity component $v_{\mathrm{app}} = \beta_{\mathrm{app}}c$ which is related to the true velocity $v = \beta c$ by

$$\beta_{\mathrm{app}} = \frac{\beta \sin\theta}{1-\beta\cos\theta} \tag{2.3}$$

A maximum value of β_{app} is obtained for $\cos\theta = \gamma^{-1}$ and thus $\sin\theta = \sqrt{1-\beta^2} = \gamma^{-1}$. This maximum excesses the speed of light for $v = \frac{c3}{\sqrt{2}}$ (e.g., Eckart 1983). From the apparent speed, one can derive a minimum value for the Lorentz factor: $\gamma_{\mathrm{min}} = \sqrt{1+\beta^2_{\mathrm{app}}}$.

In a relativistically approaching source the observed flux density S is an amplification of the true flux density S_0 via

$$S = S_0\delta^{3-\alpha} \tag{2.4}$$

where $\delta = [\gamma(1-\beta\cos\theta)]^{-1}$ is the Doppler factor and α the spectral index. This so-called Doppler boosting applies only for a single component. For a continuous jet, the exponent reduces to $(2-\alpha)$ for geometrical reasons (Scheuer & Readhead 1979). The flux density of the approaching components is amplified, whereas the flux density of the receding components is attenuated. The flux density ratio between jet (S_1) and counter-jet (S_2) can be determined as

$$R = \frac{S_1}{S_2} = \left(\frac{1+\beta\cos\theta}{1-\beta\cos\theta}\right)^{(2-\alpha)} \tag{2.5}$$

Assuming small angles to the line of sight, the estimation of Doppler factors usually yields values of up to 20 (Ghisellini et al. 1993). For small viewing angles ($\theta \to 0$), the Doppler factor approaches $\delta_{\mathrm{max}} = 2\gamma$.

2.2 Intraday Variable Sources

In the previous chapter, the variability of AGN has already been addressed. Flux density flares on time scales of weeks to months over the whole continuum have been observed, which are often followed by the ejection of new VLBI components in the core region of these sources. Relativistic shocks emanating from the core and propagating down the jet are thought to be responsible for such kinds of observations. While in the radio regime low frequency variability (LFV - below 1 GHz) and flickering can be explained by scattering processes in the interstellar medium (see, e.g., Altschuler 1989; Bondi et al. 1996 for LFV, Heeschen & Rickett 1987 for flickering), the question about the origin of the IDV seen in the cm-radio bands is still not solved unambiguously. The models that are under consideration are of either source-intrinsic or extrinsic nature and will be briefly presented in the following (see also Wagner & Witzel (1995) for a review; Cimò 2003; Fuhrmann 2004; Marchili 2009).

2.2.1 The IDV Phenomenon

Variability - if assumed to be intrinsic to the observed source - suggests the size of the compact component that is responsible for the variations due to the light travel time argument (see Chapter 1.2). The spatial resolution of the variable source is restricted to $r \leq c \cdot \Delta t$ with Δt the variability time scale. As the sources are redshifted, the time scale of the source is related to the observer's time scale via $\Delta t_{\mathrm{source}} = \Delta t_{\mathrm{obs}}/(1+z)$. The variability time scale is defined by means of the flux density S and its time derivative via

$$\Delta t_{\mathrm{var}} = \frac{S}{|\frac{\Delta S}{\Delta t_{\mathrm{obs}}}|}\frac{\delta}{1+z} \tag{2.6}$$

(see, e.g. Marscher & Gear 1985; Rybicki & Lightman 1979). The IDV behaviour is classified according to the variability time scale t into long-term variable **type I** ($t \gg 50$ hours in the observer's frame) and short-term variable **type II** ($t < 50$ hours) sources (Heeschen et al. 1987). The first order structure function $SF(\tau)$ is used to differ between the two types (Simonetti et al. 1985).

IDV is mainly observable in compact, core dominated flat-spectrum radio sources that contain ~ 80% of their total flux in the central unresolved region. Observations of a large source sample taken from the S5-radio catalogue (Kühr et al. 1981a,b) revealed that about 30% of compact blazar cores show type II IDV (e.g., Quirrenbach et al. 1992, Wagner & Witzel 1995, Kedziora-Chudczer et al. 2001; Lovell et al. 2003, 2008), one of which is the quasar 0917+624 (z=1.446), that is subject of this thesis. Compactness and small viewing angles seem crucial ingrediences in order to show IDV behaviour.

The maximum angular extend of a variable component can be derived in terms of the variability duration Δt via

$$\theta = \frac{(1+z)^2}{D_{\mathrm{L}}} c\Delta t \tag{2.7}$$

where D_{L} is the luminosity distance for flat cosmologies with cosmological constant according to Pen (1999), equation (1). Together with equation 2.2 one can derive a variability brightness temperature for this variable component which displays a flux variation ΔS using

$$T_{\mathrm{B}} = 4.5 \cdot 10^{10} \Delta S \left(\frac{\lambda D_{\mathrm{L}}}{\Delta t (1+z)^2} \right)^2 K \tag{2.8}$$

with flux density ΔS given in Jy, wavelength λ in cm, luminosity distance D_{L} in Mpc, and time scale Δt in days.

Radio IDV is characterised by pronounced variations in total as well as in linearly polarised flux density. The variability is frequency and source dependent. An important measure to describe the source variability is the so-called modulation index $m[\%] = 100 \cdot \frac{\sigma_S}{<S>}$, where σ_S is the rms flux density variation and $<S>$ the time-averaged flux density. Variations in total flux density usually range between 5-10% (e.g., Quirrenbach et al. 2000; Kraus et al. 2003), whereas variability in linear polarisation is usually stronger and faster by up to a factor of two. Total and polarised flux density variations often occur either correlated, as is the case for 0716+714, or anti-correlated as in the case of 0917+624. The variability timescale has been found to appear as quasi-periodic oscillations occuring at constant amplitudes, e.g., in 0917+624 and 0716+714 (Wagner & Witzel 1995), but also seems to vary as has been observed, e.g., in 0716+714 (Quirrenbach et al. 1991) when a transition from a daily to a weekly variability mode had occured simultaneously in the radio and optical frequency band.

The most 'extreme' cases of IDV sources known today are PKS 0405-385, PKS 1257-326 and J1819+384 (see Kedziora-Chudczer et al. 1997; Bignall et al. 2003; Dennett-Thorpe & de Bruyn 2000). Their very rapid ($\sim$ 0.5 hours) and pronounced variations suggest that these objects might perhaps form an entirely new class of IDV sources. It is, though, not yet clear whether the cause of this extraordinary variability is the same as for the classical IDV sources.

Variations of the polarisation angle are of the order of a few to a few ten degrees (e.g., Kraus et al. 2003). However, polarisation angle swings of 180° have also been observed in the case of 0917+624 (Quirrenbach et al. 1989b) or 1150+81 (Kochenov & Gabuzda 1999). A possibility to explain polarisation IDV is the assumption that the observed radio source exhibits a multiple component structure in its core region. The sub-components seem to be of different compactness, polarisation intensity and orientation of the polarisation angle. This is in good agreement with results from VLBI polarimetry observations. In contrast to flux density variations, polarisation IDV could be directly related to structural changes in the source on VLBI-scales (see, e.g., Gabuzda et al. 2000b,c; Bach 2004). However, the component sizes suggested from IDV timescales are much smaller than the angular resolution that can presently be achieved with ground and space-based VLBI observations (<0.2 mas). Daily polarisation variations have been reported in the VLBI structure of several sources also in the VLBI jet

(0716+714, Gabuzda et al. 2000a), suggesting that polarization IDV occurs frequently in at least some IDV sources.

2.2.2 Intrinsic Explanations

As already addressed in section 2.1.2, the **relativistic jet model** was introduced in order to explain the high brightness temperatures which were derived from variability studies. In this model, knots are moving relativistically in a collimated plasma flow where synchrotron radiation is beamed on small angles to the line of sight towards an observer (Blandford et al. 1977). This implies that the synchrotron radiation gets Doppler boosted, the observed frequency appears higher and the variability time scale shorter (see above). The same is valid for the observed brightness temperature. It is related to the true brightness temperature via

$$T_{\mathrm{B}}^{\mathrm{obs}} \simeq \left(\frac{D}{1+z}\right)^{3} \cdot T_{\mathrm{B}} \tag{2.9}$$

Based on the violation of the IC limit, where apparent brightness temperatures up to 10^{21}K have been deduced from variability studies, it becomes evident that Doppler factors in the range of 100 - 1000 are needed in order to reduce the brightness temperature below the IC limit of 10^{12}K. A lower limit on the brightness temperature in the range of $\sim 10^{11}$K, as was derived from equipartition arguments by Readhead (1994), would require even higher Doppler factors. However, even the fastest apparent speeds observed as of today ($\beta_{\mathrm{app}} \sim 40c$, Marscher et al. 2000) only hold for moderate Doppler factors. Since Doppler boosting is not sufficient in order to explain the occurence of extremely high apparent brightness temperatures in variable sources, further theories have been developed to overcome this problem.

Shock-in-jet models describe the afore mentioned knots in terms of a shock wave passing through an adiabatic, conical, relativistic jet (e.g., Blandford et al. 1977; Marscher 1978). The flux density increases at times when the relativistically expanding jet collides with inhomogeneities of the surrounding medium. The evolution of the emitted synchrotron spectrum follows three stages due to (i) Compton, (ii) synchrotron and (iii) adiabatic (non-radiative) losses. In the first two stages the flux density is expected to increase, whereas adiabatic losses become dominant in the last stage and the flux density decays (Marscher & Gear 1985). The outburst is expected to occur at higher frequencies first. The shock-in-jet models are successful in explaining the different timescales and spectral evolution of observed outbursts. Besides they are able to interpret polarised flux density variations as due to the compression of random magnetic fields in the jet caused by the propagation of the shock wave (e.g., Hughes et al. 1985). The often observed faster and stronger variability in polarised flux density compared to total flux density is attributed to two (or more) closely separated shock waves (Hughes et al. 1989). Furthermore, rapid variations of the polarisation angle suggest a helical structure of the magnetic field where the orientation of the shock wave changes with respect to the jet direction (Königl & Choudhuri 1985).

In order to explain IDV in terms of a shock-in-jet model, very thin shocks are required to explain flux density variations on timescales of one day. This, however, implies negligible radiation losses in contrast to the existing radiation losses in the radio regime (Marscher 1992).

The geometry of the jets also can play an important role, which is explicated in several **geometrical models**. For instance, Camenzind & Krockenberger (1992) introduce the so-called lighthouse effect where non-axisymmetric bubbles of jet plasma are propagating along relativistic magnetised jets. Taking into account the rapid rotation of plasma near a rotating black hole, they relate the observed quasi-periodic outbursts to the fundamental period of the rotating jet plasma provided the jet is well-colimated with an opening angle $\leq 0.1^\circ$.

The lighthouse effect in combination with the shock-in-jet model is used by Qian et al. (1991) in order to explain the fast variations observed in 0917+624. Gopal-Krishna & Wiita (1992) suggest a model where the direction of the shocks propagating down relativistic jets slightly changes. This simple model can reproduce the observed (anti-)correlations between the varying total and polarized flux densities as well as the time lags reported between the extrema of these quantities.

The high brightness temperature problem could also be overcome by adopting a different radiation mechanism: **coherent** anisotropic **emission** (e.g., Melrose 1991) which could replace the prevailing picture of incoherent radiation in synchrotron jets. Coherent emission can be produced by the scattering of energetic electron streams in regions of plasma turbulence as is prevailing in relativistic jets. The mechanism can be a lot more efficient than synchrotron radiation (e.g., Weatherall & Benford 1991). For instance, Lesch & Pohl (1992) suggested a model, in which electron beams emanate from magnetic reconnection zones above the accretion disk which are accelerated to relativistic energies. The electron beams cause instabilities in the plasma and subsequently excite Langmuir waves. This leads to coherent emission of electromagnetic waves by inverse Compton scattering.

Although laboratory experiments have shown that coherent emission is able to enhance synchrotron emission by factors of $\sim 10^6$ (e.g., Benford & Tzach 2000), there is no evidence that this mechanism allows to explain all IDV related phenomena, let alone whether it operates in AGN at all. Besides, it is not understood how the large scale coherent emission can be sustained that is required for distant extragalactic sources to have a significant effect on the total flux density. On the other hand, recent detections of circular polarisation (e.g., Aller et al. 2003; Macquart 2003) might be interpreted as a confirmation of the existence of coherent emission in AGN since it was predicted to occur for coherent mechanisms. It was, e.g., suggested by Begelman et al. (2005) that circular polarisation (CP) could be caused by cyclotron maser emission from relativistic jets.

2.2.3 Extrinsic Explanations

The radiation emitted by compact extragalactic sources propagates through the interstellar medium (ISM) on its way to the observer and is exposed to turbulences or inhomogeneities in the electron density distribution of the ISM. To simplify matters, a thin layer in the ISM is considered as a so-called scattering screen. If the screen is moving with respect to the observer, the phase of an incoming wave is changed due to fluctuation of the refraction index. This leads to spatial variations in the observed flux density. The mechanism is comparable to the twinkling of starlight due to scattering in the atmosphere of the Earth and is known as **Interstellar Scintillation** (ISS). One discriminates between strong and weak ISS depending on the Fresnel scale

$$r_\mathrm{F} = \sqrt{\frac{\lambda D}{2\pi}} \tag{2.10}$$

where λ is the wavelength of the incoming radiation and D is the distance between screen and observer (Narayan 1992). The diffractive scale

$$r_\mathrm{diff} = \frac{\lambda}{2\pi\theta_\mathrm{scatt}} \tag{2.11}$$

is the transverse separation over which the phase fluctuations are coherent and considered to be constant within 1 rad, where θ_scatt is the angular size associated with the electron density distribution that causes the scattering. A source only scintillates if its apparent size is smaller than θ_scatt. For **weak interstellar scintillation** (WISS) $r_\mathrm{diff} \gg r_\mathrm{F}$; and the timescale of WISS is consistent with the Fresnel timescale $t_\mathrm{F} = r_\mathrm{F}/v$ with v the screen velocity relative to the observer.

With increasing wavelength λ or distance D, one approaches the transition between weak and **strong interstellar scintillation** where the diffractive and Fresnel scales are approximately the same. This transition is expected to occur between 1 and 5 GHz (e.g., Walker 1998). A further length scale is introduced in the strong scattering regime, the refractive scale

$$r_\mathrm{ref} = \frac{r_\mathrm{F}^2}{r_\mathrm{diff}} \gg r_\mathrm{diff}. \tag{2.12}$$

If a source size is smaller than r_diff and r_ref, r_diff is dominating which is denoted as **diffractive interstellar scintillation** (DISS) with the related timescale $t_\mathrm{diff} = r_\mathrm{diff}/v$. DISS until recently had only been observed for pulsars, i.e. very small and point-like sources. In contrast IDV sources, although being very compact, are slightly extended and their angular extend merely has to be smaller than $\theta_{\text{scatt}} = r_{\text{ref}}/D$ with the related timescale $t_{\text{ref}} = r_{\text{ref}}/v$. This is referred to as **refractive interstellar scintillation** (RISS - see Figure 2.1 for an illustration of the strong scintillation length scales). However, Macquart et al. (2003) observed short-time variations in the 21 cm lightcurves of the quasar J1819+385 which they interpret in terms of DISS from an extremely compact region of the source.

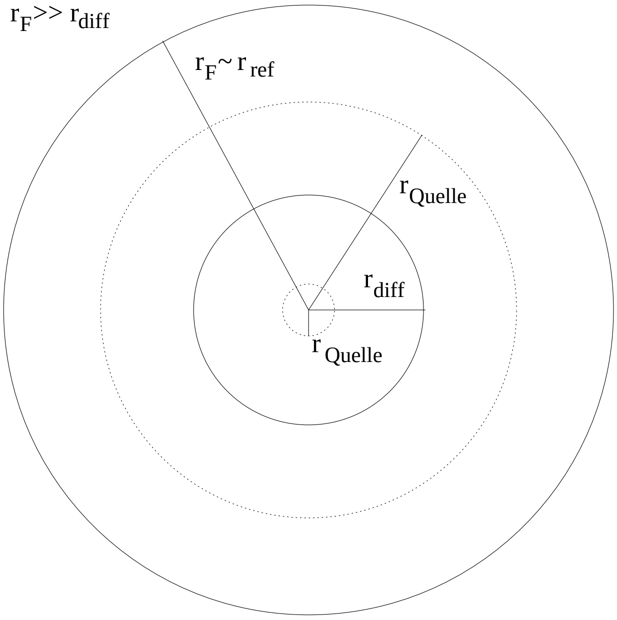

Figure 2.1: *Diagram of the scintillation scales; DISS appears in the regime where* $r_{\text{source}} \ll r_{\text{diff}}$*, RISS occurs for* $r_{\text{diff}} < r_{\text{source}} < r_{\text{ref}}$ *(Friedrichs 2003).*

If the scattering screen is located beyond the solar system and for observational frequency $\lesssim$1 GHz, the source size is always much larger than the Fresnel scale and the amplitude of the variations is quenched. The typical variability timescale is stretched by the large size of the source (Beckert et al. 2002).

Since the angular size of variable sources is typically smaller than the Fresnel scale, RISS is certainly causing short-time variability in the source flux. Moreover, polarisation variability can also be interpreted in terms of interstellar scintillation (Rickett 2001; Rickett et al. 2002a,b; Qian et al. 2002). Even the 180°-swing of the polarisation angle observed in some sources could be explained by means of multi-component models within the ISS theory (e.g., Qian et al. 2006, 2007).

Within the RISS scenario, the *annual modulation* model describes a seasonal change of the variability timescale due to the Earth's orbital motion around the sun (Bondi et al. 1994). The modulation is caused by changes of the transverse velocity of the Earth with respect to the scattering medium and depends on three different parameters: the orbital motion of the Earth, the Sun's motion towards the solar Apex and the motion of the scattering screen relative to the

Local Standard of Rest (LSR). The annual modulation scenario could successfully be applied for several IDV sources already, e.g., for J1819+3845 (Dennett-Thorpe & de Bruyn 2003), PKS 1257-326 (Bignall et al. 2003), or 1128+592 (Gabányi et al. 2007).

It was also proposed that **microlensing** could initiate short-time variability. The deflection of the light of extragalactic objects caused by the gravitational field of a foreground galaxy is known as gravitational lensing. Chang & Refsdal (1979) proposed that this effect could also be due to a single star from a foreground galaxy close to the line of sight. The amplification factor of the lense could vary because of the relative movement between source, star and observer which consequently would lead to flux density variations. There are, however, several arguments against this scenario (see, e.g., Wagner 1992): for instance, the variability timescale defined by microlensing requires relativistic velocities for the star transverse to the line of sight which is in contrast to the observed velocities of stars. Besides, microlensing effects are achromatic, i.e., the caused variability should be frequency-independent which is, however, not the case.

Interstellar scintillation in the meantime has become the broadly accepted predominant explanation of the IDV phenomenon. It is for example regarded to be the main cause of the extreme IDV cases previously described. Owing to the fact that IDV sources are found to be very small in size (typically smaller than the Fresnel scale), it is almost certain that they do vary due to ISS. But some effects remain that cannot simply be explained by means of ISS. In particular, scattering in the ISM cannot account for the quasi-periodicity that has been observed in some sources. The radio-optical correlation in the variability pattern of 0716+714 and 0954+658 (Wagner et al. 1996, 1993) is not explicable in terms of ISS either, as towards higher frequencies (optical regime) ISS is virtually non-existent. The observed brightness temperatures which have been derived for IDV sources from ISS theory are somewhat lower compared to intrinsic explanation models, and scale only linearly with the Doppler factor. Nevertheless, brightness temperatures in excess of the IC limit ($\sim 10^{13}$ - 10^{14}) continue to be observed within the ISS scenario (e.g., Rickett et al. 2002b). Therefore, a high Doppler boosting ($\sim 10^{1}$ to 10^{2}) is still necessary depending on the adopted distance of the scattering screen.

2.3 Polarisation Properties of AGN

2.3.1 Magnetic Fields and Synchrotron Radiation

As previously mentioned, magnetic fields are thought to sign responsible for the emergence and existence of the jets of AGN. In fact, the observation of linearly polarised radiation furnished proof that the radio emission of AGN is actually (non-thermal) synchrotron radiation stemming from energetic electrons spiraling around magnetic field lines. While the electrons gyrate in the magnetic field, they are accelerated and emit synchrotron photons in a collimated radiation cone. The emission frequency of the photon is directly related to the speed of the electron. The Larmor or cyclotron frequency ω of an oscillating electron is defined as

$$\omega_{\mathrm{L}} = \frac{eB}{m_{\mathrm{e}}c} \tag{2.13}$$

with magnetic field B, electron charge e, and electron mass m_{e}. In the relativistic case this results in the synchrotron frequency $\omega = \gamma^2\omega_{\mathrm{L}}$ where γ is the Lorentz factor. The relativistic electron radiates in a collimated narrow cone with width of order $1/\gamma$ in the direction of motion.

The energy distribution of an ensemble of electrons $N(E)dE$ is described as a power-law

$$N(E)dE \propto E^{-s}dE \tag{2.14}$$

with spectral index of the electron energy s, which produces a synchrotron spectrum that is also a power-law distribution

$$S(\nu) \propto \nu^{\alpha} \tag{2.15}$$

with spectral index of the synchrotron emission $\alpha = \frac{1-s}{2}$. Thus, we can derive the spectrum of the electron energy distribution s from the spectral index α. At lower frequencies the spectrum declines at the so-called turn-over frequency and the source appears optically thick due to synchrotron self-absorption. The turn-over frequency is defined as (Kellermann & Pauliny-Toth 1969)

$$\nu_{\mathrm{n}} = \frac{c}{\omega}\sqrt{\frac{2S_{\mathrm{n}}}{kT_{\mathrm{B}}\pi(1-z)}} \tag{2.16}$$

with the solid angle of the source ω, brightness temperature T_{B} in K, Boltzmann constant k, flux density at turn-over S_{n} in $\mathrm{W\,m^{-2}\ Hz^{-1}}$, and redshift z. The spectrum of a homogeneous synchrotron component is characterised by an optically thick part (optical depth τ >1 and $\nu < \nu_{\mathrm{n}}$) with a spectral index $\alpha = 2.5$, and an optically thin part (τ <1, $\nu < \nu_{\mathrm{n}}$) with α close to -0.5. Knowing the spectral shape of a source and the size of the emitting region θ, allows to calculate the magnetic field strength (in Gauss) via

$$B = 10^{-5}b(\alpha)\frac{\theta^4\nu_{\mathrm{n}}^5\delta}{S_{\nu}^2(1+z)} \tag{2.17}$$

with Doppler factor δ, source flux density S_{ν} in Jy, and $b(\alpha)$ a tabulated value of the spectral index according to Marscher (1983).

2.3.2 Polarisation and Stokes Parameters

Synchrotron radiation exhibits a high degree of polarisation, particularly in the optically thick part. If relativistic electrons are located in an ordered magnetic field, which is supposed to be the case in relativistic jets of AGN, they will produce linearly polarised radiation. The degree of linear polarisation (LP) is defined as

$$\Pi = \frac{s+1}{s+7/3}. \tag{2.18}$$

For a typical spectral index of the electron energy $s = 2$, this results in a polarisation degree of about 70%.

In the following, a brief mathematic summary on polarisation characteristics is given. More details can be found, e.g., in Friedrichs (2003) or Jackson (1975). In general, a monochromatic electromagnetic wave is elliptically polarised. This can be described by the superposition of either two linearly polarised or two circularly polarised waves. Regarding the case of two circularly polarised waves, it is

$$\mathbf{E}(\mathbf{x}, t) = (\epsilon_+ \mathbf{E}_+ + \epsilon_- \mathbf{E}_-) e^{i\mathbf{k}\cdot\mathbf{x} - i\omega t} \tag{2.19}$$

with complex orthogonal unit vectors $\epsilon_\pm$, and complex amplitudes $E_{+/-} = a_{+/-} e^{i\delta_{+/-}}$. $\delta_- - \delta_+$ is the phase difference between the two circularly polarised waves. The **Stokes parameters** are defined via

$$\begin{aligned} I &= a_+^2 + a_-^2 && (2.20)\\ Q &= 2a_+ a_- \cos(\delta_- - \delta_+) && (2.21)\\ U &= 2a_+ a_- \sin(\delta_- - \delta_+) && (2.22)\\ V &= a_+^2 - a_-^2 && (2.23) \end{aligned}$$

I describes the total intensity, Q and U taken together identify the LP, and V specifies the CP of the wave. The polarisation angle results from

$$\chi = \frac{1}{2} \arctan\left(\frac{Q}{U}\right). \tag{2.24}$$

A monochromatic wave is completely polarised which implies

$$I^2 = Q^2 + U^2 + V^2 \tag{2.25}$$

whereas in the case of a superposition of multiple waves, Stokes parameters averaged over time have to be considered. Hence, the wave is not completely polarized and it is

$$I^2 > Q^2 + U^2 + V^2 \tag{2.26}$$

Extragalactic radio sources usually exhibit LP in the order of a few percent, while mostly CP $\leq 0.1\%$ (e.g., Weiler & de Pater 1983; Komesaroff et al. 1984), which is generally below the detection limit. Hence, CP is considered to be negligble in this work and only LP is regarded.

There was a large temporal gap between early integrated CP measurements carried out from the 1970s to early 1980s and the high-resolution VLBA measurements that started in the mid 1990s. Recently, however, several observations yielded in the detection of CP in a number of extragalactic radio sources (e.g., Homan & Wardle 1999; Aller et al. 2003, 2006a,b; Homan & Lister 2006; Gabuzda et al. 2008), which could not least be attributed to the improvement of facilities (Rayner et al. 2000, Australia Telescope Compact Array - ATCA) and techniques for deriving CP information on parsec scales (Homan & Wardle 1999). Aside from CP being produced as an intrinsic component of the emitted synchrotron radiation, another more favorable mechanism is the Faraday conversion of linear polarization into circular during propagation through a magnetised plasma (Jones & Odell 1977; Wardle & Homan 2003). Faraday effects will be briefly addressed to in the following section.

2.3.3 Faraday Rotation and Depolarisation

If a linearly polarised wave travels through a magneto-optic plasma it will experience **Faraday rotation**. The incident wave is decomposed into two circularly polarized rays which propagate at different speeds which causes a rotation of the polarisation angle:

$$\Delta\chi = \mathrm{RM} \cdot \lambda^2 \tag{2.27}$$

where RM is the rotation measure that is determined by the integral of the electron density and the dot product of the magnetic field and the path length along the line of sight. Knowing the RM should in princple enable to back-extrapolate the observed polarisation angle to the true intrinsic one via $\chi(\lambda) = \chi_0 + \mathrm{RM}\lambda^2$. Two problems occur in the determination of the Faraday rotation. One is the polarisation angle suffering from a 180°-ambiguity which could be overcome by observing at two different frequencies, where $\lambda_1 = \sqrt{2}\lambda_2$ as was suggested by Reuter & Klein (1996). The other difficulty is a source-intrinsic effect where single source components at different frequencies make multiple contributions to the overall source polarisation. This cannot be resolved in single-dish observations and could mimic an additional rotation.

A further effect is the **Faraday depolarisation** of polarised waves. This is caused by different electron densities or magnetic field strengths within single patches of the magnetised medium meaning that the polarisation angle is rotated differently in each patch. If those patches are too small to be resolved by the telescope beam, the observed polarisation vector will be the sum of numerous states of the according patches which might result in a smaller degree of polarisation following

$$P(\lambda) = P(0)\exp(-const \cdot \mathrm{RM}^2 \cdot \lambda^4) \tag{2.28}$$

according to Burn (1966). This also applies to the afore mentioned intrinsic depolarisation where the superposition of several components within a source cannot be resolved by a single telescope. VLBI measurements, however, due to their higher resolution enable to observe single components in some sources with considerably higher degrees of polarisation (e.g., Gabuzda et al. 1992).

2.4 Precession of the Jet Base

From kinematic analyses of long-term VLBI observations it has been deduced that an increasing number of sources displays a regular or irregular swing of the innermost jet structural position angle in the plane of the sky (e.g., in BL Lac, Stirling et al. 2003; in OJ 287, Tateyama & Kingham 2004; in 3C 345, Lobanov & Roland 2005; in S5 0716+71, Bach et al. 2005; in 3C 273, Savolainen et al. 2006; in 1803+784 Kudryavtseva et al. 2006; in NRAO 150, Agudo et al. 2007). The reported time scales range typically between 2 and 15 years and structural position-angle oscillations show amplitudes between ~25° and 45°. This precession of the base of the jet is not yet understood but it seems to be related to jet-curvature or helical structures that have been observed in the jets of AGN also on larger scales, in the sense that the triggering mechanism is supposed to be the same in both cases. A regular precession of the accretion disk is often cited as one possible explanation. Mathematical descriptions of the precessing jet model have been given previously, e.g., in the case of 3C279 (Carrara et al. 1993; Abraham & Carrara 1998) or in the case of 3C345 (Qian et al. 1992; Steffen et al. 1995; Qian et al. 1996a). Various theories exist that are trying to shed light on the cause of this interesting phenomenon, e.g.:

- **Binary Black Holes Scenario:** As already explicated in Chapter 1.1.2, it appears likely that in the course of galactic evolution galaxies regularly undergo merging events. The central black holes of the two interacting systems will meet in the center of the newly formed system and eventually coalesce. But before they form one single supermassive black hole, there will be a period in which the two bodies encircle each other. Provided one (or both) black hole(s) is/are surrounded by an accretion disk and emit(s) jets along their rotation axis, the accretion disk(s) will experience gravitational torques which will finally lead to twisted jets. This scenario has already been proposed for several sources such as 3C345, OJ287 or PKS 0420-014 (Klare 2003; Klare et al. 2005; Lobanov & Roland 2005; Valtonen et al. 2008; Britzen et al. 2001). An example for the binary black hole model and its mathematical application to VLBI data is described in Appendix C according to Roland et al. (2008). In the framework of this thesis, the model was applied to one selected dataset that resulted from the kinematic analysis of the VLBI observations of 0917+624. The result is presented in Chapter 5.2.5.

- **Kelvin-Helmholtz Instabilities** can emerge when velocity shear is present within a continuous fluid or, when there is sufficient velocity difference across the interface between two fluids. The theory can be used to predict the origin of instability and transition to turbulent flow in fluids of different densities and speeds and was applied to model helical structures in relativistic jets (e.g., Hardee 2003; Perucho et al. 2006).

- **Lense-Thirring Effect:** Also known as rotational frame-dragging, the Lense-Thirring effect is a prediction resulting from general relativity in which the rotation of an object would alter space and time, dragging a nearby object out of position. The effect was first predicted by Austrian physicists Joseph Lense and Hans Thirring in 1918. Relativistic jets may furnish proof for the reality of frame-dragging. Gravitomagnetic forces produced by the Lense-Thirring effect within the ergosphere of rotating black holes combined with the Penrose mechanism[2] (Penrose 1969) have been used to explain the observed properties of relativistic jets. Williams (1995, 2004) proved this theory to be able to extract relativistic particle energy and subsequently showed that it is a possible mechanism for the formation of jets.

---

[2] The Penrose mechanism is a process theoretised by Sir Roger Penrose in which energy can be extracted from a black hole.

Chapter 3

The Quasar 0917+624

Extragalactic compact flat spectrum radio sources are known to be highly variable and about 30% of them show intra-day variability (IDV) (e.g., Quirrenbach et al. 1992, Wagner & Witzel 1995, Kedziora-Chudczer et al. 2001). 0917+624 is a type-II IDV quasar at a redshift of z = 1.446. The source used to be strongly variable on timescales of 0.5 to 1.6 days with modulation indices[1] m of 3 to 5% at cm-wavelengths from 1985 to 1998 (Heeschen et al. 1987, Quirrenbach et al. 1992, Kraus et al. 2003). Moreover, in the polarised flux, as well as in the polarisation angle, even faster variability was detected with modulation indices ranging between 15 and 30 %; the polarised flux usually being anti-correlated with the total flux (Quirrenbach et al. 1989b, Kraus et al. 2003). Figure 3.1 shows a typical example of lightcurves for total and polarised intensity and polarisation angle changes during a 2.5 days observation with the Effelsberg 100m telescope in June 1993. A visual inspection already reveals the afore mentioned anti-correlation between total and polarised intensity (top and middle panel respectively).

On milliacrsecond-scales, the source structure consists of a compact core with a jet emerging in north-western direction at a position angle $\Theta \sim -60°$, and after about 0.5 mas pointing in northerly direction ($\Theta \sim -30°$). 1.45 GHz-maps from the archive of the Very Large Array (VLA) reveal that on arcsecond-scales the source is mainly pointlike showing a jet-like feature developing 15 arcsecs to the south-west. Standke et al. (1996) showed a VLA-map at 8.4 GHz that displays some weak source structure 4 arcsecs from the core at a position angle of about -135° at the 5σ level which needed to be confirmed according to their estimation. However, this feature was observed earlier by Murphy et al. (1993) as well. Taken altogether, this indicates that there is a strong misalignment between the jet on the inner and outer kpc-scales (see also Figure 3.2).

---

[1] $m[\%] = 100 \cdot \frac{\sigma_S}{<S>}$, where σ_S is the rms flux density

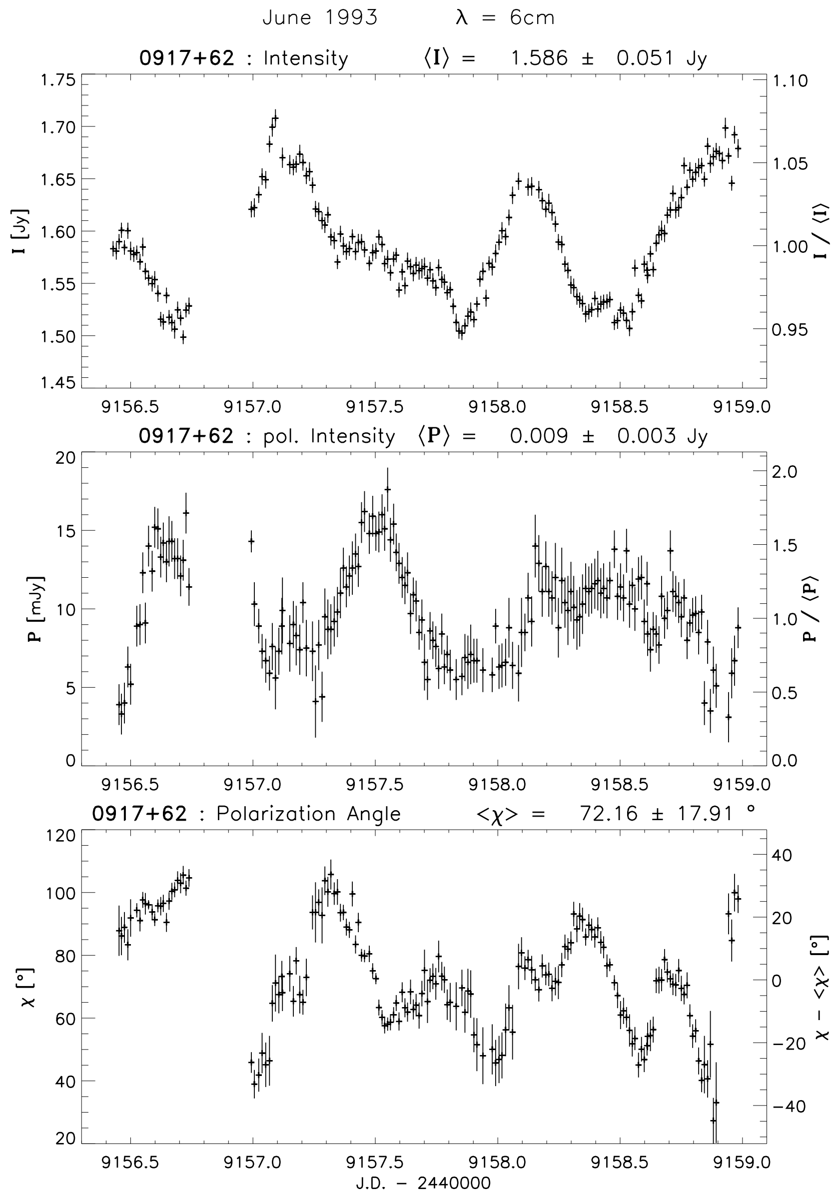

Figure 3.1: *5 GHz lightcurves of 0917+624 observed with the 100m Effelsberg telescope in July 1993, courtesy of A. Kraus. Panels show from top to bottom total intensity, polarised intensity, and polarisation angle plotted versus time (J.D. in days).*

In 1989, Quirrenbach et al. (1989b, 2000) observed a 180° polarisation angle swing event in 0917+624 within one day (J.D. 2447526). They interpreted this event in terms of a helical jet model where potentially a relativistic shock propagates along the jet, which illuminates the jet's helical magnetic field by enhanced synchrotron emission. This is an interpretation of a model proposed by Königl & Choudhuri (1985) concerning polarization angle swing events on timescales of months or years, applied to intraday timescales. Their model is based on the effects of relativistic aberration when the transverse component of the magnetic field constantly rotates along the jet.

In the subsequent years, the polarization angle swing event has been subject to numerous attempts of interpretation. For instance, Qian et al. (1991, 2002) suggested a two-component model within a relativistic shock-in-jet model with one steady polarized component and another one produced by the shock, which is variable in in its degree and angle of polarisation. The vector combination of both components could then produce the observed polarisation angle swing where the variations of the shock component only need to occur on small scales. Gopal-Krishna & Wiita (1992) proposed thin relativistic shocks moving on slightly bent trajectories causing correlated as well as anti-correlated variations in total and polarised flux in IDV sources. In this case the shock component would change its degree of polarisation because of relativistic aberration effects.

Although Rickett et al. (1995) tried to explain the variations in intensity and polarisation of 0917+624 within a scintillation model, they could not account for the polarisation angle swing event and suggested, it could be due to low-level intrinsic variability. However, it remained unclear to what extent RISS and intrinsic variability have to work together in order to produce the polarisation angle swing of 180°. Simonetti (1991) attempted to explain the swing event in terms of refractive focussing-defocussing by an interstellar shock passing in front of the source. Within this model, the source is supposed to have two polarised components with their polarisation angles differing by $\sim$ 90°. As the shock is passing the line of sight, the first component is strongly focussed, inducing a rapid increase in total and polarised intensity such that the overall source polarisation angle will be close to that of the first component. With the postshock passing in front of the source, the first component is defocussed again, showing a rapid decrease in its total and polarised intensity and the source polarisation angle is dominated by that of the second component. However, this assumption can only account for a 180° jump and not for a continuous variation, as has been observed by Quirrenbach et al. (1989b), and Simonetti (1991) suggested that some intrinsic mechanism or focussing by another cloud might be responsible for that. Besides, the rapid increase in total flux density, as proposed by the refractive focussing-defocussing model, had not been measured either.

It has been only recently, that approaches have been made to interpret short-term polarisation angle swings in terms of RISS by a continuous medium or refractive focussing-defocussing by interstellar clouds. For instance, Kochenov & Gabuzda (1999) reported a polarisation angle swing event observed in the source QSO 1150+812, which was interpreted by Qian et al. (2006) in terms of refractive focussing-defocussing by interstellar clouds serving as a plasma-lens, assuming a 3-component model. The angle swing event in 0917+624 was also explained in this sense, but here a 4-component model, consisting of one non-polarised and three polarised components, was necessary in order to substantiate the underlying physics not only concerning the angle swing but also the variations in total and polarised intensity (Qian et al. 2007).

In September 1998, Kraus et al. (1999) discovered that the rapid variability had stopped and instead a slow, monotonic increase of 7% in total flux density was observed during the 5-day observing session. Observations made in February 1999 revealed that 0917+624 was varying again on a time scale of 1.3 days. However, since September 2000 the variability of the source has ceased again, showing only moderate modulation indices of the order of $\sim$ 0.5% until April 2002 (see Fuhrmann et al. 2002, Fuhrmann 2004).

The question whether the origin of IDV is source extrinsic, i.e. due to scintillation in the Interstellar Medium (ISM), or intrinsic, is still not solved. The shock-in-jet model has, for instance, been proposed in the case of 0917+624 by Qian et al. (1991, 1996b). It is expected, though, that IDV blazar cores feature micro- or even nanoarcsecond angular sizes and therefore must scintillate through the ISM, as has also been suggested for 0917+624 (e.g., Rickett et al. 1995; Jauncey & Macquart 2001). Qian et al. (2002) present a combination of extrinsic and intrinsic effects, which could appropriately explain results obtained from multifrequency polarisation observations. After the subtraction of scintillation-induced effects, an additional variable component remained which was subsequently interpreted in terms of a shock model. Whether it be extrinsic or intrinsic, possible explanations for the reduced IDV activity could be, e.g., that the scintillating medium has changed (e.g., strength of turbulence, distance), or the flux of the scintillating component(s) has now decreased and become less dominant. Another possibility is a general change in the alignement of the source relative to the line of sight owing to the precession of the footpoint of the jet, which has been proposed in the cases of 0716+714 (Bach et al. 2005) and 1803+784 (Kudryavtseva et al. 2006). The size of the VLBI core changes with time due to its changing orientation towards the line of sight.

A possibility to explain the behavior of 0917+624 within an ISS model was given by Rickett (2001) (see also Jauncey & Macquart 2001). They suggested that the observed change in the variability time scale depends on the time of the year and thus reflects the orbital motion of the Earth relative to the ISM. Fuhrmann et al. (2002) further investigated the applicability of this so-called annual modulation scenario (see page 19) for 0917+624 by means of a one-year

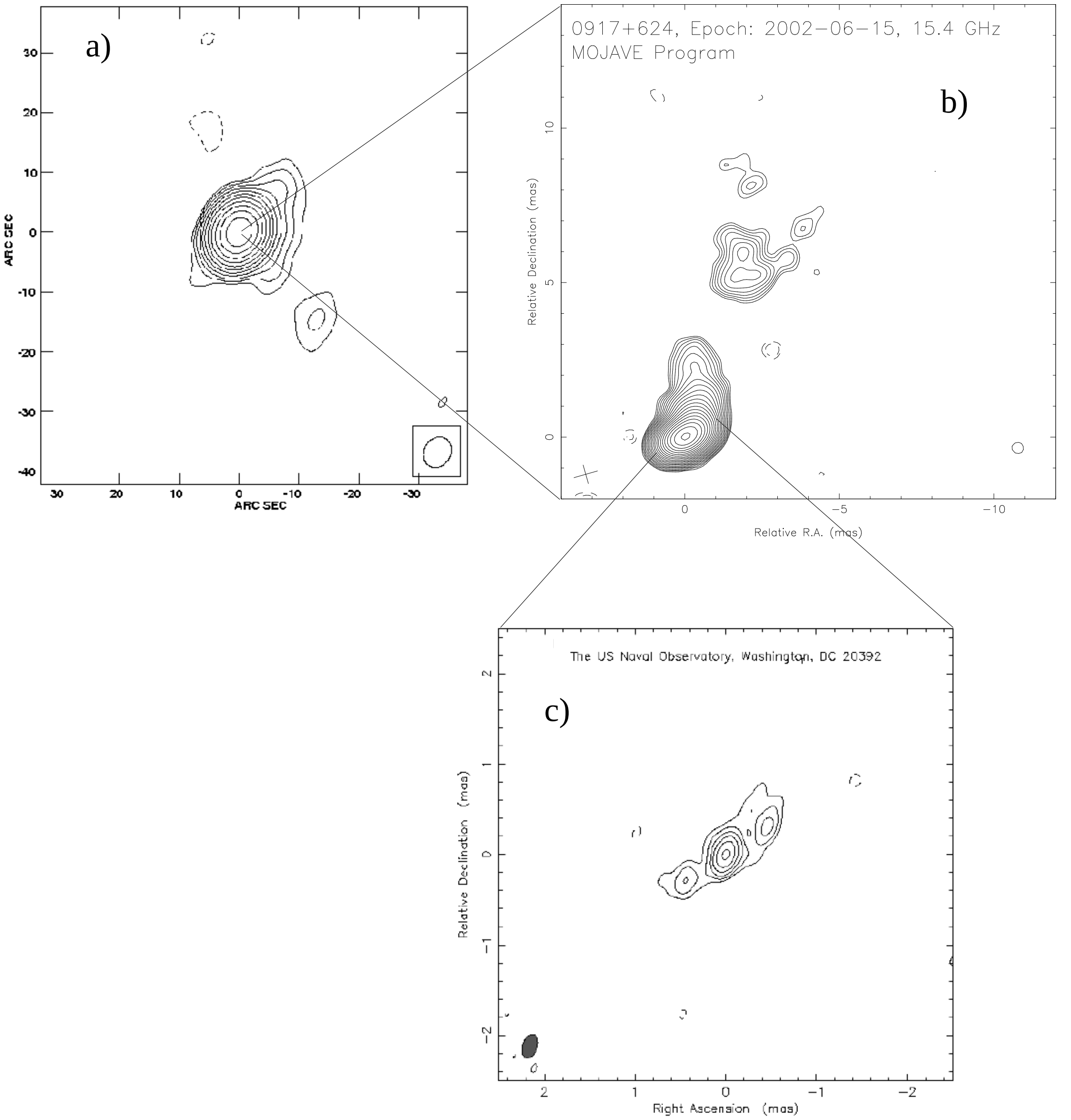

Figure 3.2: *0917+624 maps observed at different frequencies showing the strong misalignment between the jet on kpc and pc-scales; a) VLA-map at 1.45 GHz, June 1994, beam (5.34×4.41) mas; b) 15 GHz map of 0917+624 observed in June 2002, taken from the MOJAVE/2cm Survey Data Archive; 43 GHz map taken from the Radio Reference Frame Image Database (RRFID).*

6cm-flux monitoring program with the Effelsberg telescope. This could, however, not confirm the model predictions. Instead, the source showed a radical change in its IDV behaviour by reducing its variability (see above). Meanwhile though, recent studies by Marchili (2009) with the Chinese Urumqi 25-m radio telescope seem to support the applicability of an annual modulation model in the case of 0917+624 provided that the scattering screen is much closer to the earth ($\leq$ 50pc) than previoulsy concluded by Rickett et al. (1995); Rickett (2001) of the order of 170 - 200 pc.

The earlier slow-down of 0917+624 in September 1998 was interpreted by Kraus et al. (1999) as probably due to either a disappearance of the scintillating compact component or an increase in its angular size, which could be caused by the ejection of a new jet component (see also Krichbaum et al. 2002). The ejection could temporarily lead to a core size exceeding the Fresnel scale defined by the scattering medium. Consequently, only strongly quenched scintillation is observed. When the component moves further down the jet, it will separate from the core at some point whereby the size of the scintillating component decreases again. At that time, the variability is expected to reappear. However, this has not been the case - at least until April 2002. Given that the variability ceased again in 2000, even more than one component should have been emitted since. In order to test this scenario, we analysed several epochs of VLBI observations of 0917+624 over a period of eight years (1999 to 2007) which were partly performed at different frequencies. The analysis and results are described in Chapter 5.

Chapter 4

Effelsberg Flux Density Monitoring of 0917+624

As 0917+624 has established to be a prominent IDV source, it is - among other sources - frequently monitored with the Effelsberg 100-meter radio telescope of the Max-Planck-Institut für Radioastronomie in Bonn (see Figure 4.1). A monitoring program was set up in order to test the reliability of the annual modulation model and to search for new IDV and calibrator sources. The available Effelsberg data of 0917+624 observed after 2000 were so far only reduced in total intensity - that is in terms of variability analyses (Fuhrmann et al. 2002, Fuhrmann 2004). Hence, I continued the data reduction focussing also on the polarisation characteristics. My aim was to investigate the polarisation variability behavior in order to further complement our current knowledge about the source in this parameter space. The analysis of the total intensity data was carried out in left hand circular polarisation only which is still a sufficient approximation to the results for total polarised intensity since the total intensity is defined as $I = \frac{1}{2}(LL + RR)$ where R and L denote the right and left hand circular feeds of the receiving system[1]. The observing technique and data reduction steps for the Effelsberg 100m telescope have already been described in detail in previous works (see, e.g., Quirrenbach et al. 1989a, Kraus 1997, Fuhrmann 2004, Fuhrmann et al. 2008). Hence, I will merely give a brief summary on the applied methods.

4.1 Observations and Data Reduction

From the available data that have been obtained with the Effelsberg telescope at 4.85 GHz, I took a subsample observed between March 2001 and December 2004 which has a sufficient observational duration of at least 24 hours up to 80 hours. Three epochs with single measurements were added, which were observed during the VLBI experiments described in Chapter 5. The

---

[1] Is it assumed that $V \simeq 0$, i.e. $LL \simeq RR$

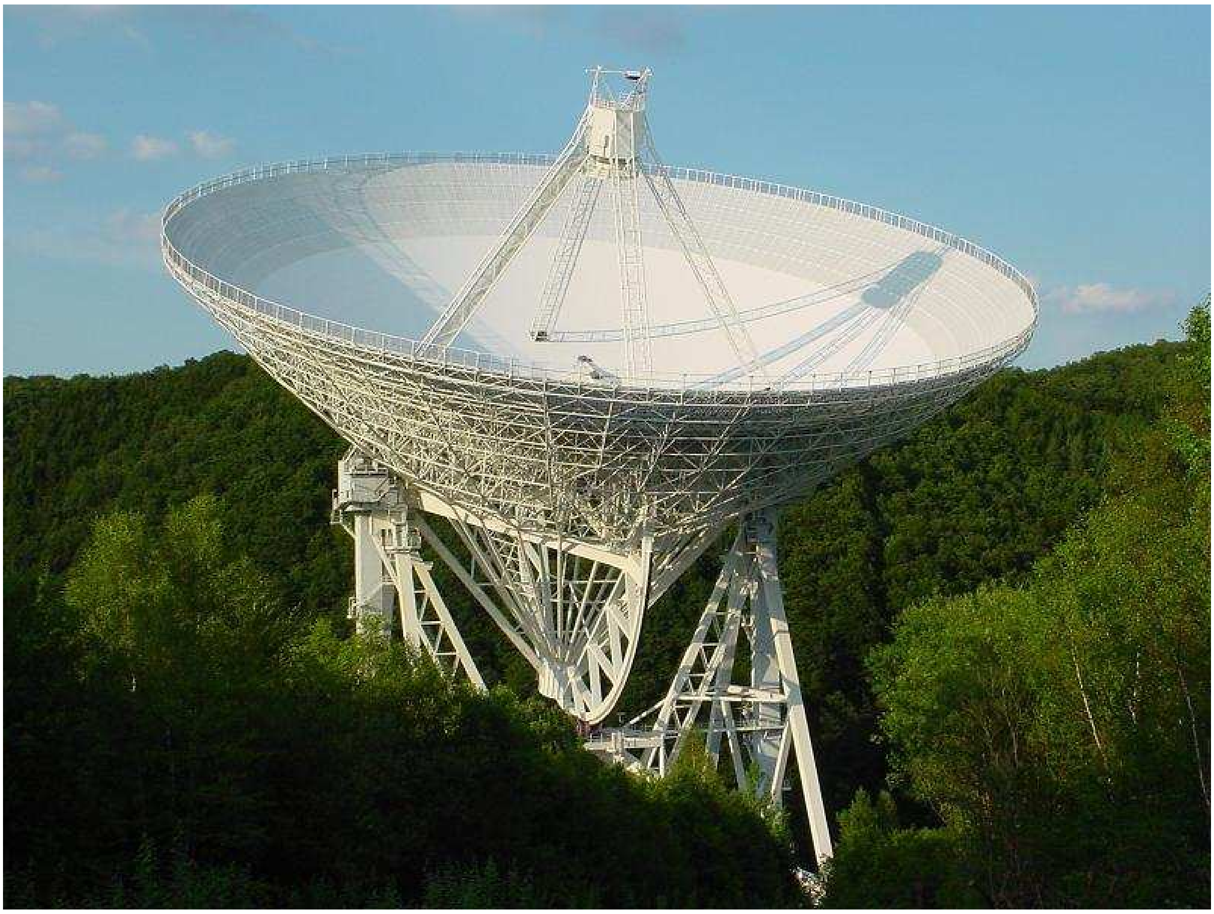

Figure 4.1: *The 100-meter telescope of the Max-Planck-Institut für Radioastronomie located in a valley near Effelsberg, Eifel region.*

appropriate epochs are listed in the first column of Table 4.1. Although various sources had been observed, I am only concentrating on the results for 0917+624. Other - non-variable - sources included in the observations for calibration purposes were, e.g., 0836+710 and 0951+699 for gain and time-dependent corrections (see below) and standard flux density calibrators such as 3C286, 3C48, and NGC7027.

The observations were carried out with the 4.85 GHz receiver, that is mounted in the telescope's secondary focus. It consists of two horns enabling 'software beam-switching' (Emerson et al. 1979): by means of a second horn, which is directed next to the source position, the atmospheric contribution to the measurements can be determined and subtracted from the source signal in the subsequent data reduction process. It is a 4-channel system, the frontend consisting of two dewars, each of them containing one horn, a cooled directional coupler, circular (RHC and LHC) transducer and 2 High Electron Mobility Transistor (HEMT) amplifiers. The backend comprises a ZF-polarimeter and delivers both total power and full polarisation information of the received signal.

The measurements were done using cross-scans in azimuth and elevation across the source position, which results in Gaussian profiles with an amplitude proportional to the measured flux density. The cross-scan method is best suited for short-time variability observations since the compact and bright sources appear point-like within the telescope beam. From the difference between real target position and observed maximum the pointing offset can be determined and be corrected. The number of sub-scans and duration depends on the source brightness at the observed frequency and in the given case was usually eight for the stronger sources (~ 1 Jy) and 12 for the weaker ones with a duration of 20-30 seconds per scan. The scan length is equivalent to 4-5 times the half power beamwidth (HPBW) of the telescope beam, which is necessary to determine the noise level and baseline left and right hand of the source. In the case of a 4.85 GHz observation, the HPBW corresponds to 144”.

4.1.1 Data Reduction Steps

- **CONT2:** For a start, the Gaussian fit is applied to the observed signal using the program CONT2 which is part of the MPIfR’s software package TOOLBOX, the standard Effelsberg data reduction package. The fit results in the signal amplitude as a measure for the flux density of the source, the pointing offset from the center position and the measured HPBW. Afterwards, poor-quality sub-scans have to be removed from the data. For IDV measurements, this procedure is based on the following criteria: the amplitude should deviate less than 5 % from the mean; the pointing error should differ less than 10 % from the HPBW and the measured HPBW should lie within 10 % of the average value. For the polarisation analysis, the Stokes parameters Q and U have to be fitted in a similar way. However, since the polarised signals are generally very weak, the sub-scans in one driving direction are first averaged using fixed position and HPBW. This implies, that the amplitude remains the only free fit parameter and makes a pointing correction redundant.

- **Pointing Correction:** The following steps make use of the software which A. Kraus developed in the scope of his thesis (Kraus 1997). In order to apply the pointing correction, first of all the mean deviation from the center position of the scans in azimuth and elevation and the average HPBW are determined. Assuming a two-dimensional Gaussian profile, one can now calculate the deviation of the measured amplitude S from the center position in one direction by means of the pointing offset in the other direction. As an exemplification, the correction in elevation is given by

$$S_{elv}^{corr} = S_{elv} \cdot exp(4 \cdot ln2 \cdot \frac{x_{azi}^2}{\theta_{azi}^2}) \tag{4.1}$$

where x_{azi} is the pointing offset and θ_{azi} is the HPBW in azimuth. By means of the average values, a correction factor is determined and applied to all sub-scans in azimuth and elevation respectively. Afterwards, all sub-scans are averaged using a weighted mean.

- **Gain Correction:** In general, the heavy construction of radio telescope parabolic dishes leads to gravitational deformation of the dish surface with changing elevation. Correspondingly, the surface accuarcy changes and the focal point is shifted which influences the sensitivity of the telescope. The Effelsberg 100m dish was constructed according to the principle of 'homologous deformation' meaning that a gravitational distortion of the dish always transfers into another paraboloid. Hence, an adjustment of the focus in three axes during changes in elevation always keeps the receiver in the focal plane. However, the sensitivity is a function of changing elevation due to the distortion of the surface, being highest around 35° and decreasing towards higher and lower elevation. Besides, the atmospheric absorption increases with decreasing elevation. This is usually corrected for separately (so-called τ correction), especially in case of higher frequencies ($> 5\,\mathrm{GHz}$). To be able to compensate for these effects, secondary non-variable calibrators are frequently observed additionally to the target sources, ideally covering a great part of the whole elevation range. The normalised amplitudes plotted versus elevation can best be represented by a second-order polynomial ('gain curve') which is used to remove the distortion effects from the data. In case of the present observations, 0836+710 and 0951+699 were regularly observed for this pupose and some other sources were added when available.

- **Time-dependent Corrections:** Additional effects on the flux density result from changes in weather, thermal expansion of the telescope dish leading to focus changes, fluctuations in the receiving system, etc. These time-dependent systematics can also be removed by means of a mean correction curve fitted to the secondary calibrator fluxes over the complete observing time range.

  Finally, the measured amplitudes of all sources have to be adjusted to the absolute flux density scale (Baars et al. 1977, Ott et al. 1994) using the primary calibrator measurements which were frequently monitored.

  It turns out that the errors according to error propagation of the applied corrections are generally smaller than the uncertainties remaining from the scatter of the secondary calibrators. Hence, the resulting errors from the uncertainties of the calibrator sources are assigned to the final error values. This leads to error measurements below one percent, under good observing conditions even $\lesssim 0.3\%$.

- **Corrections for Polarisation:** The polarisation data are calibrated according to the method of Turlo et al. (1985). The observed signal is regarded as a vector consisting of the three Stokes parameters I, Q, and U (ommitting small circular polarisation V). The true (source intrinsic) flux densities can now be described using a 3×3 matrix[2], called Müller matrix M_{ij}:

$$S^{\mathrm{obs}}(I, Q, U) = ||M_{\mathrm{ij}}||S^{\mathrm{true}}(I, Q, U) \tag{4.2}$$

with i,j=1,2,3. The Müller matrix can be decomposed into a matrix T describing the instrumental effects (D-terms) and a matrix P containing the parallactic angle (γ) rotation:

$$\left\{\begin{array}{c} I^{\mathrm{obs}} \\ Q^{\mathrm{obs}} \\ U^{\mathrm{obs}} \end{array}\right\} = \left\{\begin{array}{ccc} T_{11} & T_{12} & T_{13} \\ T_{21} & T_{22} & T_{23} \\ T_{31} & T_{32} & T_{33} \end{array}\right\} \left\{\begin{array}{ccc} 1 & 0 & 0 \\ 0 & cos2\gamma & sin2\gamma \\ 0 & -sin2\gamma & cos2\gamma \end{array}\right\} \left\{\begin{array}{c} I^{\mathrm{true}} \\ Q^{\mathrm{true}} \\ U^{\mathrm{true}} \end{array}\right\} \tag{4.3}$$

It is necessary to frequently observe calibrator sources of known high polarisation (such as 0836+710), i.e., covering an utmost large range of the parallactic angle, in order to determine the T matrix. The use of data from unpolarised sources (e.g., 0951+966) further helps to improve the analysis, in particular for the adjustment of the matrix elements T_{21} and T_{31}, which describe the instrumental polarisation. With known S^{true} and the measured quantities S^{obs} and parallactic angle γ, one can derive the elements T_{ij} by means of three least-square-fits, one for each Stokes parameter. Now the correction can be applied by inverting Equation 4.3. Since in practice the influence of polarised flux density on total flux density is usually negligible (regarding matrix elements T_{12} and T_{13}), only Stokes parameters Q and U are corrected for using I_{obs}:

$$\left\{\begin{array}{c} Q^{\mathrm{true}} \\ U^{\mathrm{true}} \end{array}\right\} = \left\{\begin{array}{cc} cos2\gamma & -sin2\gamma \\ sin2\gamma & cos2\gamma \end{array}\right\} \left\{\begin{array}{ccc} \hat{T}_{21} & \hat{T}_{22} & \hat{T}_{23} \\ \hat{T}_{31} & \hat{T}_{32} & \hat{T}_{33} \end{array}\right\} \left\{\begin{array}{c} I^{\mathrm{obs}} \\ Q^{\mathrm{obs}} \\ U^{\mathrm{obs}} \end{array}\right\} \tag{4.4}$$

where $\hat{T}_{\mathrm{ij}}$ denotes for the inverted correction matrix T^{-1}. The uncertainties are again estimated by means of the secondary calibrators as in the case of total intensity.

The final calibration of the polarisation data is done by means of the calibrator source 3C286 which has proven to be non-variable in the cm regime. At 4.85 GHz, the values are 11.0 % for percental polarisation and 33° for the polarisation angle (Kraus 1997 and references therein). The individual measurement errors are typically $\Delta P \sim 5\,\%$ for polarised intensity and $\Delta\chi$= 1-3 ° for polarisation angle. In case of highly polarised sources the errors are even lower. A gain and time-dependent correction, as done for total intensity, is usually not applied for Q and U.

---

[2] If circular polarisation has to be taken into account, the matrix has to be generalised to a 4×4 matrix.

4.1.2 Tools for IDV Analysis

The observed time dependent flux density variations yield a time series which is characterized using the following basic parameters.

- **Modulation Index** m gives the strength of the observed variability as a function of mean flux density $\langle S\rangle$ and its standard deviation σ_S:

  $$m[\%] = 100 \cdot \frac{\sigma_S}{< S >} \tag{4.5}$$

  External effects, such as changing weather conditions or receiver instabilities, are responsible for systematic changes in the variability pattern. Hence, it is useful to compare m to the average modulation index of the non-variable calibrator sources. This leads to the definition of the variability amplitude (Heeschen et al. 1987, Quirrenbach et al. 1992):

- **Variability Amplitude**

  $$Y[\%] = 3\sqrt{m^2 - m_0^2} \tag{4.6}$$

  with m_0 the mean modulation index of the secondary calibrators. In case of $m \leq m_0$ the variability amplitude of the affected source is set to zero.

The modulation indices for the polarised quantities are derived in a similar way. For the polarised intensity P, we use

$$m_P[\%] = 100 \cdot \frac{\sigma_P}{< P >} \tag{4.7}$$

$$Y_P[\%] = 3\sqrt{m_P^2 - m_{P,0}^2} \tag{4.8}$$

For the polarisation angle χ it is defined as follows:

$$m_\chi[^\circ] = \sigma_\chi \tag{4.9}$$

$$Y_\chi[^\circ] = 3\sqrt{\sigma_\chi^2 - \sigma_{\chi,0}^2} \tag{4.10}$$

So far, only the statistical variance of the data has been considered. In order to regard the individual measurement errors, one has to apply a further method.

- The χ^2**-Test** is an established method to test hypotheses (see, e.g., Bevington & Robinson 1992). In order to probe the variability of a source, in fact the hypothesis of stationarity is tested, assuming a constant source flux. The light curve of the respective source is fitted by a constant function $\langle S\rangle$ as follows (cf., e.g., Heeschen et al. 1987; Quirrenbach et al. 1992; Kraus et al. 2003):

$$\chi^2 = \sum_{i=1}^{n} \left(\frac{S_i - < S >}{\Delta S_i} \right)^2 \tag{4.11}$$

where S_i denotes the individual flux densities and ΔS_i their errors. A division of χ^2 by the degrees of freedom (here N-1, N number of measurements) leads to χ_r^2 (reduced χ^2). Only sources, for which the probability not to be modeled by a constant function is ≥99.9%, are considered to be variable. The probability can be verified by comparing the results of the χ_r^2-test to relevant collections of tables from the literature (e.g., Bronstein & Semendjajev 1989).

To analyse the differences in IDV behaviour between total and polarised flux density, a time scale analysis was performed using the correlation function.

- The **Correlation Function** $\rho(\tau)$ measures the correlation of two signals at different times (see Edelson & Krolik 1988 for more details) as

$$\rho_{S_1,S_2}(\tau) = < S_1(t+\tau) \cdot S_2(t) >_t \tag{4.12}$$

In case of $S_1 = S_2$ this results in an auto-correlation function of a time series which is a measure for the self-similarity of a time-dependent signal. Here, however, I am interested in the correlation between total and polarised intensity and therefore apply the cross-correlation function. Maxima and minima in the cross-correlation function denote correlations and anti-correlations, respectively, of the underlying data sets. In case of a complete correlation or anti-correlation, values of +1 or -1 are expected. If maxima appear at different times, this denotes the time lag between the two data sets. Correlation coefficients below 0.6 are considered to be insignificant.

4.2 Results

The resulting plots of total and polarised intensity light curves and polarisation angle are displayed in Appendix A except from epochs March 2002, July 2002, and April 2004, where only single measurements were available.

An inspection of the flux density plots (Figures A.1 - A.6, upper panels) shows that the total intensity variability is only marginal throughout all epochs compared to its former activity (cf. Fig. 3.1). This becomes especially evident when looking at the right axis, which displays the normalised flux density. It is not feasible to identify any regularities or (anti-)correlations with polarised intensity or polarisation angle by eye. On the other hand, the polarisation intensity is varying quite fast on a seemingly regular time scale of 0.4-0.5 days. The polarisation angle variations, however, are also less pronounced than before ranging from modulation indices of 0.5 to a maximum value of 1.7° in contrast to earlier observed values between 7 and 18° (Kraus et al. 2003).

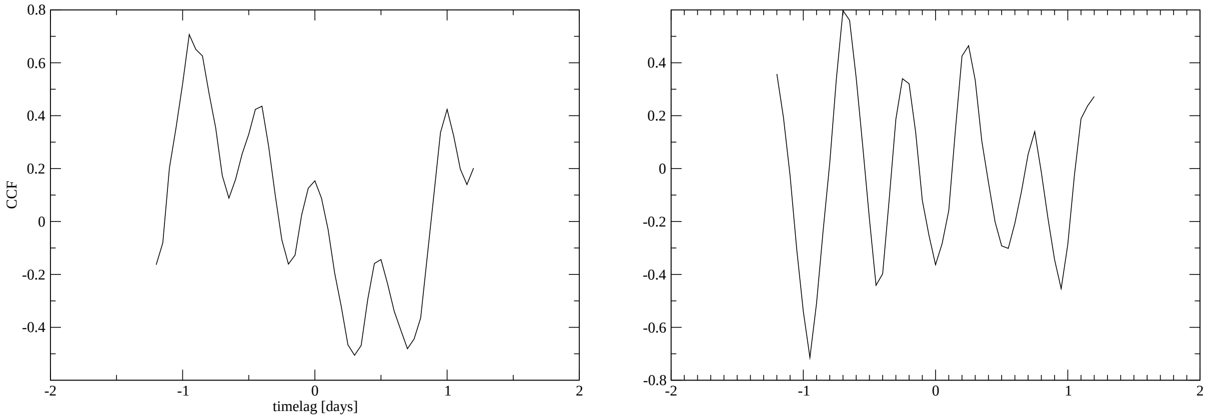

Figure 4.2: *Cross-correlation function between polarisation angle χ of 0917+624 and 0716+714 (left panel) and 0917+624 and 0954+658 (right panel) in epoch 2001-03-24; the left panel shows a systematic correlation for every 0.5 days whereas the right panel displays an anti-correlation within the same period.*

The results of the variability analysis for the IDV data on 0917+624 are listed in Table 4.1. The upper part of the table displays the total intensity I results, whereas the lower part contains the findings for polarised intensity P and polarisation angle χ. The first column gives the observing epochs; stars mark the epochs which have already been analysed in total intensity in Fuhrmann (2004). The second column shows the number of measurements N performed in each epoch. N sometimes differs for polarisation measurements (bottom part of the table) due to the removal of poor quality scans. The upper part further gives total flux density (column 3), modulation index for total intensity m_I and for comparison mean modulation index m_0 of the secondary calibrators (0836+710, 0951+699) in columns 4 and 5. The resulting variability amplitude Y is listed in column 6; column 7 displays χ^2_r followed by the reduced χ^2 (column 8) that results for a stationarity probability of 99.9 % from the given number of measurements in the respective epoch. The same arrangement holds for polarised flux density P and polarisation angle χ (columns 8 to 13) in the lower part of the table. The last column of the upper part contains the fractional polarisation[3] p of 0917+624 for each epoch.

---

[3] fractional polarisation $p=\frac{|P|}{I}$ [%], where P is the polarised and I the total intensity.

Table 4.1: *Results of the Effelsberg 4.85 GHz observations*

Epoch	N*	I [Jy]	m_I [%]	m_0 [%]	Y [%]	χ^2_r	$\chi^2_{99.9}$	$p^{\ddagger}$[%]
2001-03-24*	57	1.419±0.012	0.87	0.20	2.53	2.803	1.6868	3.85
2001-05-04*	65	1.383±0.007	0.47	0.20	1.29	3.598	1.6362	4.23
2001-08-03*	138	1.438±0.007	0.51	0.20	1.41	4.108	1.4187	4.42
2001-10-20	82	1.416±0.006	0.43	0.20	1.14	3.689	1.5566	5.01
2001-12-26*	38	1.440±0.005	0.38	0.15	1.04	3.220	1.8742	4.58
2002-03-27†	1	1.322±0.002	-	-	-	-	-	4.55
2002-04-12*	15	1.315±0.011	0.79	0.30	2.23	7.674	2.5802	4.62
2002-07-13†	2	1.214±0.001	-	-	-	-	-	4.68
2003-04-10†	1	1.057±0.006	-	-	-	-	-	4.62
2003-11-14	47	0.884±0.008	1.14	0.22	3.37	17.508	1.7696	3.54
2004-07-16	46	0.801±0.007	0.90	0.21	2.64	12.471	1.7795	2.90
2004-08-12	112	0.791±0.005	0.68	0.21	1.93	6.652	1.4689	2.90
2004-12-19	32	0.769±0.004	0.53	0.15	1.52	5.984	1.9709	3.15

Epoch	N	P [Jy]	m_P [%]	$m_{P,0}$ [%]	Y_P [%]	χ^2_r	χ [°]	m_χ[°]	$m_{\chi,0}$[°]	Y_χ[°]	χ^2_r	$\chi^2_{99.9}$
2001-03-24	55	0.055±0.0015	2.75	1.50	6.92	2.631	44.00	0.94	0.50	2.37	3.151	1.7013
2001-05-04	65	0.059±0.0015	2.50	1.20	6.57	2.889	43.27	0.65	0.30	1.73	3.759	1.6362
2001-08-03	137	0.064±0.0016	2.42	2.00	-	1.251	40.45	0.60	0.50	1.00	5.588	1.4187
2001-10-20	84	0.071±0.0015	2.07	1.00	5.43	2.802	39.58	0.65	0.40	1.53	3.331	1.5490
2001-12-26	38	0.066±0.0012	1.87	1.40	-	1.316	41.52	0.53	0.50	-	0.962	1.8742
2002-03-27	1	0.060±0.0010	-	-	-	-	44.75	0.21	-	-	-	-
2002-04-12	15	0.061±0.0015	2.41	1.50	6.42	3.101	45.61	0.91	0.50	2.67	10.438	2.5802
2002-07-13	2	0.057±0.0010	-	-	-	-	43.24	0.12	-	-	-	-
2003-04-10	1	0.049±0.0001	-	-	-	-	45.68	0.06	-	-	-	-
2003-11-14	47	0.031±0.0013	4.19	1.00	12.20	101.024	49.19	1.09	0.50	2.90	109.946	1.7696
2004-07-16	46	0.023±0.0013	5.74	1.60	16.55	10.588	54.92	1.25	0.50	3.45	5.124	1.7795
2004-08-12	107	0.023±0.0013	5.55	1.30	16.19	16.998	52.89	1.74	0.50	5.01	9.382	1.4812
2004-12-19	32	0.024±0.0014	5.78	1.70	16.56	8.192	50.26	1.57	0.30	4.63	22.162	1.9709

*Number of measurements, *total intensity also analysed in Fuhrmann (2004), †VLBI-epochs (see Chapter 5), ‡fractional polarisation

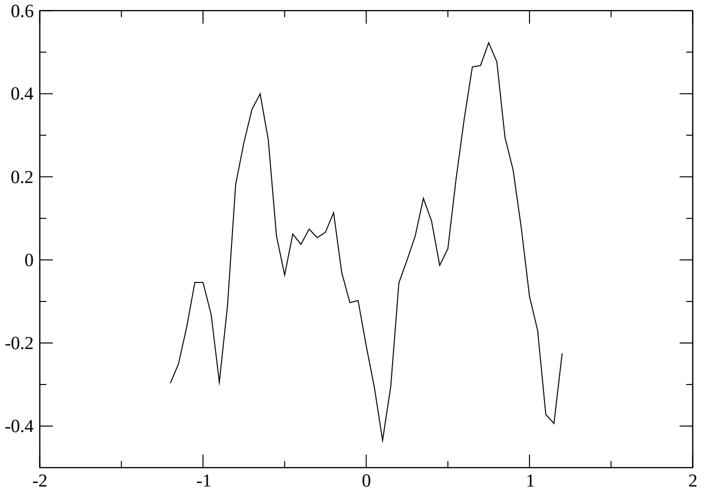

Figure 4.3: *Cross-correlation function between polarisation angle χ of 0917+624 and the unpolarised secondary calibrator 0951+699 in epoch 2001-03-24; weak systematics of 0.5 days could in principle be interpreted from this plot (cf. Figure 4.2 and text).*

Remarkably, the modulation index of the polarised flux almost triples from below 2 to almost 6 % between 2002 and December 2004, whereas at the same time m_χ only slightly increases and m_I marginally rises until the end of 2003 to a maximum value of 1.14 % (being approx. one-third of former values) and then drops off again. Still, the variability in polarisation is as well far below the formerly observed modulation indices of more than 15 %. As an example for the calibration accuracy we show in Figure A.1 (right panel) the flux density of the secondary calibrator source 0836+710 plotted versus time.

To rule out whether the deduced polarisation variations are due to some residual gain effects of the telescope, which are usually not corrected for in the polarisation analysis, I calculated the cross-correlation function between χ of 0917+624 and other polarised sources (0836+710, 0716+714 and 0954+658) since these gain systematics should also affect the data of the other sources. The cross-correlation analysis partly yielded positive results in some epochs, two example plots are given in Figure 4.2. A systematic with a half-day period in the cross-correlation of the polarisation angles is clearly visible, and the same is valid for polarised intensity (not displayed). Even the cross-correlation between χ of a polarised and an unpolarised source results in some, however, weak (anti-)correlation (cf. Figure 4.3). These systematics might be induced by the changing elevation due to the earth rotation leading to quasi-sinusoidal pattern in the light curves of the sources. Therefore, we inspected the behaviour of the Stokes parameters *Q* and *U* of the target source and of some polarisation calibrator sources with respect to elevation after the final polarisation calibration was applied to the data. In four epochs we found that, while the calibration of the Stokes parameters yields a flat curve for the calibrator source as expected, there still remain residual effects in the data of the target source. Plotting the Stokes parameters versus parallactic angle revealed similar results in terms of a sinusoidal pattern in the calibrated data of the target source which we are not able to explain at this point. In Figure 4.4, an example plot is given where the normalised *Q* and *U* values of 0917+624 and 0836+710 are plotted versus time.

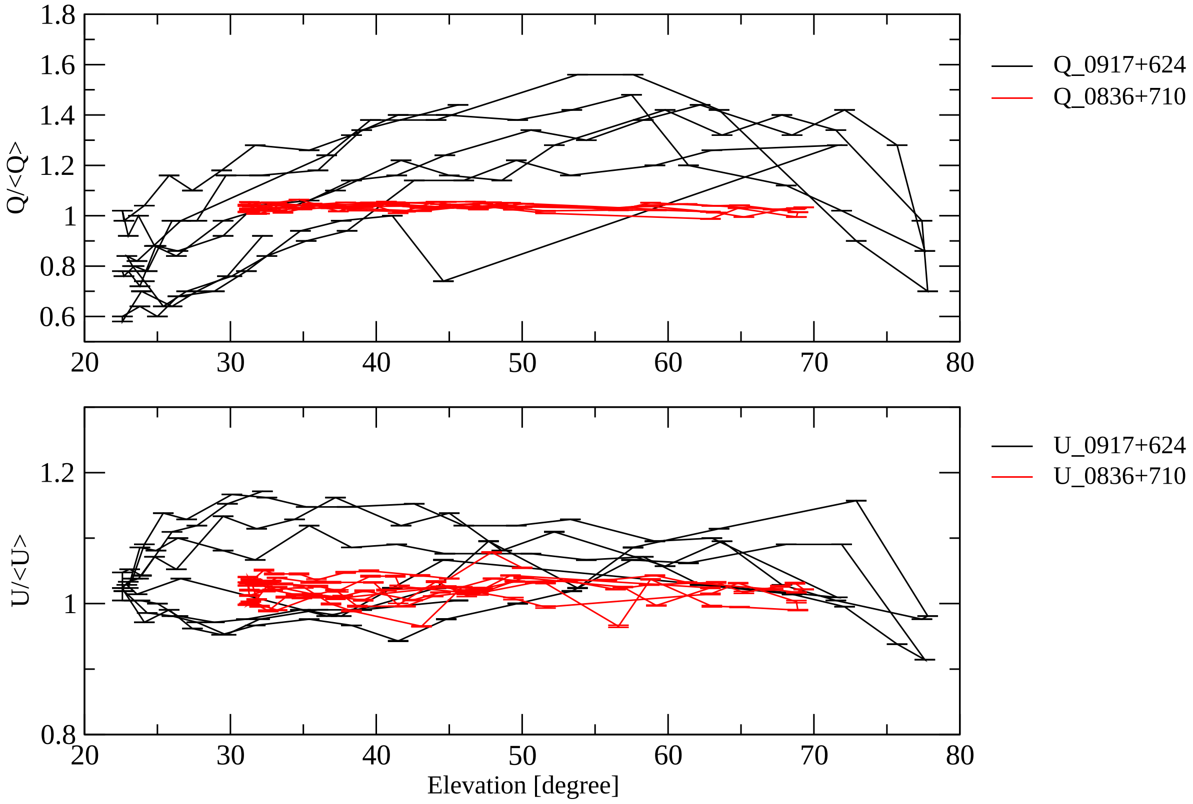

Figure 4.4: *Normalised Stokes parameters Q and U of calibrated 0917+624 and 0836+710 data plotted versus time for epoch 2004-08-12; a residual pattern is still visible in the data of the target source.*

Hence, we have to be careful in interpreting the polarisation variability as real. As the variations for 0917+624 are less pronounced than before 2000, it might well be that the variability pattern we see is dominated by systematic effects which we usually do not see when the source is much brighter and the residual variations appear less pronounced.

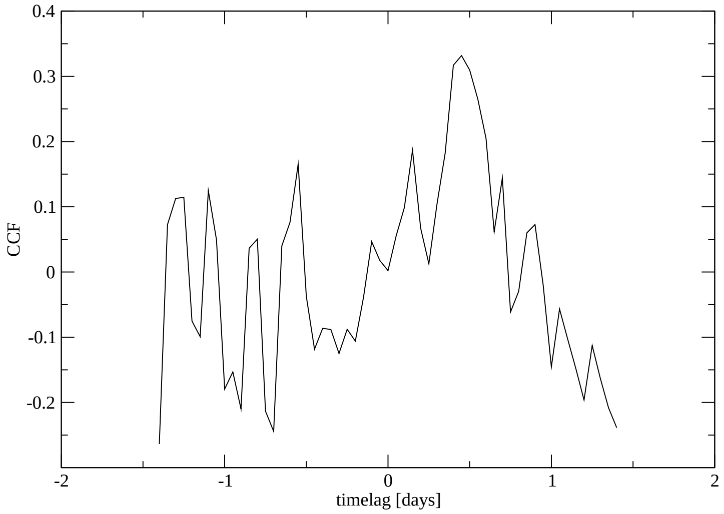

Figure 4.5: *Cross-correlation function between total and polarised flux density of epoch 2001-10-20.*

The correlation function analysis did not reveal any significant correlations between the variability pattern of I and P. For an example, the cross-correlation function of epoch 2001-10-20 is plotted in Figure 4.5.

Total and polarised flux density of 0917+624 decreased between 2001 and 2004 which is displayed in the upper panels of Figure 4.6 . The bottom panel contains the fractional polarisation p. The latter shows a slight increase towards the end of 2001 from roughly 4 to 5 % where the total intensity remains rather constant and the polarised flux is slightly increasing. The fractional polarisation then decreases until the end of the observing period (to a value around 3 %) since the decline in polarised flux is stronger compared to the decline in total intensity. As can be seen from Figure 4.7, σ_P is nearly constant throughout the observations as opposed to σ_I, whereas total and polarised flux density both decrease. Hence, it is justified to plot the modulation indices of I and P and directly compare them, as is done in the same Figure (bottom panel). During the 4 years of observations, the orientation of the polarisation angle made an overall change of ~14° between 40 and 54° (Figure 4.6, third panel), with χ and m_χ following the same fluctuations as m_P (see bottom panel of Figure 4.7).

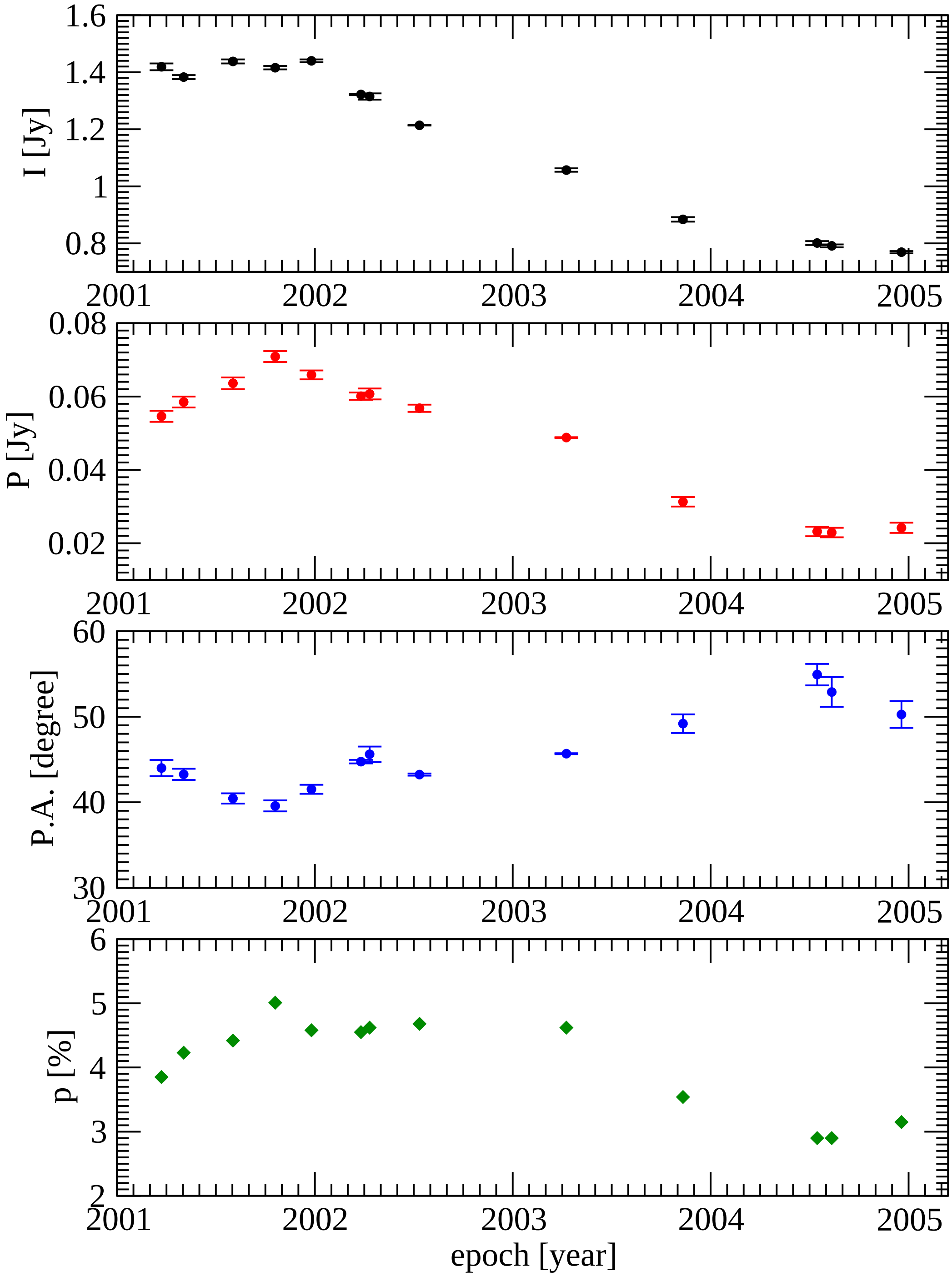

Figure 4.6: *Panels display from top to bottom: total flux density I, polarised flux density P, polarisation angle P.A. of 0917+624 observed with the Effelsberg telescope at 4.85 GHz between March 2001 and December 2004; bottom panel: fractional polarisation p.*

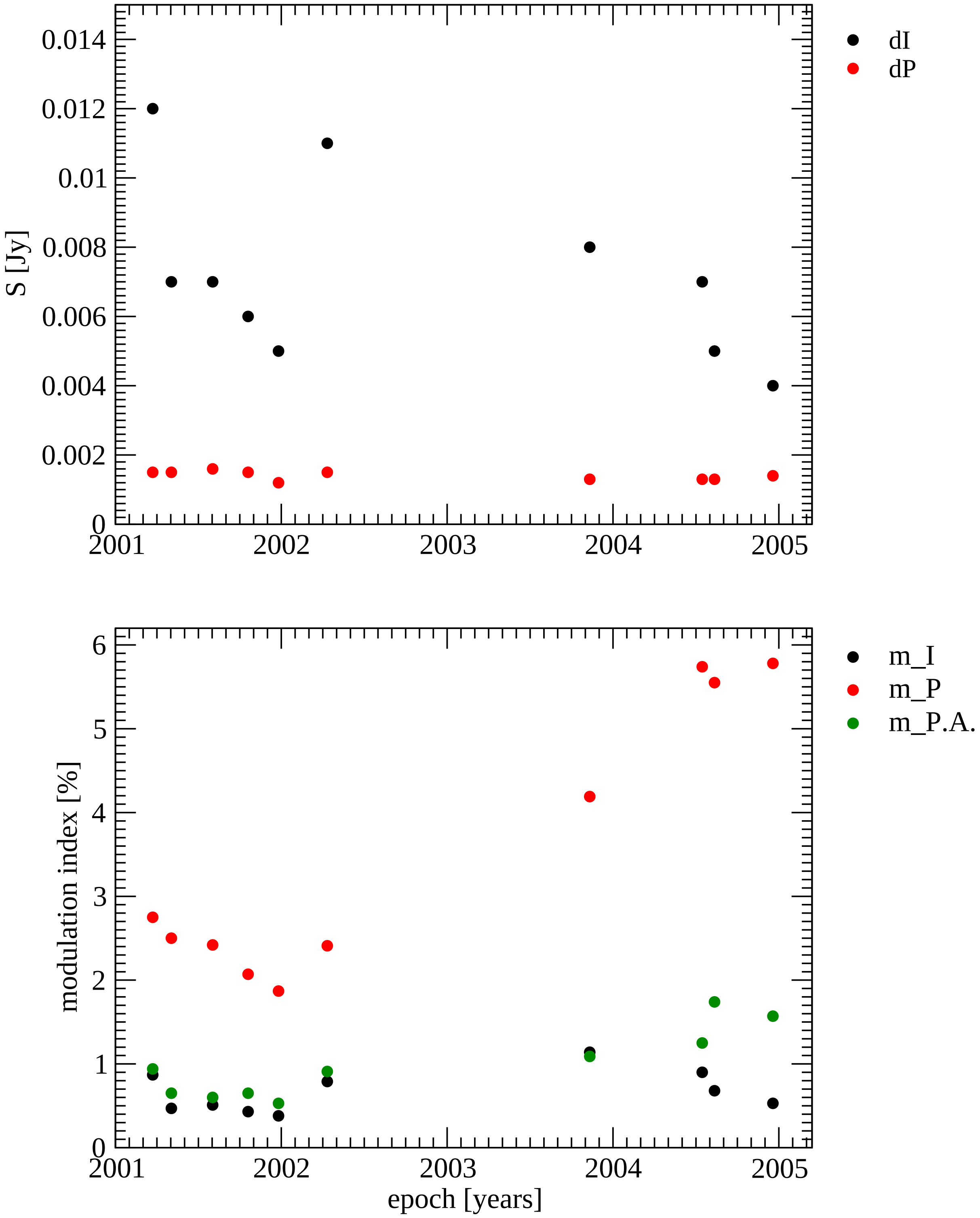

Figure 4.7: *The top panel shows the standard deviations σ_I and σ_P of 0917+624 observed with the Effelsberg telescope at 4.85 GHz between March 2001 and December 2004; bottom panel: modulation indices of I, P and χ.*

CHAPTER 5

The Kinematics of 0917+624 between 1999 and 2007 at Different Frequencies

As already pointed out in Chapter 3, in September 1998, Kraus et al. (1999) discovered that the rapid variability of 0917+624 had stopped and instead a slow, monotonic increase of 7% in total flux density was observed during the 5-day observing session. Observations made in February 1999 revealed that the source was varying again on a time scale of 1.3 days. However, since September 2000 its variability has ceased again, showing only moderate modulation indices of the order of $\sim 0.5\%$ (see Fuhrmann 2004, Fuhrmann et al. 2002 and Chapter 4), and to date the source has not restarted its former activity.

Furthermore, the earlier slow-down of 0917+624 in September 1998 was interpreted by Kraus et al. (1999) as due to a possible increase in the angular size of the scintillating component, which could be caused by the ejection of a new jet component (see also Krichbaum et al. 2002). The ejection could temporarily lead to a core size exceeding the Fresnel scale defined by the scattering medium. Consequently, only strongly quenched scintillation would be observed. When the component moves further down the jet, it will separate from the core at some point whereby the size of the scintillating component decreases again. At that time, the variability is expected to reappear. Given that the variability ceased again in 2000, even more than one component should have been emitted since. In order to test this scenario, several epochs of VLBI observations of 0917+624 were analysed which were partly performed at different frequencies.

Table 5.1: *Observing epochs and participating antennas*

#	epoch	notation	frequency [GHz]	array	comments
1	1999-11-20	1999.888	5, 15	VLBA + EB[1] + Y[2]	
2	2000-03-06	2000.183	5, 15	VLBA + EB + Y	BR[3] flagged at 15 GHz
3	2000-11-30	2000.915	5, 15	VLBA + EB + Y	
4	2001-12-26	2001.988	5, 15, 22	VLBA + EB	no IF2 for EB
5	2002-03-27	2002.241	5, 15, 22	VLBA + EB	KP[4] flagged at 22 GHz
6	2002-06-15	2002.458	15	VLBA	
7	2002-07-13	2002.536	5, 15, 22	VLBA + EB	PT[5] flagged at 15 GHz
8	2003-04-10	2003.277	5, 15, 22	VLBA + EB	no IF2 for EB, MK[6] flagged, no IF2 for SC[7] at 22 GHz
9	2003-06-15	2003.458	15	VLBA	
10	2004-02-15	2004.124	24	VLBA	
11	2004-12-14	2004.955	24	VLBA	
12	2005-02-05	2005.097	15	VLBA	
13	2005-06-15	2005.458	15	VLBA	
14	2005-09-19	2005.719	15	VLBA	
15	2006-08-09	2006.608	15	VLBA	
16	2007-06-03	2007.425	15	VLBA	
17	2007-09-06	2007.683	15	VLBA	

[1] Effelsberg telescope, [2] 1 antenna of the Very Large Array (VLA), [3] VLBA-Kitt Peak, [4] VLBA-Brewster, [5] VLBA-Kitt Peak, [6] VLBA-Mauna Kea

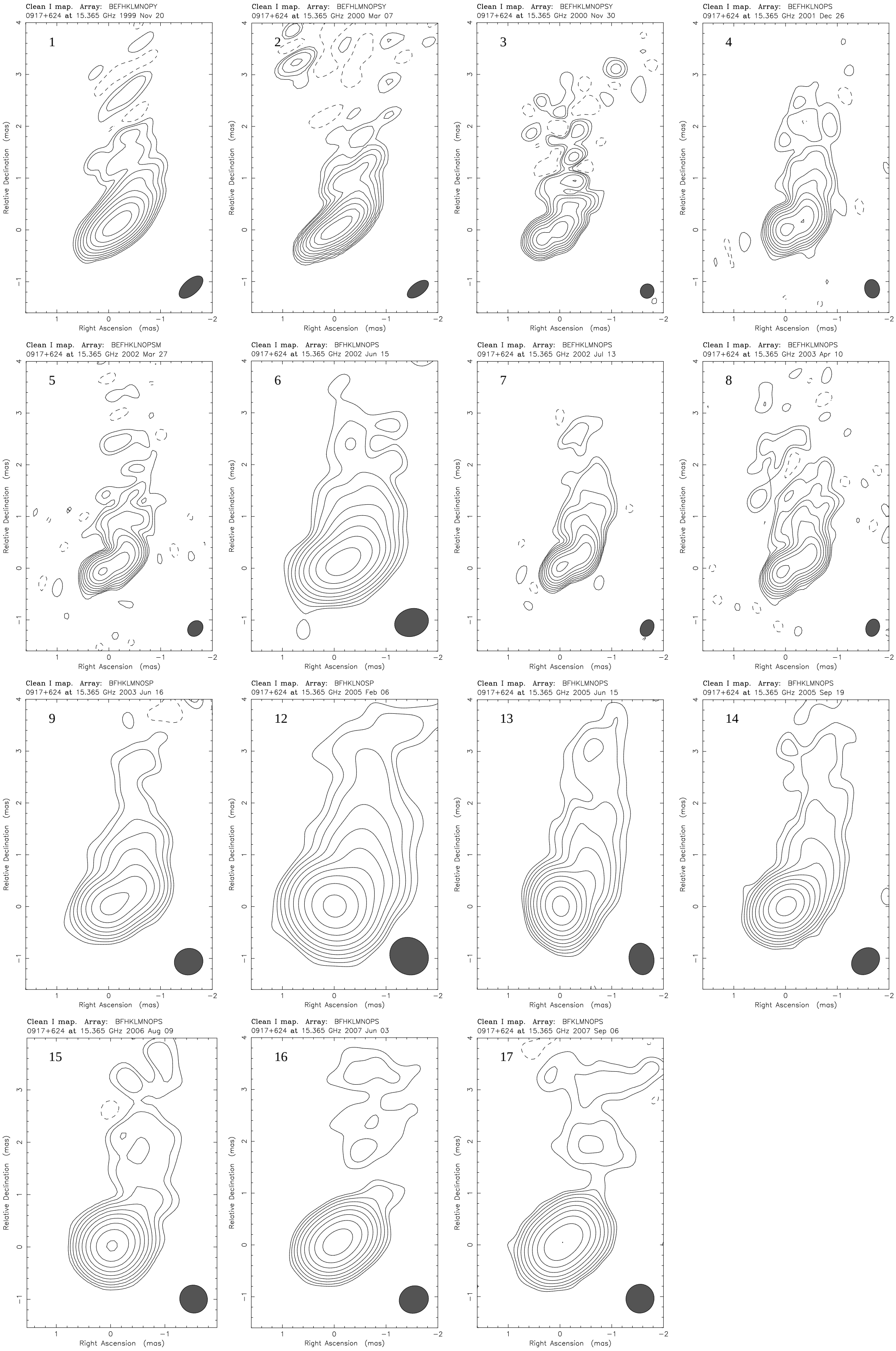

Figure 5.1: *15 GHz maps of all epochs of 0917+624; numbers denote epochs as given in Table 5.1; parameters are listed in Table 5.2; contours are given in steps of 2.*

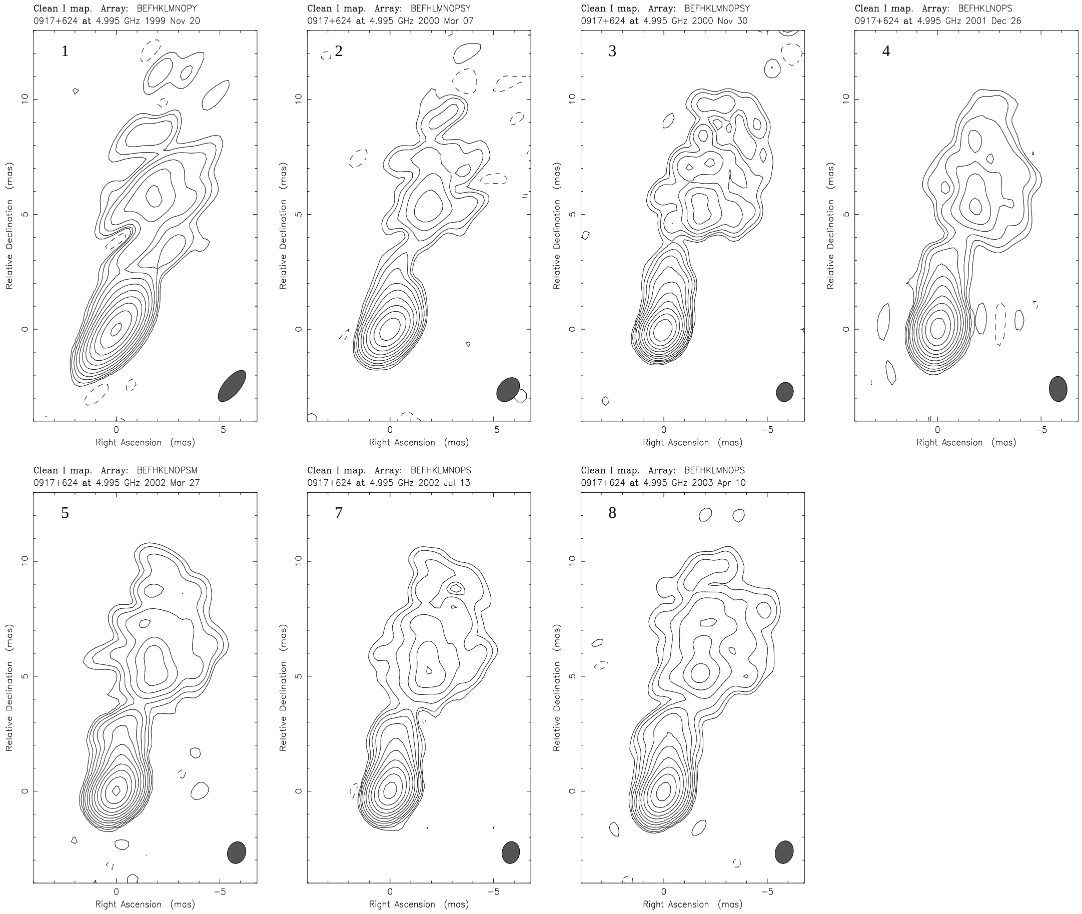

Figure 5.2: *5 GHz maps of all epochs of 0917+624; numbers denote epochs as given in Table 5.1; map parameters are listed in Table 5.2; contours are given in steps of 2.*

5.1 Observations and Data Analysis

The data were obtained from different VLBI observing campaigns. The main emphasis is lying on VLBI observations of 0917+624 at 5, 15 and 22 GHz during 4 epochs from December 2001 until April 2003, in the following called epoch 2001.988 (26 December 2001), epoch 2002.241 (27 March 2002), epoch 2002.536 (13 July 2002) and epoch 2003.277 (10 April 2003), hereafter referred to as ’core campaign’. The observations were carried out with the antennas of the Very Long Baseline Array (VLBA) together with the Effelsberg 100m telescope and lasted 12 hours, respectively. A detailed description on the principles of radio interferometry and aperture synthesis and the methods of image reconstruction can be found in, e.g., Thompson et al. (2001).

Three previous epochs between November 1999 and November 2000 were taken from an observing campaign of the target source NGC3079 with the VLBA and one antenna of the Very

Table 5.2: *Parameters of the 0917+624 maps produced by Difmap.*

epoch	S_{tot} [Jy]	Beam [mas]	bpa[1] [°]	Peak flux [Jy/beam]	lowest contours [mJy/beam]
5 GHz					
1999.888	1.49	1.76 x 0.75	-44.3	1.04	0.9
2000.183	1.41	1.25 x 0.88	-50.0	1.03	1.2
2000.915	1.36	0.87 x 0.79	-38.1	0.88	0.45
2001.988	1.36	1.10 x 0.86	3.7	0.925	0.6
2002.241	1.23	0.98 x 0.86	-31.1	0.81	0.35
2002.536	1.13	0.97 x 0.84	-17.2	0.711	0.5
2003.277	0.98	1.02 x 0.85	-26.2	0.589	0.4
15 GHz					
1999.888	1.20	0.57 x 0.28	-48.2	0.601	1.5
2000.183	1.12	0.48 x 0.24	-53.4	0.518	0.6
2000.915	1.06	0.28 x 0.27	-20.5	0.354	1.5
2001.988	1.03	0.36 x 0.29	10.7	0.405	1.2
2002.241	0.89	0.33 x 0.27	-41.1	0.353	1.2
2002.458	0.87	0.67 x 0.53	-71.4	0.497	1.3
2002.536	0.83	0.34 x 0.26	-26.9	0.276	0.9
2003.277	0.66	0.34 x 0.26	-18	0.202	0.6
2003.458	0.66	0.56 x 0.51	-72.9	0.311	1.8
2005.097	0.81	0.77 x 0.70	53.7	0.644	1.0
2005.458	0.92	0.62 x 0.48	10.8	0.746	1.1
2005.719	1.02	0.59 x 0.48	-50.3	0.856	1.2
2006.608	1.05	0.54 x 0.51	17.5	0.832	1.5
2007.425	1.04	0.58 x 0.52	-65.2	0.715	1.8
2007.683	0.98	0.56 x 0.54	-22	0.615	1.2
22/24 GHz					
2001.988	0.82	0.26 x 0.19	-24.7	0.242	1.2
2002.241	0.65	0.23 x 0.18	-37.8	0.169	1.2
2002.536	0.55	0.29 x 0.16	-33.7	0.166	0.9
2003.277	0.56	0.25 x 0.17	-21.6	0.171	0.7
2004.124	0.56	0.59 x 0.27	-4.6	0.366	5.0
2004.955	0.61	0.38 x 0.31	67.6	0.469	4.0

[1] Beam Position Angle

Large Array (VLA) plus Effelsberg at 1.6, 5 and 15 GHz in which 0917+624 was used as a calibrator. Seven additional epochs were chosen from the MOJAVE[1] (Lister & Homan 2005) and 2cm Survey (Kellermann et al. 2004) programs observed between June 2002 and September 2007 at 15 GHz. Finally two further epochs were received from the RRFID (Radio Reference Frame Image Database) observed at 24 GHz in February and December 2004. The afore listed epochs are in the following referred to as ’additional epochs’.

In Table 5.1 we summarise the experiments analysed and used in this thesis. In column 2 we show the observing epochs, column 3 gives the mean fractional observing dates denoting their further notation within this work. Column 4 lists the observing frequencies and column 5 the participating antenna arrays. The last column contains further information on problems that occured during the individual experiments and flagged antennas due to poor data quality.

The data reduction of the core campaign was done using the NRAO Astronomical Image Processing System (Aips) for the apriori calibration. Afterwards the resulting data were exported in (u, v)-fits format and further processed in Difmap (Shepherd et al. 1994), a part of the Caltech VLBI analysis programs (Pearson & Readhead 1984). Difmap uses the Clean algorithm (Hoegbom 1983) and Selfcal procedures for phase and amplitude self-calibration. The data of the additional epochs were already fully calibrated and available as (u, v)-fits files. Figures 5.1, 5.2 and 5.3 show the resulting maps of all epochs for the different frequencies respectively. The related image parameters are listed in Table 5.2 where column 2 gives the total flux density, columns 3 and 4 list the size of the beam and beam position angle, respectively. The peak flux density is given in column 5 and the lowest map contours at a 3σ-level[2] are listed in column 6.

A good description of the principles of radio interferometry, data calibration and imaging can, for instance, be found in Klare (2003). A brief list of the standard procedures for the apriori calibration in Aips is given in Bach (2004). More useful information concerning the application of the analysis programs is contained in their so-called CookBooks which can be found at `http://www.aips.nrao.edu/cook.html` and `ftp://ftp.astro.caltech.edu/pub/difmap/difmap.html`.

To investigate the jet kinematics of 0917+624, a number of circular Gaussian components was fitted to the calibrated visibilities in order to describe the brightness distribution of the source with as few parameters as possible. For each epoch and frequency we cross-identified individual model components along the jet using their distance r from the VLBI core, the flux density S and size (full width at half maximum - FWHM). In this identification scenario, we assumed that the VLBI core remained stationary. The model fitting was done repeatedly to verify

---

[1] Monitoring of Jets in Active galactic nuclei with VLBA Experiments

[2] σ is the residual noise of the map after subtraction of the model

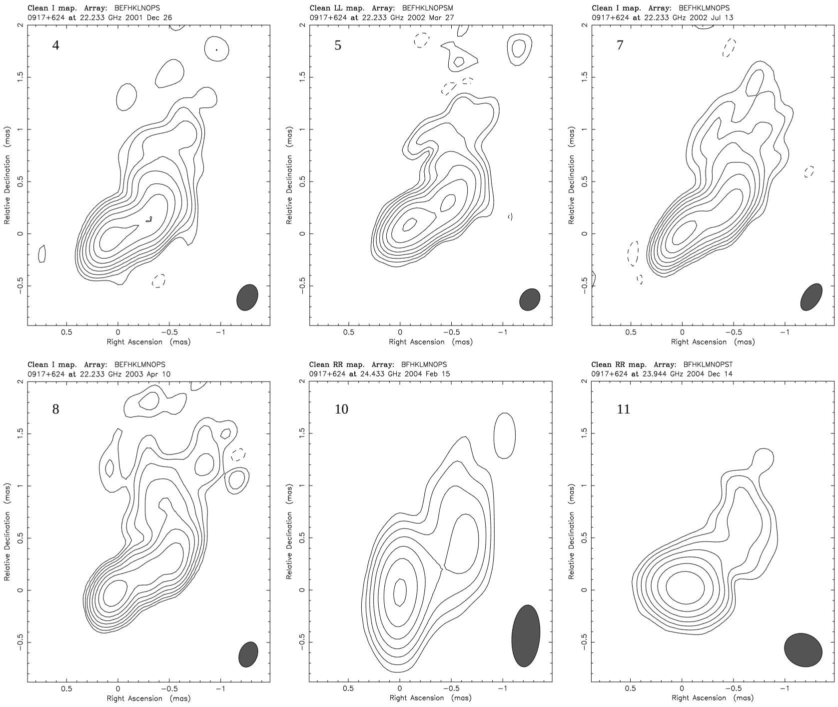

Figure 5.3: *22 GHz maps of all epochs of 0917+624; numbers denote epochs as given in Table 5.1; parameters are listed in Table 5.2; contours are given in steps of 2.*

the consistency of the number of components, and additionally the results were compared to the adjacent epochs. Literature research gave no results about 0917+624 exhibiting a counter-jet. Hence, the outermost eastern component was assumed to represent the VLBI core (i.e., the footpoint of the jet) and its position was fixed to (0,0). It appeared, that this component was not necessarily the brightest one. The positions of the other components were measured with respect to the core component which was assumed to be stationary.

The assumption of the stationarity for the VLBI core is based on the following considerations: since the observations were not carried out in phase-referencing mode, the information about the absolute source position got lost. Therefore, the final model fitting results for all frequencies of the simultaneously observed epochs were compared and inspected for position shifts due to opacity effects (Lobanov 1998; Kovalev et al. 2008). Since the position offset between higher and lower frequencies is 0.15 mas at its maximum, the VLBI core was considered to be stationary.

For the flux density, the measurement error was derived from uncertainties of the amplitude calibration as well as formal errors of the model fit procedure. The position errors were calculated according to Fomalont (1989) via $\Delta r \propto \frac{FWHM}{2\times SNR}$ where SNR is the signal-to-noise ratio. This, however, tends to underestimate the error in case of very compact small components because the resulting error lies below the cell size of the map. In that case an additional minimum error according to the map cell size was included which corresponds to 0.5 mas in case of the 5 GHz data, 0.05 mas at 15 GHz and 0.04 mas in case of 22 GHz.

In the following I will first describe the kinematic results for each individual frequency separately before directly comparing them in the subsequent section. The chapter closes with the introduction of a model calculation for a possible binary black hole scenario in the case of 0917+624.

Table 5.3: *Results for the fit on the core separation of the modelfit components at 15 GHz; given are the annual separation rate μ, apparent velocity β_{app} and time of zero core separation t_0 for each component.*

Id[1]	μ [mas/year]	β_{app} [c]	t_0
J11	0.04±0.003	2.76±0.17	2003.2±1.3
J10	0.17±0.01	10.57±0.59	2004.5±2.1
J9	0.12±0.01	7.28±0.35	2000.4±1.5
J8	0.13±0.01	7.97±0.29	1998.2±1.2
J7	0.13±0.01	8.12±0.64	1996.7±1.2
J6	0.12±0.01	7.68±0.86	1995.1±1.5
J5	0.14±0.01	9.06±0.53	1992.7±0.8
J4	0.20±0.02	12.33±1.10	1990.0±1.8
J3	0.01±0.01	0.38±0.54	-
J2	0.31±0.04	19.20±1.66	1983.2±1.9

[1] Identification of the individual components

5.2 Results and Discussion

5.2.1 Source Kinematics at 15 GHz

The available VLBI data consist of 15 observing epochs at 15 GHz covering a period of almost eight years from December 1999 until September 2007 (see Table 5.1). This enabled a more detailed kinematic analysis as for the 5 GHz and 22 GHz data. As the resolution of the individual epochs was slightly different due to the presence or absence of the longest possible baselines (i.e., observations with or without the Effelsberg telescope), the data were weighted accordingly during the model fitting process to achieve an utmost similar resolution for all epochs. Figure 5.5 presents the resulting maps from the model fitting procedure. For each epoch we cross-identified the individual model fit components along the jet using their distance from the VLBI core, the flux density and FWHM. Table B.1 in Appendix B contains the corresponding fit parameters.

Guided by a graphical analysis, which is presented in Figure 5.4, we obtained an adequate identification scheme for the kinematics in the jet of 0917+624 at 15 GHz. This scenario consists of 11 (superluminal) components in total, approximately moving linearly away from the core, the innermost 7 of which are displayed here. The higher numbered components are the ones that were expelled last.

To describe the component motion, the function f(t)= a+b*t was fitted to the trajectory of each component. The linear regression was calculated by assuming that the uncertainty σ_i is associated with the distance of each component from the VLBI core. The results of the fits

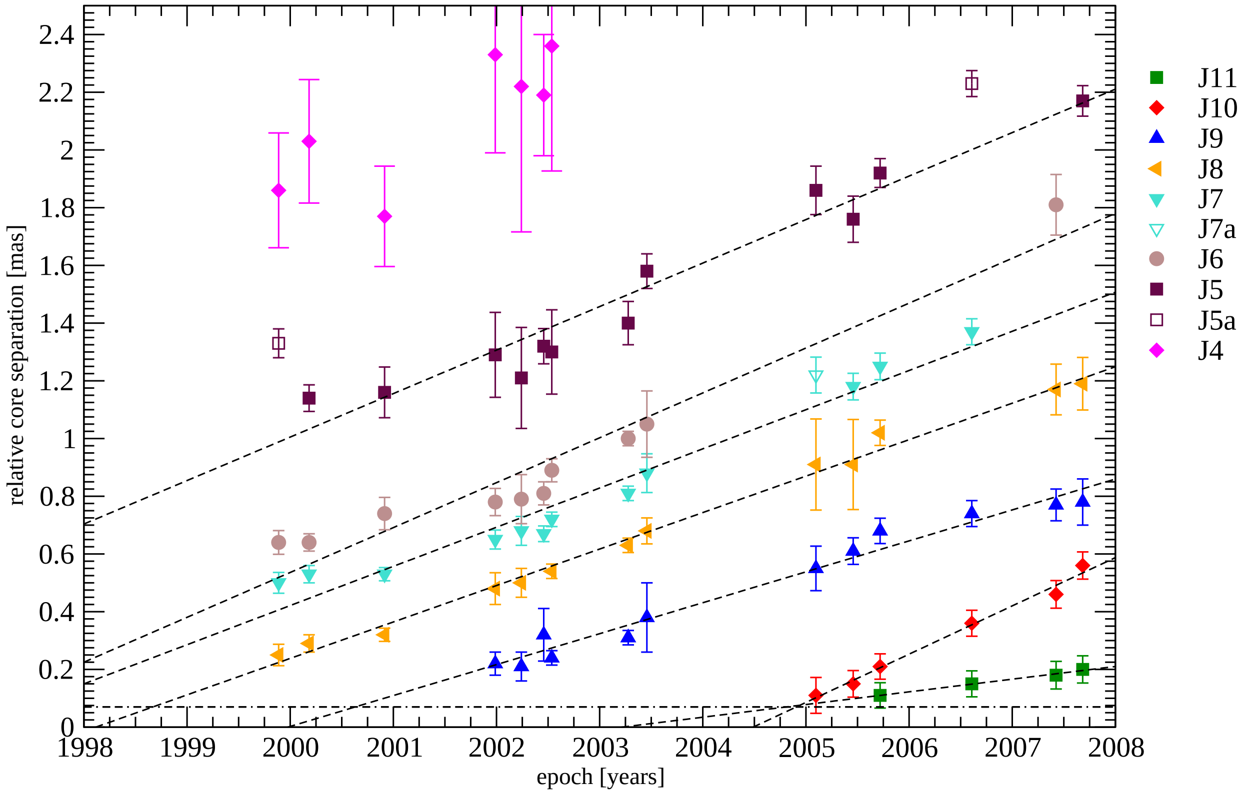

Figure 5.4: *Relative core separation of the innermost modelfit components at 15 GHz. Colors denote for different components, dashed lines give the result of a linear regression analysis. The horizontal dashed-dotted line indicates the estimate of the scattering size (~ 0.07 mas, Rickett et al. (1995)).*

are presented in Table 5.3 which gives for each component (column 1) the separation rate μ in milliarc-seconds per year in column 2, the apparent velocity in column 3, and the time of zero core separation in column 4.

For the calculation of the apparent velocity we adopted the standard cosmological parameters measured by the Wilkinson Microwave Anisotropy Probe (WMAP) following Spergel et al. (2003): a Hubble constant of H_0=71 h km s^{-1} Mpc^{-1} or (expressed in mas yr^{-1}) of 15.83×10^{-3} h mas yr^{-1}, a dark energy density of $\Omega_\Lambda = 0.7$, and a pressureless matter content of $\Omega_m = 0.3$. We adopt the analytical fit to the luminosity distance for flat cosmologies with cosmological constant according to Pen (1999), equation (1). For the transformation of apparent angular separation rates μ into spatial apparent speeds β_{app} we use

$$\beta_{app} = \frac{\mu d_L}{c(1+z)} \tag{5.1}$$

following Pearson & Zensus (1987). Applying the redshift z = 1.446 of 0917+624, one milliarcsec at the source distance corresponds to a scale of 8.5 pc.

From the slope of the linear fit to the path of the components, the individual apparent velocities can be calculated. The results are listed in Table 5.3. The inner components J10, J9, J8, J7, J6, J5 move with an apparent speed of $\beta_{app} = (7-10)$ c which is in good agreement with previous findings (Krichbaum et al. 2002). Moreover, a back-extrapolation of the fitted line to the time axis delivers an approximate ejection date, i.e. time of zero core separation for the respective component (see Table 5.3). For component J8, the ejection date lies around 1998.2, which is in the range of earlier results found by Krichbaum et al. (2002) and Fuhrmann (2004). This event corresponds to a high level of variability. The modulation index lies at ~5% and decreases in the aftermath to ~1.5% (see bottom panel of Figure 5.14). That was about the time when the size of the core and the emitted component exceed the typical scattering size of the medium (indicated by the dashed-dotted line in Figure 5.4), presumably resulting in strongly quenched scintillation. Considering the succeeding increase in the modulation index in early 1999, the behaviour of J8 would in principle confirm our working hypothesis that the earlier variability decline was caused by the ejection of a new component.

Component J9 was emitted around 2000.4, which overlaps with a period of very low variability according to the modulation indices around that time. Two more components were ejected during 2003 or 2004 as can be seen from the modelfits of the last epoch in 2004 (2004.955) and the last epoch in 2005 (2005.719). The back-extrapolation yields an approximate time of zero core separation of 2004.5 for component J10 and 2003.2 for J11. Component J11 seems to travel at a significantly lower apparent velocity ($\beta_{app} = 2.76 \pm 0.17$ c) than J10 (10.57±0.59 c). Although the present component identification appears to us to be the most

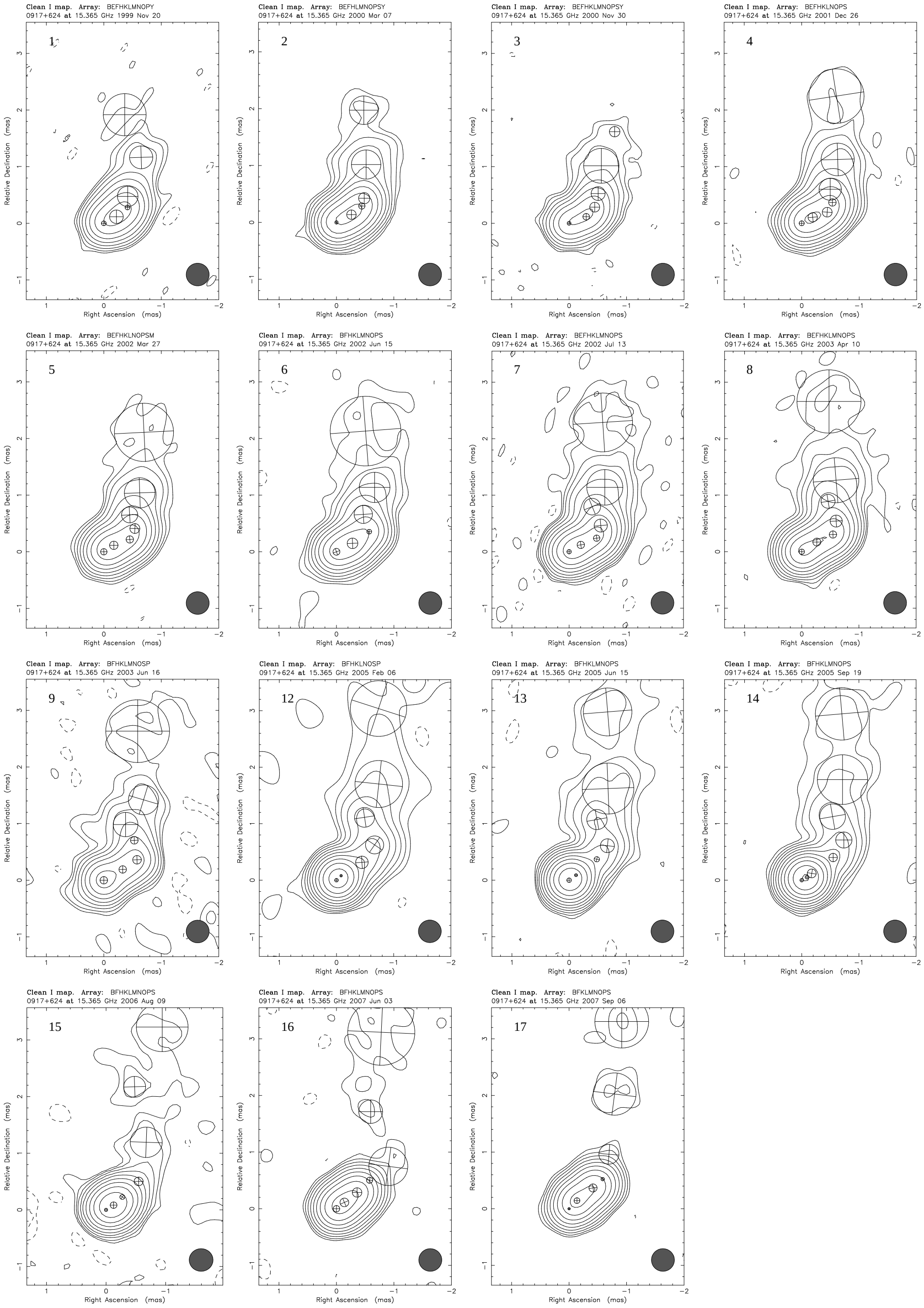

Figure 5.5: *15 GHz modelfits of 0917+624 convolved with a circular beam of (0.4×0.4) mas; numbers refer to epoch listed in Table 5.1; lowest contour starts at 0.75 mJy/beam and increases in steps of 2; lowest level skipped for maps of epochs 2, 4, 5, 6, 9, 15, 16, 17; contours of epochs 1 and 3 start at the third level.*

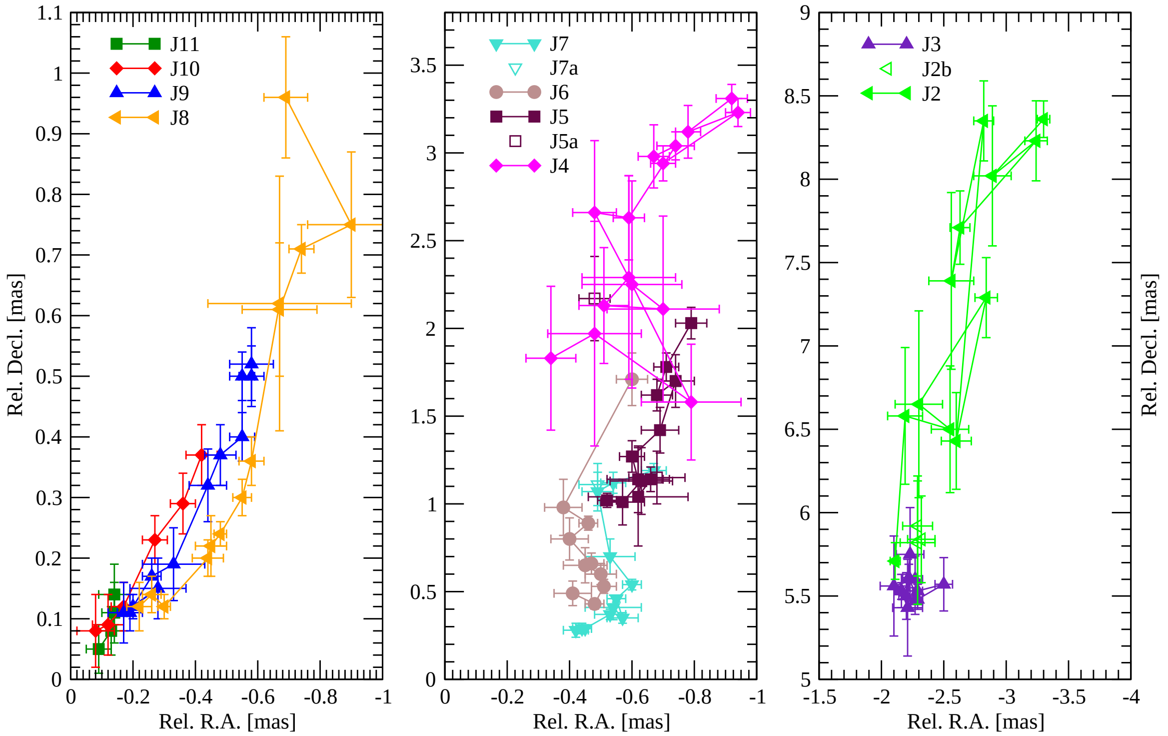

Figure 5.6: *Relative Right Ascension (rel. R.A.) plotted vs. Relative Declination (rel. Decl.) at 15 GHz starting from the inner jet components (left panel) to the outer ones (right panel).*

reasonable, it is nevertheless possible that we are dealing with blending effects due to strong activity and hence an expansion of the VLBI core, but insufficient observational resolution. We yet suspect that a further component ejection is already underway.

Component J3 at a relative core separation of ~6 mas appears to remain at a constant position with an annual core separation of (-0.01±0.01) mas. It is the only component that could be identified as stationary in position within our modelfit scenario for the 15 GHz data.

The maximum apparent velocity displayed by component J2 ($\beta_{app} = 19.20 \pm 1.66\,\mathrm{c}$) is somewhat faster than what was found by Lister et al. (2009) who give a maximum jet speed of 15.57c ($\mu = 229 \pm 17\,\mu$as/yr). Taking the apparent speed of J2, we can derive a minimum value for the Lorentz factor $\gamma_{min} = 19.23$ via $\gamma_{min} = \sqrt{1+\beta_{app}^2}$. The resulting jet inclination angle θ_{max}, for which β_{app} is maximised, is $\theta_{max} = 3.0°$. This is less than half of the value previously found by Standke et al. (1996) of 7.4°. From the minimum Lorentz factor we can calculate a minimum value for the Doppler factor using $\delta_{min} = [\gamma_{min}(1-\beta_{min}\cos\theta_{max})]^{-1}$ with $\beta_{min} = \sqrt{1-\gamma_{min}^{-2}}$, which yields $\delta_{min} = 19.23$. A maximum Doppler factor is achieved for even smaller inclination angles ($\beta \rightarrow 0$, $\delta_{max} = 2\gamma$). Hence, for component J2 we obtain Doppler factors in the range of 19 to 38 at inclination angles between 0° and 3.0°.

Figure 5.6 presents the position of the jet components on the sky in terms of Relative Right Ascension (rel. R.A.) and Relative Declination (rel. Decl.). The different panels separate the inner and outer components for purpose of clarity. The jet reveals a bent structure which becomes particularly obvious in the middle panel where the intermediate jet components J4 to J7 are displayed ranging from ~0.5 to 3.5 mas. An exception is again component J3 which barely moves during the 8 years of observations (see right panel of Fig. 5.6).

Regarding the position angle (furthermore referred to as P.A.) of the components shown in Figure 5.7, i.e., the angular distance from the core, one can see a clearly increasing trend for the innermost six components J5 to J11, apart from J10, which shows a rather convoluted behaviour like J4. A cubic or higher order fit to the latter trajectories revealed to be more appropriate than a linear fit (not plotted). The P.A. of the outer components J2 and J3 is constant. The P.A. of the inner components rotates in the range of ~ 4° on average per year – an indication for a swing

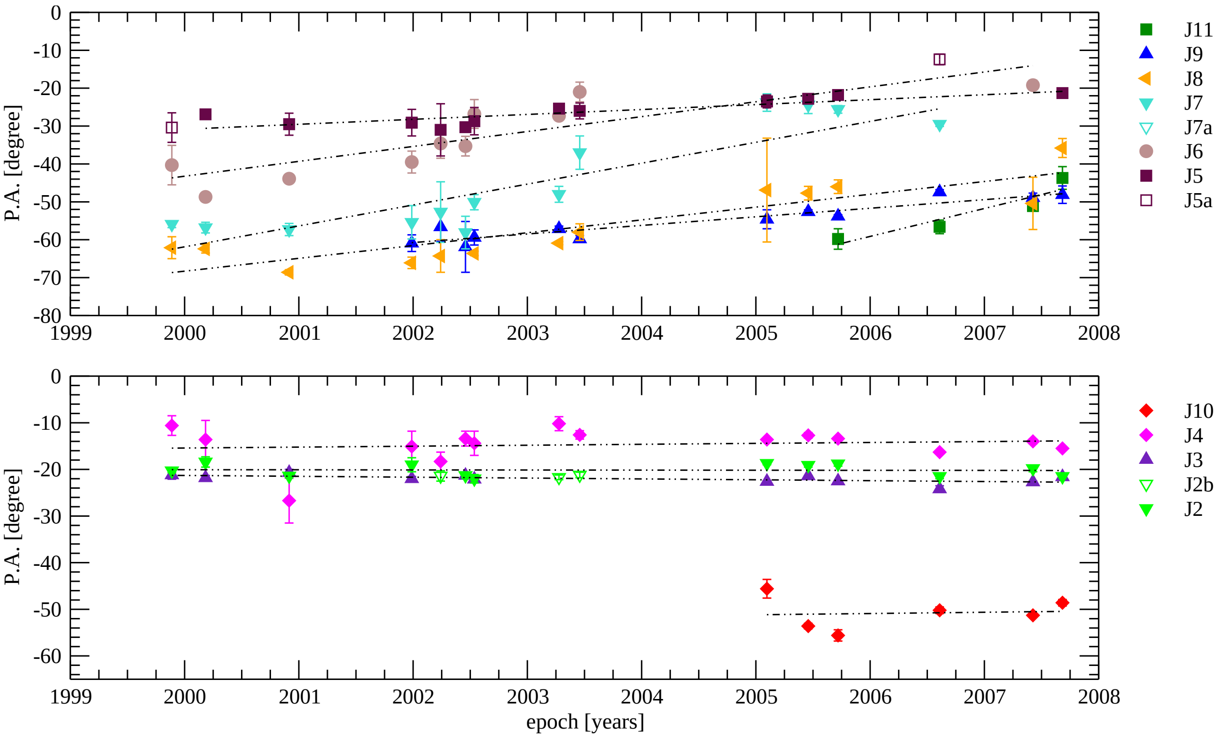

Figure 5.7: *Position angle (P.A.) of the modelfit components at 15 GHz; upper panel: inner jet components show an increase in P.A.; bottom panel: outer jet components have a rather constant P.A. whereas J10 and J4 appear quite convoluted.*

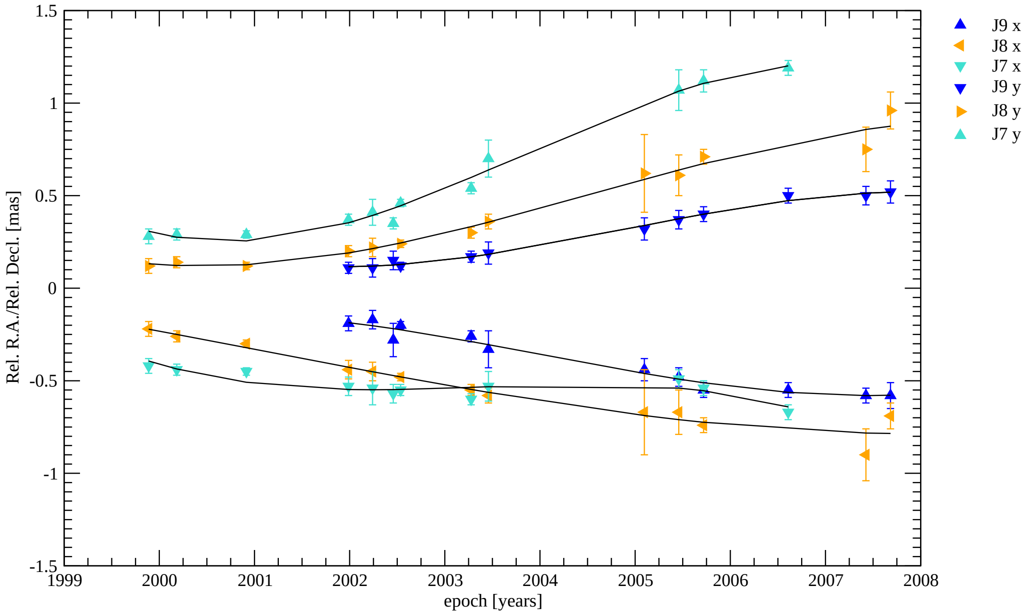

Figure 5.8: *Relative R.A. (x) and rel. Declination (y) of the modelfit components at 15 GHz plotted versus time; the black lines display cubic fits to the data which indicates that the components do not move linearly.*

of the jet base. This hypothesis is also supported by the drift in P.A. between the ejection of J8 and J11, displayed as a kind of opening cone of the jet base in the left panel of Figure 5.6. The observed changes of the P.A. with time clearly indicate motion on bent-non-ballistic trajectories.

The bent jet structure suggests that a linear fit to the component motion is possibly not the most suitable. Hence, we took the three best defined components, J7, J8, and J9, and used a cubic fit according to $y = a_0 + a_1 x + a_2 x^2 + a_3 x^3$ to model the rel. R.A. and rel. Decl. coordinates in what looks the more appropriate way. The fit parameters are presented in Table 5.4. The graphical result is presented in Figure 5.8 indicating that a linear fit is only a rough approximation to the underlying jet kinematics. This could in principle as well imply an accelerated motion of the components along the jet, which is also suggested by the increasing apparent speeds of the components with increasing distance to the VLBI core. However, J10 does not fit into this picture because its apparent velocity is twice as high as would be expected in case of a steadily accelerating jet (see Table 5.3).

Figure 5.9 displays component size (FWHM) versus P.A. of J7, which showed the strongest curvature in our analysis (cf. Figure 5.8). In Figure 5.10, the FWHM is displayed versus time. It is remarkable that the size of J7 (and also J11, J10, J8, J5) increases systematically as it separates from the core, especially beyond a distance of 0.8 mas which was reached sometime

Table 5.4: *Results for the cubic fits on the x-y coordinates of components J9, J8 and J7.*

Id[1]	a_0	a_1	a_2	a_3
J9 x	-2.2892e+07	34269	-17.1	0.0028442
J9 y	3.11e+07	46537	23.212	-0.0038592
J8 x	-5.6812e+06	8517.3	-4.2564	0.00070902
J8 y	2.2805e+07	34129	17.026	-0.0028311
J7 x	4.4647e+07	66859	33.374	-0.0055531
J7 y	7.6735e+07	1.1489e+05	57.339	-0.0095388

[1] Identification of the individual components

after 2004 (cf. also Figure 5.12). The correlation of FWHM with orientation (P.A.) suggests a geometrical origin, i.e. a projection effect. If the components are not spherical but form an intrinsically oblique structure (e.g., a thin shock), relativistic aberration effects would lead to apparent rotation in the observer's frame causing the observed patterns (cf. left panel of Figure 5.9). According to a size change from 0.1 to 0.5 mas for the FWHM of J7, the differential Doppler factor would have changed by $\Delta\delta = 5$, which for an assumed constant jet speed of $\gamma = 8.18$ could be caused by a change of the viewing angle of $\Delta\phi \sim 1.5°$.

The flux density of the individual components of 0917+624 is plotted in Figure 5.11. For the sake of clarity, the plot is split into several panels. The top panel shows the total flux density resulting from single dish measurements of the Effelsberg and UMRAO[3] radio telescopes at

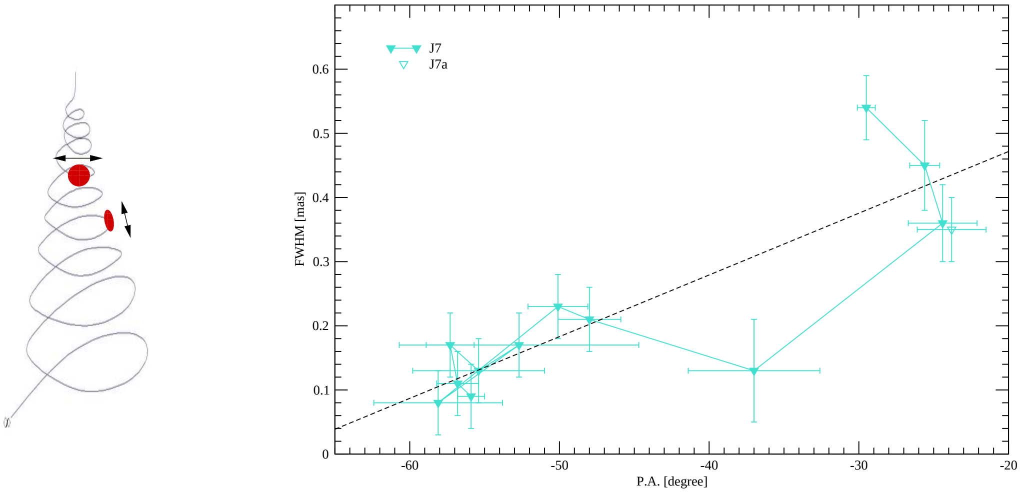

Figure 5.9: *Left panel: illustration of helical component motion in the jet; right panel: FWHM of modelfit component J7 plotted vs. P.A. at 15 GHz.*

---

[3] University of Michigan Radio Astronomy Observatory

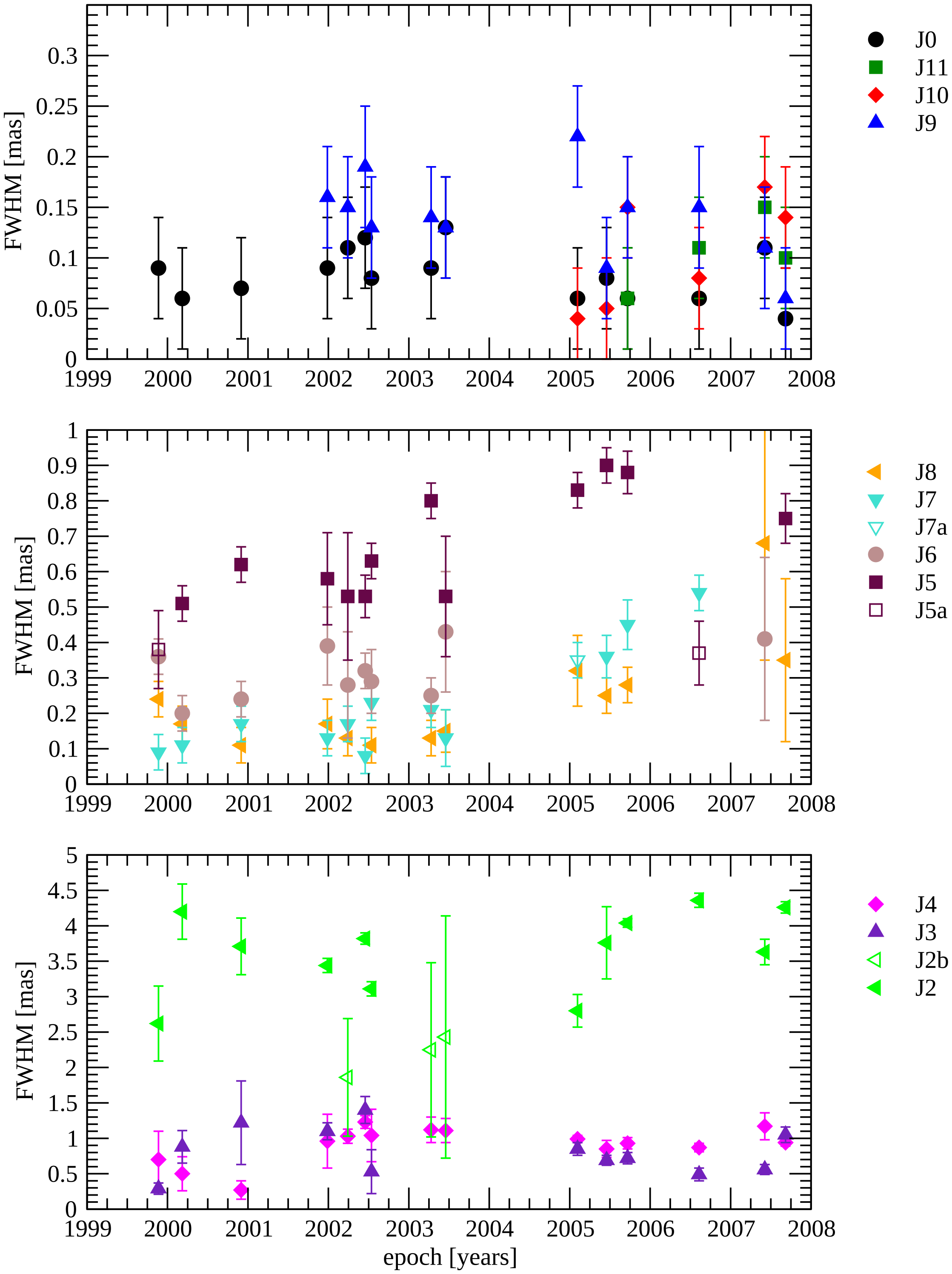

Figure 5.10: *Full width half maximum (FWHM) of the modelfit components at 15 GHz plotted versus time.*

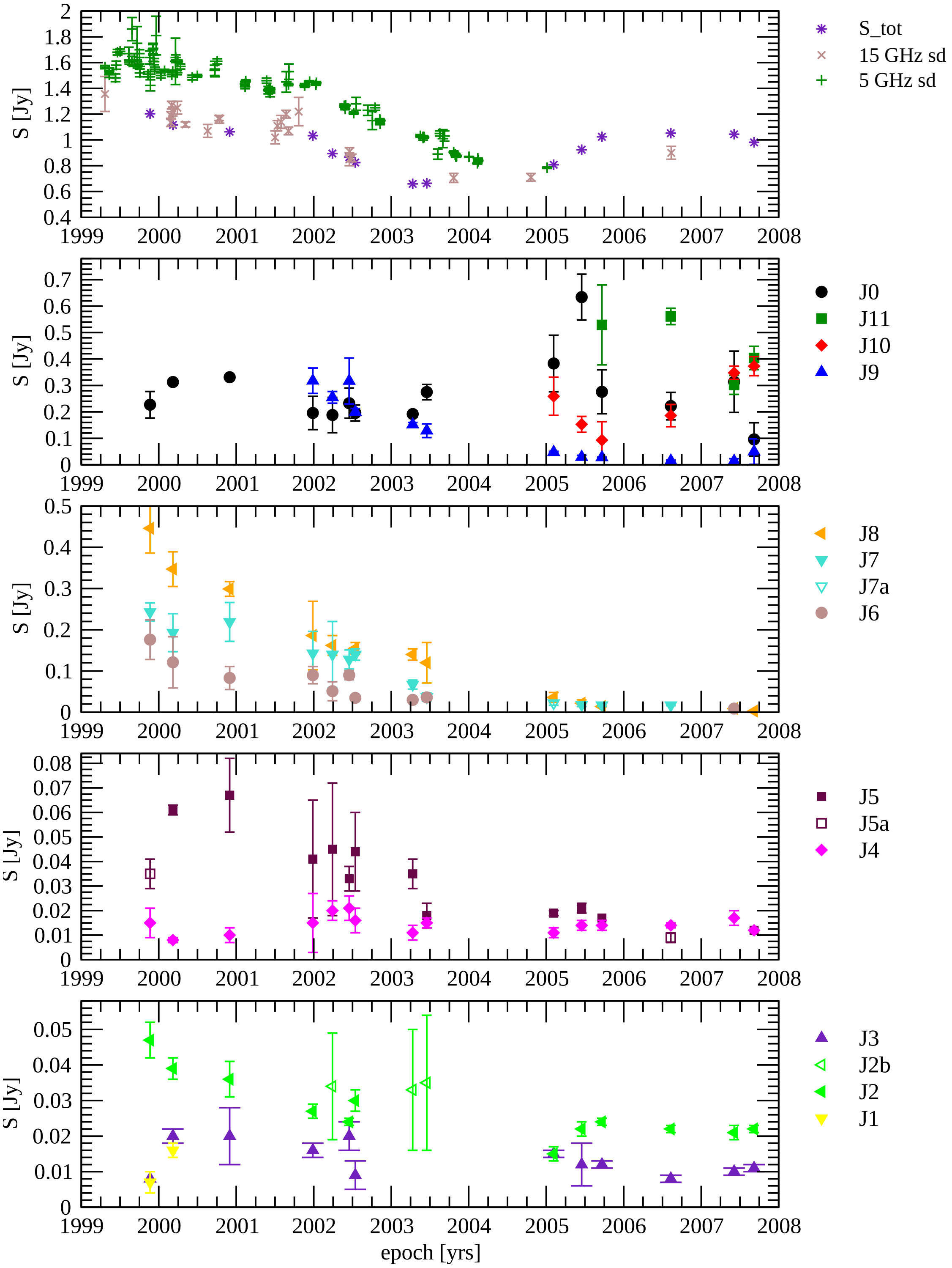

Figure 5.11: *Flux density of 0917+624 at 15 GHz plotted vs. time: the upper panel shows the total VLBI flux and single dish data from the Effelberg and UMRAO telescopes at 15 and 5 GHz; the panels below display the flux of each modelfit component.*

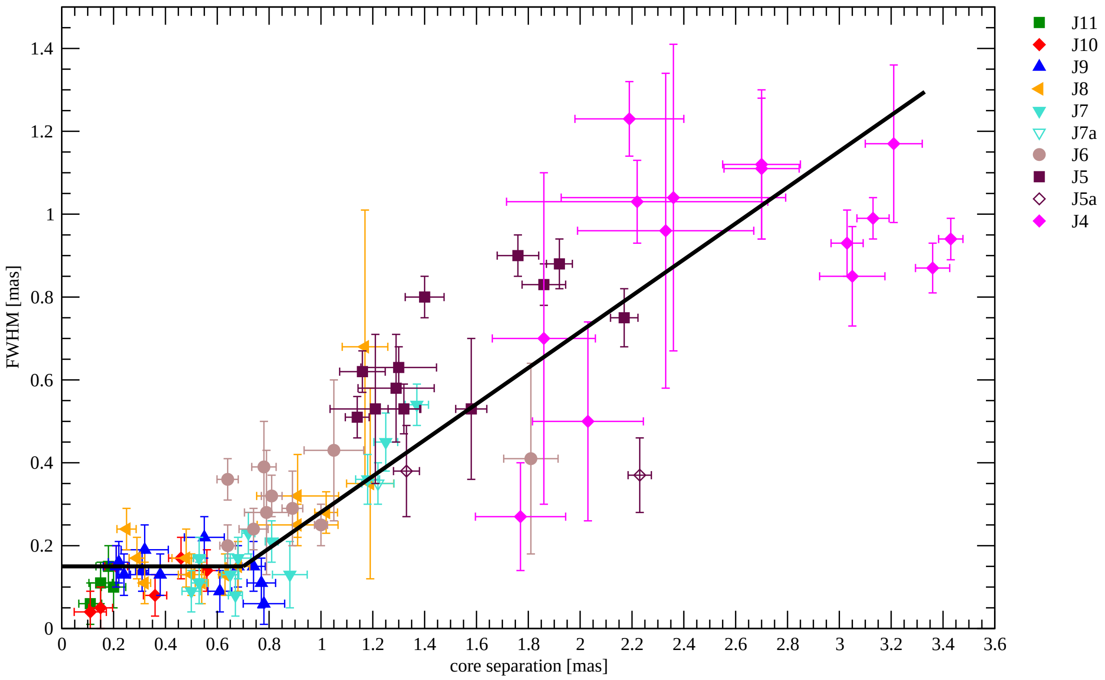

Figure 5.12: *FWHM of the modelfit components at 15 GHz plotted versus core separation; the component size or jet width increases with increasing distance to the core; the jet appears collimated within the inner 0.7 mas and starts expanding beyond; the black line represents fits to the colimated and expanding parts of the jet (see text).*

5 GHz and 15 GHz, respectively, as well as the total VLBI flux from adding up the individual component fluxes for each epoch. The total flux density decreases from the first epoch in 1999 until the end of 2004, afterwards it increases again.

There is a clear decreasing trend in flux density for the outer jet components J2 and J5 to J9. Moreover, the component size systematically increases with increasing distance to the VLBI core. This is diplayed in the top (J11, J10) and middle panel (J8, J7, J5) of Figure 5.10 and in Figure 5.12, where the FWHM is plotted versus time and distance from the core, respectively. The jet is collimated within the inner 0.7 mas and starts expanding beyond. This is in accordance with the theory of an adiabatically expanding jet (e.g., Blandford & Königl 1979). From the increasing jet width (i.e., the component size) one can deduce the opening angle of the jet via $\tan\phi = \frac{FWHM}{r}$ which results in $\phi = 20.9°$. We are now able to derive the Mach number M of the jet plasma at the point of the jet opening via $\sin\phi = \frac{1}{\mathrm{M}}$. The jet moves with a supersonic flow of $\mathrm{M} = 2.8$.

As already addressed previously, the VLBI core J0 is sometimes fainter than the first jet component (J8 and J9, respectively) until the middle of 2002 (epoch 2002.536) where the flux of the VLBI core component and the first jet component J9 are of the same order. Component J9, which was emitted around the middle of 2000, becomes first visible in epoch 2001.988, showing significantly higher flux density than J0. As the component travels down the jet it fades similar to the outer jet components, until a new component (J10) becomes visible in epoch 2005.097. Our analysis shows that in 0917+624 approx. 75% of the total flux is concentrated in the core region (cf. also Standke et al. 1996) which can be seen in the second panel of Figure 5.11. Between 2005 and 2007 the flux density in the outer jet has faded whereas the main portion is focussed within the inner 0.4 mas. A measure for the compactness is also displayed in Figure 5.13 which shows the visibility amplitudes for each epoch plotted versus the (*u*,*v*)-radius

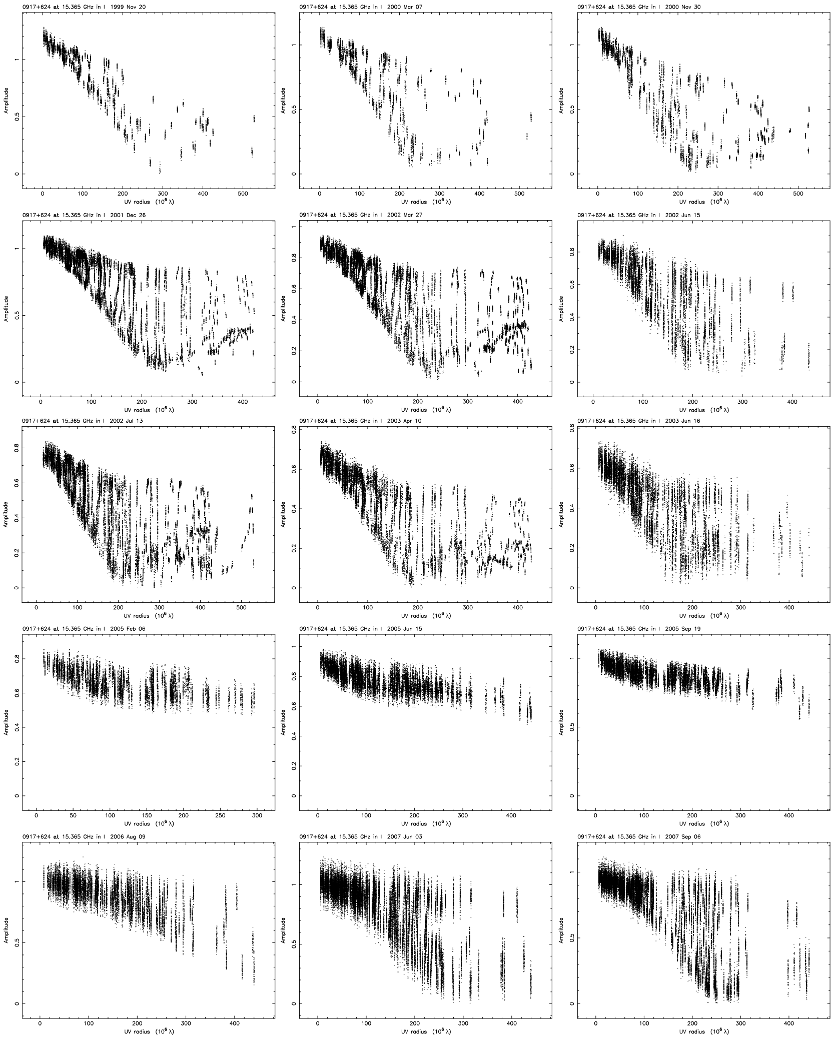

Figure 5.13: *Visibility amplitudes at 15 GHz plotted versus (u, v)-radius given in Mega-wavelength (Mλ), read from left to right starting with the first epoch in the top left panel; the distribution of visibility points according to (u, v)-distance denotes the source compactness (see text).*

at 15 GHz. The panels in the second but last row display all three epochs in 2005 where the source is most compact and contains ~90% of its total flux in the center, losing its compactness again in 2007 when component J10 moves beyond 0.4 mas distance from the core.

A summary of the results for the four innermost components J0, J11, J10, and J9 is presented in Figure 5.14. The correlation between flux and FWHM is not as clear as for the outer components J5 to J8 (cf. middle panels of Figure 5.11 and 5.10). During the first half of the observations (epochs 1999.888 to 2003.458), the overall source spectrum is slightly steeper than during the second half (see middle panel in Figure 5.14). The main source flux density is distributed among the inner 5 components (J6 to J9 and J0) at a time when the source is less compact (cf. above), hence appearing optically thinner than in single dish observations. The spectrum begins to flatten after 2003 which coincides with the time of zero core separation of component J11 (2003.2). In the second half of the observations (epoch 2005.097 to 2007.683), the overall source spectrum is dominated by the innermost components J0, J10, and J11. The components are bright and only small in size (FWHM). This is also demonstrated in the second but last panel of Figure 5.14 where the brightness temperature for each component versus time is displayed. The core exhibits the highest brightness temperature until epoch 2005.097, when component J10 occurs showing the smallest FWHM, but being the brightest component after J0. In the subsequent two epochs, J10 increases in size and decreases in intensity while travelling down the jet until in epoch 2005.719 component J11 becomes apparent with an even higher flux density than J0 and a smaller component size.

In the bottom panel of Figure 5.14, the IDV modulation indices m and variability amplitudes Y are plotted which were derived from single dish measurents with the Effelsberg (see also Chapter 4) and Urumqi 25m radio telescope at 5 GHz (Marchili 2009). The related parameters are listed in Table B.4. The arrows indicate the ejection dates of components J9, J10, and J11, respectively. A visual inspection of the complete plot does not indicate any connection between the IDV behaviour of 0917+624 and the VLBI source structure. According to our previous assumption, the source was expected to return to its former IDV activity after the ejection of a new component. This seems, however, not to be the case. Especially the time between the ejection of J9 (2000.4) and J11 (2003.2) is a quiescent period of obviously strongly quenched scintillation. Taking into account an average annual core separation $\mu = 0.16$ mas yr^{-1}, a potentially new component should meanwhile have separated from the core and passed the estimated distance above the presumed scattering size of ~ 0.07 mas (according to Rickett et al. 1995). Therefore, the quenched scintillation should stop and the former prominent variability pattern is expected to reappear. Although modulation index m and variability amplitude Y show a slight increase around the end of 2005, 0917+624 is still far from its former activity (cf. left bar in the bottom panel of Figure 5.14).

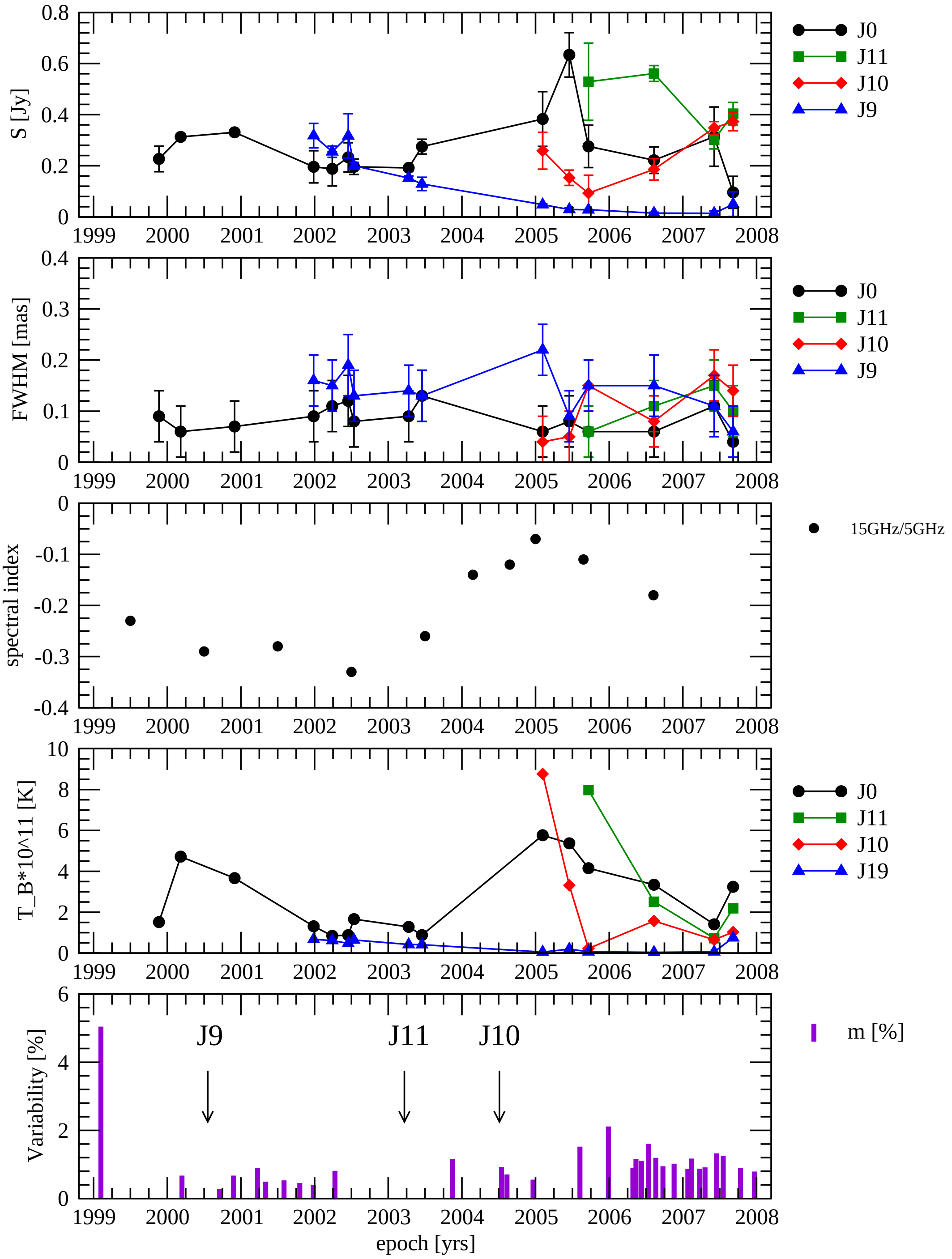

Figure 5.14: *Graphical analysis of the four innermost components J0, J11, J10, and J9 at 15 GHz; upper panel: flux density, panel below: Full Width Half Maximum, middle panel: spectral index between 15 GHz and 5 GHz determined from single dish observations with the Effelsberg and UMRAO telescopes, last but one panel: brightness temperature T_B, bottom panel: IDV modulation index m derived from observations with the Effelsberg and Urumqi telescopes; the arrows indicate the time of zero core separation of components J9, J10, and J11, respectively.*

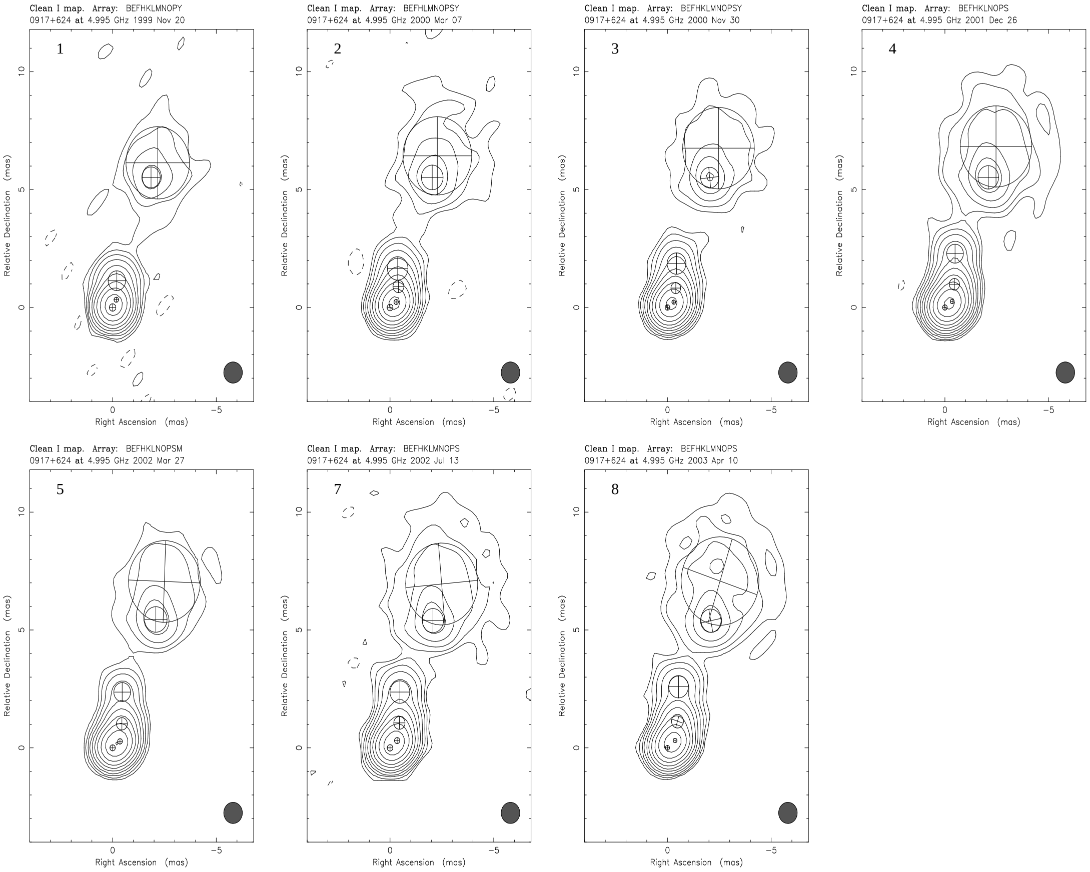

Figure 5.15: *5 GHz modelfits of 0917+624 convolved with a circular beam of (0.9×0.9) mas; numbers refer to epoch listed in Table 5.1; lowest contour starts at 0.7 mJy/beam except for epoch 1 (2.1 mJy/beam) and increases in steps of 2; lowest level skipped for maps of epochs 2, 3, and 5.*

5.2.2 Source Kinematics at 5 GHz

Seven epochs of 5 GHz VLBI data were available, including data from the core campaign from December 2001 to April 2003 (see Table 5.1). Following similar methods as applied for the 15 GHz data, Gaussian components were also fitted to the calibrated 5 GHz data. The maps are displayed in Figure 5.15. The resulting parameters of the modelfits are listed in Table B.2.

Figure 5.16 presents our graphical analysis of the component motion in 0917+624 at 5 GHz. The identification scheme consists of seven - mostly superluminal - components. The results of the linear fits to the trajectory of each component are presented in Table 5.5 which gives for each component (column 1) the separation rate μ in milliarc-seconds per year in column 2, the apparent velocity in column 3, and the time of zero core separation in column 4.

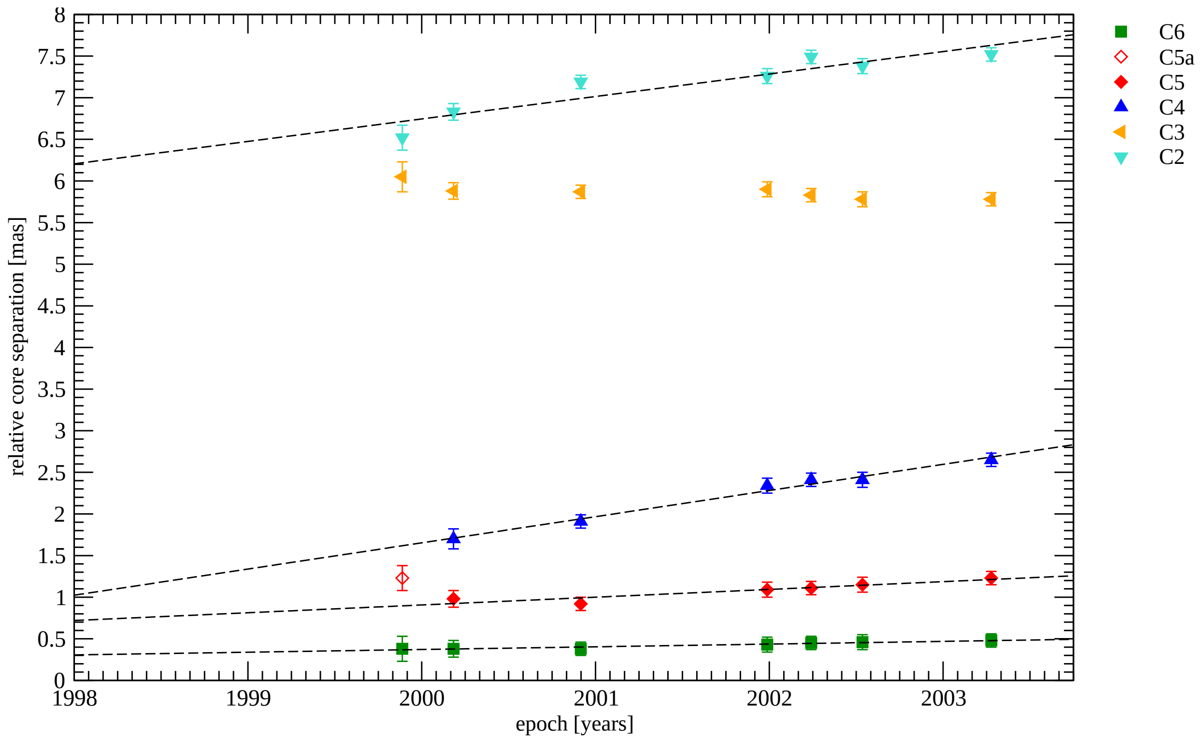

Figure 5.16: *Relative core separation of the modelfit components at 5 GHz; different colors denote for different components; dashed lines give the results of a linear regression analysis.*

The fastest component is C4 with an apparent speed of $\beta_{app} = (19.65 \pm 1.41)$ c. This is in the same range as the outer jet component J2 of the 15 GHz identification scheme and results in a maximum value for the angle to the line of sight $\theta_{max} = 2.9°$. However, C4 corresponds to component J4 at 15 GHz which has an apparent speed of (12.33 ± 1.10) c. This is rather in the

Table 5.5: *Results for the fit on the core separation of the modelfit components at 5 GHz; given are the annual separation rate μ, apparent velocity β_{app} and time of zero core separation* t_0 *for each component.*

Id[1]	μ [mas/year]	β_{app} [c]	t_0
C6	0.04±0.004	2.22±0.26	1989.7±1.4
C5	0.10±0.02	6.28±1.17	1991.1±2.3
C4	0.31±0.02	19.65±1.41	1994.7±1.0
C3	-0.05±0.02	-2.81±1.02	-
C2	0.23±0.05	14.53±2.99	1970.5±4.7
C1	0.13±0.07	7.93±4.66	1816.4±102.3

[1] Identification of the individual components

range of the second fastest component C2 ($\beta_{app} = 14.53 \pm 2.99$ c). The reversion of the velocity distribution for the two frequencies on the one hand could be explained by the undersampling of the 5 GHz data (7 epochs) compared to 15 GHz (15 epochs). The effect of the undersampling will be further discussed in section 5.2.4. On the other hand, the three times worse resolution at 5 GHz[4] produces a larger beam pattern which rather resolves large-scale structures distant from the VLBI core. The latter is already obvious in the comparison of the 5 and 15 GHz maps (Figures 5.2 and 5.1) where at 5 GHz the coherent jet structure ranges up to 10 mas compared to approx. 3 mas at 15 GHz. Besides the flux density of the outer jet components is several times higher in the lower frequency band (cf. column 1 of Tables B.2 and B.1).

---

[4] Angular resolution R $\propto \frac{\lambda}{D}$ with frequency λ and telescope diameter D

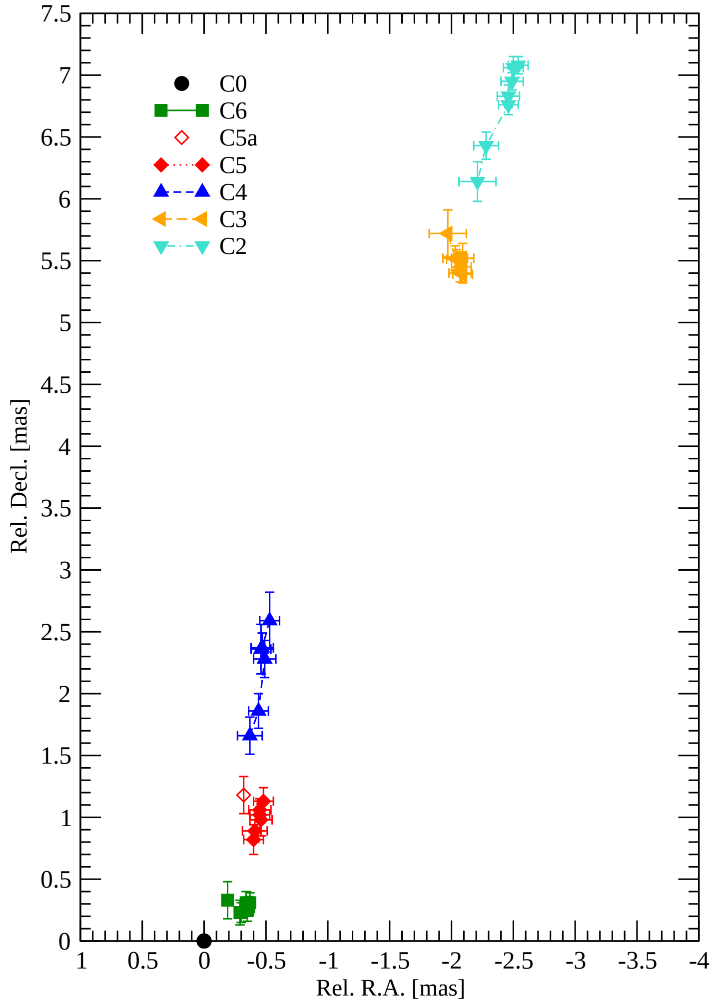

Figure 5.17: *Relative Right Ascension (rel. R.A.) plotted vs. Relative Declination (rel. Decl.) at 5 GHz.*

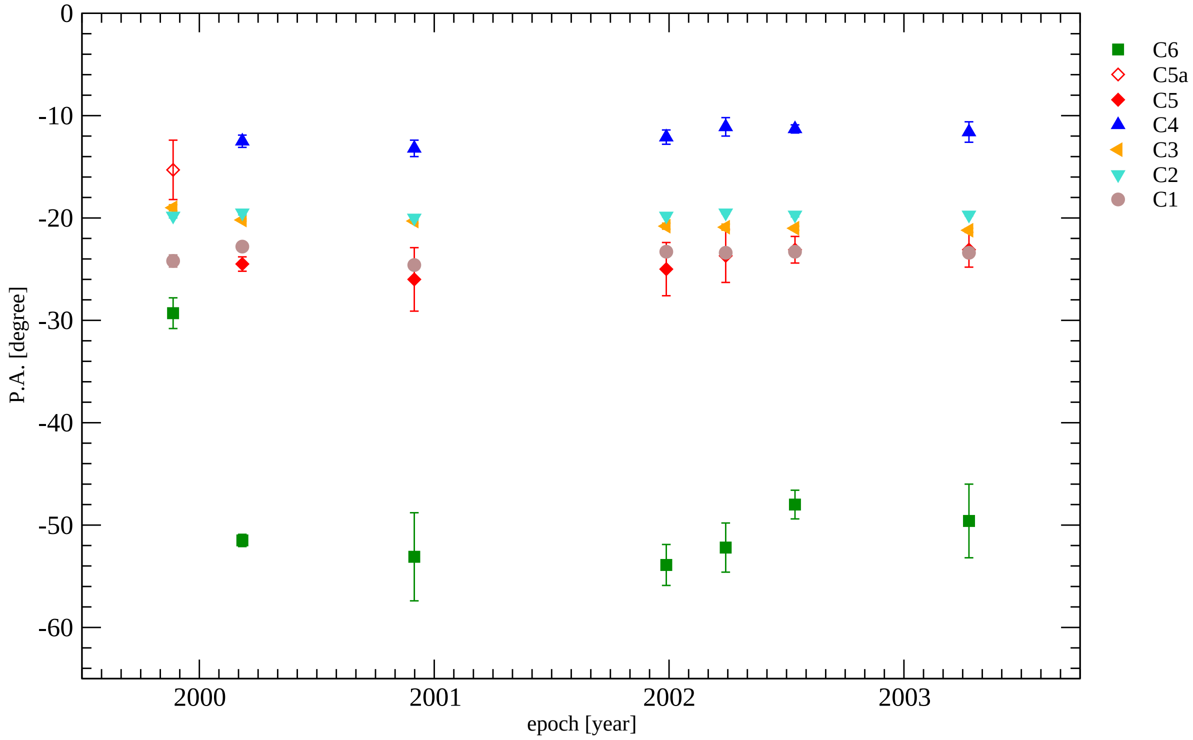

Figure 5.18: *Position angle (P.A.) of the modelfit components at 5 GHz.*

The apparent speed of the first jet component C6 of ∼2.2c is three times slower compared to the apparent speed of the inner jet components (J7, J8, J9) at 15 GHz. This can be explained by blending effects due to the worse resolution at 5 GHz. In this regime, only one component is visible whereas at the higher frequency we are able to resolve 2 different components: J7 and J8 from epoch 1999.888 to epoch 2000.915, and J8 and J9 from epoch 2001.988 on.

The rel. R.A. - rel. Decl. pathes of the jet components at 5 GHz are presented in Figure 5.17. The jet structure appears not as strongly bent as in the 15 GHz plots. At first sight, there are merely two kinks visible. This can also be credited to the lower resolution that is achieved when observing at 5 GHz. The jet emerges into northwestern direction with P.A.$\sim -50^\circ$ (cf. component C6 in Figure 5.18) and turns northward at a distance from the core of about 0.5 mas with P.A.$\sim -11^\circ$ (C4). The second kink occurs somewhere between 3 and 5 mas where the jet turns north-north-westward at P.A.$\sim -20^\circ$ (C2 and C3). The slightly bent structure becomes more obvious when plotting rel. R.A. or rel. Decl. versus time separately as is shown in Figure 5.19 where the upper panels display rel. R.A. and the bottom panels display rel. Decl. plotted versus time, respectively. For a clear arrangement, the left panels present the inner components (C4 to C6) and the right panels show the outer ones (C2, C3). However, if we compare the results for the rel. R.A. - rel. Decl. pathes at 5 GHz to the results at 15 GHz (Figure 5.8), it is apparent that the trajectories can rather be fitted linearly than by a higher-order fit. And except for C6, the P.A. of the components remains rather constant as is shown in Figure 5.18 in contrast to the increasing trend at 15 GHz (cf. Fig. 5.7). This is due to the worse resolution at 5 GHz showing only coarse jet structure in the inner region.

The flux density evolution at 5 GHz is presented in Figure 5.20. The decreasing trend of the single dish flux (top panel) can be mainly attributed to the VLBI core (C0) and first jet component (C6) as well as the outer jet components C4, C2 and C1. Component C3, which corresponds to J3 at 15 GHz, appears to be constant since it barely shows changes in its flux density, size and position (annual core separation $\mu = -0.05 \pm 0.02$mas yr^{-1}). This confirms the findings at 15 GHz and supports our component identification. In epoch 1999.888, the flux density of the VLBI core (component C0) and the first jet component C6 display large errors. The main contribution to these errors results from the model fitting process. Especially the flux density significantly altered between the repeated model fittings, most likely because of some kind of blending effect between the two components. The second jet component C5a is apparently separating into C5 and C4 in the successive epoch (2000.183) which is already suggested in Figure 5.19, but also in Figure 5.18 and Figure 5.21 where P.A. and FWHM are plotted versus time, respectively.

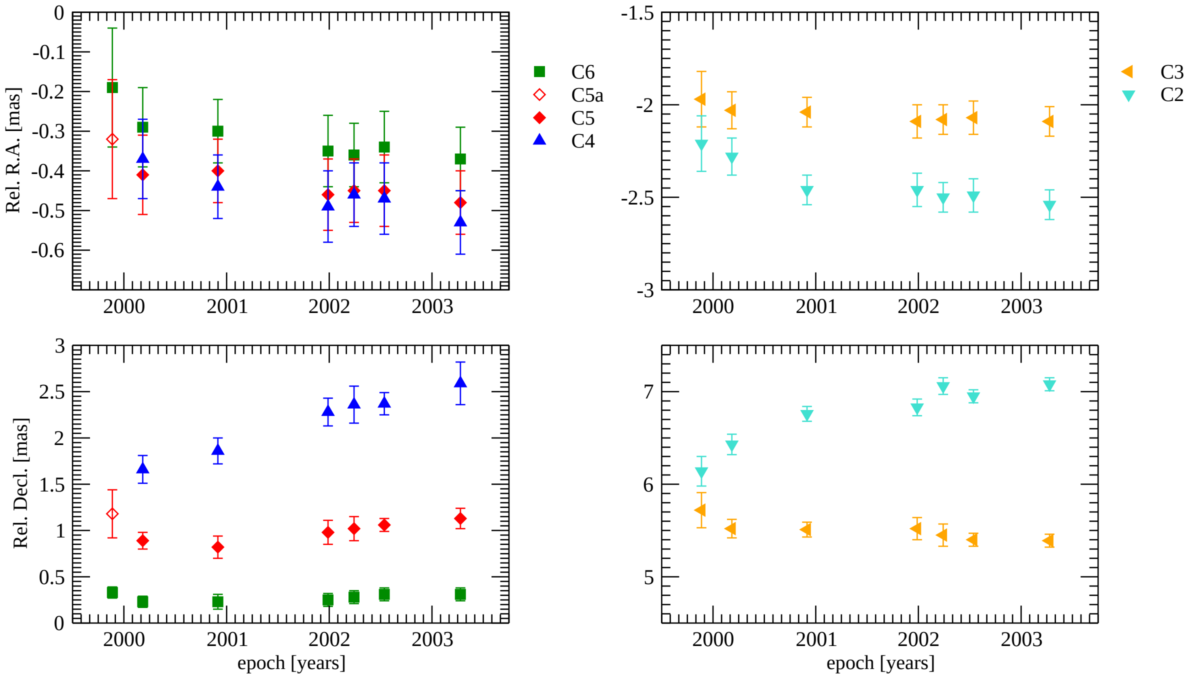

Figure 5.19: *Relative R.A. and rel. Declination of the modelfit components at 5 GHz plotted versus time.*

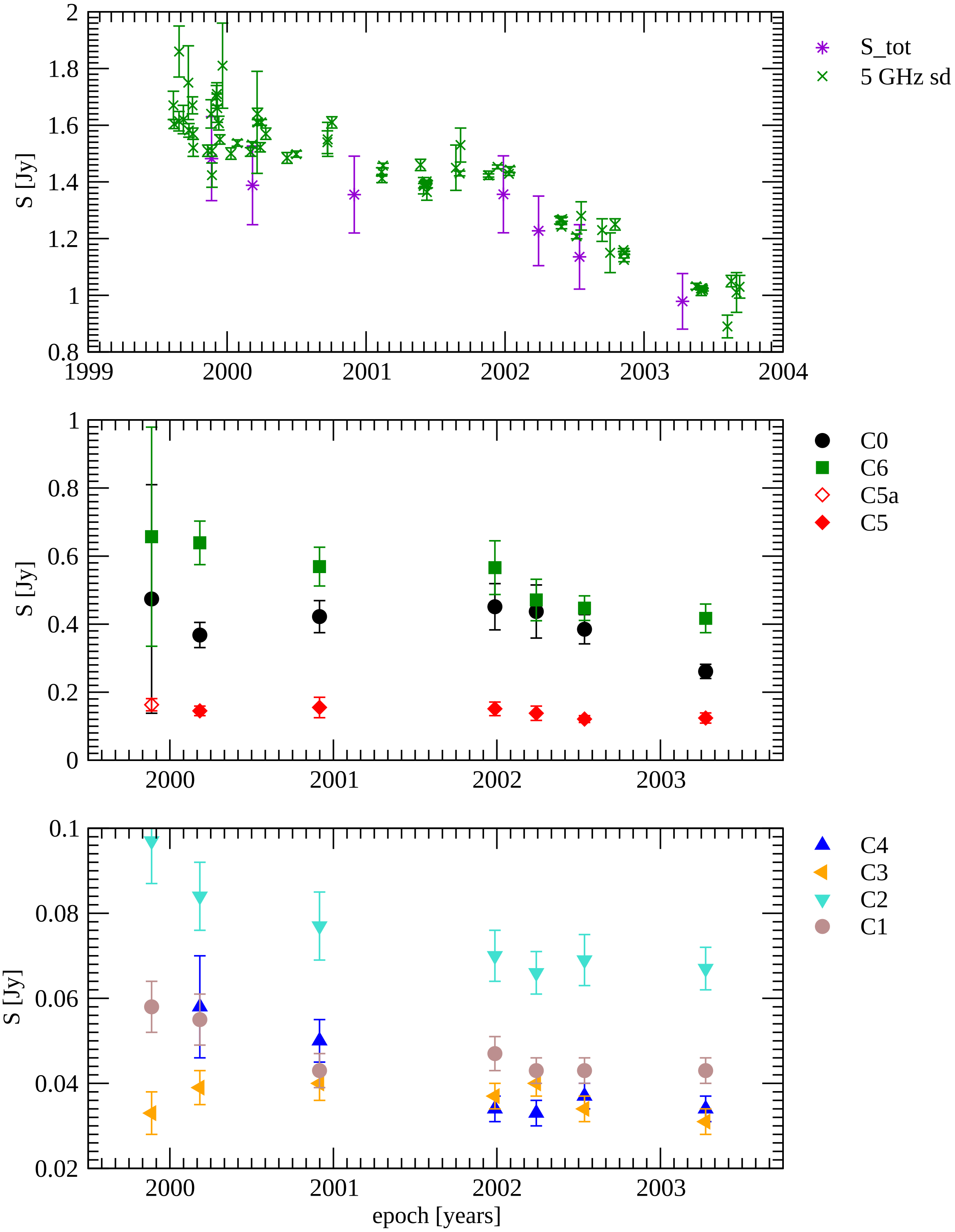

Figure 5.20: *Flux density of 0917+624 at 5 GHz plotted vs. time: the upper panel shows the total VLBI flux and single dish data from the Effelberg and UMRAO telescopes at 5 GHz; the panels below display the flux of each modelfit component.*

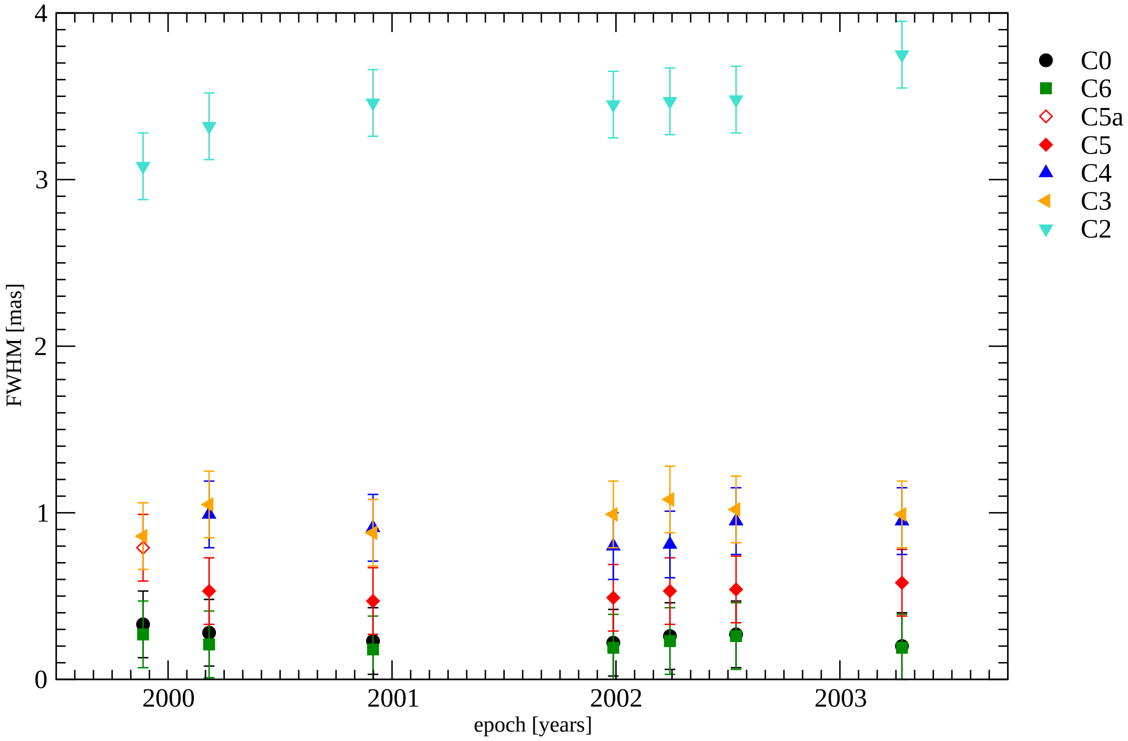

Figure 5.21: *Full width half maximum (FWHM) of the modelfit components at 5 GHz plotted versus time.*

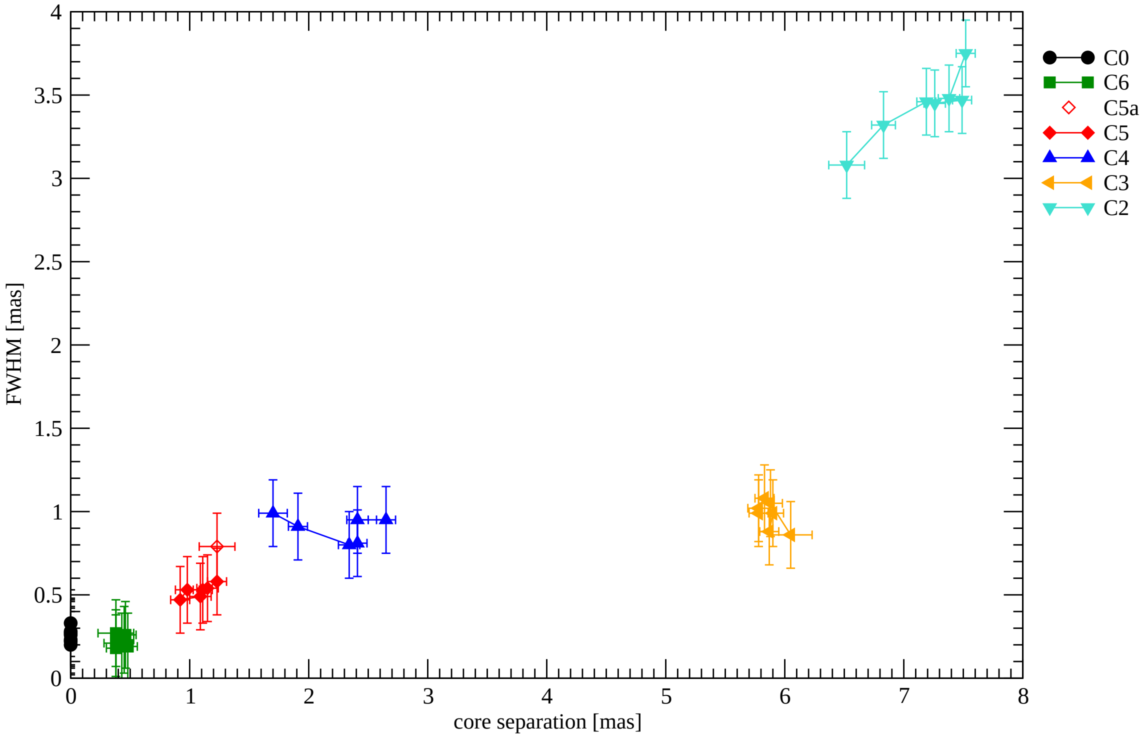

Figure 5.22: *FWHM of the modelfit components at 5 GHz plotted versus core separation.*

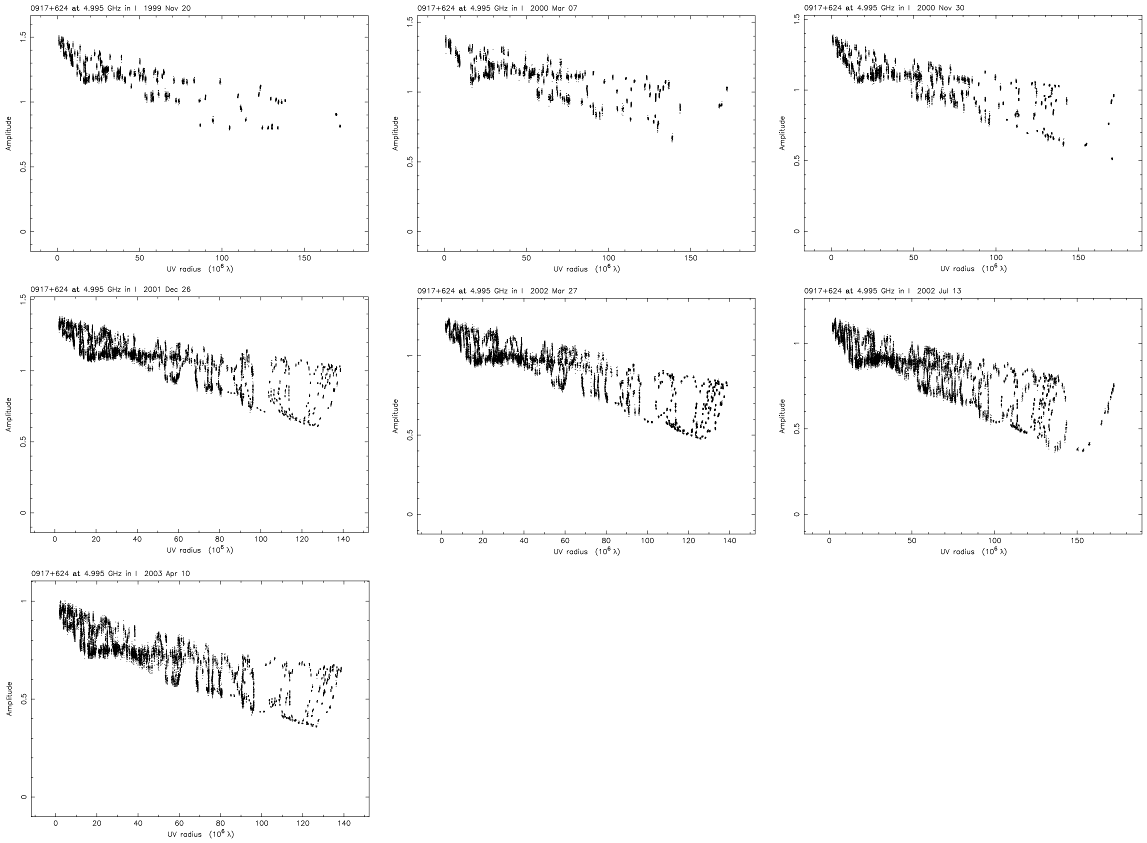

Figure 5.23: *Visibility amplitudes plotted versus the (u, v)-radius at 5 GHz; the distribution of the visibility points according to (u, v)-distance show that the source is very compact.*

The components do barely alter their FWHM except for C2 which increases in size the further it moves down the jet. This is displayed in Figures 5.21 and 5.22 where the FWHM is plotted versus time and core separation, respectively.

At 5 GHz the source reveals to be rather compact and core dominated which is also displayed in Figure 5.23 where the visibility amplitudes are plotted versus (u, v) distance. On average, 85 % of the total flux are concentrated in the inner 1.2 mas regarding the three times worse resolution compared to the 15 GHz data. Considering the inner 0.4 mas, it still remains a portion of more than 70 %.

5.2.3 Source Kinematics at 22 GHz

The 22 GHz VLBI data consist of the four epochs from the core campaign observed between December 2001 and April 2003 (see Table 5.1). Two additional epochs from the RRFID (Radio Reference Frame Image Database) observed at 24 GHz in February and December 2004 were

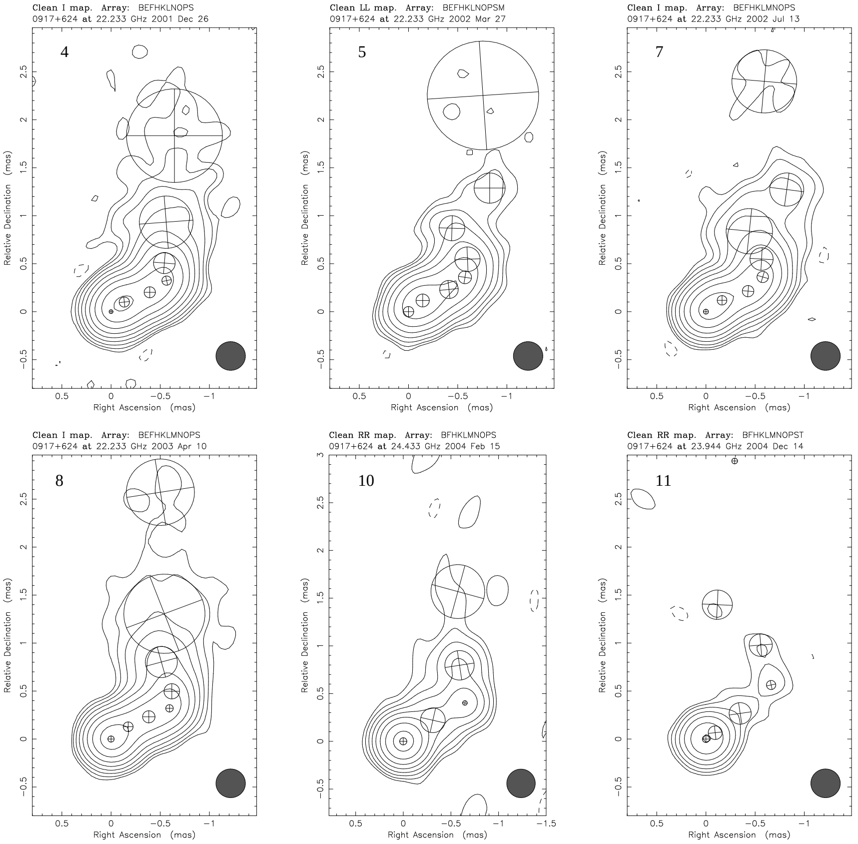

Figure 5.24: *22 GHz modelfits of all epochs of 0917+624 convolved with a circular beam of (0.3×0.3) mas; numbers refer to epoch listed in Table 5.1; lowest contour is 1 mJy/beam for maps of epochs 4, 5 and 7; 2 mJy/beam for epochs 5 and 10; 7 mJy/beam for epoch 11; contour levels increase in steps of 2.*

taken to complement the data (all epochs will in the following be referred to as 22 GHz data). Following the method that was applied for the 15 and 5 GHz data, Gaussian components were also fitted to the calibrated data. The resulting maps are displayed in Figure 5.24 and the associated parameters are listed in Table B.3.

The graphical analysis of the component motion in 0917+624 at 22 GHz is presented in Figure 5.25. The identification scheme consists of nine components. The identification of the innermost four jet components revealed to be straightforward compared to the components beyond a relative core separation of 1 mas. Several components split up into two subcomponents (K3, K2) and in some cases only one of these subcomponents was visible (e.g. K3b in the last epoch 2004.955). Apart from the innermost and the outermost components (K0 and K1), all other reveal superluminal motion. For the calculation only the main components (K6, K3, K2) were taken into consideration. The results of the linear fit to the trajectory of each component

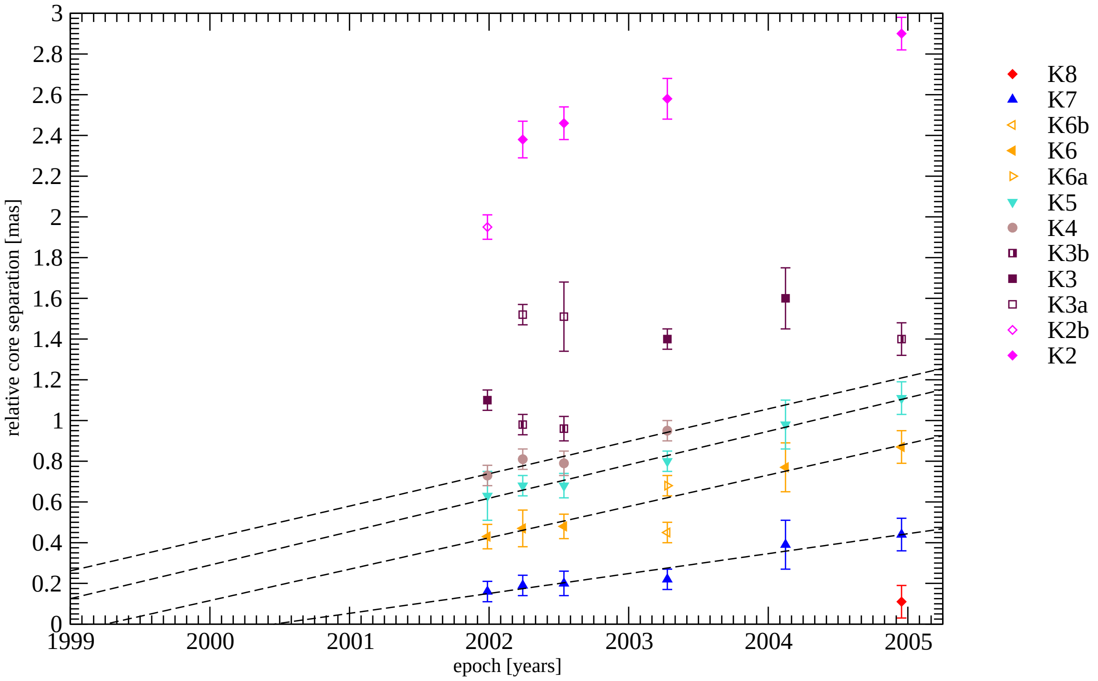

Figure 5.25: *Relative core separation of the innermost modelfit components at 22 GHz; different colors denote for different components; dashed lines give the results of a linear regression analysis.*

are presented in Table 5.6 which gives for each component (column 1) the separation rate μ in milliarc-seconds per year in column 2, the apparent velocity in column 3, and the time of zero core separation in column 4.

The fastest component is K3 with an apparent velocity $\beta_{app} \sim 14.6\,c$. This is on the one

Table 5.6: *Results for the fit on the core separation of the modelfit components at 22 GHz; given are the annual separation rate μ, apparent velocity β_{app} and time of zero core separation t_0 for each component.*

Id[1]	μ [mas/year]	β_{app} [c]	t_0
K7	0.09±0.02	5.47±0.95	2000.2±2.9
K6	0.15±0.01	9.58±0.54	1999.2±1.3
K5	0.16±0.01	10.05±0.79	1998.1±1.2
K4	0.16±0.03	10.01±2.04	1997.4±3.0
K3	0.23±0.01	14.63±0.05	1997.3±1.0
K2	0.19±0.01	11.75±0.37	1989.5±0.5
K1	0.03±0.11	2.42±7.33	-

[1] Identification of the individual components

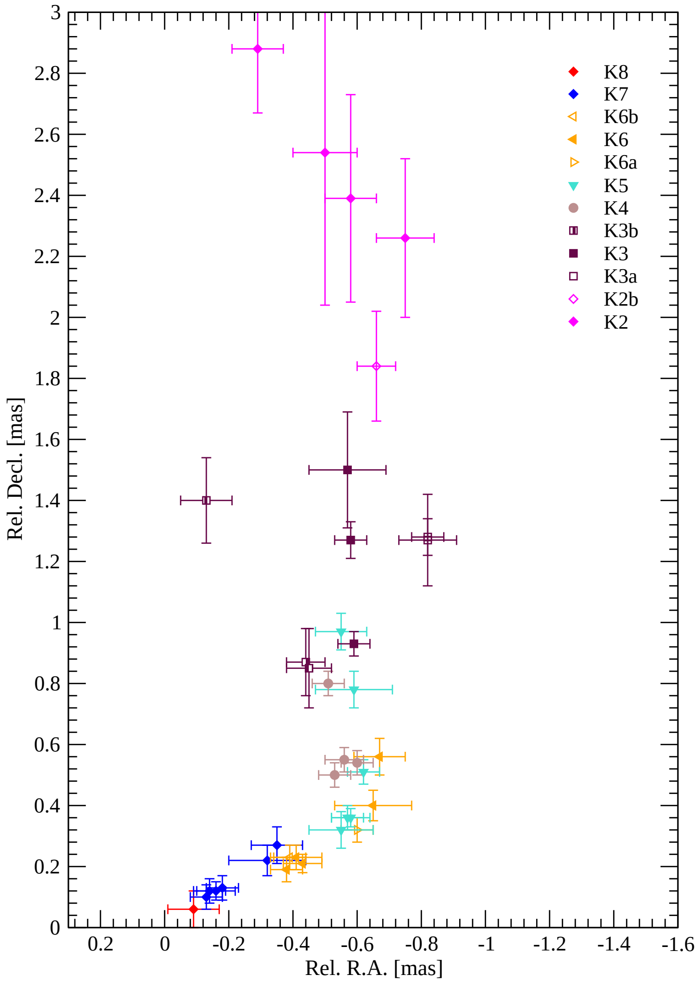

Figure 5.26: *Relative Right Ascencion plotted versus Relative Declination of 0917+624 at 22 GHz.*

hand slower than the fastest components of the other frequencies, and hence would result in a larger angle to the line of sight θ_{max} of the order of 4°. On the other hand, this is remarkably faster than the values of the corresponding components at 5 and 15 GHz. However, this result was only achieved by means of three data points which makes it less reliable. This will be further discussed in the context of sections 5.2.4 and 5.2.5 where the effect of the obvious undersampling compared to the other frequencies will be addressed in more detail.

The rel. R.A. - rel. Decl. pathes of the jet components at 22 GHz are plotted in Figure 5.26. The jet structure reveals an almost quasi-sinusoidal pattern in direction of rel. Decl.. Between 1.2 and 1.6 mas the jet seems to widen owing to the split-up into two components instead of one. Taking a closer look at the jet ridge line (the rel. R.A. - rel. Decl. pathes per epoch), that is

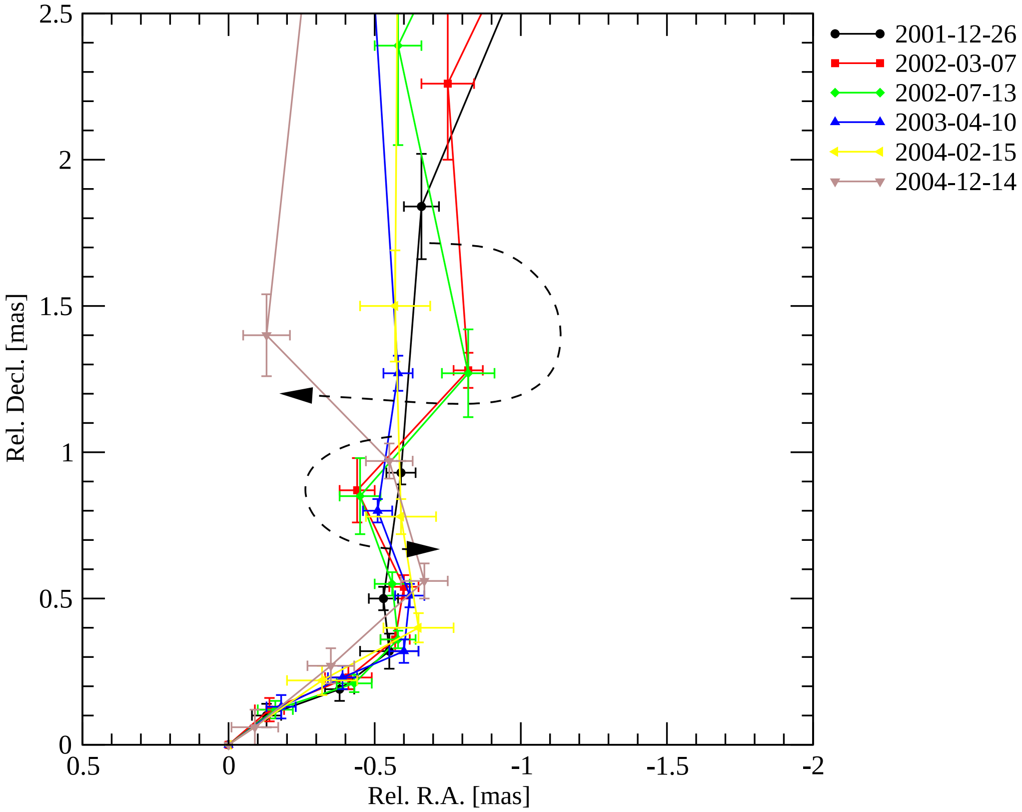

Figure 5.27: *Jet ridgeline of 0917+624 at 22 GHz; the dashed lines indicate the movement of the component trajectories in time.*

plotted in Figure 5.27, it becomes obvious that the jet does not expand but rather rotate. Here, the trajectories appear to move counterclockwise at a relative core separation around 0.9 mas, whereas around 1.5 mas the movement appears contrariwise as indicated by the dashed arrows in Figure 5.27.

Figure 5.28 shows the components' rel. R.A. and rel. Decl. plotted versus time where the upper panels display rel. R.A. and the bottom panels display rel. Decl. plotted versus time, respectively. The trajectories of the inner jet components (K7, K6, K5 – left panel) indicate a bent structure whereas the outer components are mainly moving in direction of rel. Decl. and stay rather constant in direction of rel. R.A.. The trajectories of component K1 remain constant in both directions which makes it an equivalent to J3 at 15 GHz and C3 at 5 GHz. In principle a linear fit could well represent the trajectories of all components in both directions except for the movement in rel. R.A. of the inner components K5, K6, and K7 (see bottom left panel of Figure 5.28). It seems that the components experience a slight acceleration in this direction similar to what could be concluded from the 15 GHz data (cf. Figure 5.8).

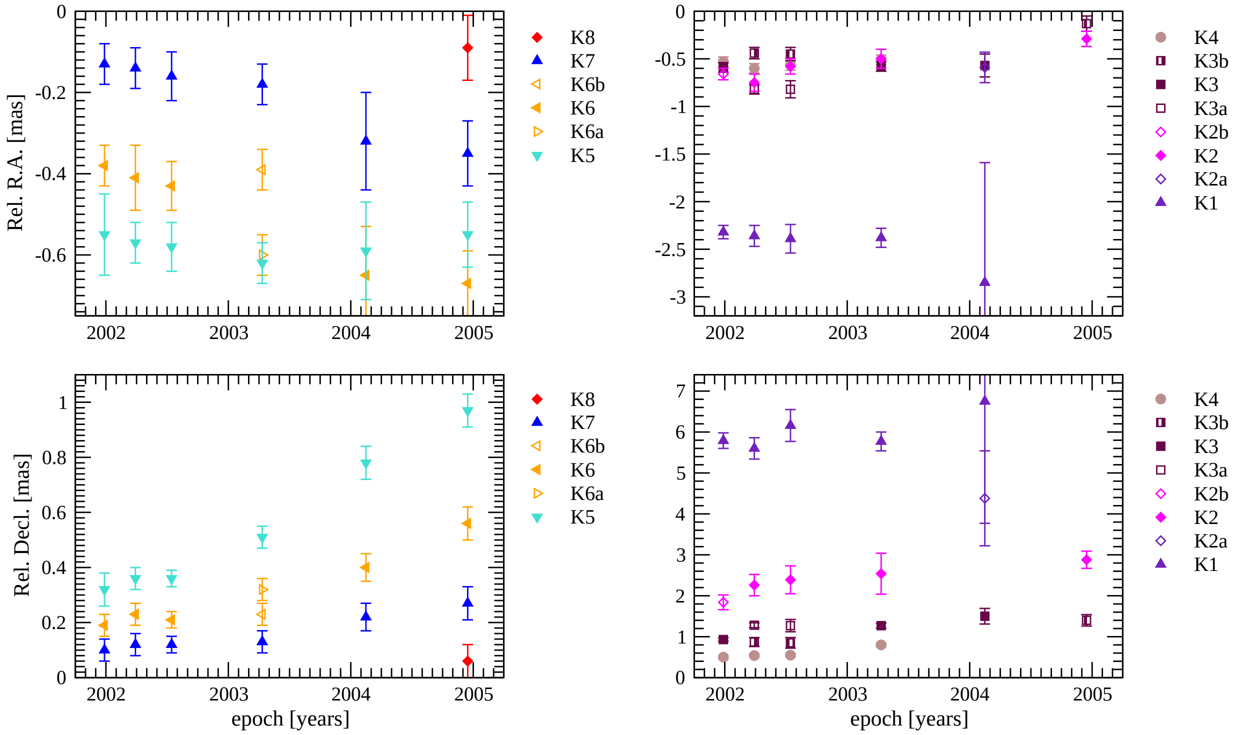

Figure 5.28: *Relative Right Ascencion (upper panels) and Relative Declination (lower panels) of 0917+624 at 22 GHz plotted vs. time.*

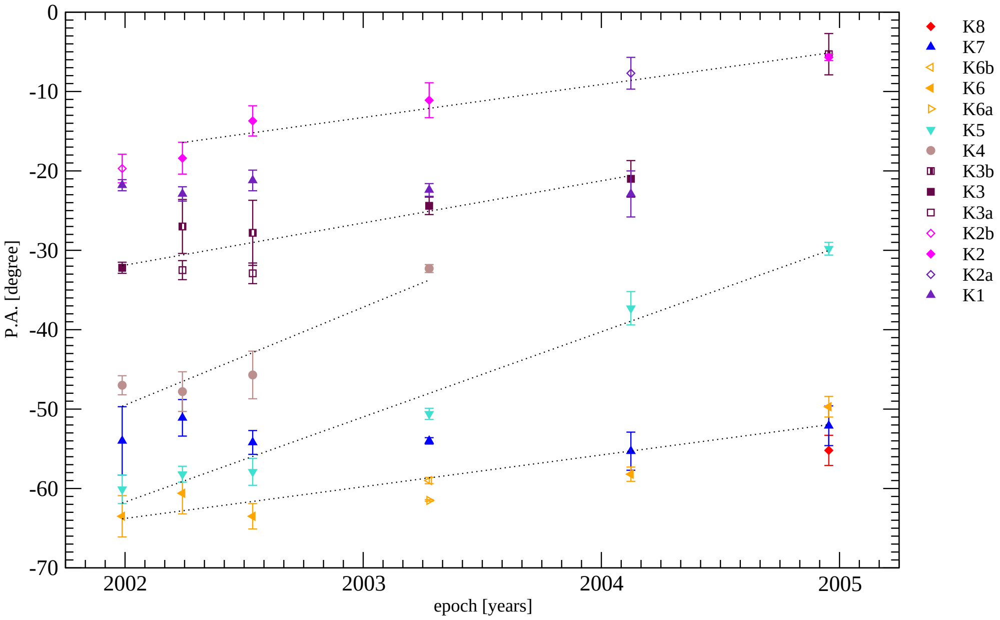

Figure 5.29: *Position angle of the modelfit components at 22 GHz.*

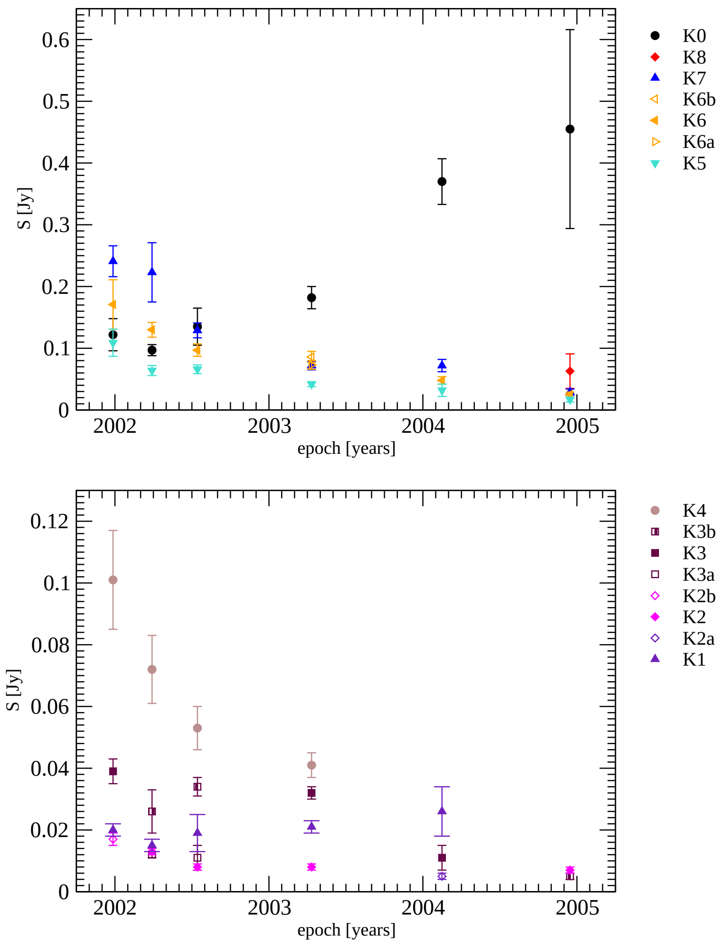

Figure 5.30: *Flux density of 0917+624 at 22 GHz plotted vs. time.*

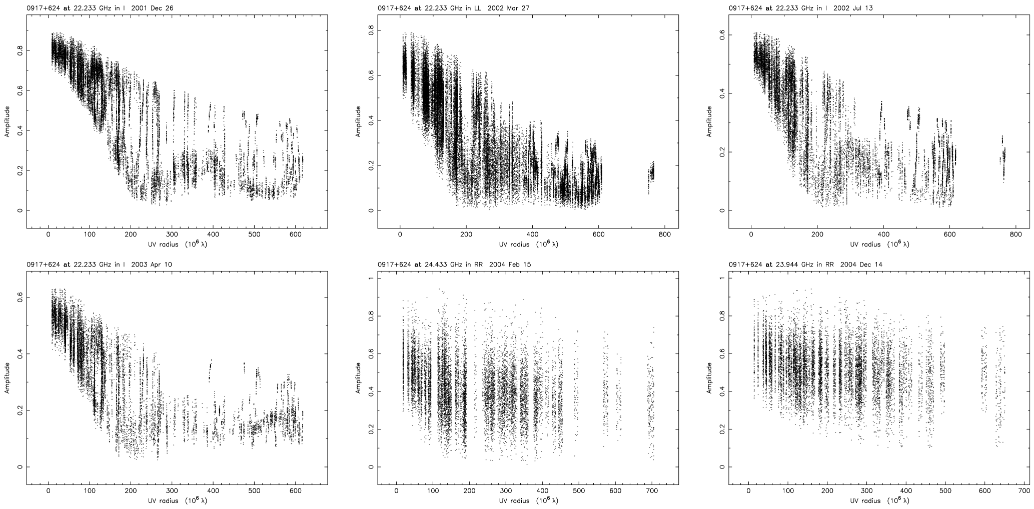

Figure 5.31: *Visibility amplitudes plotted versus the (u, v)-radius at 22 GHz; the distribution of the visibility points according to (u, v)-distance gives a hint to the compactness of the source: the structure of 0917+624 is resolved in the first four epochs and becomes core dominated in the last two.*

The P.A. of the modelfit components at 22 GHz is displayed in Figure 5.29 showing a clearly increasing trend except for the more or less constant P.A. of K7 and K1. The annual change of the P.A. is in the range of ~ 4.2° on average. This is an indication for a rotation of the jet base and confirms our findings of the 15 GHz analysis (cf. Figure 5.7).

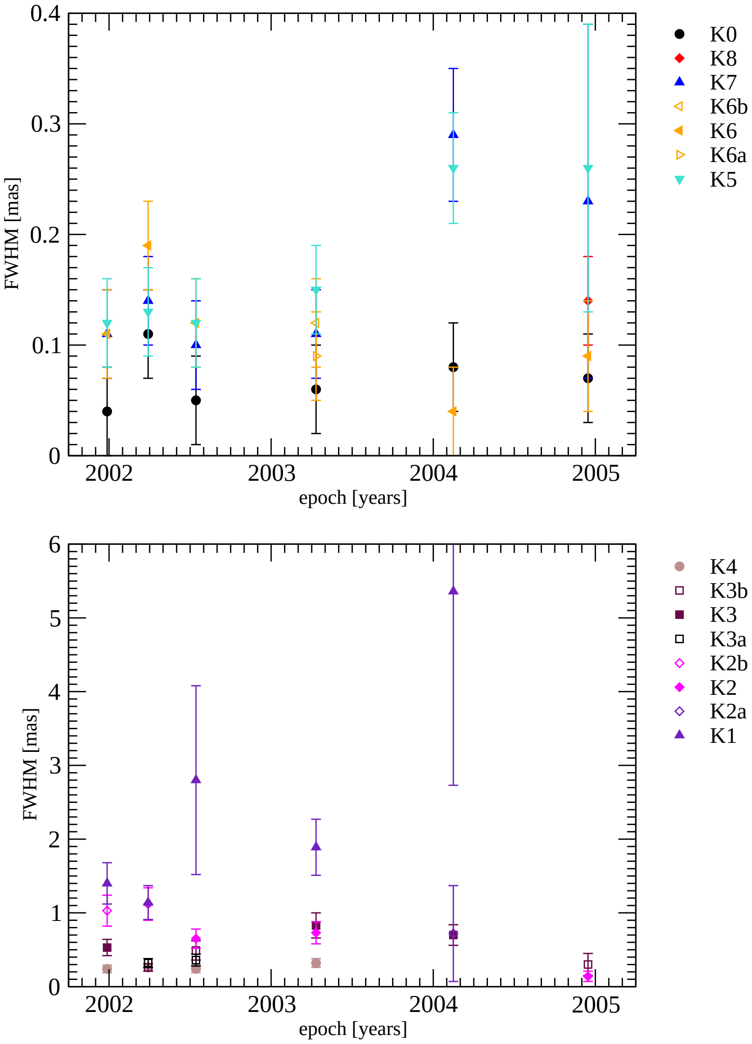

Figure 5.32: *FWHM of 0917+624 at 22 GHz plotted vs. time; top panel displays the inner, bottom panel the outer jet components.*

The flux density of the 22 GHz components is plotted in Figure 5.30. The jet components show a decreasing trend in flux density from the first to the last observing epoch except for K1, whose flux density remains constant. This implies that K1 is equivalent to J3 and C3 of the 15 and 5 GHz component identification schemes. In contrast to the jet components at 22 GHz, the flux density of the VLBI core (K0) constantly increases starting with a smaller value than the inner jet components K7 and K6 in the first two epochs. This is also in accordance with the 15 GHz results (cf. Figure 5.11). The source structure is resolved in the first four epochs and becomes core dominated in the last two epochs (2004.124 and 2004.955) when the flux density of K0 reaches its maximum and a newly ejected component (K8) turns up. The compactness of the source is displayed in Figure 5.31 where the distribution of the visibility points according to (*u*, *v*)-distance is plotted. This plot bridges the observational gap in the 15 GHz data and shows the period (2004) when 0917+624 becomes core dominated due to the ejection of a new component.

The development of the component size (FWHM) during the observations is shown in Figure 5.32. In contrast to the 15 GHz data, only K7, K5 and K1 appear to expand whereas K6 and K2 even seem to reconfine during the observations. This is also demonstrated in Figure 5.33 where the FWHM is plotted versus core separation. It seems that the jet starts expanding to a width of ~0.3 mas until a relative distance to the core of approx. 0.4 mas. Then it contracts to a width of 0.2 mas at a distance of 0.7 mas. Afterwards it widens to around 1.1 mas at a core separation of approx. 2.4 mas before it strongly constricts around 3 mas. This lateral displacement is in contrast to the 15 GHz result and can be attributed to the slightly better resolution at 22 GHz that enables to reveal more details on the small scale structure closer to the VLBI core. It becomes clearer in a direct comparison in Figure 5.34 where larger-scale plots of FWHM versus relative core separation at both 15 and 22 GHz are shown. Obviously, the contraction of the 22 GHz jet structure (bottom panel) around 2 mas is more pronounced

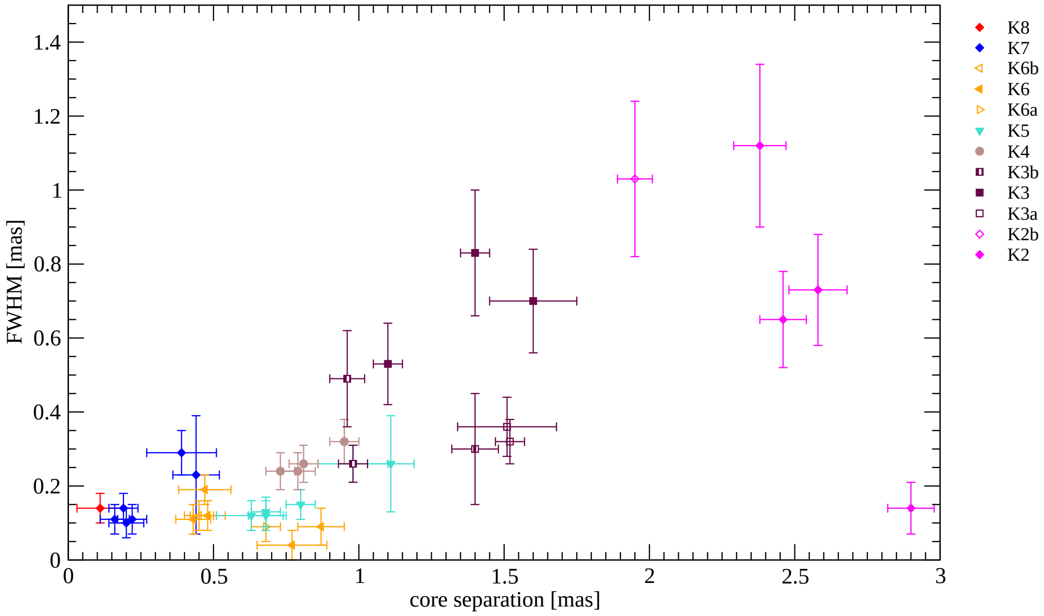

Figure 5.33: *FWHM of the modelfit components at 22 GHz plotted versus core separation.*

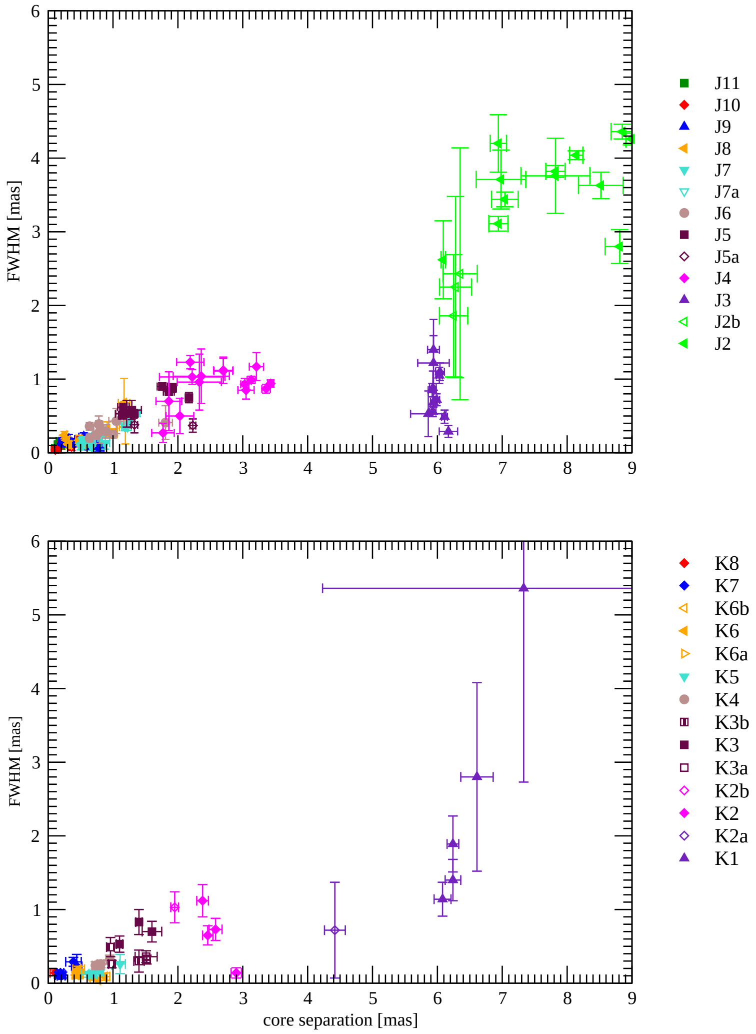

Figure 5.34: *FWHM of the modelfit components at 15 GHz (top panel) and 22 GHz (bottom panel) plotted versus core separation.*

compared to 15 GHz (top panel).

The repeated expansion and restriction of the jet within the inner 3 mas results in two different opening angles ($\phi_1 = 36.9°$ and $\phi_2 = 24.6°$). Calculating the according Mach numbers results in M_1=1.7 and M_2=2.4. The latter number is in the range of the one deduced from the 15 GHz analysis.

The lateral displacement of the 22 GHz components from the jet ridge line at lower frequencies (5 and 15 GHz) has previously been observed in the case of 0836+710 (Otterbein et al. 1998). It could be explained either by applying the theory of Kelvin-Helmholtz instabilites or by geometrical changes due to variations in the viewing angle of the jet (Lobanov et al. 1998). The latter case can in principle be supported by the change of the viewing angle we found in the analysis of the 15 GHz data (see p. 61).

5.2.4 Combining All Frequencies - Spectral Evolution

The combination of all epochs also served to cross-identify the components at the three different frequencies. It turns out that the model fitting and identification has been quite accurate within the individual epochs. For a better comparison, the core separation of the inner modelfit components is plotted versus time in Figure 5.35. The left panel shows all components of all epochs and frequencies except for the outermost component C1. The right panel displays only epochs between 1999 and 2005 within a relative core separation of 1.8 mas. Additionally, Table 5.7 contains the cross-identification between the components of different frequencies and the respective results for the deduced apparent velocities.

Table 5.7: *Cross-identification for all frequencies from model-fitting.*

Id[1]	β_{app}^{5GHz} [c]	β_{app}^{15GHz} [c]	β_{app}^{22GHz} [c]
C0 = J0 = K0	-	-	-
J9 = K7	-	7.28±0.35	5.47±0.95
C6 = J8 = K6	2.22±0.26	7.97±0.29	9.58±0.54
J7 = K5	-	8.12±0.64	10.05±0.79
J6 = K4	-	7.68±0.86	10.01±2.04
C5 = J5 = K3	6.28±1.17	9.00±0.51	14.63±0.05
C4 = J4 = K2	19.65±1.41	12.33±1.10	11.75±0.37
C3 = J3 = K1	-2.81±1.02	0.38±0.54	2.42±7.33
C2 = J2	14.53±2.99	19.20±1.66	-
C1	7.93±4.66	-	-

[1] Identification of the individual components

Regarding the significant differences in the apparent velocity and the parameters derived from it, not only the resolution but especially the time sampling at the individual frequencies obviously plays the most important role in a combined analysis of several different frequencies. We will see in the following section that important kinematic features might occur during the long-term observation of individual sources, such as a temporal slowdown or acceleration of the jet, which could simply not be detected with an insufficient amount of observing data. This seems also to be the case for the 5 GHz and 22 GHz data of 0917+624. Hence, the results of the well-sampled 15 GHz observations are considered the most reliable with regard to the calculation of apparent velocities, Doppler factor, opening angles, and the like.

In order to point out the significance of the time sampling, the relative core separation of the inner jet components is plotted in Figure 5.36 with separate panels for each cross-identified component. The top panel already shows an example of the afore mentioned features which can only occur when a satisfactory amount of data is available. Component J9 seems to experience a slowdown reaching an almost constant distance to the VLBI core in 2007. J7 on the other hand (third panel) and also J6 (bottom panel) obviously start on a more constant level and run through a phase of acceleration towards the end of the observations. This has already been accounted for in the 15 GHz analysis where the rel. R.A. and Decl. of J9, J8 and J7 have been fitted by a third-order fit (cf. Figure 5.8). The 5 and 22 GHz data, however, only span a shorter timerange where the component movement can only be fitted by a linear trend.

Another instance of the importance of the time sampling are the times of zero core separation

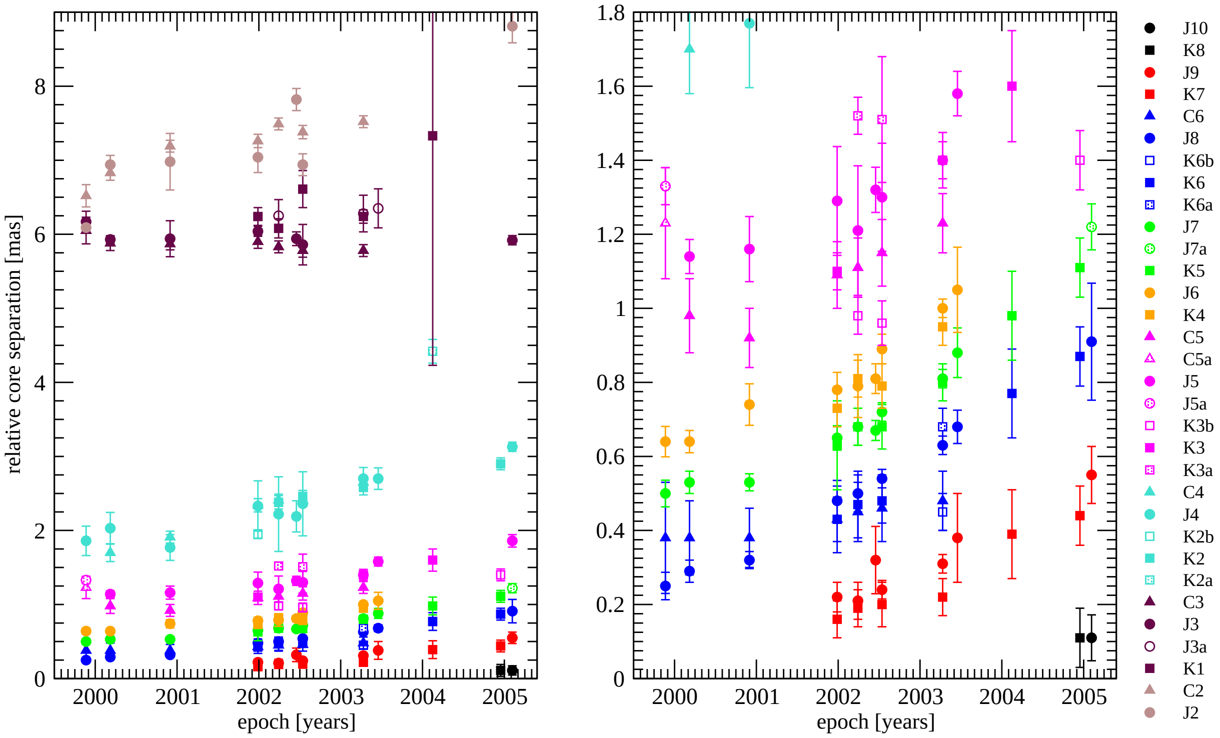

Figure 5.35: *Relative core separation of the modelfit components at all frequencies plotted vs. time; cross-identified components are denoted with the same color but different symbols; left panel shows all components of all frequencies except for C1; right panel displays only epochs including at least two frequencies focussed on the innermost jet region.*

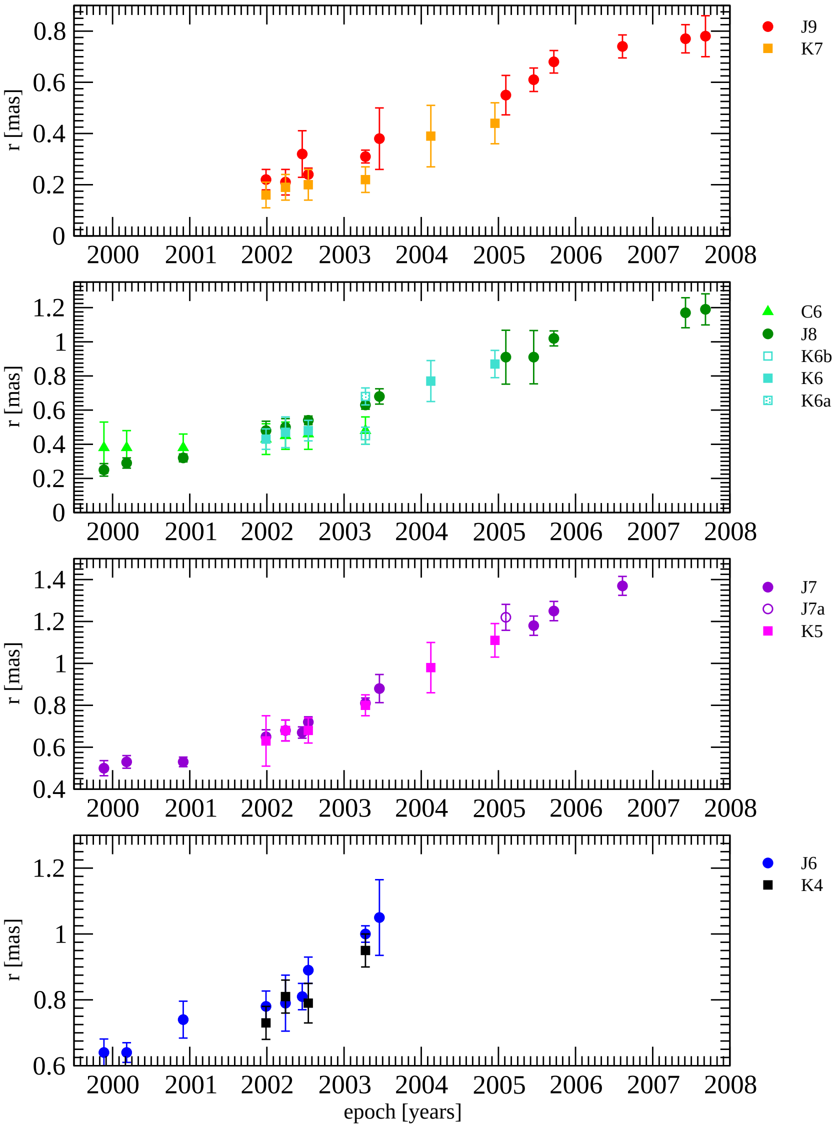

Figure 5.36: *Relative core separation of the modelfit components at all frequencies plotted vs. time for single components (inner jet region).*

of the components at the three frequencies. The results are again summarized in Table 5.8. As already pointed out, the 15 GHz results are considered the most reliable because of the higher amount of observing epochs. The time of zero core separation - or in other words the time a new component has been ejected from the VLBI core - can be confirmed for the following 15 GHz components within their error ranges: J9 and K7, J8 and K6, J6 and K4, C5 and J5, J4 and K2. Consequently, a new component has been ejected on average every 2 years between 1990 and 2000.4.

Table 5.8: *Time of zero core separation of cross-identified modelfit components.*

Id[1]	$t_{0/5GHz}$	$t_{0/15GHz}$	$t_{0/22GHz}$
J9/K7	-	2000.4±1.5	2000.2±2.9
C6/J8/K6	1989.7±1.4	1998.2±1.2	1999.2±1.3
J7/K5	-	1996.7±1.2	1998.1±1.2
J6/K4	-	1995.1±1.5	1997.4±3.0
C5/J5/K3	1991.1±2.3	1992.6±0.8	1997.3±1.0
C4/J4/K2	1994.7±1.0	1990.0±1.8	1989.5±0.5
C3/J3/K1	-	-	-
C2/J2	1970.5±4.7	1983.2±1.9	-

[1] Identification of the individual components

The development of the flux density across the three frequencies is displayed in Figure 5.37 using the example of four cross-identified components, namely the VLBI core, the first, second and third correlated jet components (see Table 5.7). Here, only epochs between 1999 and 2003 are considered where 0917+624 was observed at least at two frequencies per epoch. Not all components could be equally identified in all epochs and frequencies.

As we have already seen previously from the three different frequencies' flux plots (cf. Figures 5.11, 5.20 and 5.30), Figure 5.37 shows that the flux density decreases with increasing core distance. If the components now expand they become optically thin turning from a flat into a steep spectrum. This is, however, only applicable for the 15 GHz data except for component J4 that increases in size but also keeps an almost constant flux density as is the case for all of the examined 5 GHz components (cf. Fig. 5.21). The 22 GHz components K6 and K2 even show a decrease in FWHM (cf. Fig. 5.32). This is reflected in the development of the spectral indices $\alpha_{5/15GHz}$ and $\alpha_{15/22GHz}$ that have been derived for each component separately. They are listed in Tables 5.9 and 5.10, respectively, and plotted in Figure 5.38. The dotted lines are linear fits to the spectral indices and indicate their overall trend during the observations.

The spectral index $\alpha_{5/15GHz}$ of the VLBI core is flat as expected from the unresolved optically thick core region, varying between slightly steeper and flatter values (~ -0.8 to -0.2), except for the first epoch (1999.888). Here the VLBI core at 5 GHz shows a higher flux density than the first jet component (C6) whereas at 15 GHz it is reversed. The further the 5 and 15 GHz components move away from the core they expand and hence become optically thinner (C6/J8 and C5/J5). The third correlated jet component (C4/J4) initially follows this behaviour. However, its spectrum flattens in 2002 when the C4 flux density has decreased while the one of J4 has increased and its FWHM exceeds that of the 5 GHz component.

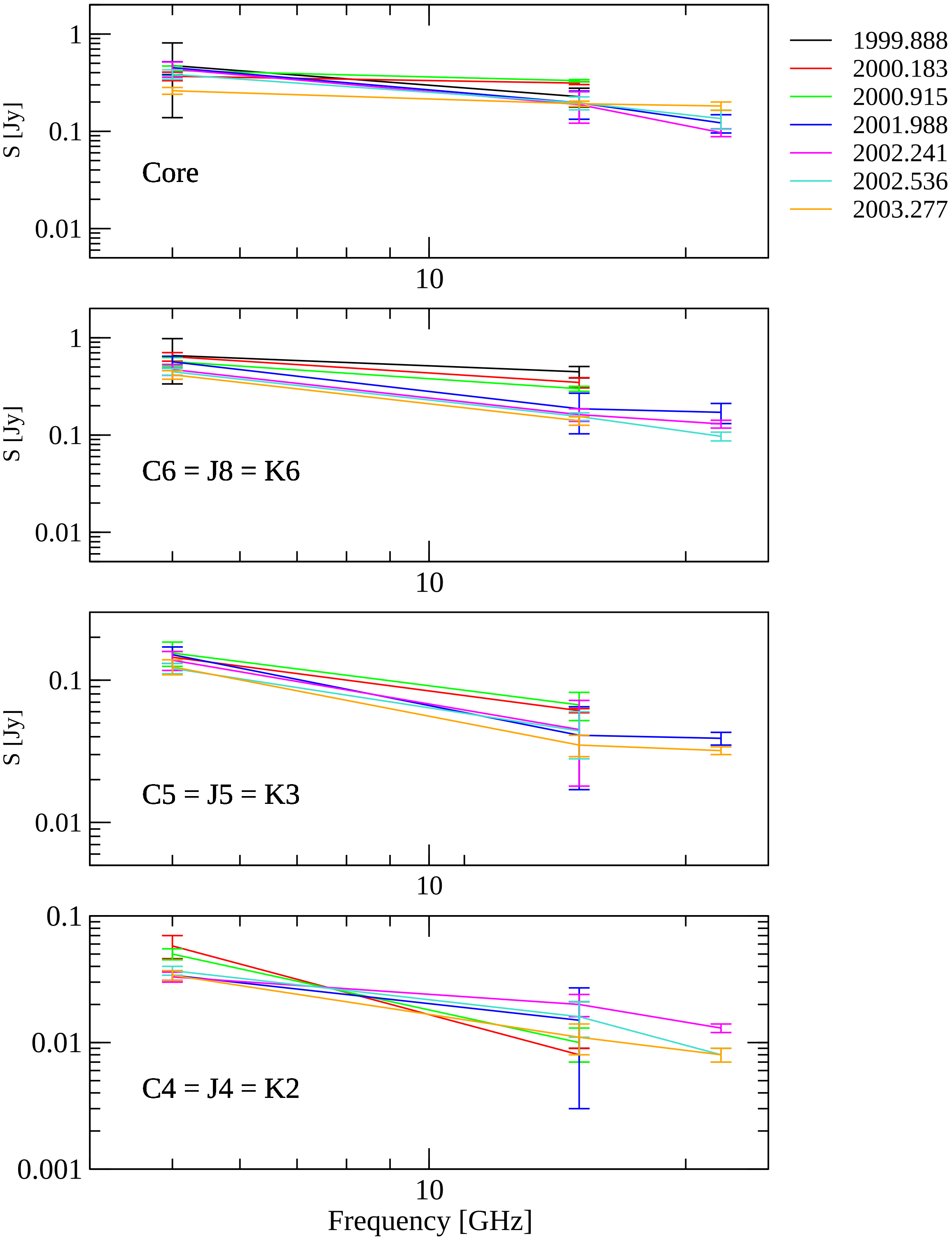

Figure 5.37: *Flux density of the modelfit components at 5, 15 and 22 GHz.*

Table 5.9: *Spectral Index $\alpha_{5/15GHz}$ of four different components.*

epoch	$\alpha_{(C0=J0)}$	$\alpha_{(C6=J8)}$	$\alpha_{(C5=J5)}$	$\alpha_{(C4=J4)}$
1999.888	-0.67±0.68	-0.35±0.46	-	-
2000.183	-0.15±0.10	-0.56±0.14	-0.79±0.09	-1.80±0.22
2000.915	-0.22±0.10	-0.59±0.11	-0.76±0.27	-1.46±0.29
2001.988	-0.76±0.32	-1.01±0.43	-1.19±0.55	-0.74±0.73
2002.241	-0.77±0.36	-0.97±0.18	-1.02±0.56	-0.46±0.20
2002.536	-0.62±0.17	-0.96±0.11	-0.92±0.34	-0.76±0.29
2003.277	-0.28±0.09	-0.99±0.13	-1.15±0.19	-1.03±0.26

Table 5.10: *Spectral Index $\alpha_{15/22GHz}$ of four different components.*

epoch	$\alpha_{(J0=K0)}$	$\alpha_{(J8=K6)}$	$\alpha_{(J5=K3)}$	$\alpha_{(J4=K2)}$
2001.988	-1.24±1.01	-0.22±1.32	-0.13±1.55	-
2002.241	-1.73±0.96	-0.57±0.46	-	-1.12±0.56
2002.536	-0.97±0.79	-1.22±0.36	-	-1.81±0.88
2003.277	-0.14±0.31	-	-0.23±0.48	-0.83±0.78

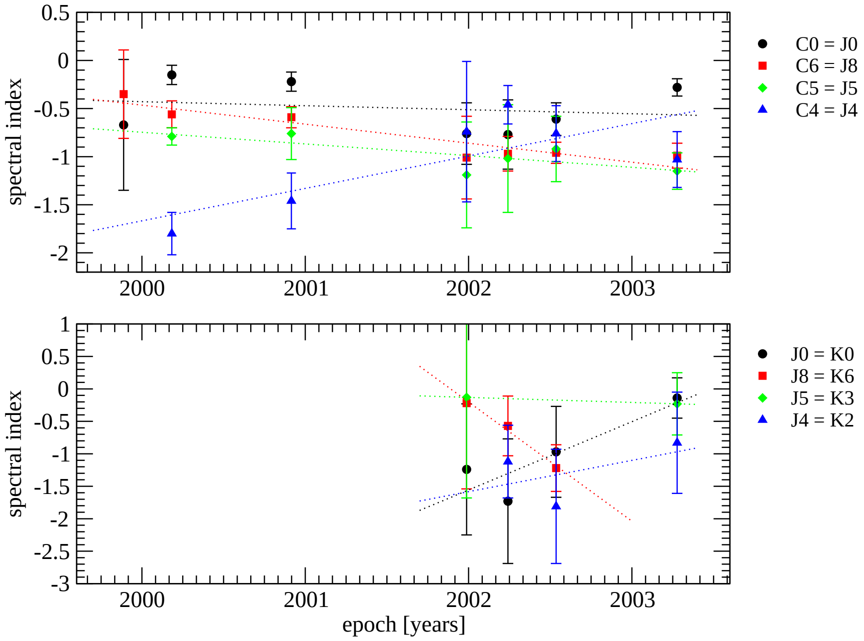

Figure 5.38: *Spectral Indices $\alpha_{5/15GHz}$ (top panel) and $\alpha_{15/22GHz}$ (bottom panel) plotted for four different components; dotted lines are linear fits representing the overall trend for each component.*

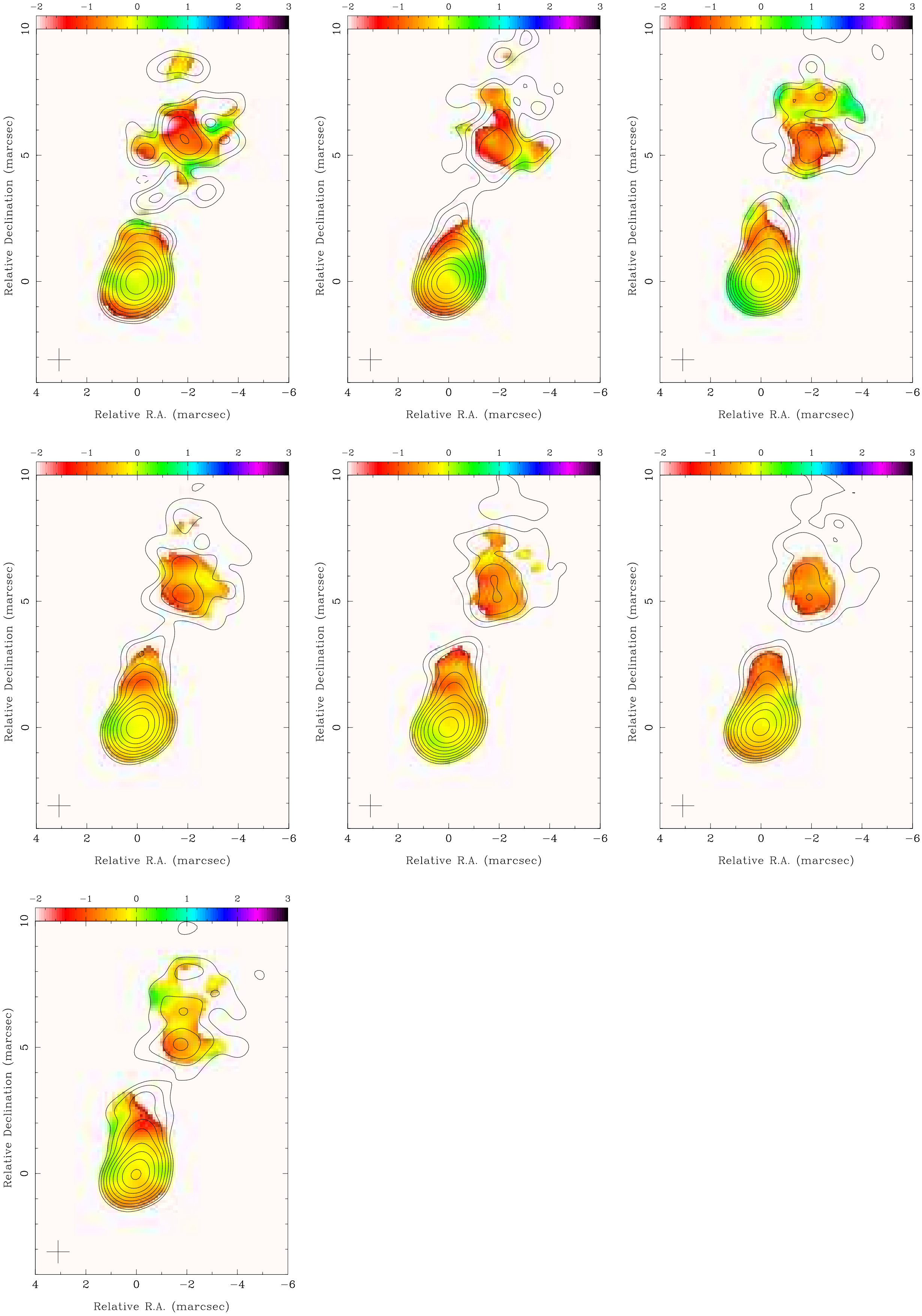

Figure 5.39: *Spectral index maps* $\alpha_{5/15\mathrm{GHz}}$ *between 1999 and 2003 with a circular beam of (0.9×0.9) mas; spectral index is shown by color; contours represent the 5 GHz maps.*

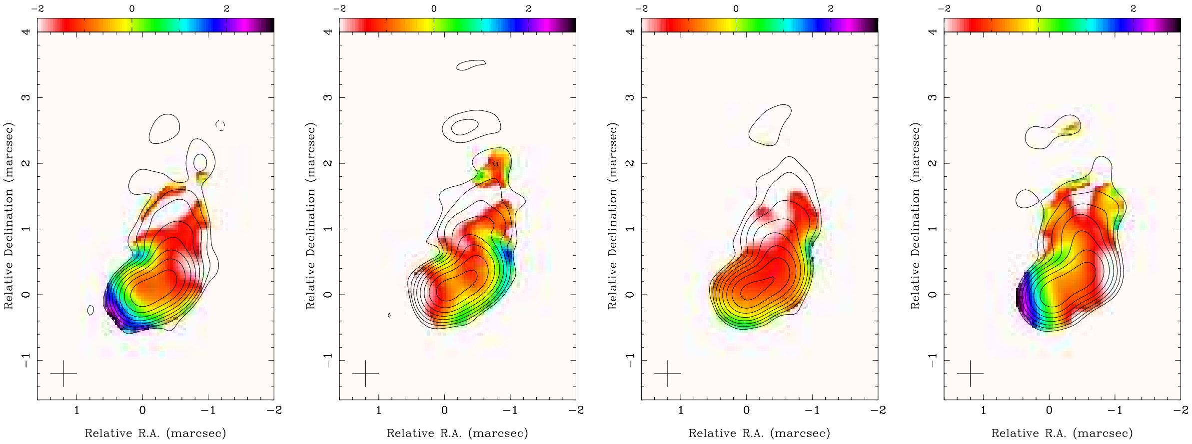

Figure 5.40: *Spectral index maps $\alpha_{15/22GHz}$ between 2001 and 2003 with a circular beam of (0.4×0.4) mas; spectral index is shown by color, contours represent the 15 GHz maps.*

The VLBI core (J0/K0) shows a steeper spectral index $\alpha_{15/22GHz}$ in the first epoch (2001.984) when its flux density is lower than the first jet component's (J8/K6) which has now become the most compact part of the source. The flat spectrum of J8/K6 steepens gradually as the flux density decreases below the VLBI core flux density. The reverse holds for the spectrum and flux density developement of J0/K0 that flattens towards the last epoch (2003.277) while its flux density is increasing. The spectrum of the second jet component (J5/K3) is slightly flatter compared to $\alpha_{5/15GHz}$ as the flux densities of J5 and K3 are of almost the same value. The flattening trend of the spectral index $\alpha_{15/22GHz}$ of the third jet component is comparable to the behaviour between 5 and 15 GHz.

To complete the picture, coloured contour maps of the spectral indices are displayed in Figures 5.39 ($\alpha_{5/15GHz}$) and 5.40 ($\alpha_{15/22GHz}$) where the spectral index is shown by color; contours represent the 5 and 15 GHz maps, respectively.

Figure 5.39 clearly depicts the results for $\alpha_{5/15GHz}$. The color gradient changes from a flat spectrum close to the VLBI core to a steep spectrum in the jet region. Also the flattening of the spectral index of the third correlated jet component (C4/J4) is clearly visible in the jet in last four epochs (see middle and bottom panels). In Figure 5.40 especially the flattening of $\alpha_{15/22GHz}$ of the VLBI core accompanied by the steepening of the first jet component's spectral index is brought out by the colour change in the innermost 1 mas region.

In conclusion, the spectrum of the VLBI core varies between steep and flat bcoming flattest in 2000 and 2003 ($\sim$ 0.2, cf. Tables 5.9 and 5.10). These dates coincide with the ejection of new components (J9 and J11) around 2000.4 and 2003.2.

5.2.5 The binary black hole scenario for 0917+624

The kinematic analysis of the VLBI data revealed that 0917+624 shows a strong jet curvature. This makes it a good candidate for the binary black hole scenario as explained in Chapter 2.4. Prof. Jacques Roland from the Institut dAstrophysique of the University of Paris developed a method to fit the variations of both coordinates (R.A. and Decl.) of a VLBI component as a function of time, assuming that the nucleus of the radio source contains a binary black hole system (BBH system). The presence of such a BBH system produces two perturbations of the ejected VLBI components' trajectories, namely the precession of the accretion disk and the motion of the two black holes around their common center of gravity. By using only the VLBI coordinates, the problem reduces to an astrometric one. Hence, given the kinematic information of a trajectory, one is able to deduce the inclination angle of the source and the bulk Lorentz factor of the ejected component. Based on these assumptions, Prof. Roland developed a software program that is able to calculate the afore mentioned parameters from a set of observational data.

So far the method has been applied only to the trajectory of the 15 GHz component J8. The starting parameters that are required in order to run the program are the coordinates of the VLBI component (rel. R.A. and Decl. - in the following referred to as X and Y coordinate) listed in Table B.1 in Appendix B, as well as the components' time of zero core separation t_0 = 1998.2.

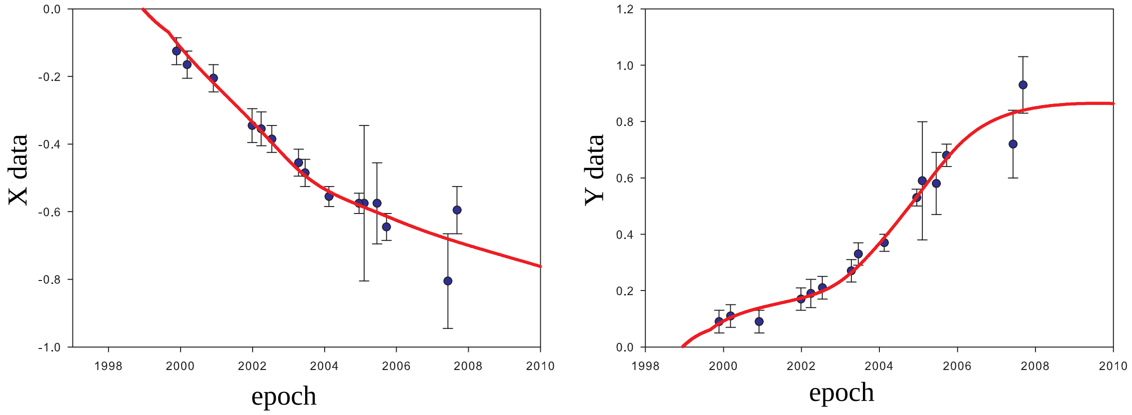

Figure 5.41: *Fits to the X (left) and Y (right panel) trajectories of component J8 indicated by solid red lines.*

The modelling process is started with the assumption that the two black holes have equal mass. Then it is searched for an inclination angle i_o that provides the best χ^2 fit (see C.33), i.e., χ^2

should present a minimum.

Figure 5.41 shows the results of separate fits to the X and Y trajectories of component J8 indicated by a red line. The right panel displays one interesting feature that results from the fitting process: the time of zero core separation $t_0 \sim 1999$, which is the intersection of the red curve with the abscissa, differs by one year from the one derived in the kinematic analysis. In fact, a smooth χ^2 fit could only be achieved if the origin of the ejection of the VLBI component was shifted from 1998.2 to 1999 since otherwise no minimum could be found.

The shift of the time of zero core separation supports the hypothesis of the 15 GHz kinematic analysis that a higher-order fit to the VLBI trajectories is probably more suitable than a linear one (cf. page 60). The shape of the trajectory of component J8 suggests a slow-down after its ejection followed by an accelerated phase between 2002 and 2006. Afterwards it seems to reach again a plateau of decelerated motion. This structure is even better visible for component J9 (cf. Figures 5.4 and 5.8). The acceleration and deceleration phases can be explained by a geometrical effect. When the component is moving on a kink towards the observer, its radiation is boosted in this direction causing the effect of an accelerated motion. If it is moving across the jet cone the component seems to slow down in speed (see also Figure 5.9, left panel).

The case of a non-linear fit to a component trajectory only becomes apparent if a sufficient amount of observational data is available that covers a suitable timerange - as is the case for the 15 GHz data. Since the 5 and 22 GHz observations do not meet these requirements, we can only try to embed the results of the component identification between the different frequencies in order to further test the modelling process.

The resulting parameters of the modelling process are as follows:

- the masses of the two black holes were assumed to be equal, $M_1 = M_2 = 4.58 \cdot 10^7 M_\odot$;
- the inclination angle i_o could not be derived;
- ϕ_o, the phase of the precession at $t = 0$ was found to be -125;
- the rotation angle in the plane perpendicular to the line of sight (see C.1 and C.2) $\Delta\Xi = 44.6^\circ$,
- the opening angle of the precession cone (see C.8) $\Omega = 1.12^\circ$,
- the maximum amplitude of the perturbation (see C.7) $R_o = 445 \gg 1$,
- the precession period of the accretion disk T_p resulted in 14000 years;
- T_d, the characteristic time for the damping of the beam perturbation, was found to be 1900 years;

- the bulk Lorentz factor of the VLBI component γ_c is in the range of $8 \ll \gamma_c \ll 20$, which overlaps with our kinematic results from the 15 GHz analysis where a minimum Lorentz factor of 19.23 was derived.
- ψ_o, the phase of the BBH system at $t = 0$, was calculated to be 151;
- the period of the BBH system $T_b = 5800$ years;
- the origin of the ejection of the VLBI component or time of zero core separation $t_o = 1999$;
- the Alfvén speed V_a, which is the propagation speed of the perturbations, was derived as $V_a \simeq 0.02c$;
- n_{rad}, the number of steps to describe the extension of the VLBI component along the beam, was chosen to be 110.

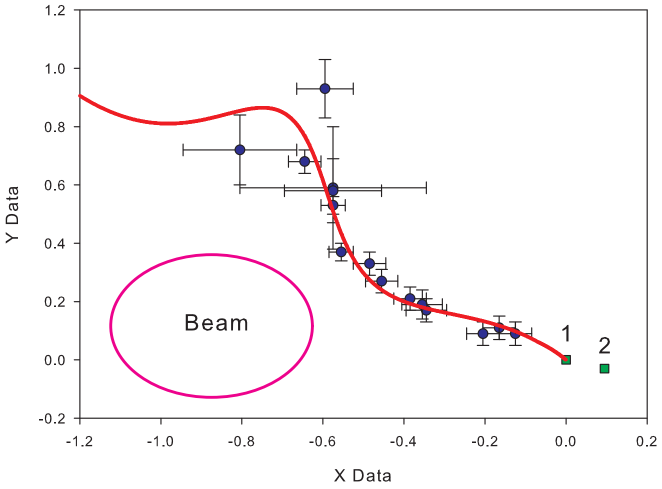

Figure 5.42: *Fit to the X-Y trajectory of component J8 indicated by a solid red line; squares 1 and 2 denote the two black holes; the plot is mirror-inverted on the X axis.*

The temporal shift for the origin of the ejection of the VLBI component from 1998.2 to 1999 entails a spatial difference $\sigma = 0.098$ mas which is larger than the error range of the VLBI components in the core region. Hence, we interprete the shift as the distance between the two black holes (see also Figure5.42). If this result can be verified, it would be the first time that the distance between two black holes of a binary black hole system could be 'measured' by means of a plain astrometric analysis.

As already depicted in Chapter 5.2.1, components J7, J8, and J9 could best be represented by a higher-order fit (cf. Figure 5.8) which fits well to the theory of a helically twisted jet due to the interaction of two black holes in the central region of the AGN. However, the trajectory of component J10 does not meet this criterion since it is directed rather straight (according to the number of data points available so far) moving with a slightly higher apparent velocity compared to the afore mentioned components. A tentative interpretation could be that this component was ejected by the second black hole since it could also be separated observationally from the VLBI core at a point much closer than the other components (cf. Figure 5.4).

In order to examine the reliability of our preliminary results, the program is currently applied to all suitable trajectories that have resulted from the data analysis. However, this is still work in progress and beyond the scope of the thesis.

CHAPTER 6

VLBI Polarimetry of 0917+624

6.1 Observations and Data Analysis

The underlying data were obtained from the VLBI polarimetry observations of 0917+624 at 5, 15 and 22 GHz during the ’core campaign’ (see Chapter 5.1) from December 2001 until April 2003, hereafter called epoch 2001.984 (26 December 2001), epoch 2002.235 (27 March 2002), epoch 2002.531 (13 July 2002) and epoch 2003.273 (10 April 2003). The data were complemented by the three previous epochs observed between November 1999 and November 2000 at 5 and 15 GHz (epochs 1999.888, 2000.183, and 2000.915).

In the analysis of the polarisation data several difficulties had to be coped with. The experiment was not optimised for polarisation observations because the total bandwidth was 16 MHz, hence, the bandwidth per IF reduced to 8 MHz. Besides no adequate polarisation calibrator was observed simultaneously. Thus, the calibration of the polarisation vector had to be done by means of the target source itself (see below). The third, and most crucial point is, that nothing is known about the rotation measure (RM) of 0917+624. Taylor (1998, 2000) found that VLBI measurements reveal absolute Faraday RMs in excess of 1000 rad m^{-2} in the central regions of seven out of eight strong quasars. But beyond a projected distance of ~20 pc the jets are found to have |RM|<100 rad m^{-2}. For 0917+624 this implies that there could possibly be a sharp rotation gradient between the inner 2.4 mas region and the jet further out. A determination of the RM of 0917+624 would have been desireable, yet not possible. The reasons for this will be explicated thereinafter.

Nevertheless, a polarisation analysis was worked out since only little is known about the recent polarisation behaviour of the source apart from what was summarised in Chapter 3. For epoch 2002.235, the data calibration turned out to be insufficient yielding only in a map of left circular polarisation. Thus, it was excluded from further polarisation analysis. Finally, it can be added that no circular polarisation was found in the MOJAVE 15 GHz polarisation measurements (Homan & Lister 2006).

After the processing of the data in Difmap for the kinematic analysis, the self-calibrated data were reimported into AIPS for the calibration of the so-called antenna D-terms and the polarization imaging. The D-terms represent the leakage of circular polarisation from right into left antenna feed and vice versa. In order to distinguished between the source intrinsic and the feed induced antenna polarisation, a total intensity image of the source has to be divided into several components with similar polarisation properties. This can be done by means of task CCEDT. Task LPCAL then determines the effective parameters for each antenna feed and writes them to a table.

In polarisation imaging these antenna tables are now applied when first producing separate maps of the Stokes parameters I, Q and U (see Chapter 2.3.2) by means of task IMAGR. Subsequently the Q and U maps are joined to a linear polarisation intensity map (via $I = \sqrt{Q^2 + U^2}$) by means of task COMB which also produces a map containing information on the EVPA. The maps of total intensity, total polarised intensity and EVPA are finally combined in one plot using task KNTR (or PCNTR or the like) which enables to produce contour plots including line vectors that represent the position of the electric field vector. The detected polarizations were required to be above the 5σ-level where σ is described by the rms noise in the polarisation maps.

In the analysis by means of AIPS, the same parameters were used for all epochs in the production of the polarisation maps. Since the first three epochs were simply snapshot observations, the (u,v)-coverage was poor compared to the other epochs (cf. Figure 6.1). But in order not to loose the good resolution of the four core VLBI epochs, the maps were produced by means of uniform weighting which increased the noise level for the maps of the first epochs. In order to compensate for this, I decided not to use a robustness parameter (robustness 0) because a weighting towards a uniform weighting increases the noise in the maps of the first three epochs even more whereas a use of the robustness parameter towards natural weighting would have degraded the map resolution of the four main epochs.

6.2 Results and Discussion

The final step in the imaging process is the calibration of the orientation of the EVPA. For 5 and 15 GHz this could be done by means of single dish observations of 0917+624 performed with the Effelsberg and Urumqi radio telescopes simultaneously with or close to the epochs of

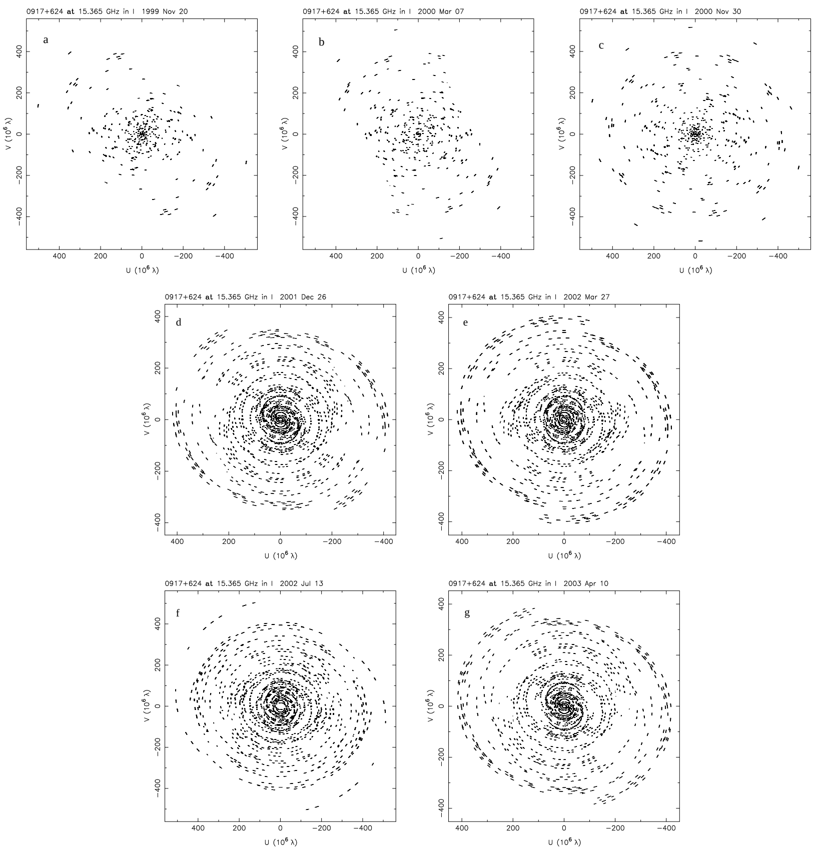

Figure 6.1: *(u,v)-coverage at 15 GHz; letters denote epochs: a) 1999.888, b) 2000.178, c) 2000.913, d) 2001.984, e) 2002.233, f) 2002.529, g) 2003.252; a, b and c were snapshot observations with only poor (u,v)-coverage.*

the available data. When no simultaneous data were at hand the values of the missing epochs could be derived through a linear extrapolation. This can be justified by the fact that the source has shown to be rather invariant in the observations with single telescopes showing only small gradual changes in polarisation angle (cf. Chapter 4) during the relevant period.

Since no 22 GHz single dish measurements were available, the EVPA had to be extrapolated from the 5 and 15 GHz data according to equation 2.27 assuming that the RM did not change during the respective period. The result is displayed in Figure 6.2; parameters are listed in Table 6.1. The polarization angle, or apparent orientation of the projected E vectors on the sky, is measured from north towards east. Finally, the value of the EVPA from the VLBI measurements is subtracted from the one of the single dish observations resulting in the correction value for the VLBI data (column 5 in Table 6.1). It can be applied as parameter ROTATE in the imaging task IMAGR to produce the final polarisation maps.

Table 6.1: *EVPAs derived from single dish and VLBI measurements and resulting correction values.*

epoch	ν [GHz]	EVPA$^{1}_{sd}$ [°]	EVPA$_{VLBI}$ [°]	δEVPA [°]
1999.888	5	53	81	-28
2000.178	5	33	113	-80
2000.913	5	48	107	-59
2001.984	5	41.5	111	-69.5
2002.233	5	45	108	-63
2002.529	5	43	111.5	-68.5
2003.252	5	46	114	-68
1999.888	15	45	87	-42
2000.178	15	42	134	-92
2000.913	15	40	95.5	-55.5
2001.984	15	37	127	-90
2002.233	15	36	115	-79
2002.529	15	35	137	-102
2003.252	15	33	135	-102
2001.984	22	33	112	-82
2002.531	22	29	163	-139
2003.273	22	24	47	-31

[1] single dish EVPA

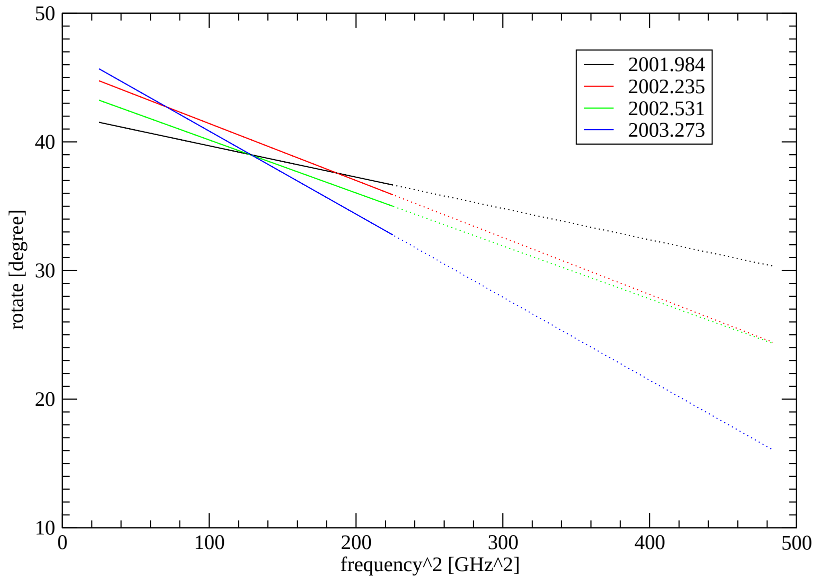

Figure 6.2: *Extrapolation plot for EVPA corrections at 22 GHz.*

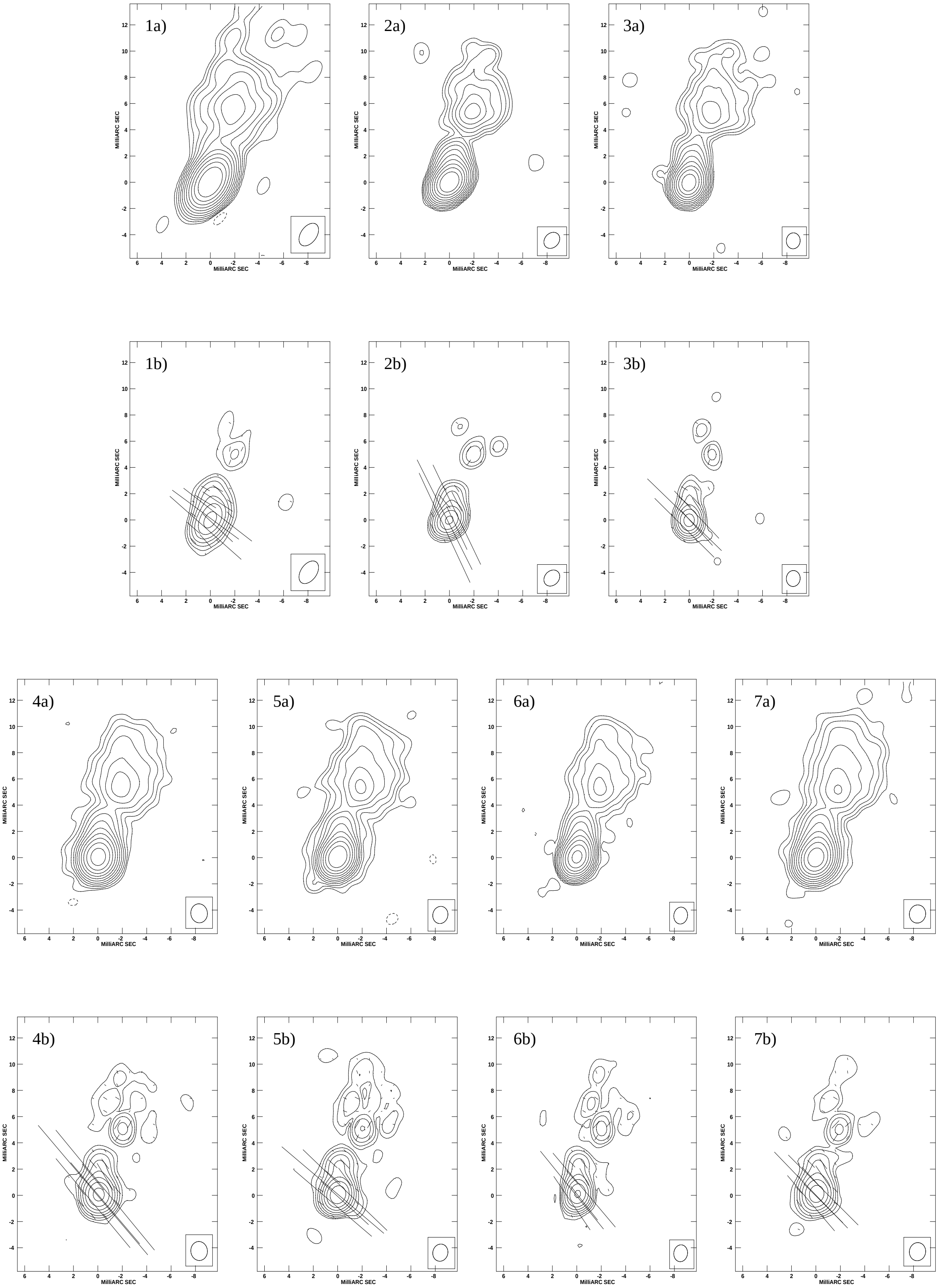

Figure 6.3: *Polarisation maps at 5 GHz; the first and third row (a) diplay the contour maps of total intensity while the rows beneath (b) show the polarisation maps with corresponding electric field vectors; epochs 1 to 7 according to order of Table 6.2 which contains the map parameters; the length of the electric vector is proportional to the strength of the polarisation (1 mas = 25 mJy/beam).*

6.2.1 Polarisation at 5 GHz

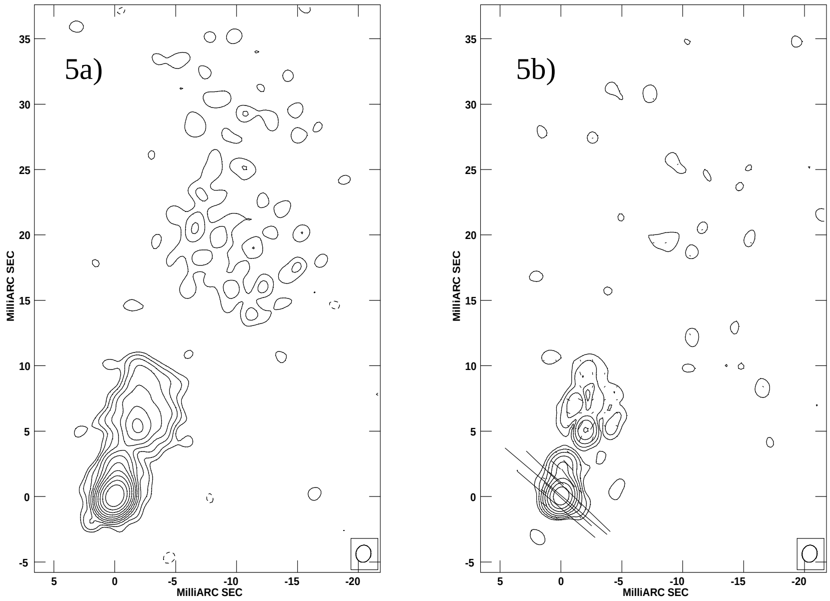

Figure 6.4: *Example of a large scale polarisation map at 5 GHz of epoch 2002.233; left panel: total intensity map, right panel: polarisation map with corresponding electric field vectors (1 mas = 25 mJy/beam); parameters are listed in Table 6.2.*

The images of the 5 GHz polarisation analysis are presented in Figure 6.3. First and third row display the total intesnity maps and second and fourth row the according polarisation maps with electric field vectors. The map parameters are listed in Table 6.2. Total and polarised intensity and polarisation angle were measured for the position of the VLBI core and four points along the VLBI jet at a rel. Decl. of approximately 2, 6, 7, and 23 mas, respectively. These points correspond to the positions of the modelfit components resulting from the kinematic analysis and are in the following also referred to as components.

Since the polarisation structure is poorly visible at 23 mas, only the inner 10 mas of 0917+624 are diplayed in Figure 6.3. As an example for the outer jet structure, epoch 2002.233 is presented in Figure 6.4 which shows the most distinc polarisation structure beyond 10 mas. However, the measurement errors of the corresponding EVPAs at 23 mas distance are relatively large in all epochs due to the diffuse jet structure and should thus be considered to be less reliable.

The measurements were done by means of AIPS tasks TVWIN and IMSTAT. The latter integrates over a rectangular region that has been set by the first task. This is certainly suboptimal to represent the true component structure and hence the measurements were performed serveral

Table 6.2: *Parameters of* Aips *maps for total and polarised intensity at 5 GHz; displayed are total intensities of five identified components, the lowest map contour levels, beam and beam position angle (top panel); polarised intensity and lowest map contours (middle panel); according polarisation vectors* χ*, and the difference between the EVPAs of the jet and core components (bottom panel).*

epoch	I_{Core} [mJy/beam]	I_{2mas} [mJy/beam]	I_{6mas} [mJy/beam]	I_{7mas} [mJy/beam]	I_{23mas} [mJy/beam]	lowest contours [mJy/beam]	beam [mas]	bpa [°]
1999.888	864.7±86.5	57.8±10.2	44.0±5.8	16.6±3.4	22.3±3.4	0.40	1.99 x 1.27	-40.01
2000.183	965.6±73.2	34.2±5.8	47.1±4.8	13.4±2.5	15.0±2.8	0.40	1.39 x 1.11	-52.65
2000.915	965.9±63.4	38.9±6.1	45.3±4.6	16.1±2.9	29.2±2.7	0.50	1.22 x 1.13	-10.99
2001.988	771.0±125.8	48.0±13.0	37.3±16.4	11.0±1.6	27.7±9.0	0.60	1.45 x 1.36	13.65
2002.241	745.4±97.2	43.9±11.0	31.3±6.9	10.8±1.4	24.8±8.0	0.35	1.33 x 1.22	-25.67
2002.536	702.9±87.8	44.1±11.1	30.1±6.6	10.1±1.4	24.4±7.6	0.55	1.29 x 1.12	-11.95
2003.277	529.1±74.7	41.0±9.1	26.0±5.7	9.2±1.2	24.7±8.2	0.35	1.39 x 1.32	-23.24
Average	792.1	44.0	37.3	12.4	24.0			
σ_I	155.6	7.5	8.4	3.0	4.6			
σ_I/Average [%]	19.7	17.0	22.4	23.9	19.1			

epoch	P_{Core} [mJy/beam]	P_{2mas} [mJy/beam]	P_{6mas} [mJy/beam]	P_{7mas} [mJy/beam]	P_{23mas} [mJy/beam]	lowest contour [mJy/beam]
1999.888	20.0±2.0	2.9±0.4	1.1±0.1	0.5±0.1	3.2±0.5	0.30
2000.183	41.2±2.9	2.9±0.3	2.1±0.1	0.7±0.1	5.3±0.7	0.30
2000.915	35.9±2.3	3.1±0.5	2.3±0.5	1.2±0.1	8.2±0.9	0.40
2001.988	38.0±6.1	3.4±0.5	2.3±0.2	1.1±0.1	5.8±2.6	0.30
2002.241	37.9±4.7	3.9±0.4	2.6±0.3	1.3±0.1	6.6±2.7	0.18
2002.536	31.8±3.9	3.5±0.5	2.8±0.3	1.2±0.1	7.1±3.2	0.25
2003.277	25.8±3.8	3.5±0.5	2.3±0.2	1.0±0.1	5.5±2.6	0.30
Average	32.9	3.3	2.2	1.0	5.9	
σ_P	7.6	0.4	0.5	0.3	1.6	
σ_P/Average [%]	23.1	11.0	23.7	31.7	26.6	

epoch	χ_{Core} [°]	χ_{2mas} [°]	χ_{6mas} [°]	χ_{7mas} [°]	χ_{23mas} [°]	$\Delta\chi_{2mas-Core}$ [°]	$\Delta\chi_{6mas-Core}$ [°]	$\Delta\chi_{7mas-Core}$ [°]	$\Delta\chi_{23mas-Core}$ [°]
1999.89	-129.5±6	-120±2	-17±17	-141±40	-44±52	9.5	112.5	-11.5	85.5
2000.18	-150±5	-141±6	-42±12	-120±21	-94±46	9	108	30	56
2000.92	-130±5	-120±28	-33±30	-109±33	-77±41	10	97	21	53
2001.99	-138±1	-141±4	-37±9	-119±8	-75±41	-3	101	19	63
2002.24	-130±2	-133±5	-35±13	-113±10	-75±37	-3	95	17	55
2002.54	-140±2	-139±5	-43±12	-118±7	-77±41	1	97	22	63
2003.28	-134±2	-138±6	-47±9	-113±7	-73±46	-4	87	21	61
Average	-135.9	-133.1	-36.3	-119.0	-73.6				
σ_χ	7.5	9.4	9.8	10.5	14.8				
σ_χ/Average [%]	5.5	7.0	27.4	8.8	20.2				

times to receive an adequate error from the scattering of the individual measurements.

Figure 6.5 summarises the measurement results for total and polarised intensity and EVPA of the inner four components. The flux density in total intensity of the VLBI core region again follows the same decreasing trend that has already been found previously from single dish measurements (cf. Chapter 4). Besides, the result is in accordance with the kinematic analysis if we consider the VLBI core component as a partial superposition of components C0 and C6. The jet component at 2 mas can at least in the last four epochs clearly be identified with C4, while the jet components at 6 and 7 mas correspond to C3 and C2, respectively. The total intensity variations during the observing period are in the range of ~20 % (see Table 6.2, σ_I/Average). Any deviations of the flux density values from the results of the kinematic analysis can clearly be attributed to blending effects due to the use of TVWIN.

The polarisation analysis shows a similar behaviour for the development of the polarised intensity except for the first epoch (1999.888) when the polarised intensity of the VLBI core component shows only half the value of the second epoch (2000.178). The variations in polarised intensity are least pronounced at a 2 mas distance from the VLBI core (11 %) and strongest around 7 mas (~32 %). The latter could, however, be due to blending effects with the component located around 6 mas.

In the core region of 0917+624, the EVPA is oriented almost perpendicular to the jet ridge line which implies a magnetic field nearly perpendicular to the jet axis. This result is in good agreement with previous findings (e.g., Pollack et al. 2003). In the outer jet between 4 and 10 mas, however, the orientation of the EVPA changes from parallel to the jet axis to perpendicular and back to parallel. This indicates a toroidal structure of the jet axis which is not directly visible at 5 GHz resolution.

The EVPA remains rather constant for all components at 5 GHz in the second half of the observations. But changes from the first to the second epoch of the electric vector of the VLBI core and two inner jet components are of the order of 20° and are already visible in the innermost jet region in an inspection by eye of the maps in Figure 6.3. At least the slight change in the orientation of the EVPA could be caused by an incorrect calibration of the overall orientation of this vector in either the first or the second epoch.

In order to avoid a misinterpretation of the changes in the electric vector position angle if the calibration of the EVPA should be unreliable (or in cases when a calibration is simply not possible due to the lack of appropriate single dish data), one can still make a statement about the relative changes between the different epochs by regarding the differences of the EVPA between the VLBI core and a certain jet component. If these differences change significantly, obviously one of the two components (if not both) underwent a change in its polarisation characteristics. This has also been considered in our analysis and the resulting differences $\Delta\chi$ are listed in the bottom panel of Table 6.2.

There seems to be a significant variation in the EVPA of the jet components at 6 and 7 mas from the first to the third epoch (2000.913). However, since these two components are located relatively close to each other it is more likely that we are simply dealing with a blending effect between the EVPAs of those two components and that within the errors the electric vector of the jet components remains constant throughout the observations.

The variation in $\Delta\chi_{2mas-Core}$ of about 13° from the third to the fourth epoch (2001.984) can certainly be considered as real, even though minor, since this can be explained by a

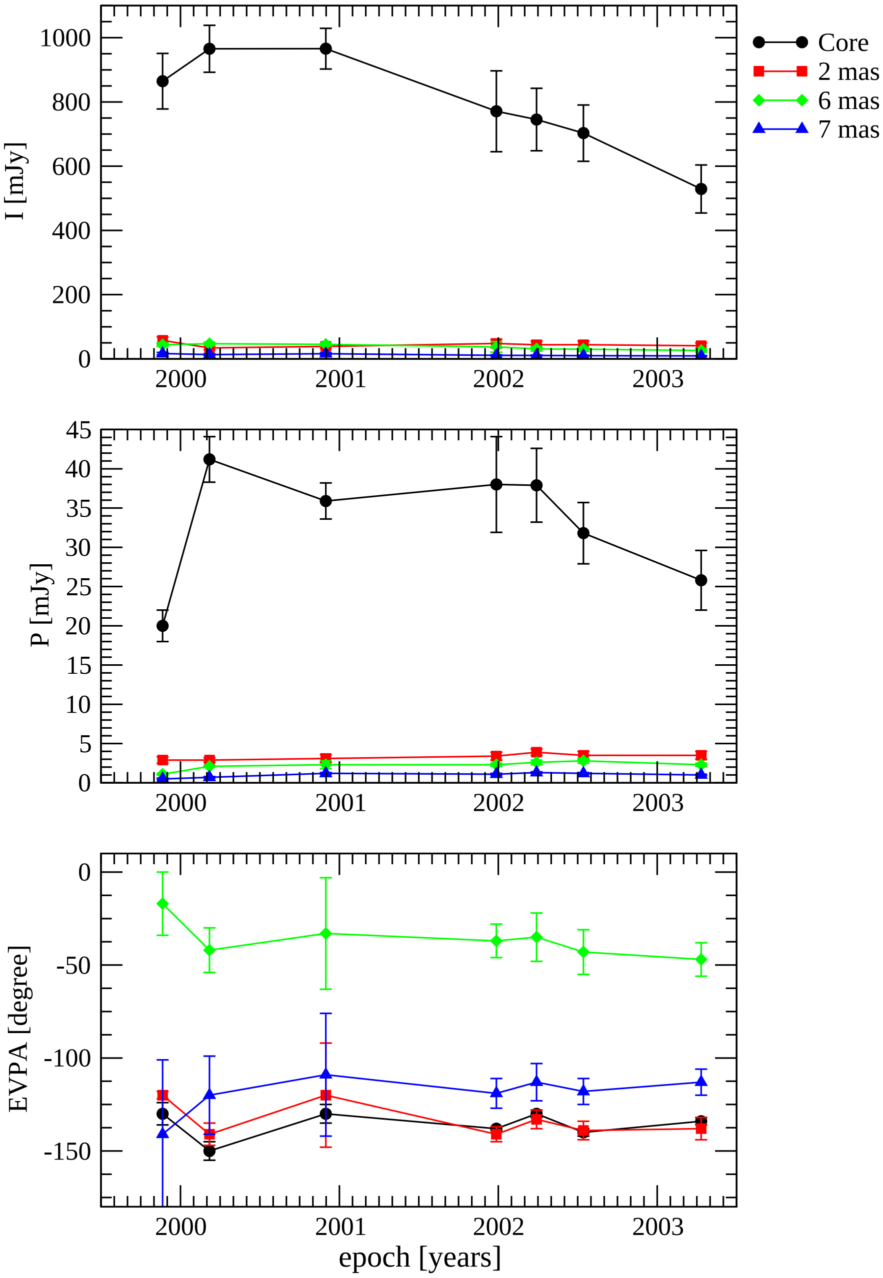

Figure 6.5: *Analysis plot of 5 GHz polarisation maps; top panel: total flux density of VLBI core and jet components at 2, 6 and 7 mas, middle: polarised flux density, bottom: EVPAs of jet and VLBI core components.*

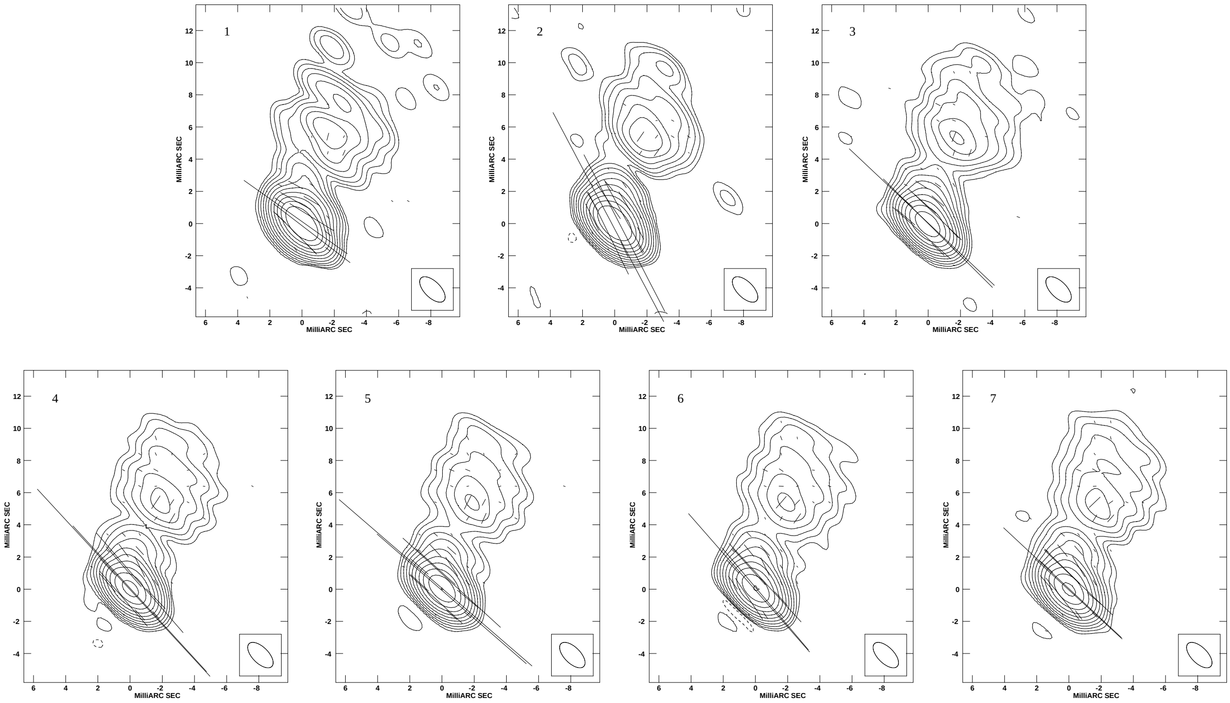

Figure 6.6: *Total intensity maps with electric field vector at 5 GHz (1 mas = 25 mJy/beam) convoluted with a 'pencil'-shaped beam of (2×1) mas with the major beam axis perpendicular to the jet ridge line of the inner 2 mas; epochs 1 to 7 according to order of Table 6.2.*

broadening of the VLBI core due to the upcoming ejection of a new jet component. It would as well imply the increase in polarised flux density from the first to the second epoch. The results of the kinematic analysis of the previous chapter do support these findings: the time of zero core separation for the next ejected component was found to be around 2000.4. After the ejection of the new component, i.e. from epoch 2001.984 on, the polarised intensity gradually decreases and $\Delta\chi_{2mas-Core}$ remains almost constant.

For a better comparison of the results of the individual epochs, all maps were convolved with the same ellipcitc 'pencil-shaped' beam of (2×1) mas with the major beam axis approximately perpendicular to the jet axis of the inner 2 mas. Then slices were cut through the source structure following the jet axis by means of the AIPS task SLICE. The results are intensity profiles of all epochs always taken at the same position. This of course implies that in some epochs the profiles might not show the real intensity maxima but rather slopes of the intensity peaks. Nevertheless, one can clearly see the allocation of different maxima within jet structure. The profile plots are displayed in Figure 6.2.1 where different colors denote different epochs. Top and middle panels show total (I) and polarised (P) flux density, respectively, bottom panels present the fractional polarisation p[1] throughout the jet.

Due to the comparably poor resolution at 5 GHz, there is only one peak in the core region visible in the total and polarised intensity profiles. In the jet one can barely distinguish a second peak around -6 mas distance form the core, which is slightly more pronounced in polarisation than in total intensity. The fractional polarisation profiles, however, disclose that there are more components present in the jet than is revealed by the simple intensity profiles. One can distinguish four to five maxima which, however, do not correspond to the components that have been found in the kinematic analysis of the previous chapter - apart from a maximum at approx. 2 mas. The fractional polarisation is higher in the jet than in the core region which is well in accordance with previous findings (e.g., Cawthorne et al. 1993). It increases from moderate maximum values of 6 % to approximately 17 % at a core distance of about 3.5 mas in the last epoch (cf. bottom right panel in Figure 6.2.1).

The general decreasing trend in total flux density is again present in the profile plots. Also the increase in polarised intensity from the first to the second epoch and the subsequent gradual decline after 2002 is visible similar to the middle panel in Figure 6.5. The fractional polarisation plots in the bottom panels of Figure 6.2.1 reveal that the polarisation in the jet reduces to a lesser extent than the total intensity. This is best displayed in the bottom panel of the last epoch (2003-04-10).

In summary, the 5 GHz polarisation analysis of the 0917+624 data shows an overall decreasing trend in total flux density and also, from 2002 on, in polarised intensity. Besides the value of the polarised intensity doubles from the first to the second epoch. The EVPA remains rather constant except for a minor change in $\Delta\chi_{2mas-Core}$ of about 13° from the third to the fourth epoch which can be interpreted in the context of an upcoming ejection of a new component from the VLBI core. The orientation of the EVPA is almost perpendicular to the jet ridge line in the core region, which implies a magnetic field nearly perpendicular to the jet axis. On the other hand, in the outer jet between 4 and 10 mas the EVPA orientation changes between parallel to the jet axis and perpendicular indicating a toroidal structure of the jet.

---

[1] $p = P/I$ [%]

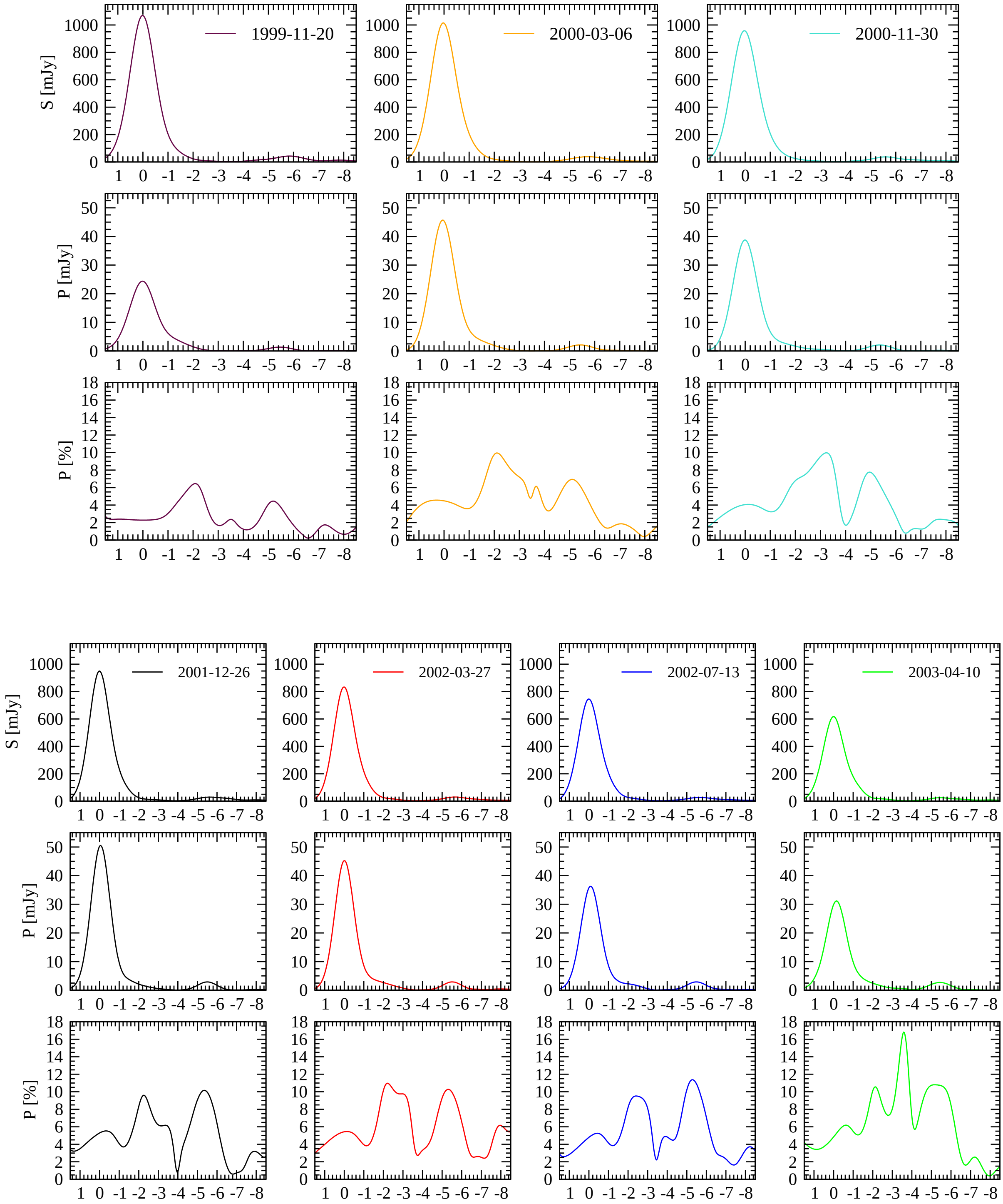

Figure 6.7: *Profile plots at 5 GHz derived from cuts along the jet; different colors denote different epochs; panels display profiles as follows: top: total flux density I, middle: polarised flux density P, bottom: percentage of polarisation; maps were convoluted with pencil shape beam of (2×1) mas with the major beam axis perpendicular to the jet ridge line.*

6.2.2 Polarisation at 15 GHz

The resulting maps of the 15 GHz polarisation analysis are presented in Figure 6.8. First and third row again display the total intensity maps and second and fourth row the according polarisation maps with electric field vectors. The map parameters are listed in Table 6.3. At 15 GHz resolution it was possible to display diffuse polarised intensity structure in the jet up to approximately 7 mas distance in rel. Decl. from the VLBI core. Nevertheless, at higher frequencies the structure of the inner jet region is more significant and thus Figure 6.9 shows a close-up of the inner 3-mas jet.

Table 6.3: *Parameters of* AIPS *maps for total and polarised intensity at 15 GHz; displayed are total intensities of four identified components, the lowest map contour levels, beam and beam position angle (top panel); polarised intensity and lowest map contours (middle panel); according polarisation vectors χ, and the difference between the EVPAs of the jet and core components (bottom panel).*

epoch	I_{Core} [mJy/beam]	$I_{0.5mas}$ [mJy/beam]	I_{1mas} [mJy/beam]	I_{2mas} [mJy/beam]	lowest contours [mJy/beam]	beam [mas]	bpa [°]
1999.888	367.6±68.1	281.6±71.0	42.3±11.4	12.6±1.5	0.40	0.78 x 0.61	41.21
2000.183	531.9±72.8	300.3±87.8	19.9±4.2	5.4 ±0.2	2.00	0.57 x 0.38	-49.41
2000.915	486.4±68.7	279.2±85.4	20.4±5.9	11.5±0.9	4.00	0.40 x 0.37	-52.14
2001.988	369.4±33.3	339.7±37.5	49.4±14.2	16.5±3.3	2.00	0.50 x 0.48	35.33
2002.241	401.3±47.8	241.3±43.3	40.9±13.6	14.3±2.2	1.50	0.44 x 0.40	-55.65
2002.536	279.1±26.5	315.4±30.8	56.4±16.6	16.1±4.9	2.30	0.43 x 0.36	-36.73
2003.277	233.1±24.6	203.7±19.3	45.8±12.7	14.1±3.4	0.60	0.44 x 0.42	-1.04
Average	381.3	280.2	39.3	12.9			
σ_I	105.6	45.7	14.0	3.8			
σ_I/Average [%]	27.7	16.3	35.7	29.1			

epoch	P_{Core} [mJy/beam]	$P_{0.5mas}$ [mJy/beam]	P_{1mas} [mJy/beam]	P_{2mas} [mJy/beam]	lowest contour [mJy/beam]
1999.888	5.3±0.7	3.6±1.2	1.1±0.2	1.2±0.1	0.35
2000.183	16.7±2.0	11.6±4.0	0.9±0.2	1.3±0.3	0.40
2000.915	10.1±1.7	10.2±2.7	1.3±0.2	2.0±0.4	0.60
2001.988	19.3±2.0	20.5±2.0	1.9±0.7	1.6±0.6	0.45
2002.241	25.4±3.0	11.8±2.7	2.1±0.6	1.5±0.2	0.45
2002.536	10.1±0.9	14.4±1.3	3.3±1.1	1.8±0.5	0.40
2003.277	9.0 ±1.0	10.7±1.1	3.5±1.4	1.7±0.6	0.40
Average	13.7	11.8	2.0	1.6	
σ_P	7.0	5.1	1.0	0.3	
σ_P/Average [%]	51.1	42.9	50.0	18.4	

epoch	χ_{Core} [°]	$\chi_{0.5mas}$ [°]	χ_{1mas} [°]	χ_{2mas} [°]	$\Delta\chi_{0.5mas-Core}$ [°]	$\Delta\chi_{1mas-Core}$ [°]	$\Delta\chi_{2mas-Core}$ [°]
1999.888	-149±30	-174±64	-65±79	-81±36	-25	84	68
2000.183	-138±7	-130±32	-109±52	-108±46	8	29	30
2000.915	-44±78	-96±64	-45±69	-54±55	-52	-1	-10
2001.988	-148±4	-137±4	-145±46	-141±27	11	3	7
2002.241	-146±4	-141±11	-63±75	-105±61	5	83	41
2002.536	-162±8	-136±10	-142±28	-135±37	26	20	27
2003.277	-152±4	-143±7	-145±12	-151±17	9	7	1
Average	-134.1	-136.7	-102	-110.7			
σ_χ	40.4	54.0	43.8	34.8			
σ_χ/Average [%]	30.1	16.8	42.9	31.4			

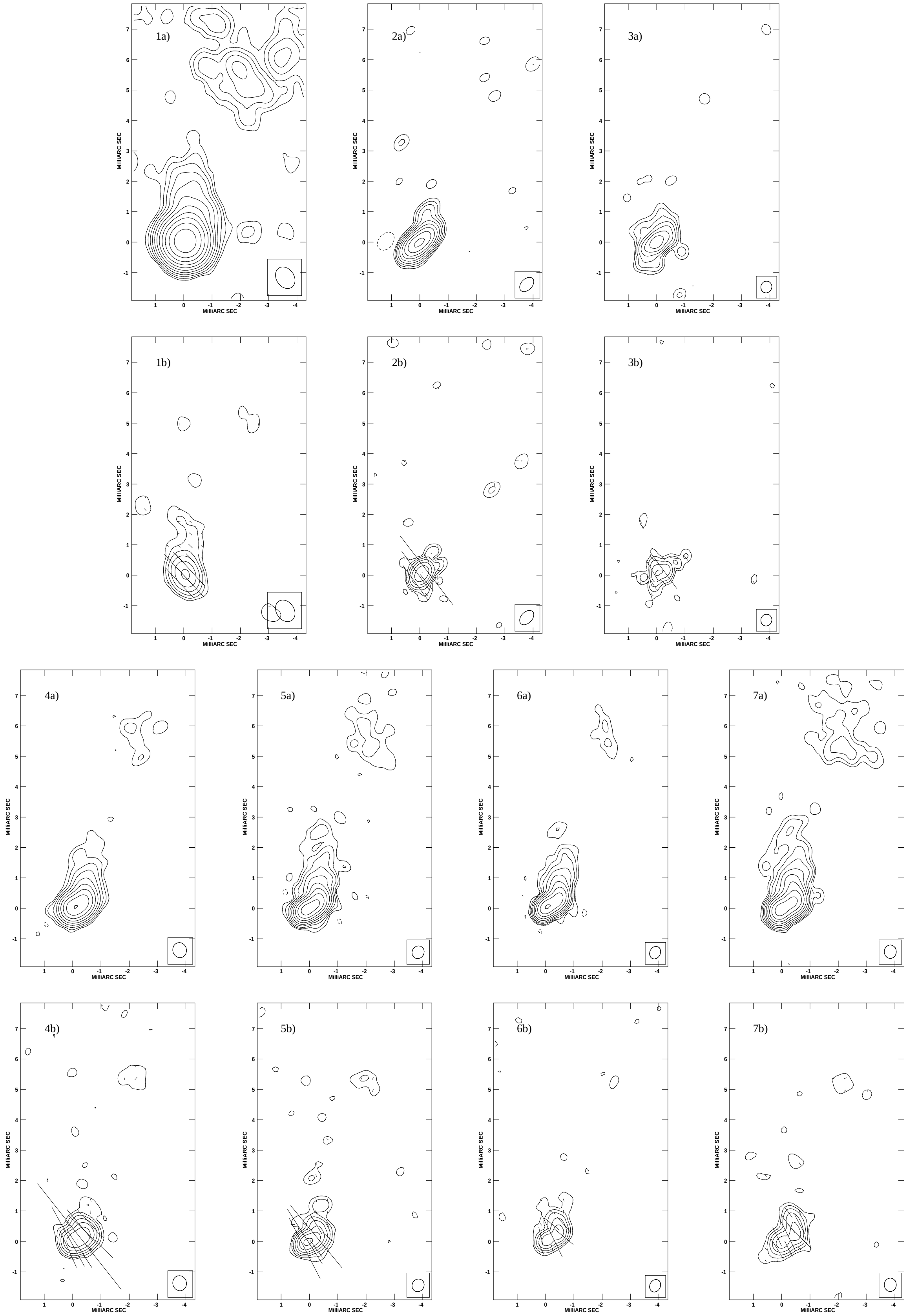

Figure 6.8: *Polarisation maps at 15 GHz; the first and third row (a) diplay the contour maps of total intensity while the rows beneath (b) show the polarisation maps with corresponding electric field vectors (1 mas = 62.5 mJy/beam); epochs 1 to 7 according to order of Table 6.3 which contains the map parameters.*

Figure 6.9: *Polarisation maps at 15 GHz, inner region; order of plots and map parameters according to Figure 6.8.*

Total and polarised intensity and polarisation angle were measured for the position of the VLBI core and three points along the VLBI jet around a rel. Decl. of 0.5, 1 and 2 mas, respectively, corresponding to the positions of the modelfit components found in the kinematic analysis. The results are summarised in Figure 6.10.

The top panel shows that the total flux density of the VLBI core component increases from the first to the second epoch and then gradually decreases until the last epoch (2003.277). This is in accordance with the results from the kinematic analysis displayed in the second panel of Figure 5.11. However, the amount of flux density was much less in the kinematic analysis, rather comparable with the flux density of the first jet component in Figure 6.10. This is most likely caused by previously mentioned blending effects in the use of TVWIN. The VLBI core component possibly is a combination of components J0, J8 and J9 from the kinematic analysis which reasonably explains the high flux density values.

The total flux density of the first jet component at a distance of 0.5 mas from the VLBI core remains almost constant showing only a slight decrease in the last epoch. This component probably corresponds to a superposition of components J7 and J8 from the kinematic analysis. The components at 1 and 2 mas core distance appear to be almost constant in their flux density, the 1 mas component showing just a slight increase in the last four epochs. The 1 and 2 mas component could be consistent with J5 and J4, repectively, although the flux densities do only correspond approximately if they are added up. This can as well be attributed to blending effects in the determination of the single component flux densities by means of TVWIN.

In the middle panel, the polarised flux density is displayed. The variability of the VLBI core, first and second jet components are much stronger (σ_P/Average $\sim 40 - 50\,\%$) compared to total intensity (σ_I/Average $\leq 36\,\%$, cf. Table 6.3), while for the outermost jet component at 2 mas this is reversed (29 % vs. 18 %). Interestingly, the variations in total and polarised flux density of the VLBI core and first jet component are correlated from epoch 2001.988 to epoch 2002.536, although somewhat more pronounced in polarisation, whereas the EVPA changes of these components are only marginal during the same period (cf. bottom panel of Figure 6.10).

Provided the calibration of the absolute postion of the EVPA has been performed correctly, the EVPA is oriented perpendicular to the jet axis in the innermost 1 mas jet, in the first epoch (1999.888) even up to a distance of 2 mas. This is consistent with the findings at 5 GHz. But starting at around 1 mas distance from the core, the orientation already changes to parallel which can best be seen in the plots of epochs 4, 5, 6 and 7 in Figure 6.9. This is owing to the improved resolution compared to the 5 GHz data.

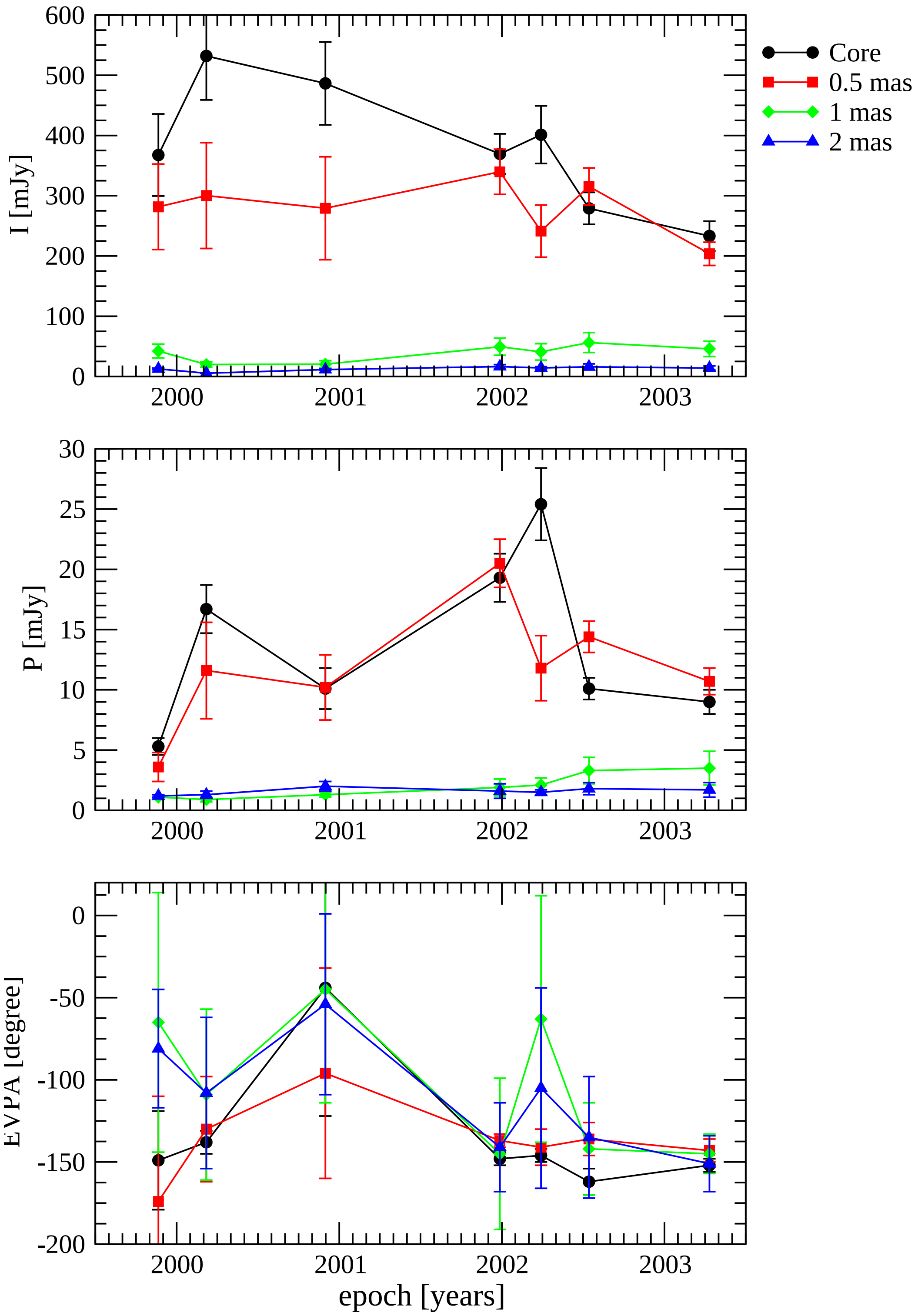

Figure 6.10: *Analysis plot of 15 GHz polarisation maps; top panel: total flux density of VLBI core and jet components at 0.5, 1 and 2 mas, middle: polarised flux density, bottom: EVPAs of jet and VLBI core components.*

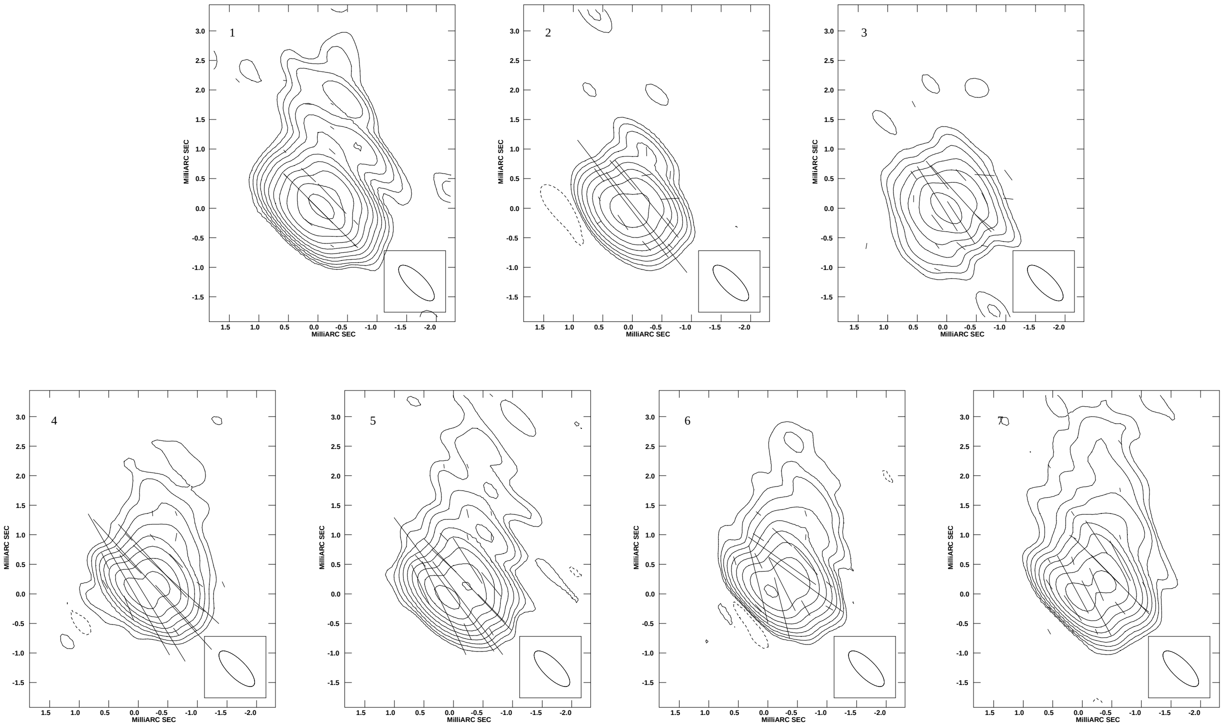

Figure 6.11: *Total intensity maps with EVPA at 15 GHz (1 mas = 62.5 mJy/beam) convoluted with a 'pencil'-shaped beam of (0.8×0.3) mas with the major beam axis perpendicular to the jet ridge line of the inner 1 mas; epochs 1 to 7 according to order of Table 6.3.*

The changes of the EVPA are much more pronounced at 15 GHz than at 5 GHz which can already be seen in the values of $\Delta\chi$ (Table 6.3, bottom right panel). Due to the higher resolution the inner jet region reveals a number of subcomponents, each having individual polarisation characteristics, which sum up as only one component with rather constant polarisation characteristics at the lower frequency. The component at 0.5 mas distance from the VLBI core appears to vary only moderately (σ_χ/Average = 16.8 %) comparable to its variations in total intensity (16.3 %). The variability pattern of the 1 mas jet component turns out to be strongest in all three cases (cf. σ/Average in Table 6.3).

As was done for the 5 GHz data, the 15 GHz maps were convolved with the same ellipcitc 'pencil-shaped' beam of (0.8×0.3) mas with the major beam axis approximately perpendicular to the jet ridge line of the inner 1 mas (see Figure 6.11). Out of these maps profile plots were produced for total and polarised intensity and for the electric vector. The results are presented in Figure 6.12.

From the total and polarised intensity profiles one can clearly distinguish two separate components in the innermost 0.5 to 0.8 mas, especially for the last four epochs (bottom panels). The upper panels represent the first three epochs with a worse *u,v*-coverage leading to a larger beam size in the original maps and hence a worse resolution: the first jet component that is moving away from the VLBI core, is not separated as clearly as in the last four epochs; in polarisation only one component is visible; the first jet component, that appears in the second epoch (2000-03-06), does not seem to correspond to the one in total intensity since it is shifted outwards for approximately 0.2 mas; only in the third epoch (2000-11-30), the central peak in polarised intensity has broadened, obviously because the component is disconnecting from the VLBI core. It is possibly consistent with component J8 from the kinematic analysis whose date of zero core separation has been determined to be approximately 1998.2. The worse resolution also manifests in the fractional polarisation which is higher in the jet than in the core region as was the case for the 5 GHz data because the VLBI core is not resolved.

On the other hand, the fractional polarisation is almost equal in the innermost region during the epochs between 2001 and 2002. This can be explained by the better resolution which leads to a resolved core region showing the VLBI core and a component moving from 0.4 mas (epoch 2001-12-26) to 0.6 mas distance (epoch 2003-04-10). Only in the last epoch the fractional polarisation is again higher in the jet when the emitted component has finally disconnected from the VLBI core. Since there is more than one year time difference between the third and the fourth epoch, this jet component most likely corresponds to J9 of the kinematic analysis which has been ejected from the core around 2000.4.

Summing up, the four epochs evaluated in the 15 GHz polarisation analysis reveal to be much more variable in polarisation compared to the 5 GHz data. Owing to the better resolution, the inner jet region separates into several subcomponents with individual polarisation characteristics, which are represented by only one component with rather constant polarisation characteristics at the lower frequency. The jet component at 1 mas shows the strongest variability in total and polarised intensity as well as for the EVPA values. The predominance of the 1 mas component might also explain the change of the EVPA orientation from perpendicular to the jet axis to parallel at this distance. The 0.5 mas component reveals the least variations in total flux density and for the electric vector, but is still highly variable in total polarisation.

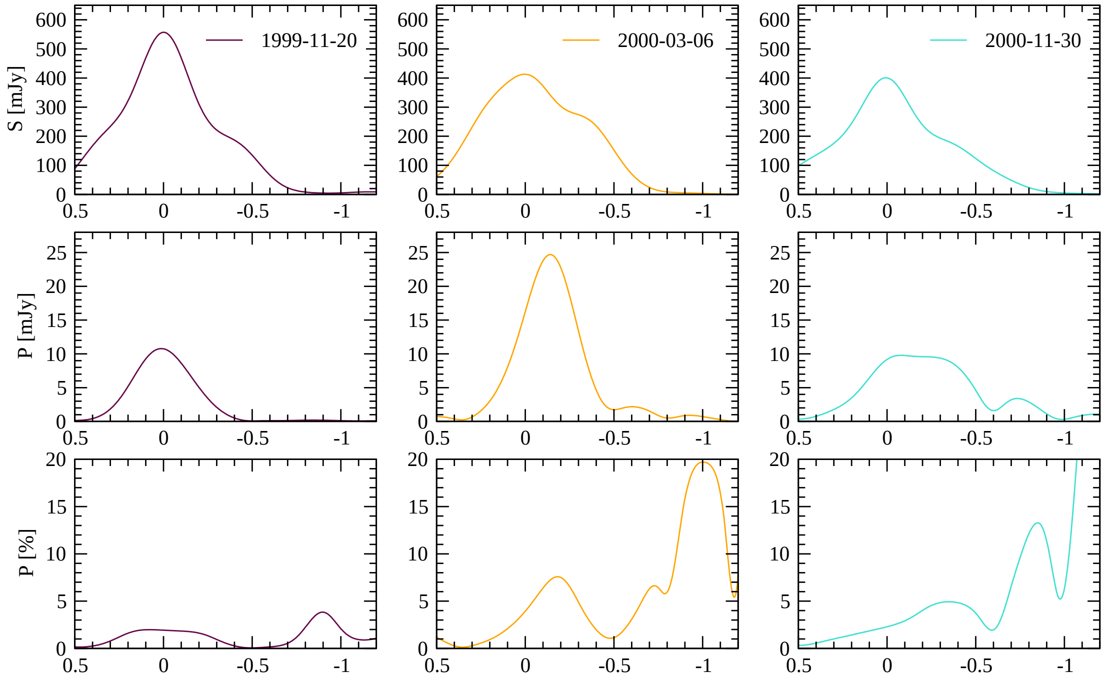

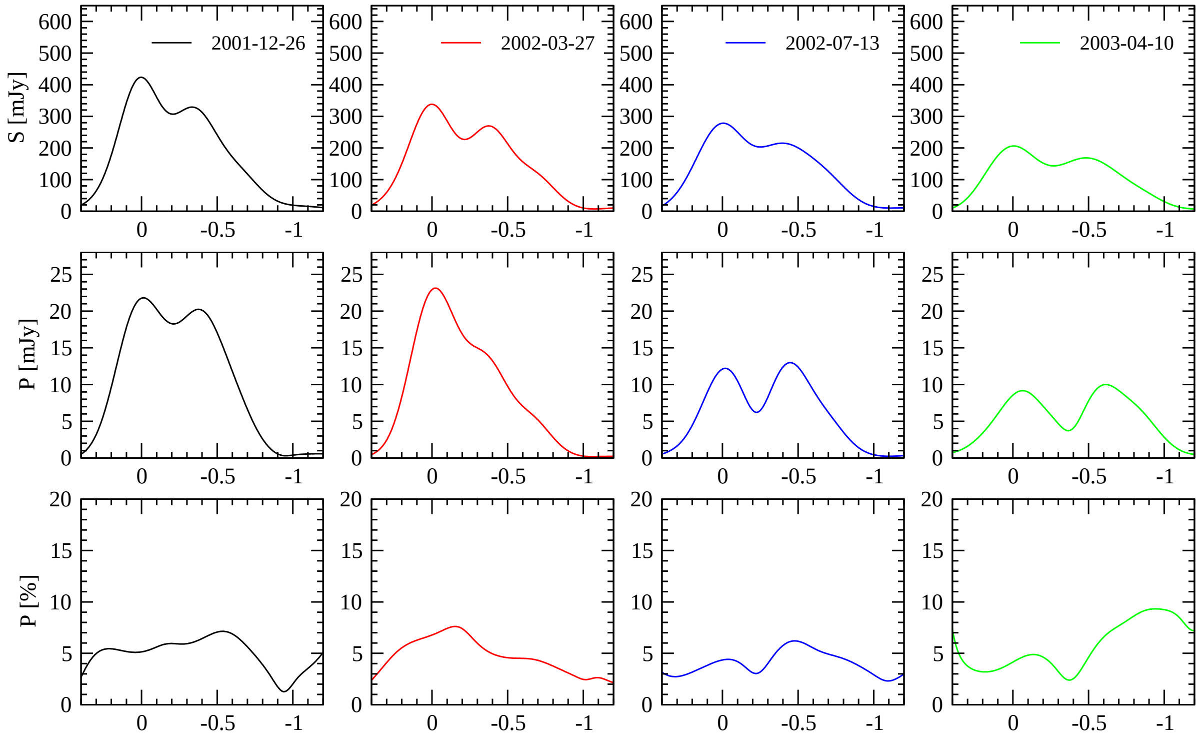

Figure 6.12: *Profile plots at 15 GHz derived from cuts along the jet; different colors denote different epochs; panels display profiles as follows: top: total flux density, middle: polarised flux density, bottom: percentage of polarisation; epochs from 2001 to 2003; maps were convoluted with pencil shape beam of (0.8×0.3) mas with the major beam axis perpendicular to the jet ridge line.*

6.2.3 Polarisation at 22 GHz

The resulting maps of the three epochs, which were available for the 22 GHz polarisation analysis, are presented in Figure 6.13 showing the total intensity contour maps in the top panel and the corresponding polarised intensity maps and electric vectors in the bottom panel. The map parameters are listed in Table 6.4.

Table 6.4: *Parameters of* Aips *maps for total and polarised intensity at 22 GHz; displayed are total intensities of three identified components, the lowest map contour levels, beam and beam position angle (top panel); polarised intensity and lowest map contours (middle panel); according polarisation vectors χ, and the difference between the EVPAs of the jet and core components (bottom panel).*

epoch	I_{Core} [mJy/beam]	$I_{0.5mas}$ [mJy/beam]	I_{1mas} [mJy/beam]	lowest contours [mJy/beam]	beam [mas]	bpa [°]
2001.988	419.3±52.2	224.3±49.8	42.7±11.2	0.80	0.34 x 0.31	-13.01
2002.536	233.0±32.3	178.5±26.1	43.4±11.8	2.00	0.35 x 0.24	-27.64
2003.277	242.7±27.7	178.9±23.5	55.8±10.7	1.20	0.33 x 0.27	-10.06
Average	298.3	193.9	47.3			
σ_I	104.9	26.3	7.4			
σ_I/Average [%]	35.2	13.6	15.6			

epoch	P_{Core} [mJy/beam]	$P_{0.5mas}$ [mJy/beam]	P_{1mas} [mJy/beam]	lowest contour [mJy/beam]
2001.988	22.4±3.6	13.9±3.1	2.1±0.5	0.75
2002.536	6.5±1.4	8.3±0.8	2.3±0.4	0.80
2003.277	8.7±1.1	7.4±1.2	3.4±0.6	1.00
Average	12.5	9.9	2.6	
σ_P	8.6	3.5	0.7	
σ_P/Average [%]	68.5	35.4	26.1	

epoch	χ_{Core} [°]	$\chi_{0.5mas}$ [°]	χ_{1mas} [°]	$\Delta\chi_{0.5mas-Core}$ [°]	$\Delta\chi_{1mas-Core}$ [°]
2001.988	-157±5	-140±26	-88±67	17	69
2002.536	-164±16	-126±14	-136±30	38	28
2003.277	-166±13	-172±12	-177±26	-6	-11
Average	-162.3	-146.0	-75.7		
σ_χ	2.9	23.6	67.4		
σ_χ/Average [%]	2.9	16.2	89.0		

In the 22 GHz polarisation analysis it was possible to identify two jet components, aside from the VLBI core, in the innermost 1 mas region, although some diffuse total intensity flux is also visible up to a distance from the VLBI core in rel. Decl. of 2.5 mas in the first and last epochs

(2001.988 and 2003.277). One component is located approximately at 0.5 mas, the other at 1 mas distance (rel. Decl.) from the VLBI core. The resulting parameters of the map analysis are presented in Figure 6.14. The VLBI core component seems to correspond to a blending of components K0 and K7 from the kinematic analysis, while the 0.5 mas component probably is related to components K5 and K6 and the 1 mas component likely is consistent with K4.

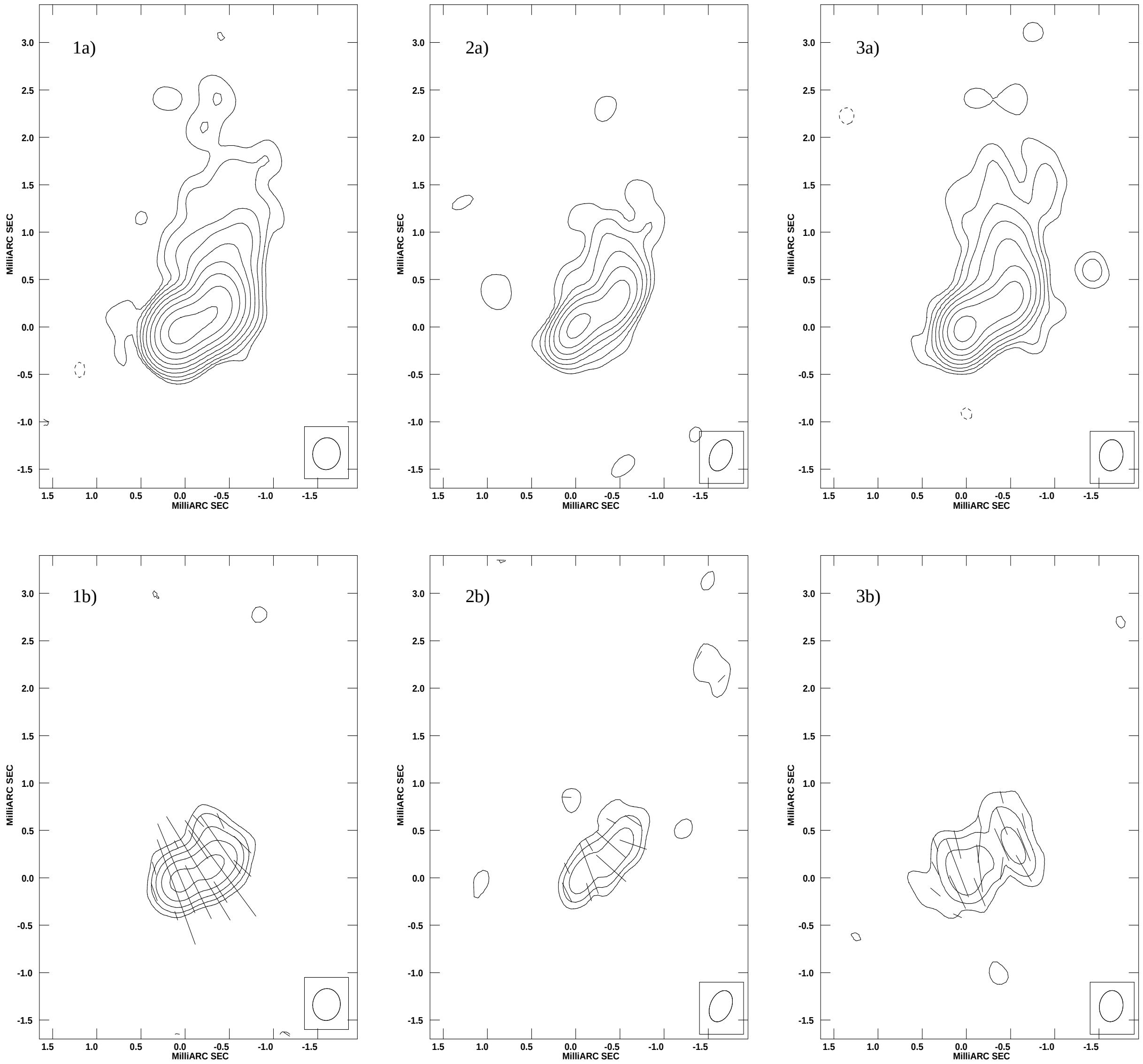

Figure 6.13: *Polarisation maps at 22 GHz; the top row (a) diplays the contour maps of total intensity while the bottom row (b) shows the polarisation maps with corresponding electric field vectors (1 mas = 100 mJy/beam); epochs 1 to 3 according to order of Table 6.4 which contains the map parameters.*

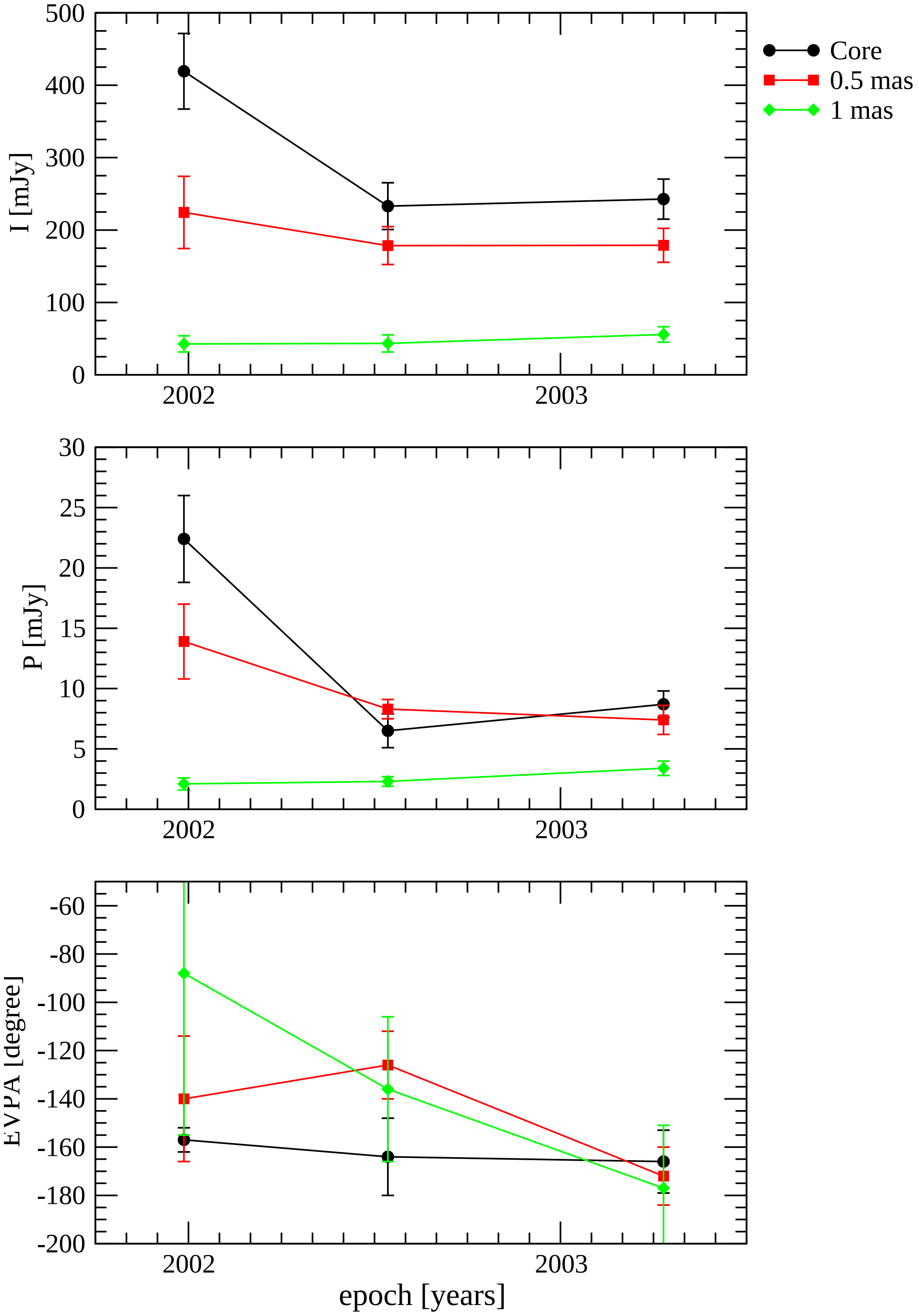

Figure 6.14: *Analysis plot of 22 GHz polarisation maps; top panel: total flux density of VLBI core and jet components at 0.5 and 1 mas, middle: polarised flux density, bottom: EVPAs of jet and VLBI core components.*

With only three available epochs it is inadequate to make a clear statement about the quality of the measurement variations. Nevertheless, the developement of both total and polarised intensity (top and middle panel in Figure 6.14) exactly confirms the results of the 15 GHz analysis for all three components: the clear decrease in flux density of the VLBI core component and the slight increase for the 1 mas component while the total flux density of the 0.5 mas remains almost constant and the polarised flux density shows a small decline.

Concerning the polarised intensity electric vectors, the orientation in the core region up to approximately 0.8 mas is again perpendicular to the jet axis (bottom panel in Figure 6.13) according to the findings at 5 and 15 GHz. Beyond this distance no electric vectors could be displayed due to the increased signal-to-noise level at this high frequency.

The bottom panel of Figure 6.14 displays that the core vector seems to be almost constant ($\langle\chi_{Core}\rangle$ = -162°) whereas the vector of the 0.5 mas component shows slight changes ($\langle\chi_{0.5}\rangle$ = -146°, σ_χ = 24°). This is, however, in contrast to what was found in the 15 GHz polarisation analysis where the 0.5 mas component revealed the least variations. The obviously strong gradient in the value of the 1 mas component electric vector, on the other hand, again coincides with the findings at 15 GHz where the 1 mas component appeared to be the strongest variable one.

To complete the picture, the maps were also convolved with a 'pencil'-shaped beam (0.5×0.2 mas, see Figure 6.15) and intensity profiles were taken along the inner 0.9 mas of the jet axis. The total and polarised intensity profiles as well as the fractional polarisation are presented in Figure 6.16.

Now the higher resolution of the 22 GHz observations as compared to 15 GHz is disclosed. In the intensity profile plots one can distinguish three components in the inner 0.8 mas jet instead of two as was the case for the 15 GHz data. The development of the fractional polarisation (bottom panels in Figure 6.16) is comparable to the 15 GHz results in that it is almost the same in the core and innermost displayed jet region in the first and second epoch (2001.988 and 2002.536) whereas in the last epoch (2003.277) the core fractional polarisation is somewhat lower than in the jet.

Interestingly, the fractional polarisation plot of the last epoch reveals a fourth component at a distance of 0.2 mas from the core region which is only slightly indicated by the elongated core component of the above polarised intensity profile but not visible in total intensity at all. This component could be consistent with K7 from the kinematic analysis that is about to separate from the VLBI core. The fractional polarisation plots are evidently a helpful tool for the component identification without the necessity of performing model fits.

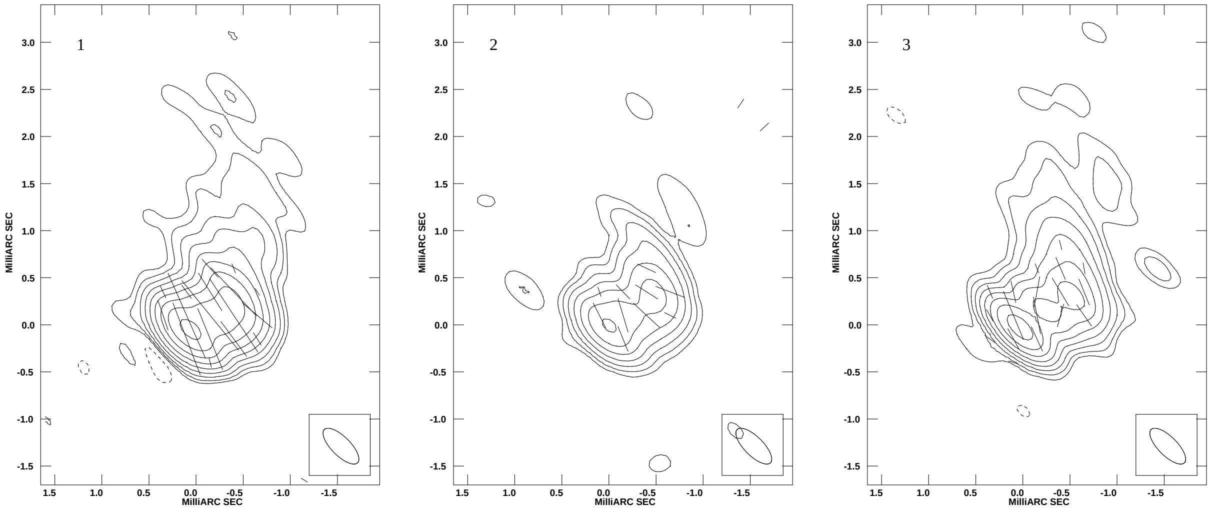

Figure 6.15: *Total intensity maps with EVPA at 22 GHz (1 mas = 100 mJy/beam) convoluted with a 'pencil'-shaped beam of (0.5×0.2) mas with the major beam axis perpendicular to the jet ridge line of the inner 0.8 mas; epochs 1 to 3 according to order of Table 6.4.*

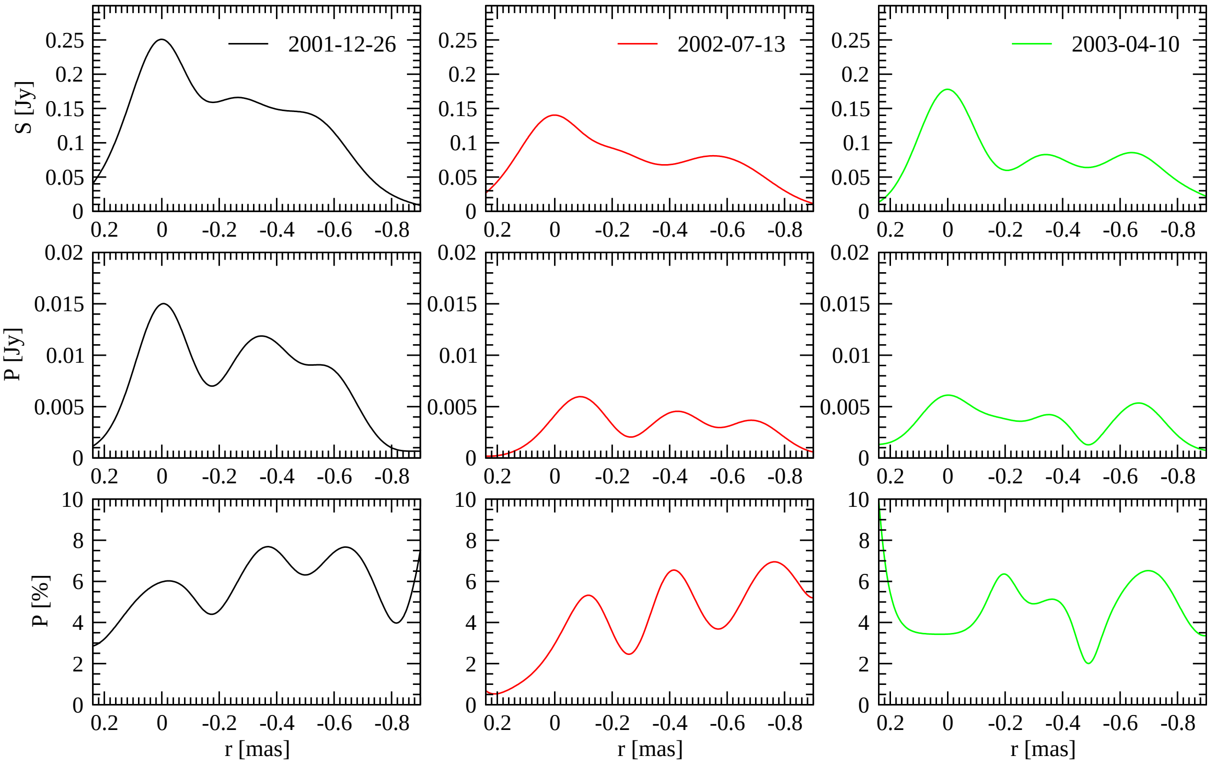

Figure 6.16: *Profile plots at 22 GHz derived from cuts along the jet; different colors denote different epochs; panels display profiles as follows: top: total flux density, middle: polarised flux density, bottom: EVPA; maps were convoluted with pencil shape beam of (0.5×0.2) mas with the major beam axis perpendicular to the jet ridge line.*

Table 6.5: *EVPAs of the convoluted maps at all frequencies; values are already corrected for the absolute orientation of the EVPA according to Table 6.1.*

epoch	ν [GHz]	EVPA$_{Core}$ [°]
2001.984	5	-140±3
2002.529	5	-142±3
2003.252	5	-134±4
2001.984	15	-142±13
2002.529	15	-149±11
2003.252	15	-148±10
2001.984	22	-149±26
2002.531	22	-137±21
2003.273	22	-169±7

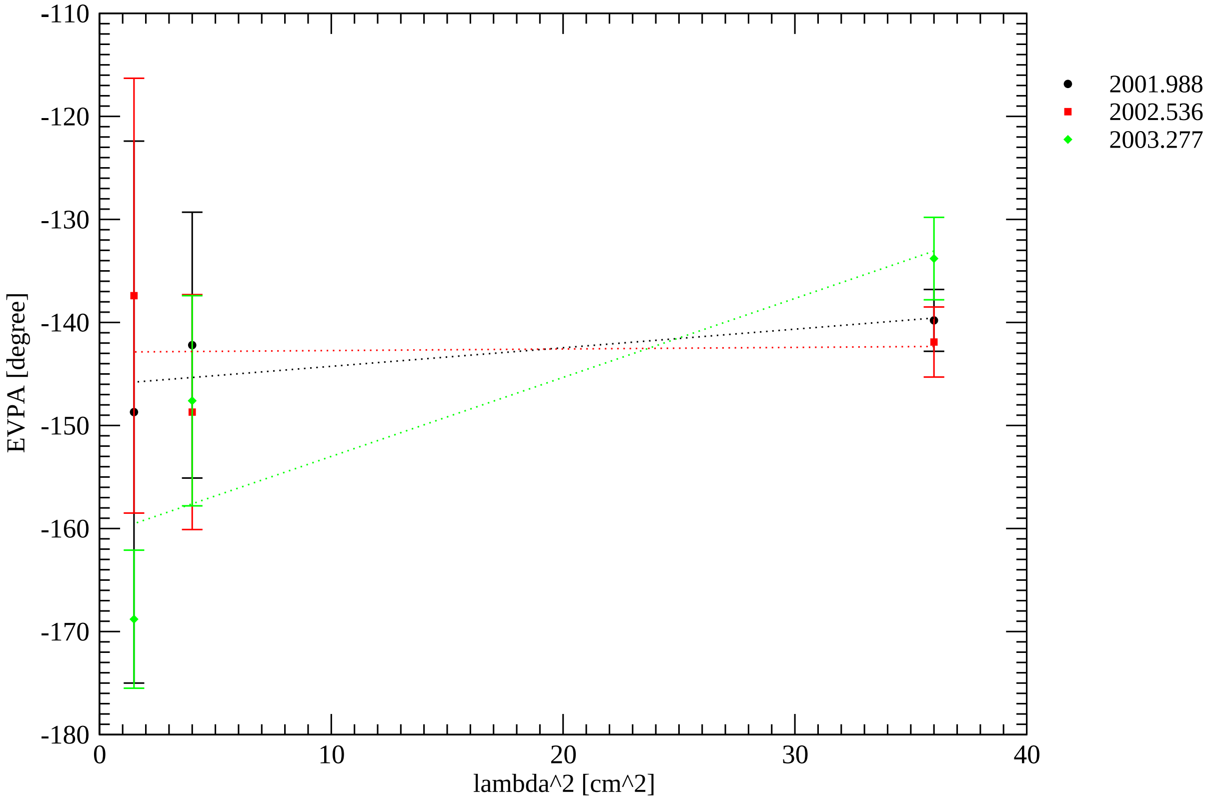

Figure 6.17: *EVPA plotted versus λ^2 for the core region; dotted lines denote linear fits to the data points of each epoch.*

6.2.4 Rotation Measure

A final step would now be to deduce the rotation measure (further denoted as RM) from the EVPAs of the three available frequencies. However, we already had to derive the 22 GHz polarisation vector, that was used for the calibration of the EVPA in the VLBI measurements, from 5 and 15 GHz single dish measurements. Hence, a deduction of the RM would be a circular argument. Nevertheless, I will give a short demonstration on how to derive it in principle.

Provided that for each frequency we got an independently calibrated value for the EVPA, one can plot these values versus λ^2 and fit a straight line to the graph. We can derive the RM from the slope of this fit according to $\chi(\lambda) = \chi_0 + \mathrm{RM}\lambda^2$. As we have three different epochs, it is also possible to calculate the change of the RM with time. In order to do so, it is necessary to convolve the maps of the different frequencies with the same beam pattern, preferably close to the synthesized beam pattern of the lowest frequency to avoid undesirable features due to hyper-resolution. In the present case I chose a beam size of (1.2×1.2) mas. The mapping procedure and determination of the EVPAs was done as described previously for the general polarisation analysis.

If resolution permits, one could also plot the EVPA of one or more jet components at different frequencies. In such way one gets a gradient of the RM along the jet axis. In our case, we only obtained components which are equivalent in two frequencies: two components at a relative core separation of 0.5 and 1 mas, respectively, resolved at 15 and 22 GHz, and a further jet component at 6 mas distance visible at 5 and 15 GHz. The convolution of the higher frequency maps still revealed components at 2 and 6 mas distance from the VLBI core. Nevertheless, the determination of the EVPA yielded in errors of order of several tens of degrees making a derivation of the RM highly unreliable. Thus, we merely derived the RM of the core component of 0917+624 as an estimate of the real RM. The detected EVPAs of the convoluted maps at all frequencies are listed in Table 6.5 and graphically displayed in Figure 6.17. The values are already corrected for the absolute orientation of the EVPA according to the last column of Table 6.1.

Table 6.6: *Estimate of the RM for the VLBI core component.*

epoch	RM [rad/m^2]
2001.984	1800
2002.529	150
2003.252	7700

From Figure 6.17 the RM of the three epochs could be derived and the results are presented in Table 6.6. The strong change of the EVPA in epoch 2003.273 at 22 GHz from previously -137° to now -169° and the associated increase in RM can be explained due to blending effects. In epochs 2001.984 and 2002.529 the core component of the maps with larger beam consists of the previously determined VLBI core and the 0.5 mas component. In the last epoch (2003.252) another component reveals which is located around 0.2 mas. It cannot be separated in the mapping procedure but becomes visible in the profile plots (cf. Figure 6.16, bottom right panel). Its polarisation characteristics likely contribute to those of the 0.5 mas component which would in principle explain the change of the EVPA from -126° in epoch 2002.529 to -176° in epoch 2003.252 (cf. bottom panel of Table 6.4).

Even though the RM deduction is only a rough estimate, it already indicates that 0917+624 might also belong to the group of quasars which (at least sometimes) show RMs in excess of 1000 rad m^{-2} in their central region. Nevertheless, a proper EVPA calibration for 0917+624 is inevitable for a clear statement about the changes in the electric field vector!

Chapter 7

Discussion and Conclusions

In this section I will combine the results of the analyses from single dish and VLBI observations to give an interpretation in view of Intraday Variability and complement the picture of 0917+624 in terms of jet characteristics of quasar sources.

The results of the analysis of the Effelsberg 5 GHz data do not yet offer a clear solution for the cause of the reduced IDV behavior. 0917+624 still reveals only moderate IDV in total intensity which has increased only slightly towards the end of the present observations ($m_I \sim 1\,\%$) but was still far from the strength it used to reveal before September 2000 ($m_I \sim 3 - 5\,\%$). The same holds for the variability in polarised intensity: although the increase of the modulation index m_P is much stronger compared to m_I, it is as well far below the formerly observed modulation indices of more than 15 %. Two different scenarios could be possible explanations for it.

Changes in the size of the scattering medium:

This solution has already been explained in more detail by Fuhrmann (2004). He suggests that in the weak ISS or RISS regime, a decrease in the strength of the turbulence in the scattering medium or an increase in the distance towards it could lead to such extremely quenched variability, the latter case leading to unrealistic high Doppler factors, though. The most probable cause of the decline in IDV could either be a gap in the scintillation screen or the sudden disappearance of a moving foreground layer or clump after 1999. This may have led to an abrupt decrease in the strength of the turbulence in the scattering medium. Hence, a lower limit of $1.2\,\mathrm{m\,s^{-1}}$ can be assigned to the velocity in the scattering screen at a distance of 150 pc. Indeed, the angular scales of such inhomogeneities should be less than the angular separation of 0917+624 from other sources ($\leq$ 5-10°) because other sources outside this region still exhibit prominent IDV.

Source-intrinsic structural changes:

This second approach is based upon variations in the internal source structure scaled in the range of the scattering size. Fuhrmann (2004) in his above mentioned model assumed the size of the source component, that is responsible for the scintillation, to be of the order of ~0.1 mas. Corncerning the strongly quenched scintillation, this component could now either have disappeared or it has increased in size such that it will exceed the Fresnel angular scale. If he assumes a screen distance between 100 and 200 pc, the component size should have enlarged to approximately 0.7-0.8 mas in order to diminish m_I from former values of 5-6 % down to 0.5 %. This growth in component size should be unveiled in the analysis of the VLBI observations of Chapter 5.

However, the assumption of only one scintillating component might not hold for the faster and more pronounced variations that are usually observed in polarized intensity, even in the present case of 0917+624. Rickett et al. (2002a) suggested in the case of the rapid variations in polarisation of the quasar PKS 0405-385 a multi-component model (see also Rickett et al. 1995, Rickett et al. 2002b) where one or more components with quasi independent flux density variations, but each retaining fixed values of P and χ, have to be summed up. This, though, also implies a scattering screen located much closer to the earth as previously expected (3-30 pc), which meanwhile indeed could be confirmed by recent studies of Marchili (2009). He found that an annual modulation model can be applied in the case of 0917+624 provided that the scattering screen is much closer to the earth ($\leq$ 50pc) than previoulsy concluded by Rickett et al. (1995); Rickett (2001) of the order of 170 - 200 pc.

Source kinematics:

Within the kinematic analysis I was able to identify a maximum number of 12 components at 15 GHz (resulting from 15 observing epochs), seven components at 5 GHz (7 epochs), and nine components at 22 GHz (6 epochs) including the VLBI core. All components could be cross-identified for two frequencies at least. One of these components at a relative core separation of ~6 mas turned out to be constant in position and size and showed only a marginal decreas in flux density at all three observing frequencies.

We in fact determined in the kinematic analysis of the 15 GHz VLBI data, that during the time of the underlying Effelsberg observations 2 new components were emitted around 2003.2 (J11) and 2004.5 (J10). The ejection dates are marked by arrows in the bottom panel of Figure 7.1. One earlier component was ejected around 2000.4 (J9). Yet, one immediately notices, that the time between the emission of the component of 2000 and that of 2003 is far longer than would be expected for a component to travel down the jet and separate from the core. Therefore, the IDV activity should meanwhile have resumed which is, though, not the case.

The general kinematic analysis of all frequencies shows that a new component has been ejected on average every two years between 1990 and 2000. One of these components is J8 (resulting from the 15 GHz analysis) with a determined time of zero core separation around 1998.2, which is in the range of earlier results found by Krichbaum et al. (2002) and Fuhrmann (2004). This event corresponds to a high level of variability. The modulation index lies at ~5% and decreases in the aftermath to ~1.5% (see bottom panel of Figure 5.14) which was about the time when the size of the core and the emitted component exceed the typical scattering size of the medium, presumably resulting in strongly quenched scintillation. Afterwards the modulation index increased again in early 1999 to a value of ~5%. Hence, the behaviour of J8 could in principle confirm our working hypothesis that the earlier variability decline was caused by the ejection of a new component.

Component J9 was emitted around 2000.4, which overlaps with a period when the vari-

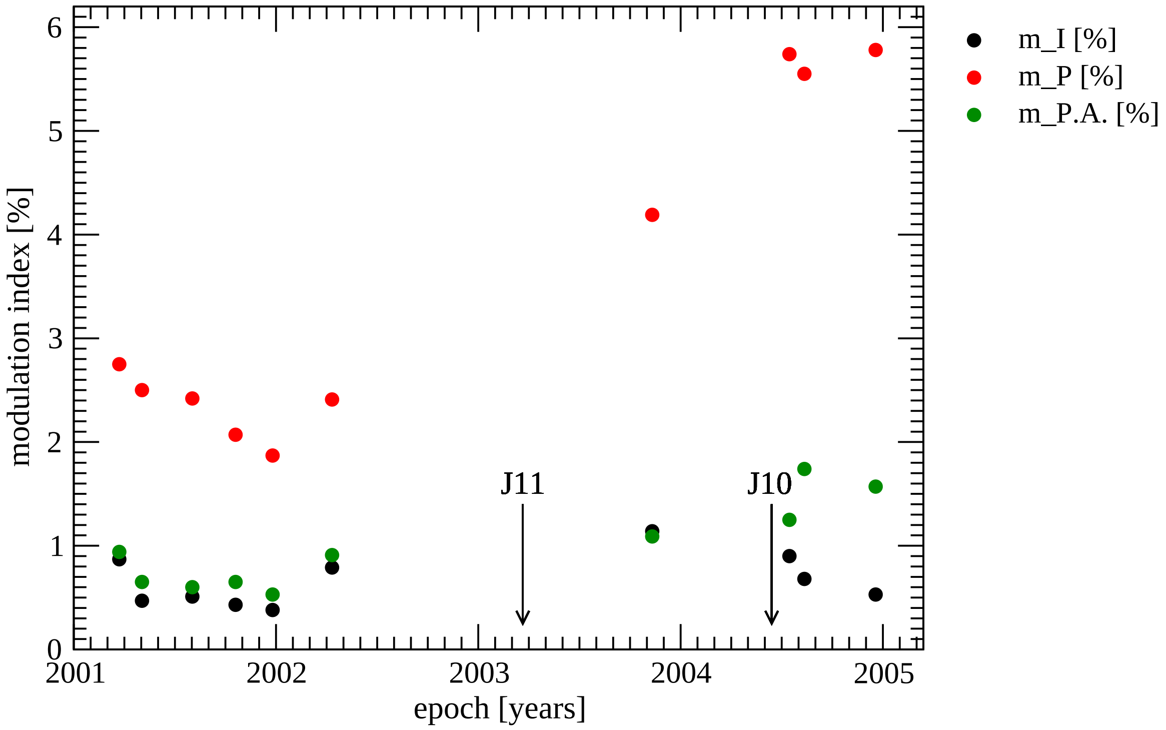

Figure 7.1: *Modulation Indices of 0917+624 total and polarised intensity and EVPA combined with the time of zero core separation for wo components derived in the 15 GHz kinematic analysis.*

ability was already low according to the modulation indices around that time ($m_I \leq 0.65\,\%$, cf. Table B.4). In fact, a further slight decrease has been observed afterwards ($m_I \sim 0.3\,\%$ in 2000.710), followed by a moderate increase up to 0.9 % (2001.225) which could be regarded as an additional confirmation of our assumption. Nevertheless, these modulation indices are still much lower than previously and the ejection of new components alone can not explain the overall damping of the modulation index in both total and polarised intensity.

The multi-component model could at least explain the detection of the stronger variability that we see in the polarisation pattern of 0917+624, especially considering the ejection dates of new components in 2003 and 2004. Since there is unfortunately an observational gap between the middle of 2002 and the end of 2003, we do not know whether the modulation indices m_I and m_P decreased before the new components had been ejected, but we see a clear increase especially in m_P after this gap. So in principle this increase could be attributed to the ejection of component J11, which would imply that the expected increase in variability after the ejection of a new component is detectable in polarisation prior to total intensity.

The polarimetric analysis also supports the multi-component model. While at 5 GHz only one polarised component is visible in the core region within 1 mas, at 15 GHz one can already distinguish between two separate components, each showing individual polarisation characteristics. The 22 GHz data even reveal 3 different components in the inner 0.8 mas jet, and the fractional polarisation profile of the last epoch (2003.277) yet indicates a fourth component located around 0.2 mas distance from the VLBI core which could be related to K7 from the 22 GHz kinematic analysis.

Further results from the analysis of the VLBI data:

The kinematic anlysis revealed several superluminal components for all frequencies. The inner 15 GHz jet components J10, J9, J8, J7, J6, J5 move with an apparent speed of $\beta_{app} = (7 - 10)\,$c which is in good agreement with previous findings (Krichbaum et al. 2002). The same components at 22 GHz (K3, K4, K5, K6) travel with a somewhat higher velocity of $\beta_{app} = (10 - 14)\,$c except for K7 ($\beta_{app} \sim 5.5$) c) which corresponds to J9. Owing to the three times worse resolution at 5 GHz, the innermost jet component C6 is a composite of two or more higher frequency components and therefore exhibits a three times lower apparent velocity than the 15 GHz components. The superluminal motion at 5 GHz reveals to increase further down the jet reaching its maximum at a distance from the core of around 6 mas ($\beta_{app} \sim 20$) c) and then decreases again towards 23 mas ($\beta_{app} \sim 8$) c). This behaviour has also been observed previously, e.g., in the case of 0836+710 (Lobanov 1998).

Since the 5 GHz and 22 GHz data are undersampled compared to the 15 epochs available at 15 GHz, the analysis of the latter is regarded best for the determination of apparent velocities or changes in the position angle (P.A.) and parameters deduced out of it. Besides, since we are interested in the innermost jet region close to the VLBI core, i.e., the footpoint of the jet, the results of the higher frequency analysis reveal deeper insight into this region due to their better resolution. The plots of rel. R.A. versus rel. Decl. at both 15 GHz and 22 GHz (cf. pp. 58 and 78) display a twisted jet structure with several bends on the inner 3.5 mas whereas at 5 GHz only one kink is visible on the same range. In order to investigate the bent jet structure, components J7, J8 and J9 were fitted by a third-order fit which could better represent their trajectories than a linear fit. However, this could not be confirmed in the 5 GHz and 22 GHz analyses due to the insufficient amount of available observations. The shape of the trajectory of component J8 suggests a slow-down after its ejection followed by an accelerated phase between 2002 and 2006. Afterwards it seems to reach again a plateau of decelerated motion. Component J9 even better represents this behaviour (cf. Figures 5.4 and 5.8). The acceleration and deceleration phases can be explained by geometrical effects due to the twisted jet structure. When the component is moving on a kink towards the observer, its radiation is boosted towards him causing the effect of an accelerated motion. A movement across the jet cone pretends a slow-down.

J2 turned out to be the fastest component showing an apparent speed of $\beta_{app} = 19.2\,\mathrm{c}$. This leads to a minimum value for the Lorentz factor $\gamma_{min} = 19.23$, Doppler factors in the range of 19 to 38 at inclination angles between 0° and 3°. Furthermore the P.A. of the inner jet components appears to rotate approximately 4° on average per year. This could be indicative for a swing of the jet base of 0917+624 which has already been observed previously in a number of sources such as 3C345, OJ287 or PKS 0420-014 (Klare 2003; Klare et al. 2005; Lobanov & Roland 2005; Valtonen et al. 2008; Britzen et al. 2001) and seems to be associated with jet-curvature or helical structures that have been observed in the jets of AGN also on larger scales as well as in the present case of 0917+624.

One possibility to explain the cause of helical or twisted jet structures is the presence of a binary black hole system in the center of the AGN. Since 0917+624 also exhibits a bent jet structure, it proves to be an applicable candidate for such a binary black hole scenario. The precession of the accretion disk and the motion of the two black holes around their common center of gravity cause perturbations in the trajectories of the VLBI components. As the coordinates of the VLBI components are known from VLBI observations, we merely need to handle a pure astrometrical problem. Thus, by means of the software he developed, Prof. Roland was able to calculate several parameters of the binary black hole system based on the coordinates of component J8 from the 15 GHz analysis. The bulk Lorentz factor that resulted from the modelling process, γ_c, is in the range of $8 \ll \gamma_c \ll 20$, which supports our kinematic results from the 15 GHz analysis where a minimum Lorentz factor of 19.23 was derived for J8.

Certainly the most important result from the binary black hole model calculations is, however, that the time of zero core separation, which was deduced to lie around 1998.2, has to be shifted to 1999, because otherwise no minimum could be found for the necessary χ^2 fit. The shift of the time of zero core separation supports the hypothesis of the 15 GHz kinematic analysis that a higher-order fit to the VLBI trajectories is probably more suitable than a linear one as it describes in a more appropriate way states of accelerated or constant component motion during certain periods. The temporal shift for the ejection date of component J9 is equivalent to a spatial difference $\sigma = 0.098$ and we dare to interprete it as the distance between the two black holes.

Component J11 seems to travel at a significantly lower apparent velocity ($\beta_{app} = 2.76 \pm 0.17$ c). It is possible, though, that this could be attributed to blending effects in the component identification due to strong activity and hence an expansion of the VLBI core, but insufficient observational resolution. Nevertheless, in view of the results from the binary black hole modelling, we tentatively interprete J11 to be ejected by the second black hole which might be a possible explanation for the different shape of its trajectory as compared to J5 – J10.

In addition, the size of the inner VLBI components (FWHM) was found to increase systematically as they travel along the jet. The correlation of FWHM with P.A. suggests a geometrical origin. If the components are not spherical but form an intrinsically oblique structure (e.g., a thin shock), relativistic aberration effects would lead to apparent rotation in the observer's frame causing the observed component expansion (cf. left panel of Figure 5.9, p. 61). Furthermore, the relation between FWHM and core separation of the components displays that the jet is collimated within the inner 0.7 mas and starts expanding beyond. This is in accordance with the theory of an adiabatically expanding jet (e.g., Blandford & Königl 1979). The opening angle of the jet was determined to be $\phi = 20.9^\circ$ which results in a Mach number M of the jet plasma at the point of the jet opening of $M = 2.8$. This number could be confirmed in the 22 GHz analysis. However, the jet at 22 GHz shows an additional reconfinement around a distance from the core of 0.7 mas. This lateral displacement of the 22 GHz components from the jet axis at the lower frequencies in principle can be explained by the afore mentioned geometrical changes in the viewing angle of the jet and has previously also been investigated in the case of 0836+710 (Lobanov 1998).

The analysis of the flux density development is in accordance with results from single dish observations with the Effelsberg and UMRAO telescopes for all three frequencies. They find a decrease in flux density from 1999 to the middle of 2004 followed by a moderate increase towards the end of the present VLBI observations in 2007. Besides the VLBI analysis revealed that approx. 75 % of the total flux is concentrated in the core region which is in agreement with previous findings from Standke et al. (1996). Moreover, this so-called 'core fraction', which tends to be higher in quasar and BL Lac objects, is expected from AGN unification schemes because the core fraction is a strong function of orientation.

As is known for compact sources, the analysis of the spectral index evolution reveals that it is flat in the compact core region and gradually turns steeper in the resolved jet region. The development of the spectral index between the higher frequencies $\alpha_{15/22GHz}$ even reflects the fact that the VLBI core component is not necessarily the brightest one. This is best demonstrated in the spectral index change of component J8/K6 from epoch 2001.988 ($\alpha_{15/22GHz} \sim -0.2$), when its flux density was brighter than the core flux, to epoch 2002.536 ($\alpha_{15/22GHz} \sim -1.2$), when the VLBI core had become brighter again.

In the polarimetric analysis we found that the fractional polarisation of the jet is much higher than of the core region which is well in accordance with previous findings (e.g., Helmboldt et al. 2007; Lister & Homan 2005; Pollack et al. 2003). Besides - always provided that the absolute position calibration of the electric field vector is reliable - the EVPA is oriented perpendicular to the jet axis in the core region ($\lesssim$4 mas at 5 GHz, $\lesssim$ 1 mas at 15 GHz and 22 GHz). This result also agrees with previous findings (e.g., Pollack et al. 2003). Further down the jet the orientation changes between parallel and transverse to the jet axis. These changes are, however, only detectable at 5 GHz where the polarisation properties of the jet could be resolved to a distance from the core of ~ 8 mas. Where the polarisation electric vectors in the parsecscale jets are aligned with the local jet direction, it is implied that the corresponding magnetic field is transverse to the jet as the jet emission is optically thin. This has commonly been interpreted as evidence for relativistic shocks that enhance the magnetic field component in the plane of compression perpendicular to the propagation direction of the shock (e.g., Hughes et al. 1989) and also explains the increase of fractional polarisation towards the edge of the jet (Laing 1980).

The fact that the EVPA of the VLBI core is oriented perpendicular to the jet axis, and thus apparently does not correlate with the source structure, could be owing to a magnetic field that changes from transverse to longitudinal from the core to the jets because of strong shocks in the jet perpendicular to the plane. This was, e.g., postulated in the case of 3C 345 and 3C 279 (Leppänen et al. 1995).

A further result from the polarimetric analysis is the remarkable increase in polarised intensity of the VLBI core from 1999 to 2000 where the polarised intensity (more than) doubles at both 5 GHz and 15 GHz. The single dish analysis suggests that the increase in polarised intensity overlaps with the strong decline of the modulation index in 2000.

Regarding the polarisation characteristics, a Faraday RM gradient across the jet is also considered a good indicator for helical magnetic fields in the jet. These gradients should appear due to the systematic change in the net line-of-sight component of the magnetic field across the jet, with increasing values toward the jet boundaries (e.g., Blandford 1993). Taylor (1998) suggests that the high RMs, which he found in his observations, possibly are generated in the same region that produces the narrow optical emission lines. The high RM gradients between the core region and the extended jet cannot be produced by cluster or galactic scale magnetic fields but are rather caused by organised magnetic fields and ionised gas close to the center of activity. This is also likely the case for the change of the core RM with time that we found for 0917+624.

Even if the RM, that could be derived for the core component of 0917+624, can only be a rough estimate of the true RM, the high values in the first epoch (2001.984) of 1800 rad m^2 and last epoch (2003.252) of 7700 rad m^2 already indicate that internal structural changes can influence the determination of a proper RM. The assuption that the RM follows a straight λ^2 law, which I used in order to derive the integrated EVPA for the correction of the absolute position, can only be applied if the Faraday rotation is negligible which is obviously not the case for 0917+624. Thus, the calibration of the absolute position of the electric field vector should be determined in a proper measurement at the required frequency. Otherwise a clear statement about the changes of the EVPA with time between multiple observing epochs likely turns out to be unreliable.

CHAPTER 8

Summary and Outlook

Within the scope of this thesis, 10(+3) epochs of 4.85 GHz observations of the prominent IDV quasar 0917+624, performed between 2001 and the end of 2004 with the Effelsberg 100-meter radio telescope, were analysed in total and polarised intensity regarding the short-time variability behaviour of the source. Furthermore, 28 epochs of VLBI observations at 15 GHz (15 epochs), 5 GHz (7 epochs) and 22 (+24) GHz (4+2 epochs) between 1999 and 2007 have been analysed. Finally, a polarisation analysis of the VLBI epochs observed between 1999 and 2003 was carried out. The primary aim of these observations was to find out whether structural changes of the variable part of 0917+624 have caused the variability decline that was detected after September 2000 by Fuhrmann et al. (2002). The ejection of a new VLBI component could temporarily lead to a core size exceeding the Fresnel scale, which is determined by the scattering medium. Consequently, only strongly quenched scintillation would be observed. After the component has separated from the VLBI core at some point, the size of the scintillating component decreases again and stronger variability is expected to resume.

We found from the single dish measurements that the IDV activity of 0917+624 has decreased significantly during the time of our single dish observations between 2001 and 2005 in both total and polarised intensity compared to former measurements between 1985 and 1999 - from previous modulation indices for I of 3-5% to 0.4-1.1 % maximum. This is in agreement with previous findings from Fuhrmann et al. (2002) who analysed observations between September 2000 and April 2002. The kinematic analysis of the VLBI data revealed that three new components have been ejected from the VLBI core at 2000.4, 2003.4 and 2004.2. Accordingly, the slight increase in the modulation index of the polarised intensity of the single dish measurements, m_P, from 2003 to the end of 2004 might be explained in terms of the multi-component model of Rickett et al. (1995). However, we have to be careful in interpreting the measured polarisation modulation indices as real because of possible elevation-dependent effects that were possibly found in the analysis of the single dish polarisation data. The potential elevation-dependency of the results from single dish polarisation analyses still requires further investigation.

Besides, the gap between the ejection dates of the two components in 2000 and 2003 is too long compared to the time needed for a component to move down the jet and separate from the core. Hence, the IDV activity should meanwhile have resumed. Since this is not the case, the hypothesis of a quenched scintillation scenario is not conclusive.

The suggestion by Rickett (2001), that the observed change in the variability time scale could be explained by a so-called annual modulation scenario could be confirmed recently by Marchili (2009) provided that the scattering screen is much closer to the earth ($\sim$ 50 pc) than previously assumed. Nevertheless, the source showed a radical change in its IDV behaviour by reducing its variability. This does not necessarily mean, that the seasonal cycle is not the right option. It may at present simply not be visible due to the structural changes in the central region, which were found in the kinematic and polarimetric analysis of the VLBI data.

Since the annual modulation scenario for 0917+624 has only been tested in terms of total intensity, it might be an interesting project to study the polarised variability pattern in this regard. Further polarisation analysis of already obtained single dish data and continuing observations should be performed in order to achieve a thorough investigation of the polarisation behavior. It may be worthwhile to study the question whether it is in principle possible to observe annual modulation in polarised rather than in total intensity also for other sources than 0917+624.

The kinematic analysis of the VLBI data furthermore revealed apparent superluminal motion in the jet ranging from 2 c to almost 20 c. From the apparent jet speed we derive a Lorentz factor > 19.23 and an inclination angle $< 3°$. Hence, for the fastest jet component we obtain Doppler factors in the range of 19 to 38 which can help to reduce brightness temperature values in excess of 10^{16} K, as have been derived from IDV observations of 0917+624 (Quirrenbach et al. 1989b; Kraus et al. 1999), below the inverse Compton limit of 10^{12} K. The higher jet speeds of ~ 20 c differ from the maximum jet speed of 15.57c found by Lister et al. (2009) within the scope of the MOJAVE project. The difference is certainly owing to the even better sampling of the MOJAVE data. We found that an undersampling of observations can in fact cause higher jet speeds, as was the case for the 5 GHz and 22 GHz data, since a temporal slowdown, a period of constant motion or acceleration of the jet could simply not be detected with an insufficient amount of observing data.

The 15 GHz kinematic analysis revealed a quasi-helical jet structure for 0917+624 with several bends in the trajectories of the jet components. The observed change in the position angle (P.A.) of the inner components of approximately 4° per year on average is indicative for a swing of the jet base, also yielding a helical jet structure, and clearly indicates motion on bent-non-ballistic trajectories. The mechanism, which could cause such ’jet wobbling’ (cf. Agudo et al. 2007), is still not understood but precession of the accretion disk is a popular explanatory model usually based on the assumption of a binary system in the galactic center. We further found a correlation of component size with orientation (P.A.) suggestive of a projection effect due to the jet geometry.

The spectral index evolution of the VLBI core shows that it varies from steep to flat whereas the spectral index of the outer components is clearly steeper (between -0.7 and -1.5). The flatness of the core’s spectral index coincides with times when new components are ejected (around 2000.4 and 2003.2), which is also displayed in the middle panel of Figure 5.14 (p. 67) where the spectral index $\alpha_{5/15GHz}$ of single dish measurements with the Effelsberg and UMRAO telescope is shown. It gradually steepens after 2003 when component J11 has separated from the VLBI core. This supports the assumption that the components are shocks which expand adiabatically as they travel down the jet. After the component separation, the VLBI core becomes the most compact part of the source again and thus reveals the flattest spectral index. In the analysis of the VLBI data we found that the VLBI core contains approximately 75 % of the total source flux which makes it the dominant unresolved part in single dish measurements.

The helical jet structure of 0917+624 makes the source a good candidate for an AGN consisting of a binary black hole system. In our model calculations we found that a temporal shift for the origin of the ejection of the VLBI component from 1998.2 to 1999 was necessary since otherwise no minimum in the χ^2 fit, which has to be performed within the analysis, could be achieved. The shift of the time of zero core separation supports the hypothesis of the 15 GHz kinematic analysis that a higher-order fit to the VLBI trajectories is probably more suitable than a linear one. The temporal shift entails a spatial difference $\sigma = 0.098$ mas or 0.83 pc which we interpret as the distance between the two black holes. In order to test the reliability of our preliminary results, the model is currently applied to all suitable trajectories that have resulted from the data analysis of all three frequencies. If the result can be verified, it would be the first time that the distance between two black holes of a binary black hole system could be ’measured’ by means of a ’plain’ astrometric analysis.

The polarimetric analysis of the high frequency VLBI data at 15 GHz and 22 GHz disclosed that the VLBI core region consists of three to four subcomponents. In this context the fractional polarisation turns out to be a helpful tool to display the source components without performing model fits of the polarised intensity data. Particularly when the total or polarised intensity profiles only show one broadened peak, the fractional polarisation plot can already reveal two different peaks within. The results of the 15 GHz and 22 GHz polarimetric analysis indeed support the theory of a multi-component model, such as the 4-component model which was applied by Qian et al. (2007), not only to explain the previously observed polarisation angle swing in 0917+624, but also the variations in total and polarised intensity.

The estimate of the VLBI core RM reveals that it is variable. It reaches high values in excess of 1000 rad m^{-2}, which are likely caused by intrinsic changes in organised magnetic fields and ionised gas close to the center of activity. This could be the reason for the observed variability of polarised intensity and EVPA. For future VLBI polarimetric observations it is in general of utmost importance to obtain simultaneous data of polarisation calibrators in order to achieve a proper calibration of the EVPA. With regard to this crucial point, the results concerning the orientation of the EVPA in the core region of 0917+624 are still uncertain. Nevertheless, an orientation of the EVPA parallel to the jet axis as was found from the 5 GHz analysis, which implies a magnetic field perpendicular to the jet, is in accordance with the expectations for optically thin synchrotron emission. On the other hand, a magnetic field aligned with the jet axis in the core region - provided the result is indeed correct - can either be explained by strong shocks in the jet perpendicular to the plane, as was done in case of 3C345 and 3C 279 (Leppänen et al. 1995), or it indicates further bent jet structure in the inner core region which can not be resolved at the observed frequencies.

The determined RM changes might not be real but caused by blending effects. Hence, future RM-tomography according to, e.g., the Faraday rotation measure synthesis as suggested by Brentjens & de Bruyn (2005), is necessary to disentangle the underlying effects.

It will be a future goal to do phase referencing observations of 0917+624 at, e.g., 22/15 GHz in order to determine whether the jet base is moving. A further important test, for which this source turned out to be ideally suited, is to figure out how the changes in polarised intensity and polarisation angle do relate to intraday variability. This could be done by means of simultaneous multi-epoch/multi-frequency VLBI and single dish observations at preferably high frequencies (43/22 GHz).

Furthermore, it would be desirable to study 0917+624 with the GMVA at 86 GHz which features a resolution of $\sim 50\mu as$. But the flux density of the source is a bit weak for present day VLBI recording techniques. Therefore, the implementation of the already existing Mark5C VLBI data system at the observing facilities would be of great value. It will be able to record data at a sustained rate of 4Gbit/s with a bandwidth of 1 GHz which would enormously increase the recording sensitivity. With these observations we will not only be able to discover internal jet structure close to the VLBI core on even smaller scales. Moreover, concerning the binary black hole scenario, the observational resolution will be half of the distance between the two black holes that have been found from our calculations. Hence, provided that we are dealing with two black holes, each of them showing jet structure, we should be able to disentangle between the footpoints of two different jets.

APPENDIX A

Appendix A

The following figures show plots of the Effelsberg single dish observations of 0917+624. The upper panel contains the total intensity measurements, the middle panel shows results for the polarised intensity and the bottom panel displays the polarisation angle as a function of J.D. for each epoch.

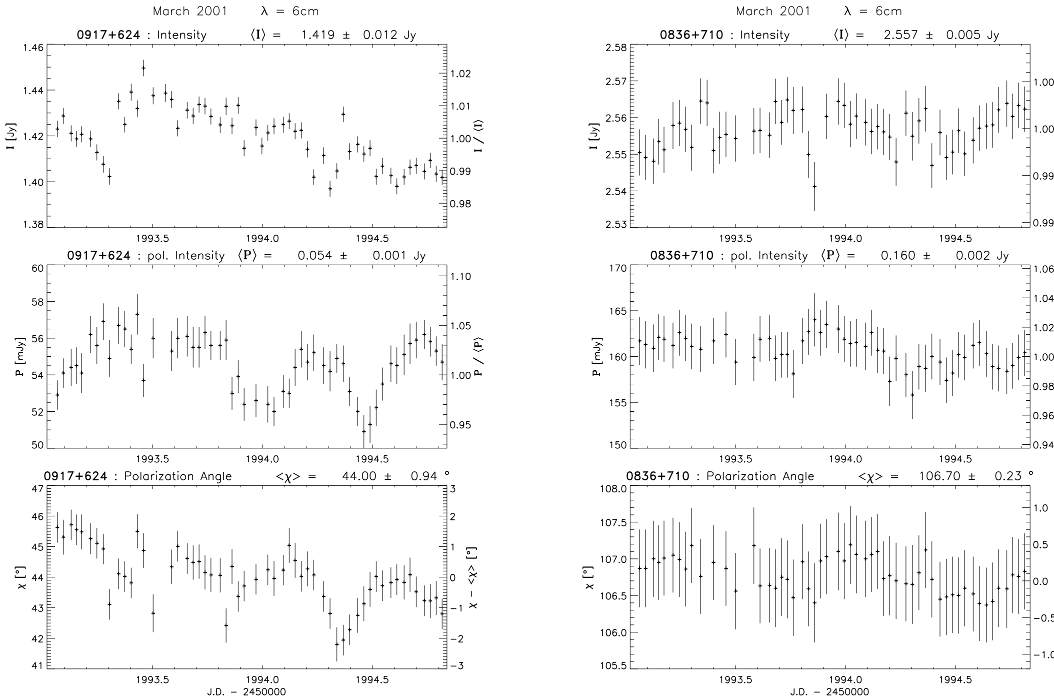

Figure A.1: *Plots of Effelsberg single dish data at 5 GHz for 0917+624 and one example plot of the calibrator source 0836+710 observed on Mar. 24, 2001*

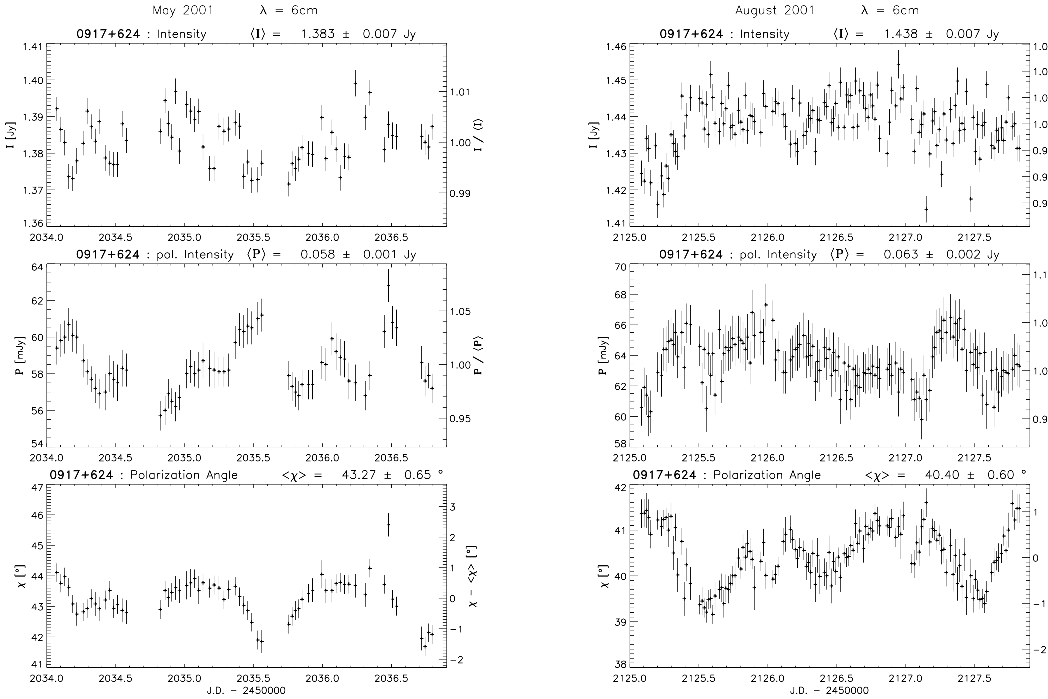

Figure A.2: *0917+624 plots of Effelsberg single dish data at 5 GHz observed on May 4, 2001 (left panel), Aug. 3, 2001 (right panel).*

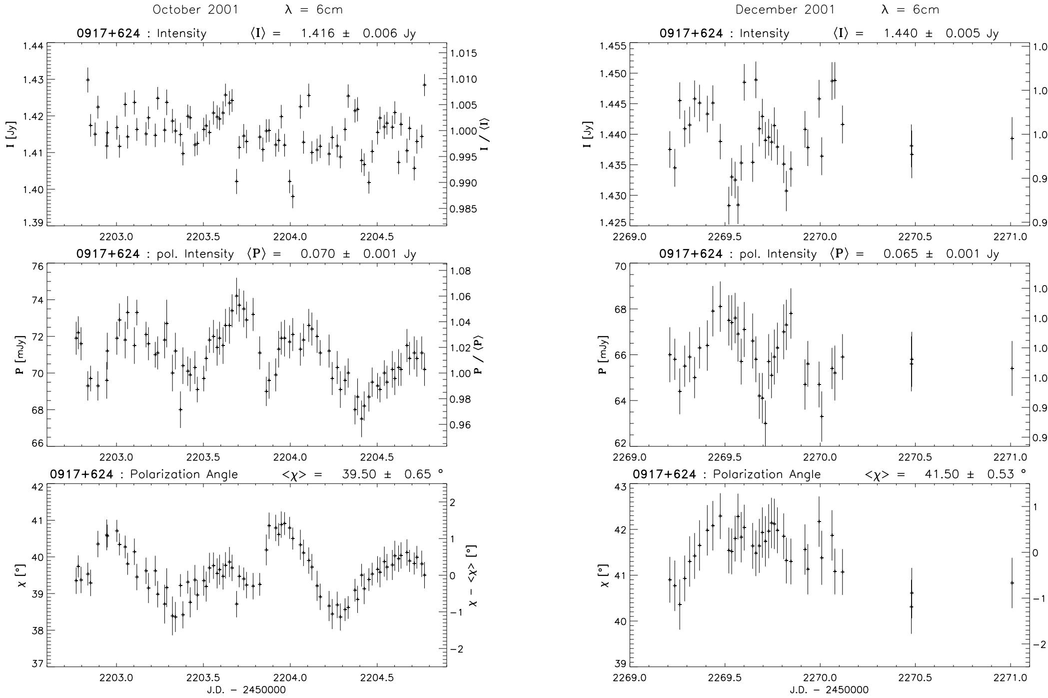

Figure A.3: *0917+624 plots of Effelsberg single dish data at 5 GHz observed on Oct. 20, 2001 (left panel), Dec. 26, 2001 (right panel).*

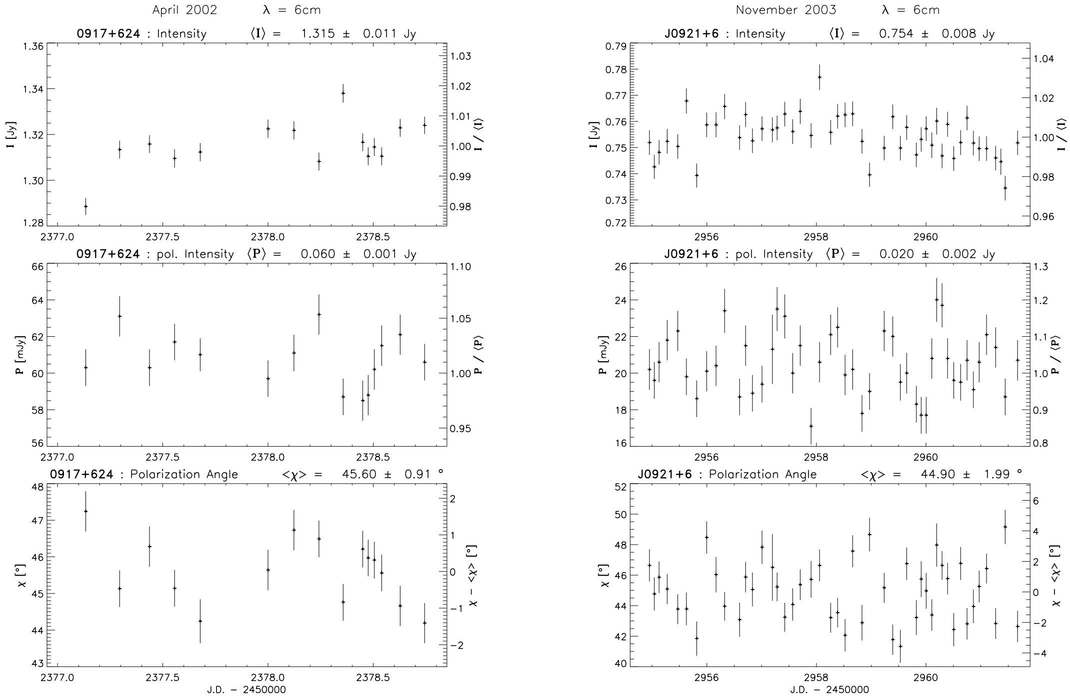

Figure A.4: *0917+624 plots of Effelsberg single dish data at 5 GHz observed on Apr. 12, 2002 (left panel) and around Nov. 14, 2003 (right panel - during the INTEGRAL observing campain of 0716+714, Fuhrmann et al. 2008, source name according to J2000 coordinates).*

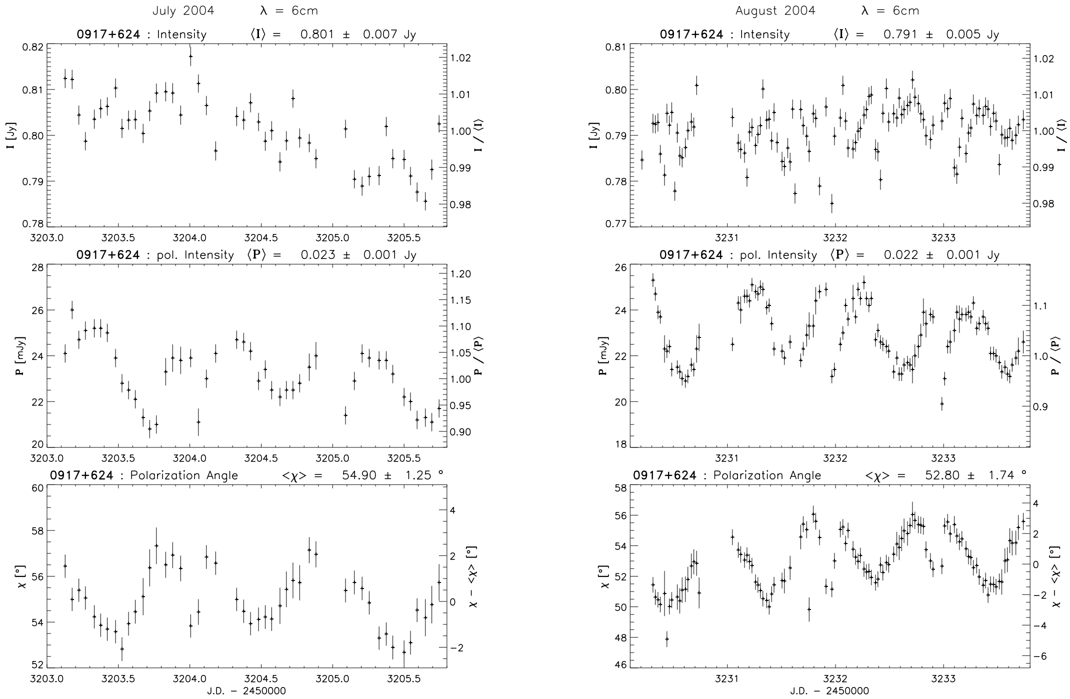

Figure A.5: *0917+624 plots of Effelsberg single dish data at 5 GHz observed on Jul. 16, 2004 (left panel) and Aug. 12, 2004 (right panel).*

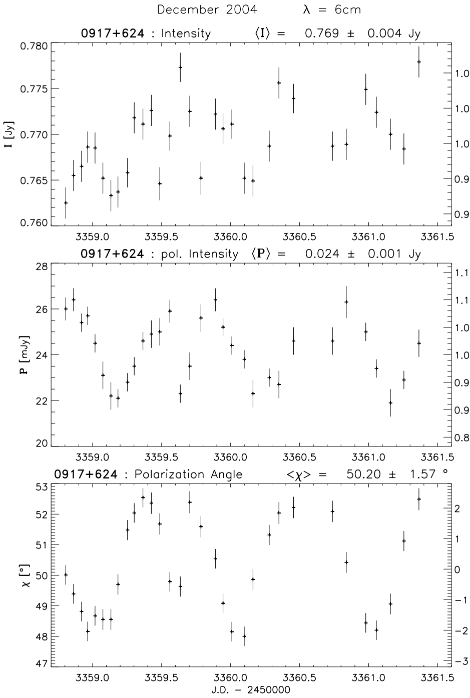

Figure A.6: *0917+624 plots of Effelsberg single dish data at 5 GHz observed on Dec. 19, 2004.*

Appendix B

The following tables contain the results of the model fitting for all epochs, giving the component flux density (column 1), rel. R.A. (column 2) and rel. Decl. (column 3) with respect to the core, distance r to the core (column 4) and position angle θ (column 5), Full Width Half Maximum (FWHM, column 6), and brightness temperature T_B (column 7). Column 8 denotes the component identification.

Table B.1: Results of the Gaussian model fitting for all epochs at 15 GHz.

s [Jy]	x [mas]	y [mas]	r [mas]	θ [°]	FWHM [mas]	T_B [K]	Id.[1]
1999.888							
0.227±0.050	0.00±0.00	0.00±0.00	0.00±0.00	0.0±0.0	0.09±0.04	1.52E+11	Core
0.446±0.060	-0.22±0.04	0.12±0.04	0.25±0.04	-62.1±2.9	0.24±0.02	4.20E+10	J8
0.243±0.022	-0.42±0.04	0.28±0.04	0.50±0.04	-55.9±0.9	0.09±0.02	1.62E+11	J7
0.176±0.048	-0.41±0.06	0.49±0.07	0.64±0.04	-40.3±5.2	0.36±0.05	7.36E+09	J6
0.035±0.006	-0.68±0.09	1.15±0.15	1.33±0.05	-30.4±3.9	0.38±0.11	1.32E+09	J5a
0.015±0.006	-0.34±0.08	1.83±0.41	1.86±0.20	-10.6±2.1	0.70±0.40	1.64E+08	J4
0.008±0.000	-2.23±0.11	5.75±0.28	6.17±0.14	-21.2±0.9	0.29±0.08	5.29E+08	J3
0.047±0.005	-2.11±0.04	5.71±0.11	6.09±0.04	-20.3±0.4	2.62±0.53	3.72E+07	J2
0.007±0.003	-8.20±1.68	25.99±5.33	27.25±5.31	-17.5±1.1	4.47±2.11	1.93E+06	J1
2000.183							
0.313±0.011	0.00±0.00	0.00±0.00	0.00±0.00	0.0±0.0	0.06±0.01	4.72E+11	Core
0.347±0.042	-0.26±0.03	0.14±0.03	0.29±0.03	-62.4±1.1	0.17±0.01	6.52E+10	J8

s	x	y	r	θ	FWHM	T_B	Id.[1]
[Jy]	[mas]	[mas]	[mas]	[°]	[mas]	[K]	
0.193±0.046	-0.44±0.03	0.29±0.03	0.53±0.03	-56.8±1.4	0.11±0.03	8.63E+10	J7
0.121±0.062	-0.48±0.03	0.43±0.03	0.64±0.03	-48.7±1.1	0.20±0.05	1.64E+10	J6
0.061±0.002	-0.52±0.03	1.02±0.04	1.14±0.05	-26.9±0.4	0.51±0.03	1.26E+09	J5
0.008±0.001	-0.48±0.15	1.97±0.64	2.03±0.21	-13.6±4.1	0.50±0.24	1.78E+08	J4
0.020±0.002	-2.20±0.06	5.50±0.14	5.93±0.05	-21.8±0.5	0.88±0.23	1.37E+08	J3
0.039±0.003	-2.19±0.14	6.58±0.41	6.94±0.13	-18.4±1.1	4.20±0.39	1.20E+07	J2
0.016±0.002	-11.00±0.71	20.88±1.34	23.60±0.18	-27.8±1.8	7.84±0.79	1.37E+06	J1
2000.915							
0.331±0.009	0.00±0.00	0.00±0.00	0.00±0.00	0.0±0.0	0.07±0.03	3.67E+11	Core
0.299±0.018	-0.30±0.02	0.12±0.02	0.32±0.02	-68.6±0.7	0.11±0.03	1.34E+11	J8
0.219±0.047	-0.45±0.02	0.29±0.02	0.53±0.02	-57.3±1.6	0.17±0.03	4.10E+10	J7
0.083±0.028	-0.51±0.04	0.53±0.04	0.74±0.06	-43.9±0.7	0.24±0.03	7.81E+09	J6
0.067±0.015	-0.57±0.07	1.01±0.13	1.16±0.09	-29.5±2.9	0.62±0.04	9.39E+08	J5
0.010±0.003	-0.79±0.16	1.58±0.33	1.77±0.17	-26.7±4.8	0.27±0.13	7.07E+08	J4
0.020±0.008	-2.10±0.11	5.56±0.30	5.94±0.24	-20.7±0.7	1.22±0.59	7.25E+07	J3
0.036±0.005	-2.55±0.15	6.50±0.38	6.98±0.38	-21.4±0.4	3.71±0.40	1.41E+07	J2
2001.988							
0.196±0.063	0.00±0.00	0.00±0.00	0.00±0.00	0.0±0.0	0.09±0.02	1.31E+11	Core
0.318±0.048	-0.19±0.04	0.11±0.03	0.22±0.04	-60.9±2.2	0.16±0.02	6.74E+10	J9
0.186±0.083	-0.44±0.05	0.20±0.03	0.48±0.06	-66.1±1.5	0.17±0.07	3.50E+10	J8
0.143±0.053	-0.53±0.05	0.37±0.03	0.65±0.03	-55.4±4.4	0.13±0.04	4.60E+10	J7
0.090±0.021	-0.50±0.05	0.60±0.06	0.78±0.05	-39.5±2.9	0.39±0.11	3.21E+09	J6
0.041±0.024	-0.63±0.10	1.13±0.19	1.29±0.15	-29.1±3.5	0.58±0.13	6.66E+08	J5
0.015±0.012	-0.60±0.16	2.25±0.59	2.33±0.34	-15.1±3.3	0.96±0.38	9.00E+07	J4
0.016±0.002	-2.27±0.06	5.60±0.14	6.04±0.07	-22.0±0.5	1.10±0.12	7.17E+07	J3
0.027±0.002	-2.30±0.19	6.65±0.56	7.04±0.21	-19.0±1.5	3.44±0.10	1.23E+07	J2
2002.241							
0.188±0.067	0.00±0.00	0.00±0.00	0.00±0.00	0.0±0.0	0.11±0.04	8.43E+10	Core
0.255±0.022	-0.17±0.05	0.11±0.05	0.21±0.05	-56.6±3.8	0.15±0.03	6.15E+10	J9
0.162±0.024	-0.45±0.05	0.22±0.05	0.50±0.05	-64.3±4.3	0.13±0.02	5.19E+10	J8
0.140±0.080	-0.54±0.09	0.41±0.07	0.68±0.05	-52.7±8.0	0.17±0.05	2.63E+10	J7
0.051±0.023	-0.45±0.07	0.65±0.10	0.79±0.09	-34.6±3.9	0.28±0.15	3.49E+09	J6
0.045±0.027	-0.62±0.16	1.04±0.28	1.21±0.18	-31.0±6.9	0.53±0.18	8.72E+08	J5
0.020±0.004	-0.70±0.18	2.11±0.53	2.22±0.50	-18.3±2.0	1.03±0.10	1.01E+08	J4
0.034±0.015	-2.29±0.14	5.82±0.37	6.25±0.22	-21.4±1.1	1.86±0.83	5.27E+07	J3a
2002.458							

s [Jy]	x [mas]	y [mas]	r [mas]	θ [°]	FWHM [mas]	T_B [K]	Id.[1]
0.233±0.057	0.00±0.00	0.00±0.00	0.00±0.00	0.0±0.0	0.12±0.05	8.78E+10	Core
0.317±0.087	-0.28±0.09	0.15±0.05	0.32±0.09	-61.9±6.7	0.19±0.06	4.77E+10	J9
0.128±0.023	-0.57±0.05	0.35±0.03	0.67±0.03	-58.1±4.3	0.08±0.05	1.09E+11	J7
0.090±0.011	-0.47±0.04	0.66±0.06	0.81±0.04	-35.3±2.6	0.32±0.04	4.74E+09	J6
0.033±0.005	-0.66±0.04	1.14±0.07	1.32±0.06	-30.3±1.3	0.53±0.06	6.37E+08	J5
0.021±0.005	-0.51±0.08	2.13±0.33	2.19±0.21	-13.4±1.6	1.23±0.09	7.60E+07	J4
0.020±0.004	-2.16±0.04	5.53±0.10	5.94±0.09	-21.3±0.2	1.40±0.19	5.45E+07	J3
0.024±0.001	-2.84±0.09	7.29±0.24	7.82±0.15	-21.3±0.6	3.82±0.08	9.03E+06	J2
2002.536							
0.196±0.030	0.00±0.00	0.00±0.00	0.00±0.00	0.0±0.0	0.08±0.02	1.66E+11	Core
0.200±0.013	-0.20±0.02	0.12±0.02	0.24±0.03	-59.4±2.0	0.13±0.03	6.43E+10	J9
0.155±0.014	-0.48±0.02	0.24±0.02	0.54±0.03	-63.6±0.6	0.11±0.02	6.95E+10	J8
0.140±0.014	-0.55±0.03	0.46±0.02	0.72±0.03	-50.1±2.0	0.23±0.04	1.44E+10	J7
0.035±0.005	-0.40±0.06	0.80±0.12	0.89±0.04	-26.8±3.8	0.29±0.09	2.22E+09	J6
0.044±0.016	-0.62±0.10	1.14±0.19	1.30±0.15	-28.7±3.6	0.63±0.02	5.98E+08	J5
0.016±0.005	-0.59±0.15	2.29±0.58	2.36±0.43	-14.4±2.6	1.04±0.37	7.87E+07	J4
0.009±0.004	-2.21±0.12	5.43±0.29	5.86±0.27	-22.1±0.6	0.53±0.31	1.80E+08	J3
0.030±0.003	-2.60±0.12	6.43±0.29	6.94±0.15	-22.0±0.9	3.11±0.10	1.68E+07	J2
2003.277							
0.192±0.012	0.00±0.00	0.00±0.00	0.00±0.00	0.0±0.0	0.09±0.02	1.28E+11	Core
0.152±0.008	-0.26±0.03	0.17±0.03	0.31±0.03	-57.1±0.7	0.14±0.02	4.21E+10	J9
0.140±0.014	-0.55±0.03	0.30±0.03	0.63±0.03	-60.9±0.4	0.13±0.01	4.50E+10	J8
0.067±0.011	-0.60±0.03	0.54±0.03	0.81±0.03	-48.0±2.1	0.21±0.02	8.25E+09	J7
0.030±0.005	-0.46±0.03	0.89±0.04	1.00±0.03	-27.3±1.1	0.25±0.03	2.62E+09	J6
0.035±0.006	-0.60±0.04	1.27±0.09	1.40±0.08	-25.4±1.3	0.80±0.05	2.93E+08	J5
0.011±0.003	-0.48±0.07	2.66±0.41	2.70±0.15	-10.2±1.5	1.12±0.18	4.67E+07	J4
0.033±0.017	-2.32±0.11	5.84±0.26	6.28±0.25	-21.7±0.5	2.25±1.23	3.48E+07	J3a
2003.458							
0.275±0.029	0.00±0.00	0.00±0.00	0.00±0.00	0.0±0.0	0.13±0.03	8.82E+10	Core
0.129±0.026	-0.33±0.10	0.19±0.06	0.38±0.12	-59.8±0.9	0.13±0.04	4.14E+10	J9
0.120±0.049	-0.58±0.04	0.36±0.04	0.68±0.05	-58.0±2.2	0.15±0.06	2.88E+10	J8
0.037±0.010	-0.53±0.08	0.70±0.10	0.88±0.07	-37.0±4.4	0.13±0.08	1.18E+10	J7
0.036±0.007	-0.38±0.06	0.98±0.16	1.05±0.12	-21.0±2.6	0.43±0.17	1.06E+09	J6
0.018±0.005	-0.69±0.06	1.42±0.13	1.58±0.06	-26.0±2.1	0.53±0.17	3.47E+08	J5
0.015±0.002	-0.59±0.05	2.63±0.24	2.70±0.15	-12.6±0.9	1.11±0.17	6.47E+07	J4
0.035±0.019	-2.29±0.12	5.92±0.30	6.35±0.26	-21.2±0.6	2.43±1.71	3.22E+07	J3a

s [Jy]	x [mas]	y [mas]	r [mas]	θ [°]	FWHM [mas]	T_B [K]	Id.[1]
2005.097							
0.383±0.107	0.00±0.00	0.00±0.00	0.00±0.00	0.0±0.0	0.06±0.02	5.76E+11	Core
0.259±0.072	-0.08±0.06	0.08±0.06	0.11±0.06	-45.6±2.0	0.04±0.01	8.76E+11	J10
0.048±0.003	-0.44±0.06	0.32±0.06	0.55±0.08	-54.6±2.5	0.22±0.03	5.39E+09	J9
0.036±0.012	-0.67±0.23	0.62±0.21	0.91±0.16	-46.9±13.7	0.32±0.10	1.91E+09	J8
0.022±0.005	-0.49±0.06	1.11±0.12	1.22±0.06	-23.8±2.3	0.35±0.05	9.65E+08	J7a
0.019±0.001	-0.74±0.06	1.70±0.15	1.86±0.08	-23.5±1.7	0.83±0.05	1.50E+08	J5
0.011±0.002	-0.74±0.06	3.04±0.08	3.13±0.06	-13.6±0.2	0.99±0.04	6.31E+07	J4
0.015±0.001	-2.27±0.06	5.47±0.08	5.92±0.06	-22.6±0.2	0.85±0.09	1.11E+08	J3
0.015±0.002	-2.82±0.08	8.35±0.24	8.81±0.22	-18.7±0.3	2.80±0.23	1.04E+07	J2
2005.458							
0.634±0.087	0.00±0.00	0.00±0.00	0.00±0.00	0.0±0.0	0.08±0.02	5.37E+11	Core
0.153±0.030	-0.12±0.05	0.09±0.05	0.15±0.05	-53.6±0.6	0.05±0.01	3.32E+11	J10
0.029±0.007	-0.48±0.05	0.37±0.05	0.61±0.05	-52.6±0.5	0.09±0.04	1.95E+10	J9
0.022±0.008	-0.67±0.12	0.61±0.11	0.91±0.16	-47.7±1.8	0.25±0.04	1.91E+09	J8
0.018±0.004	-0.49±0.05	1.07±0.11	1.18±0.05	-24.4±2.3	0.36±0.06	7.57E+08	J7
0.021±0.002	-0.68±0.05	1.62±0.09	1.76±0.08	-22.8±0.7	0.90±0.01	1.40E+08	J5
0.014±0.002	-0.67±0.05	2.98±0.18	3.05±0.13	-12.7±0.6	0.85±0.12	1.03E+08	J4
0.012±0.006	-2.16±0.05	5.53±0.05	5.94±0.05	-21.4±0.1	0.69±0.07	1.33E+08	J3
0.022±0.002	-2.56±0.18	7.39±0.53	7.82±0.53	-19.1±0.4	3.76±0.51	8.55E+06	J2
2005.719							
0.276±0.083	0.00±0.00	0.00±0.00	0.00±0.00	0.0±0.0	0.06±0.02	4.15E+11	Core
0.529±0.151	-0.09±0.04	0.05±0.04	0.11±0.04	-59.8±2.7	0.06±0.01	7.97E+11	J11
0.093±0.070	-0.17±0.04	0.12±0.04	0.21±0.04	-55.6±1.2	0.15±0.03	2.25E+10	J10
0.028±0.001	-0.55±0.04	0.40±0.04	0.68±0.04	-53.8±0.4	0.15±0.02	6.70E+09	J9
0.014±0.001	-0.74±0.04	0.71±0.04	1.02±0.04	-46.0±1.8	0.28±0.05	9.54E+08	J8
0.017±0.003	-0.54±0.04	1.12±0.06	1.25±0.05	-25.6±1.0	0.45±0.07	4.63E+08	J7
0.017±0.000	-0.71±0.04	1.78±0.08	1.92±0.05	-21.8±0.9	0.88±0.06	1.16E+08	J5
0.014±0.002	-0.70±0.04	2.94±0.10	3.03±0.06	-13.4±0.3	0.93±0.08	8.96E+07	J4
0.012±0.001	-2.29±0.04	5.53±0.04	5.99±0.04	-22.5±0.1	0.72±0.08	1.27E+08	J3
0.024±0.001	-2.63±0.08	7.71±0.22	8.14±0.10	-18.8±0.5	4.04±0.06	8.01E+06	J2
2006.608							
0.222±0.052	0.00±0.00	0.00±0.00	0.00±0.00	0.0±0.0	0.06±0.01	3.35E+11	Core
0.561±0.031	-0.13±0.04	0.08±0.04	0.15±0.05	-56.6±1.8	0.11±0.01	2.51E+11	J11
0.186±0.042	-0.27±0.04	0.23±0.04	0.36±0.05	-50.2±0.7	0.08±0.01	1.57E+11	J10
0.015±0.003	-0.55±0.04	0.50±0.04	0.74±0.05	-47.4±0.6	0.15±0.06	3.69E+09	J9

s [Jy]	x [mas]	y [mas]	r [mas]	θ [°]	FWHM [mas]	T_B [K]	Id.[1]
0.017±0.001	-0.67±0.04	1.19±0.04	1.37±0.05	-29.5±0.6	0.54±0.05	3.18E+08	J7
0.009±0.002	-0.48±0.05	2.17±0.24	2.23±0.05	-12.4±1.4	0.37±0.09	3.37E+08	J5a
0.014±0.001	-0.94±0.04	3.23±0.08	3.36±0.07	-16.3±0.2	0.87±0.06	9.67E+07	J4
0.008±0.001	-2.50±0.07	5.57±0.16	6.11±0.05	-24.2±0.7	0.49±0.09	1.83E+08	J3
0.022±0.001	-3.24±0.09	8.23±0.24	8.85±0.17	-21.5±0.5	4.36±0.10	6.19E+06	J2
2007.425							
0.314±0.116	0.00±0.00	0.00±0.00	0.00±0.00	0.0±0.0	0.11±0.05	1.41E+11	Core
0.302±0.036	-0.14±0.04	0.11±0.05	0.18±0.05	-51.1±0.7	0.15±0.03	7.28E+10	J11
0.348±0.025	-0.36±0.04	0.29±0.05	0.46±0.05	-51.3±0.2	0.17±0.02	6.53E+10	J10
0.014±0.009	-0.58±0.04	0.50±0.05	0.77±0.06	-48.9±1.2	0.11±0.06	6.23E+09	J9
0.009±0.003	-0.90±0.14	0.75±0.12	1.17±0.09	-50.4±6.9	0.68±0.33	1.09E+08	J8
0.009±0.003	-0.60±0.05	1.71±0.15	1.81±0.11	-19.2±1.3	0.41±0.23	2.87E+08	J6
0.017±0.003	-0.78±0.04	3.12±0.15	3.21±0.11	-14.0±0.5	1.17±0.19	6.69E+07	J4
0.010±0.001	-2.29±0.04	5.48±0.06	5.93±0.05	-22.7±0.2	0.56±0.07	1.71E+08	J3
0.021±0.002	-2.89±0.15	8.02±0.42	8.52±0.35	-19.8±0.7	3.63±0.18	8.48E+06	J2
2007.683							
0.096±0.063	0.00±0.00	0.00±0.00	0.00±0.00	0.0±0.0	0.04±0.01	3.24E+11	Core
0.404±0.044	-0.14±0.05	0.14±0.05	0.20±0.05	-43.7±3.0	0.10±0.01	2.19E+11	J11
0.373±0.036	-0.42±0.05	0.37±0.05	0.56±0.05	-48.6±0.7	0.14±0.01	1.03E+11	J10
0.050±0.048	-0.58±0.07	0.52±0.06	0.78±0.08	-48.1±2.3	0.06±0.03	7.53E+10	J9
0.003±0.000	-0.69±0.07	0.96±0.10	1.19±0.09	-35.8±2.5	0.35±0.23	1.20E+08	J8
0.012±0.000	-0.79±0.05	2.03±0.09	2.17±0.05	-21.3±0.8	0.75±0.07	1.11E+08	J5
0.012±0.000	-0.92±0.05	3.31±0.08	3.43±0.05	-15.5±0.3	0.94±0.05	7.18E+07	J4
0.011±0.001	-2.22±0.05	5.61±0.08	6.03±0.05	-21.6±0.2	1.05±0.11	5.41E+07	J3
0.022±0.001	-3.30±0.05	8.36±0.11	8.99±0.08	-21.5±0.2	4.26±0.08	6.69E+06	J2

[1] Identification of the individual components

Table B.2: Results of the Gaussian model fitting for all epochs at 5 GHz.

s [Jy]	x [mas]	y [mas]	r [mas]	θ [°]	FWHM [mas]	T_B [K]	Id.[1]
1999.888							
0.474±0.336	0.00±0.00	0.00±0.00	0.00±0.00	0.0±0.0	0.33±0.20	2.12E+11	Core
0.657±0.322	-0.19±0.15	0.33±0.06	0.38±0.15	-29.3±1.5	0.27±0.20	4.40E+11	C6
0.163±0.018	-0.32±0.15	1.18±0.26	1.23±0.15	-15.3±2.9	0.79±0.20	1.28E+10	C5a

s [Jy]	x [mas]	y [mas]	r [mas]	θ [°]	FWHM [mas]	T_B [K]	Id.[1]
0.033±0.005	-1.97±0.15	5.72±0.19	6.05±0.18	-19.0±0.3	0.86±0.20	2.15E+09	C3
0.097±0.010	-2.21±0.15	6.14±0.16	6.52±0.15	-19.8±0.2	3.08±0.20	4.99E+08	C2
0.058±0.006	-9.76±0.30	21.75±0.68	23.84±0.38	-24.2±0.6	18.24±0.74	8.45E+06	C1
2000.183							
0.368±0.037	0.00±0.00	0.00±0.00	0.00±0.00	0.0±0.0	0.28±0.20	2.29E+11	Core
0.639±0.064	-0.29±0.10	0.23±0.06	0.38±0.10	-51.5±0.6	0.21±0.20	7.07E+11	C6
0.145±0.014	-0.41±0.10	0.89±0.09	0.98±0.10	-24.5±0.7	0.53±0.20	2.51E+10	C5
0.058±0.012	-0.37±0.10	1.66±0.15	1.70±0.12	-12.5±0.6	0.99±0.20	2.91E+09	C4
0.039±0.004	-2.03±0.10	5.52±0.10	5.88±0.10	-20.2±0.1	1.05±0.20	1.74E+09	C3
0.084±0.008	-2.28±0.10	6.43±0.11	6.83±0.10	-19.5±0.2	3.32±0.20	3.74E+08	C2
0.055±0.006	-8.86±0.12	21.03±0.29	22.82±0.20	-22.8±0.2	18.51±0.20	7.85E+06	C1
2000.915							
0.422±0.047	0.00±0.00	0.00±0.00	0.00±0.00	0.0±0.0	0.23±0.20	3.89E+11	Core
0.569±0.057	-0.30±0.08	0.23±0.08	0.38±0.08	-53.1±4.3	0.18±0.20	8.57E+11	C6
0.155±0.030	-0.40±0.08	0.82±0.12	0.92±0.08	-26.0±3.1	0.47±0.20	3.42E+10	C5
0.050±0.005	-0.44±0.08	1.86±0.14	1.91±0.08	-13.2±0.8	0.91±0.20	2.93E+09	C4
0.040±0.004	-2.04±0.08	5.51±0.08	5.87±0.08	-20.3±0.2	0.88±0.20	2.50E+09	C3
0.077±0.008	-2.46±0.08	6.76±0.08	7.19±0.08	-20.0±0.2	3.46±0.20	3.15E+08	C2
0.043±0.004	-9.67±0.16	21.11±0.36	23.22±0.12	-24.6±0.4	14.36±0.20	1.02E+07	C1
2001.988							
0.451±0.068	0.00±0.00	0.00±0.00	0.00±0.00	0.0±0.0	0.22±0.20	4.55E+11	Core
0.566±0.079	-0.35±0.09	0.25±0.07	0.43±0.09	-53.9±2.0	0.19±0.20	7.66E+11	C6
0.151±0.020	-0.46±0.09	0.98±0.13	1.09±0.09	-25.0±2.6	0.49±0.20	3.06E+10	C5
0.034±0.003	-0.49±0.09	2.28±0.15	2.34±0.09	-12.1±0.7	0.80±0.20	2.60E+09	C4
0.037±0.003	-2.09±0.09	5.52±0.12	5.90±0.09	-20.8±0.3	0.99±0.20	1.83E+09	C3
0.070±0.006	-2.46±0.09	6.83±0.09	7.26±0.09	-19.8±0.1	3.45±0.20	2.88E+08	C2
0.047±0.004	-9.32±0.09	21.65±0.17	23.57±0.09	-23.3±0.2	14.03±0.20	1.17E+07	C1
2002.241							
0.437±0.078	0.00±0.00	0.00±0.00	0.00±0.00	0.0±0.0	0.26±0.20	3.15E+11	Core
0.471±0.061	-0.36±0.08	0.28±0.07	0.45±0.08	-52.2±2.4	0.23±0.20	4.35E+11	C6
0.138±0.021	-0.45±0.08	1.02±0.13	1.11±0.08	-23.7±2.6	0.53±0.20	2.39E+10	C5
0.033±0.003	-0.46±0.08	2.36±0.20	2.41±0.08	-11.1±0.9	0.81±0.20	2.42E+09	C4
0.040±0.003	-2.08±0.08	5.45±0.12	5.83±0.08	-20.9±0.3	1.08±0.20	1.69E+09	C3
0.066±0.005	-2.50±0.08	7.06±0.09	7.49±0.08	-19.5±0.1	3.47±0.20	2.67E+08	C2
0.043±0.003	-9.35±0.15	21.56±0.35	23.50±0.08	-23.4±0.4	13.43±0.20	1.16E+07	C1
2002.536							

s [Jy]	x [mas]	y [mas]	r [mas]	θ [°]	FWHM [mas]	T_B [K]	Id.[1]
0.385±0.043	0.00±0.00	0.00±0.00	0.00±0.00	0.0±0.0	0.27±0.20	2.58E+11	Core
0.447±0.036	-0.34±0.09	0.31±0.07	0.46±0.09	-48.0±1.4	0.26±0.20	3.23E+11	C6
0.121±0.010	-0.45±0.09	1.06±0.07	1.15±0.09	-23.1±1.3	0.54±0.20	2.02E+10	C5
0.037±0.003	-0.47±0.09	2.37±0.12	2.41±0.09	-11.3±0.4	0.95±0.20	2.01E+09	C4
0.034±0.003	-2.07±0.09	5.40±0.07	5.78±0.09	-21.0±0.2	1.02±0.20	1.59E+09	C3
0.069±0.006	-2.49±0.09	6.95±0.07	7.38±0.09	-19.7±0.2	3.48±0.20	2.78E+08	C2
0.043±0.003	-9.33±0.09	21.69±0.16	23.61±0.09	-23.3±0.2	13.56±0.20	1.14E+07	C1
2003.277							
0.261±0.021	0.00±0.00	0.00±0.00	0.00±0.00	0.0±0.0	0.20±0.20	3.19E+11	Core
0.417±0.042	-0.37±0.08	0.31±0.07	0.48±0.08	-49.6±3.6	0.19±0.20	5.64E+11	C6
0.124±0.015	-0.48±0.08	1.13±0.11	1.23±0.08	-23.1±1.7	0.58±0.20	1.80E+10	C5
0.034±0.003	-0.53±0.08	2.59±0.23	2.65±0.08	-11.6±1.0	0.95±0.20	1.83E+09	C4
0.031±0.003	-2.09±0.08	5.39±0.07	5.78±0.08	-21.2±0.2	0.99±0.20	1.56E+09	C3
0.067±0.005	-2.54±0.08	7.08±0.07	7.52±0.08	-19.7±0.1	3.75±0.20	2.33E+08	C2
0.043±0.003	-9.34±0.08	21.56±0.07	23.50±0.08	-23.4±0.1	13.64±0.20	1.14E+07	C1

[1] Identification of the individual components

Table B.3: Results of the Gaussian model fitting for all epochs at 22 GHz.

s [Jy]	x [mas]	y [mas]	r [mas]	θ [°]	FWHM [mas]	T_B [K]	Id.[1]
2001.988							
0.122±0.026	0.00±0.00	0.00±0.00	0.00±0.00	0.0±0.0	0.04±0.04	1.93E+11	Core
0.241±0.025	-0.13±0.05	0.10±0.04	0.16±0.05	-54.0±4.3	0.11±0.04	5.01E+10	K7
0.171±0.040	-0.38±0.05	0.19±0.04	0.43±0.06	-63.5±2.6	0.11±0.04	3.56E+10	K6
0.109±0.022	-0.55±0.10	0.32±0.06	0.63±0.12	-60.1±1.8	0.12±0.04	1.91E+10	K5
0.101±0.016	-0.53±0.05	0.50±0.04	0.73±0.05	-47.0±1.2	0.24±0.05	4.43E+09	K4
0.039±0.004	-0.59±0.05	0.93±0.04	1.10±0.05	-32.2±0.7	0.53±0.11	3.50E+08	K3
0.017±0.002	-0.66±0.06	1.84±0.18	1.95±0.06	-19.7±1.8	1.03±0.21	4.04E+07	K2b
0.020±0.002	-2.32±0.07	5.79±0.19	6.24±0.12	-21.8±0.7	1.40±0.28	2.51E+07	K1
2002.241							
0.097±0.009	0.00±0.00	0.00±0.00	0.00±0.00	0.0±0.0	0.11±0.04	2.02E+10	Core
0.223±0.048	-0.14±0.05	0.12±0.04	0.19±0.05	-51.1±2.3	0.14±0.04	2.87E+10	K7
0.130±0.012	-0.41±0.08	0.23±0.04	0.47±0.09	-60.6±2.6	0.19±0.04	9.06E+09	K6
0.064±0.008	-0.57±0.05	0.36±0.04	0.68±0.05	-58.2±1.0	0.13±0.04	9.49E+09	K5

s [Jy]	x [mas]	y [mas]	r [mas]	θ [°]	FWHM [mas]	T_B [K]	Id.[1]
0.072±0.011	-0.60±0.05	0.54±0.04	0.81±0.05	-47.8±2.5	0.26±0.05	2.67E+09	K4
0.026±0.007	-0.44±0.06	0.87±0.11	0.98±0.05	-27.0±3.4	0.26±0.05	9.51E+08	K3b
0.012±0.001	-0.82±0.05	1.28±0.06	1.52±0.05	-32.5±1.2	0.32±0.06	2.93E+08	K3a
0.013±0.001	-0.75±0.09	2.26±0.26	2.38±0.09	-18.4±2.0	1.12±0.22	2.63E+07	K2
0.015±0.002	-2.36±0.11	5.60±0.26	6.08±0.13	-22.9±0.9	1.14±0.23	2.83E+07	K1
2002.536							
0.135±0.030	0.00±0.00	0.00±0.00	0.00±0.00	0.0±0.0	0.05±0.04	1.36E+11	Core
0.129±0.012	-0.16±0.06	0.12±0.03	0.20±0.06	-54.2±1.5	0.10±0.04	3.25E+10	K7
0.097±0.010	-0.43±0.06	0.21±0.03	0.48±0.06	-63.5±1.6	0.12±0.04	1.70E+10	K6
0.066±0.007	-0.58±0.06	0.36±0.03	0.68±0.06	-57.9±1.7	0.12±0.04	1.15E+10	K5
0.053±0.007	-0.56±0.06	0.55±0.04	0.79±0.06	-45.7±3.0	0.24±0.05	2.31E+09	K4
0.034±0.003	-0.45±0.07	0.85±0.13	0.96±0.06	-27.8±4.1	0.49±0.13	3.56E+08	K3b
0.011±0.004	-0.82±0.09	1.27±0.15	1.51±0.17	-32.9±1.3	0.36±0.08	2.06E+08	K3a
0.008±0.001	-0.58±0.08	2.39±0.34	2.46±0.08	-13.7±1.9	0.65±0.13	4.83E+07	K2
0.019±0.006	-2.39±0.15	6.16±0.39	6.61±0.25	-21.2±1.3	2.80±1.28	6.17E+06	K1
2003.277							
0.182±0.018	0.00±0.00	0.00±0.00	0.00±0.00	0.0±0.0	0.06±0.04	1.28E+11	Core
0.072±0.007	-0.18±0.05	0.13±0.04	0.22±0.05	-54.0±0.3	0.11±0.04	1.51E+10	K7
0.086±0.009	-0.39±0.05	0.23±0.04	0.45±0.05	-59.0±0.4	0.12±0.04	1.51E+10	K6b
0.073±0.007	-0.60±0.05	0.32±0.04	0.68±0.05	-61.5±0.1	0.09±0.04	2.28E+10	K6a
0.042±0.004	-0.62±0.05	0.51±0.04	0.80±0.05	-50.6±0.7	0.15±0.04	4.65E+09	K5
0.041±0.004	-0.51±0.05	0.80±0.04	0.95±0.05	-32.3±0.5	0.32±0.06	1.00E+09	K4
0.032±0.002	-0.58±0.05	1.27±0.06	1.40±0.05	-24.4±1.1	0.83±0.17	1.16E+08	K3
0.008±0.001	-0.50±0.10	2.54±0.50	2.58±0.10	-11.1±2.2	0.73±0.15	3.55E+07	K2
0.021±0.002	-2.38±0.10	5.77±0.23	6.24±0.09	-22.4±0.8	1.89±0.38	1.45E+07	K1
2004.124							
0.370±0.037	0.00±0.00	0.00±0.00	0.00±0.00	0.0±0.0	0.08±0.04	1.22E+11	Core
0.072±0.010	-0.32±0.12	0.22±0.05	0.39±0.12	-55.3±2.4	0.29±0.06	1.81E+09	K7
0.048±0.006	-0.65±0.12	0.40±0.05	0.77±0.12	-58.2±0.9	0.04±0.04	6.41E+10	K6
0.032±0.010	-0.59±0.12	0.78±0.06	0.98±0.12	-37.3±2.1	0.26±0.05	1.02E+09	K5
0.011±0.004	-0.57±0.12	1.50±0.19	1.60±0.15	-21.0±2.3	0.70±0.14	4.71E+07	K3
0.005±0.001	-0.59±0.16	4.38±1.16	4.42±0.16	-7.7 ±2.0	0.72±0.65	1.88E+07	K2a
0.026±0.008	-2.85±1.26	6.75±2.98	7.33±3.10	-22.9±2.9	5.36±2.63	1.95E+06	K1
2004.955							
0.455±0.161	0.00±0.00	0.00±0.00	0.00±0.00	0.0±0.0	0.07±0.04	1.97E+11	Core
0.063±0.028	-0.09±0.08	0.06±0.06	0.11±0.08	-55.2±1.9	0.14±0.04	6.79E+09	K8

s [Jy]	x [mas]	y [mas]	r [mas]	θ [°]	FWHM [mas]	T_B [K]	Id.[1]
0.029±0.005	-0.35±0.08	0.27±0.06	0.44±0.08	-52.1±2.5	0.23±0.16	1.15E+09	K7
0.025±0.004	-0.67±0.08	0.56±0.06	0.87±0.08	-49.7±1.3	0.09±0.05	6.62E+09	K6
0.017±0.004	-0.55±0.08	0.97±0.06	1.11±0.08	-29.8±0.8	0.26±0.13	5.17E+08	K5
0.005±0.001	-0.13±0.08	1.40±0.14	1.40±0.08	-5.3 ±2.6	0.30±0.15	1.11E+08	K3b
0.007±0.001	-0.29±0.08	2.88±0.21	2.90±0.08	-5.7 ±0.4	0.14±0.07	7.46E+08	K2

[1] Identification of the individual components

Table B.4: *Modulation index m and variability amplitude Y of Effelsberg and Urumqi measurements at 5 GHz.*

epoch	m[%]	Y[%]
1999.100	5.02	14.94
2000.200	0.65	1.52
2000.710	0.26	0.71
2000.900	0.65	1.81
2001.225	0.87	2.53
2001.337	0.47	1.29
2001.586	0.51	1.41
2001.800	0.43	1.14
2001.983	0.38	1.04
2002.277	0.79	2.23
2003.871	1.14	3.37
2004.538	0.90	2.64
2004.612	0.68	1.93
2004.967	0.53	1.52
2005.603	1.50	4.26
2005.989	2.09	5.12
2006.364	1.13	3.06
2006.321	0.88	2.16
2006.438	1.08	2.88
2006.534	1.58	4.25
2006.633	1.17	2.81
2006.729	0.92	1.35
2006.881	1.00	2.41
2007.068	0.84	1.41
2007.118	1.15	2.73
2007.227	0.85	0.00
2007.301	0.89	0.00
2007.457	1.30	3.46
2007.548	1.23	3.03
2007.784	0.87	2.44
2007.971	0.77	1.74

Appendix C

Here, the binary black hole model and its application to the data analysis of Chapter 5.2.5 are described according to Roland et al. (2008) by courtesy of Prof. Roland.

C.1 The model

Introduction: The two-fluid model

At first, the ejection of a VLBI component in the framework of the two-fluid model (Sol et al. 1989; Pelletier & Roland 1989, 1990; Pelletier & Sol 1992) is described. The two-fluid description of the outflow is adopted with the following assumptions :

1. The outflow consists of an $e^- - p$ plasma (hereafter *the jet*) moving at mildly relativistic speed $v_j \leq 0.4 \times c$ and an $e^\pm$ plasma (hereafter *the beam*) moving at highly relativistic speed (with corresponding Lorentz factor $\gamma_b \leq 30$).
2. The magnetic field lines are parallel to the flow in the beam and the mixing layer, and are toroidal in the jet (see Figure 1 of Lobanov & Roland 2005).

The $e^- - p$ jet carries most of the mass and the kinetic energy ejected by the nucleus. It is responsible for the formation of kpc-jets, hot spots and extended lobes (Muxlow et al. 1988; Roland et al. 1988; Roland & Hetem 1996). The relativistic $e^\pm$ beam moves in a channel through the mildly relativistic jet and is responsible for the formation of superluminal sources and their γ-ray emission (Roland et al. 1994). The relativistic beam can propagate if the magnetic field B is parallel to the flow in the beam and in the mixing layer between the beam and the jet and if it is greater than a critical value (Pelletier et al. 1988; Achatz & Schlickeiser 1993). The magnetic field in the jet becomes rapidly toroidal (Pelletier & Roland 1990).

The observational evidence for the two-fluid model has been discussed by, e.g., Roland & Hetem (1996). Recent observational evidence for relativistic ejection of an $e^{\pm}$ beam come from the γ-ray observations of MeV sources (Roland & Hermsen 1995; Skibo et al. 1997) and from VLBI polarization observations (Attridge et al. 1999).

The formation of X-ray and γ-ray spectra, assuming relativistic ejection of $e^{\pm}$ beams, has been investigated by Marcowith et al. (1995, 1998) in the case of Centaurus A.

The possible existence of VLBI components with two different speeds has been recently pointed out in the case of the radio galaxies Centaurus A (Tingay et al. 1998), Virgo A (Biretta et al. 1999) and 3C 120 (Gómez et al. 2001). If the relativistic beam transfers some energy and/or relativistic particles to the jet, the relativistic particles in the jet will radiate and a new VLBI component with a mildly relativistic speed will be observed (3C 120 is a good example of a source showing this effect).

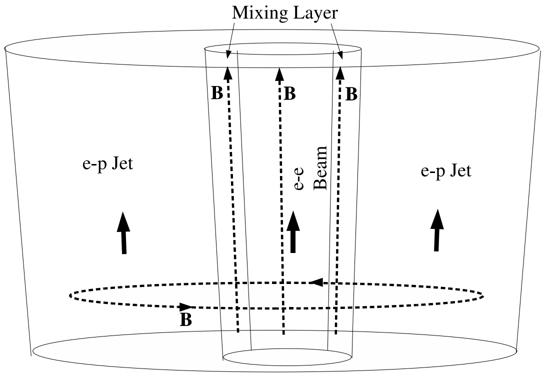

Figure C.1: *The two-fluid model*

The geometry of the model

Let Ω be the angle between the accretion disk and the orbital plane (XOY) of the BBH system. The ejection of the component will be on a cone with its axis in the $Z'OZ$ direction and opening angle Ω. We will assume that the line of sight is in the plane (YOZ) and forms an angle i_o with the axis $Z'OZ$ (see Figure C.2). The plane perpendicular to the line of sight is the plane (ηOX). We will call $\Delta\Xi$ the angle of the rotation in the plane perpendicular to the line of sight, in order to transform the coordinates η and X into coordinates N (North) and W (West), which are directly comparable with the VLBI observations. We have

$$W = x\cos(\Delta\Xi) - (z\sin(i_o) + y\cos(i_o))\sin(\Delta\Xi)\ , \tag{C.1}$$

$$N = x\sin(\Delta\Xi) + (z\sin(i_o) + y\cos(i_o))\cos(\Delta\Xi)\ . \tag{C.2}$$

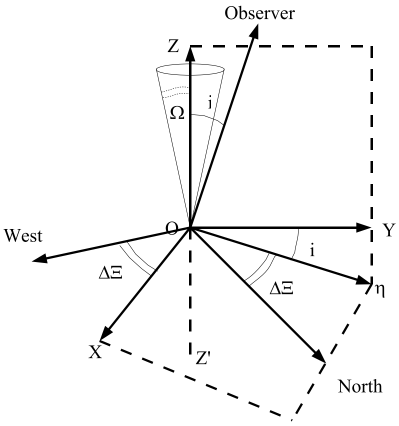

Figure C.2: *The geometry of the problem*

The precession model

This section describes the precession of the accretion disk. The coordinates of a component moving in the perturbed beam are given by

$$x_c = R_o(z)cos(\omega_p t - k_p z(t) + \phi_o)\ , \tag{C.3}$$

$$y_c = R_o(z)sin(\omega_p t - k_p z(t) + \phi_o)\ , \tag{C.4}$$

$$z_c = z_c(t)\ , \tag{C.5}$$

where $\omega_p = 2\pi/T_p$, T_p is the precession period, and k_p is defined by

$$k_p = 2\pi/T_p V_a\ , \tag{C.6}$$

where V_a is the speed of the propagation of the perturbations and a free parameter of the problem. We will assume that the amplitude of the perturbation first increases linearly, and we take the form of the amplitude $R(z_c(t))$ to be

$$R(z_c(t)) = \frac{R_o z_c(t)}{(a + z_c(t))} \; , \tag{C.7}$$

where a is

$$a = R_o/(2\ tan\Omega) \; . \tag{C.8}$$

The binary system model

To explain the origin of the precession of the accretion disk, we propose that the nucleus hosts a BBH system. As stated above, the two black holes orbit in the plane (XOY), and the origin of our coordinate system is centered on the mass center of the system. The elliptical orbit is given by

$$r = \frac{p}{1 + e\ cos(\varphi)} \; , \tag{C.9}$$

where e and p are respectively the eccentricity and the parameter or the semi-latus rectum of the orbit. We will assume that the two black holes have circular orbits, i.e. $e = 0$ and we will define the black hole that ejects the VLBI component with index 1. Its coordinates are:

$$X_1(t) = -\frac{M_2}{M_1 + M_2} p \cos(\psi(t)) \; , \tag{C.10}$$

$$Y_1(t) = -\frac{M_2}{M_1 + M_2} p \sin(\psi(t)) \; . \tag{C.11}$$

As the orbits are circular, we have $\psi(t) = \omega_b t + \psi_o$. Writing

$$x_1 = y_1 = -\frac{pM_2}{M_1 + M_2} \; , \tag{C.12}$$

we have

$$x_1 = -\frac{M_2}{M_1 + M_2} \times \left[\frac{T_b^2}{4\pi^2} G(M_1 + M_2) \right]^{1/3} \; , \tag{C.13}$$

where T_b is the period of the BBH system. We define R_{bbh} the distance between the two black holes as the size of the BBH system, it is:

$$R_{bbh} = \left[\frac{T_b^2}{4\pi^2} G(M_1 + M_2) \right]^{1/3} \; . \tag{C.14}$$

The coordinates of black hole 1 can be written

$$X_1(t) = x_1 \cos(\omega_b t + \psi_o) \; , \tag{C.15}$$

$$Y_1(t) = y_1 \sin(\omega_b t + \psi_o) \; . \tag{C.16}$$

Finally, we suppose that the perturbation of the beam is damped with a characteristic time T_d.

For VLBI observations the origin of the coordinates is black hole 1, i.e. the black hole ejecting the VLBI components. Therefore, the coordinates of the moving components in the frame of reference where black hole 1 is considered the origin are

$$\begin{aligned} x_c &= [R_o(z)\cos(\omega_p t - k_p z(t) + \phi_o) \\ &\quad + x_1 cos(\omega_b t - k_b z(t) + \psi_o) - x_1\cos(\psi_o)] \\ &\quad exp(-t/T_d) \; , \end{aligned} \tag{C.17}$$

$$\begin{aligned} y_c &= [R_o(z)\sin(\omega_p t - k_p z(t) + \phi_o) \\ &\quad + y_1\sin(\omega_b t - k_b z(t) + \psi_o) - y_1\sin(\psi_o)] \\ &\quad exp(-t/T_d) \; , \end{aligned} \tag{C.18}$$

$$z_c = z_c(t) \; , \tag{C.19}$$

where $\omega_b = 2\pi/T_b$, and k_b is defined by

$$k_b = \frac{2\pi}{T_b V_a}. \tag{C.20}$$

The differential equation governing the evolution of $z_c(t)$ can be obtained through the relation for the speed of the component

$$v_c^2 = \left(\frac{dx_c(t)}{dt}\right)^2 + \left(\frac{dy_c(t)}{dt}\right)^2 + \left(\frac{dz_c(t)}{dt}\right)^2 \; , \tag{C.21}$$

where v_c is related to the bulk Lorentz factor by $v_c/c = \sqrt{(1 - 1/\gamma_c^2)}$.

Using C.3, C.4 and C.5, we find from C.21 that dz_c/dt is the solution of the equation

$$A\left(\frac{dz_c}{dt}\right)^2 + B\left(\frac{dz_c}{dt}\right) + C = 0 \; . \tag{C.22}$$

The coefficients A, B and C can be calculated as follows: Let us call

$$\phi(t) = \omega_p t - k_p z(t) + \phi_o \; , \tag{C.23}$$

and

$$\psi(t) = \omega_b t - k_b z(t) + \psi_o \ . \tag{C.24}$$

With

$$x_1 = y_1 = -\frac{M_2}{M_1 + M_2}\left[\frac{T_b^2}{4\pi^2} G(M_1 + M_2)\right]^{1/3} , \tag{C.25}$$

the coefficients *A*, *B* and *C* of equation C.22 are given by

$$\begin{aligned} A \ &= \ \exp(-2t/T_d)\left[\frac{\omega_b \omega_p R(z)}{V_a^2}(y_1 + x_1)\cos(\psi(t) - \phi(t)) + \right. \\ &\frac{\omega_b}{V_a}\frac{dR}{dz}(x_1 + y_1)\sin(\psi(t) - \phi(t)) + \frac{\omega_p^2 R(z)^2}{V_a^2} + \\ &\left.\left(\frac{dR}{dz}\right)^2 + \frac{\omega_b^2}{2V_a^2}(x_1^2 + y_1^2)\right] + 1 \ . \end{aligned} \tag{C.26}$$

$$\begin{aligned} B \ &= \ \exp(-2t/T_d)\left[\frac{2x_1\omega_b x_1\cos(\psi_o)}{T_d V_a}\sin(\psi(t)) - \right. \\ &\frac{2y_1\omega_b y_1\sin(\psi_o)}{T_d V_a}\cos(\psi(t)) + \\ &2\left(\frac{dR(z)}{dz}x_1\cos(\psi_o) - \frac{y_1\sin(\psi_o)R(z)\omega_p}{V_a}\right)\cos(\phi(t)) + \\ &2\left(\frac{dR(z)}{dz}y_1\sin(\psi_o) + \frac{x_1\cos(\psi_o)R(z)\omega_p}{V_a}\right)\sin(\phi(t)) + \\ &\sin(\psi(t) - \phi(t))\left\{-\omega_b\frac{dR(z)}{dz}(x_1 + y_1) + \right. \\ &\left.\frac{(\omega_p - \omega_b)R(z)}{V_a}(x_1 + y_1)/T_d\right\} + \\ &\cos(\psi(t) - \phi(t))\left\{-\frac{2\omega_p\omega_b R(z)}{V_a}(x_1 + y_1) - \right. \\ &\left.\frac{dR(z)}{dz}(x_1 + y_1)/T_d\right\} - \frac{\omega_b^2}{V_a}\left(x_1^2 + y_1^2\right) \\ &\left. -\frac{2\omega_p^2 R^2(z)}{V_a} - \frac{2dR(z)}{dz}\frac{R(z)}{T_d}\right] \ . \end{aligned} \tag{C.27}$$

$$\begin{aligned}
C \;=\; & \exp(-2t/T_d)\Bigg[\frac{(x_1\cos(\psi_o))^2+(y_1\sin(\psi_o))^2}{T_d^2}+ \\
& 2\left(\frac{y_1\omega_b y_1\sin(\psi_o)}{T_d}-\frac{x_1 x_1\cos(\psi_o)}{T_d^2}\right)\cos(\psi(t))- \\
& 2\left(\frac{x_1\omega_b x_1\cos(\psi_o)}{T_d}-\frac{y_1 y_1\sin(\psi_o)}{T_d^2}\right)\sin(\psi(t))+ \\
& 2R(z)\left(\frac{y_1\sin(\psi_o)\omega_p}{T_d}-\frac{x_1\cos(\psi_o)}{T_d^2}\right)\cos(\phi(t))- \\
& 2R(z)\left(\frac{x_1\cos(\psi_o)\omega_p}{T_d}+\frac{y_1\sin(\psi_o)}{T_d^2}\right)\sin(\phi(t))+ \\
& \sin(\psi(t)-\phi(t))\left\{-(\omega_b-\omega_p)R(z)\left(x_1+y_1\right)/T_d\right\}+ \\
& \cos(\psi(t)-\phi(t))\Big\{\omega_p\omega_b R(z)\left(x_1+y_1\right)- \\
& R(z)\left(x_1+y_1\right)/T_d^2\Big\}+\frac{\omega_b^2}{2}\left(x_1^2+y_1^2\right)+R^2(z)\omega_p^2+ \\
& \left(R^2(z)+\frac{x_1^2+y_1^2}{2}\right)/T_d^2\Bigg]-v^2\,. \qquad \text{(C.28)}
\end{aligned}$$

Equation C.22 admits two solutions corresponding to the jet and the counter-jet.

We assumed that the line of sight is in the plane (YOZ) and forms an angle i_o with the z axis (see Figure C.2). Thus following Camenzind & Krockenberger (1992), if we call θ the angle between the velocity of the component and the line of sight we have

$$cos(\theta(t)) = \left(\frac{dy_c}{dt}sin\ i_o + \frac{dz_c}{dt}cos\ i_o\right)/v_c\,. \qquad \text{(C.29)}$$

The Doppler beaming factor δ, characterizing the anisotropic emission of the moving component, is

$$\delta_c(t) = \frac{1}{\gamma_c\left[1-\beta_c cos(\theta(t))\right]}\,, \qquad \text{(C.30)}$$

where $\beta_c = v_c/c$. The observed flux density is

$$S_c = \frac{1}{D^2}\delta_c(t)^{2+\alpha_r}(1+z)^{1-\alpha_r}\int_c j_c dV\,, \qquad \text{(C.31)}$$

where D is the luminosity distance of the source, z its redshift, j_c is the emissivity of the component, and α_r is the synchrotron spectral index (a negative definition of the spectral index, $S \propto \nu^{-\alpha}$ is used). As the component is moving relativistically towards the observer, the observed time is shortened and is given by

$$t_{obs} = \int_0^t [1 - \beta_c cos(\theta(t'))]\,(1+z)\,dt' \; . \tag{C.32}$$

C.2 The global method

Introduction

In Lobanov & Roland (2005) we provide a method to determine the characteristic parameters of the BBH system using radio and optical observations. The method consists of two steps, i.e. in a first step we use VLBI observations to model the precession (without a BBH system) and in a second step we use optical observations to obtain the characteristic parameters of the BBH system.

The above described method has the following problems:

1. Using a simple precession model, we find for 3C 345 that a bulk Lorentz factor increasing with time is necessary.

2. Using the parameters of the precession found in the first step, the BBH solution obtained in the second step is not necessarily consistent with the precession solution found previously. Indeed, in the limit $M_2 \to 0$ the BBH solution is not necessarily able to reproduce the results of the precession model found in the first step. The limit $M_2 \to 0$ corresponds to a single black hole and the precession of the accretion disk is due to the Lens-Thirring effect in that case.

The above problems can be solved if we directly model the VLBI observations with a BBH system instead of a simple precession model. In the BBH system model, the bulk Lorentz factor is constant, and the model explains the apparent variations of the speed of the VLBI component when it escapes from the nucleus (the apparent speed of the ejected component changes by a factor of four with a constant bulk Lorentz factor and it is not necessary to involve any acceleration or decceleration of the VLBI component). Since the BBH system and the precession solution are obtained simultaneously, they are obviously self-consistent.

The presented method is called the global method. In the global method, we calculate the projected trajectory on the plane of the sky of a component ejected by a BBH system and we determine the parameters of the model to simultaneously produce the best fit for both the West and North coordinates, i.e. $W_c(t)$, $N_c(t)$. So, the parameters found are such that minimize

$$\chi^2_t = \chi^2(W_c(t)) + \chi^2(N_c(t)) \; , \tag{C.33}$$

where $\chi^2(W_c(t))$ and $\chi^2(N_c(t))$ are the χ^2 calculated by comparing the VLBI observations with the calculated coordinates $W_c(t)$ and $N_c(t)$ of the component.

The coordinates of the VLBI component

Solving C.22, we determine the coordinate $z_c(t)$ of a point source component ejected relativistically in the perturbed beam. Then, using C.17 and C.18, we can find the coordinates $x_c(t)$ and $y_c(t)$ of the component. In addition, for each point of the trajectory, we can calculate the derivatives dx_c/dt, dy_c/dt, dz_c/dt and then deduce $\cos\theta$ from C.29, δ_c from C.30, S_ν from C.31 and t_{obs} from C.32.

When the coordinates $x_c(t)$, $y_c(t)$ and $z_c(t)$ have been calculated, they can be transformed to $w_c(t)$ (West) and $n_c(t)$ (North) coordinates using C.1 and C.2.

As explained in Britzen et al. (2001) and Lobanov & Roland (2005), the radio VLBI component has to be described as an extended component along the beam. Let us call n_{rad} the number of points (or steps along the beam) for which we integrate, in order to model the component. The coordinates $W_c(t)$, $N_c(t)$ of the VLBI component are then

$$W_c(t) = \left(\sum_{i=1}^{n_{rad}} w_{ci}(t) \right) / n_{rad} \ , \tag{C.34}$$

$$N_c(t) = \left(\sum_{i=1}^{n_{rad}} n_{ci}(t) \right) / n_{rad} \ . \tag{C.35}$$

and can be compared with the observed coordinates of the VLBI component.

The parameters of the model

In this section, we list what a priori the free parameters of the model are:

- i_o the inclination angle,
- ϕ_o the phase of the precession at $t = 0$,
- $\Delta\Xi$ the rotation angle in the plane perpendicular to the line of sight (see C.1 and C.2),
- Ω the opening angle of the precession cone (see C.8),
- R_o the maximum amplitude of the perturbation (see C.7),
- T_p the precession period of the accretion disk,
- T_d the characteristic time for the damping of the beam perturbation,

- M_1 the mass of the black hole ejecting the radio jet,
- M_2 the mass of the secondary black hole,
- γ_c the bulk Lorentz factor of the VLBI component,
- ψ_o the phase of the BBH system at $t = 0$,
- T_b the period of the BBH system,
- t_o the origin of the ejection of the VLBI component,
- V_a the propagation speed of the perturbations,
- n_{rad} is the number of steps to describe the extension of the VLBI component along the beam.

To begin with, we assume that $M_1 = M_2$ and when the corresponding solution is obtained, we calculate the family $M_1(M_2)$ which provides the same fit. So, the problem we have to solve is a 14 free parameters problem.

If, in addition to the radio, optical observations are available that peak in the light curve, this optical emission can be modelled as the synchrotron emission of a point source ejected in the perturbed beam (Britzen et al. 2001 and Lobanov & Roland 2005). This short burst of very energetic relativistic $e^{\pm}$ is followed immediately by a very long burst of less energetic relativistic $e^{\pm}$. This long burst is modelled as an extended structure along the beam and is responsible for the VLBI radio emission. In that case the origin t_o of the VLBI component is the beginning of the first peak of the optical light curve and is not a free parameter of the model.

We have to investigate the different possible scenarios with regard to the sense of the rotation of the accretion disk and the sense of the orbital rotation of the BBH system. These possibilities correspond to $\pm\, \omega_p(t - z/V_a)$ and $\pm\, \omega_b(t - z/V_a)$. As the sense of the precession is always opposite to the sense of the orbital motion, we will study the two cases denoted by $+-$ and $-+$ where we have $\omega_p(t - z/V_a)$, $-\omega_b(t - z/V_a)$ and $-\omega_p(t - z/V_a)$, $\omega_b(t - z/V_a)$ respectively.

The method to solve the problem

To find a solution for the above described problem we use the following method. As mentioned before, we start with the assumption that $M_1 = M_2$, i.e., that the two masses of the BBH system are equal.

First, we find the inclination angle that provides the best fit. To do that we minimize

$\chi_t^2(i_o)$ (see C.33) when the inclination angle varies gradually between two values. At each step of i_o, we determine each free parameter λ such that $\partial\chi_t^2/\partial\lambda = 0$ and χ_t^2 presents a minimum.

Furthermore, using the inclination angle determined previously, we explore the space of the solutions, for a varying mass of the BBH system (while still assuming $M_1 = M_2$). This allows us to find whether the solution of the BBH system presents a degeneration or if there are other solutions with different masses, that fit the observations. When exploring the solutions space, we always vary one parameter in a step-wise manner, with each step minimizing χ_t^2 for each of the free parameters.

The space of the solutions can be explored for each of the free parameters if necessary.

Because the problem is a non-linear one, we calculate again the variations of $\chi_t^2(i_o)$ for the best solution found previously, starting from the inclination angle obtained in the first step. Where $\chi_t^2(i_o)$ reaches its minimum, we have

$$\left(\frac{\partial\chi^2}{\partial i_o}\right)_{min} = A\ (i_o - i_{o,min})\ , \tag{C.36}$$

and the 1 σ error bar, $(\Delta i_o)_{1\sigma}$, corresponding to the parameter i_o is then given by

$$(\Delta i_o)_{1\sigma} = 1/A\ . \tag{C.37}$$

This assumes that around the minimum, $\chi_t^2(i_o)$ is a parabola, however, for large variations of i_o, the parabola approximation is not valid and a better determination of the 1 σ error bar can be obtained using the definition

$$(\Delta i_o)_{1\sigma} = |i_o(\chi^2_{min} + 1) - i_o(\chi^2_{min})|\ , \tag{C.38}$$

which provides two values $(\Delta i_o)_{1\sigma+}$ and $(\Delta i_o)_{1\sigma-}$ (see Lampton et al. 1976 and Hébrard et al. 2002).

Because we calculated $\chi_t^2(i_o)$ by minimizing $\chi_t^2(\lambda)$ at each step and for each free parameter λ, we can deduce the range of values corresponding to 1 σ for each parameter when the inclination varies between $i_o = i_{o,min} - (\Delta i_o)_{1\sigma-}$ and $i_o = i_{o,min} + (\Delta i_o)_{1\sigma+}$.

Finally, when the best solution corresponding to $M_1 = M_2$ is obtained, we can determine the family of BBH systems with $M_1 \neq M_2$ that provides the same fit.

One important point is that using this phenomenological method, we do not have the proof that the minimum found is unique, since for a completely different set of values for the parameters of the problem, another minimum could exist. Nevertheless, as we will explore a wide range of inclination angles, i.e. $1^o \leq i_o \leq 25^o$ and an equally wide range of BBH system masses, i.e. $10^6 \times M_\odot \leq M \leq 10^{11} \times M_\odot$, we minimize the possibility of missing the best solution. Another way to overcome this difficulty is to explore the space of possible values of the parameters using, for instance, a Monte Carlo Markov chain algorithm (MCMC algorithm). However this is out of the scope of this work.

Bibliography

Abraham, Z. & Carrara, E. A. 1998, ApJ, 496, 172

Achatz, U. & Schlickeiser, R. 1993, A&A, 274, 165

Agudo, I., Bach, U., Krichbaum, T. P., Marscher, A. P., Gonidakis, I., Diamond, P. J., Perucho, M., Alef, W., Graham, D. A., Witzel, A., Zensus, J. A., Bremer, M., Acosta-Pulido, J. A., & Barrena, R. 2007, A&A, 476, L17

Aller, H. D., Aller, M. F., & Hughes, P. A. 2006a, in Bulletin of the American Astronomical Society, Vol. 38, Bulletin of the American Astronomical Society, 1226–+

Aller, H. D., Aller, M. F., Plotkin, R. M., Hughes, P. A., & Hodge, P. E. 2003, in Bulletin of the American Astronomical Society, Vol. 35, Bulletin of the American Astronomical Society, 1310–+

Aller, M. F., Aller, H. D., & Hughes, P. A. 2006b, in Bulletin of the American Astronomical Society, Vol. 38, Bulletin of the American Astronomical Society, 904–+

Altschuler, D. R. 1989, Fundamentals of Cosmic Physics, 14, 37

Antonucci, R. R. J. & Miller, J. S. 1985, ApJ, 297, 621

Attridge, J. M., Roberts, D. H., & Wardle, J. F. C. 1999, ApJ, 518, L87

Baars, J. W. M., Genzel, R., Pauliny-Toth, I. I. K., & Witzel, A. 1977, A&A, 61, 99

Bach, U. 2004, PhD Thesis, Univ. of Bonn

Bach, U., Krichbaum, T. P., Ros, E., Britzen, S., Tian, W. W., Kraus, A., Witzel, A., & Zensus, J. A. 2005, A&A, 433, 815

Barnes, J. E. & Hernquist, L. 1992, ARA&A, 30, 705

Beckert, T., Fuhrmann, L., Cimò, G., Krichbaum, T. P., Witzel, A., & Zensus, J. A. 2002, in Proceedings of the 6th EVN Symposium, ed. E. Ros, R. W. Porcas, A. P. Lobanov, & J. A. Zensus, 79–+

Begelman, M. C., Blandford, R. D., & Rees, M. J. 1984, Reviews of Modern Physics, 56, 255

Begelman, M. C., Ergun, R. E., & Rees, M. J. 2005, ApJ, 625, 51

Benford, G. & Tzach, D. 2000, MNRAS, 317, 497

Bevington, P. R. & Robinson, D. K. 1992, Data reduction and error analysis for the physical sciences (New York: McGraw-Hill, —c1992, 2nd ed.)

Bignall, H. E., Jauncey, D. L., Lovell, J. E. J., Tzioumis, A. K., Kedziora-Chudczer, L., Macquart, J.-P., Tingay, S. J., Rayner, D. P., & Clay, R. W. 2003, ApJ, 585, 653

Biretta, J. A., Sparks, W. B., & Macchetto, F. 1999, ApJ, 520, 621

Blandford, R. 1993, in Astrophysics and Space Science Library, Vol. 103, Astrophysics and Space Science Library, 15–33

Blandford, R. D. & Königl, A. 1979, ApJ, 232, 34

Blandford, R. D., McKee, C. F., & Rees, M. J. 1977, Nature, 267, 211

Bondi, M., Padrielli, L., Fanti, R., Ficarra, A., Gregorini, L., & Mantovani, F. 1996, A&AS, 120, 89

Bondi, M., Padrielli, L., Gregorini, L., Mantovani, F., Shapirovskaya, N., & Spangler, S. R. 1994, A&A, 287, 390

Brentjens, M. A. & de Bruyn, A. G. 2005, A&A, 441, 1217

Bridle, A. H. & Perley, R. A. 1984, ARA&A, 22, 319

Britzen, S., Roland, J., Laskar, J., Kokkotas, K., Campbell, R. M., & Witzel, A. 2001, A&A, 374, 784

Britzen, S., Vermeulen, R. C., Campbell, R. M., Taylor, G. B., Pearson, T. J., Readhead, A. C. S., Xu, W., Browne, I. W., Henstock, D. R., & Wilkinson, P. 2008, A&A, 484, 119

Bronstein, I. N. & Semendjajev, K. A. 1989, Taschenbuch der Mathematik (Verlag Harri Deutsch)

Burn, B. J. 1966, MNRAS, 133, 67

Camenzind, M. & Krockenberger, M. 1992, A&A, 255, 59

Canalizo, G. & Stockton, A. 2001, ApJ, 555, 719

Carrara, E. A., Abraham, Z., Unwin, S. C., & Zensus, J. A. 1993, A&A, 279, 83

Cawthorne, T. V., Wardle, J. F. C., Roberts, D. H., & Gabuzda, D. C. 1993, ApJ, 416, 519

Chang, K. & Refsdal, S. 1979, Nature, 282, 561

Cimò, G. 2003, PhD thesis, Univ. of Bonn

Cohen, M. H., Pearson, T. J., Readhead, A. C. S., Seielstad, G. A., Simon, R. S., & Walker, R. C. 1979, ApJ, 231, 293

Dennett-Thorpe, J. & de Bruyn, A. G. 2000, ApJ, 529, L65

—. 2003, A&A, 404, 113

Dent, W. A. 1965, Science, 148, 1458

Eckart, A. 1983, Ph.D. Thesis

Edelson, R. 1992, ApJ, 401, 516

Edelson, R. A. & Krolik, J. H. 1988, ApJ, 333, 646

Emerson, D. T., Klein, U., & Haslam, C. G. T. 1979, A&A, 76, 92

Fanaroff, B. L. & Riley, J. M. 1974, MNRAS, 167, 31P

Fomalont, E. B. 1989, in Astronomical Society of the Pacific Conference Series, Vol. 6, Synthesis Imaging in Radio Astronomy, ed. R. A. Perley, F. R. Schwab, & A. H. Bridle, 213–+

Friedrichs, S. 2003, Diploma thesis, University of Bonn, Germany

Fuhrmann, L. 2004, PhD thesis, University of Bonn, Germany

Fuhrmann, L., Krichbaum, T. P., Cimò, G., Beckert, T., Kraus, A., Witzel, A., Zensus, J. A., QIAN, S. J., & Rickett, B. J. 2002, Publications of the Astronomical Society of Australia, 19, 64

Fuhrmann, L., Krichbaum, T. P., Witzel, A., Kraus, A., Britzen, S., Bernhart, S., Impellizzeri, V., Agudo, I., Klare, J., Sohn, B., Angelakis, E., Bach, U., Gabányi, K., Körding, E., Pagels, A., Zensus, J. A., Wagner, S. J., Ostorero, L., Ungerechts, H., Grewing, M., Tornikoski, M., Apponi, A. J., Vila-Vilar, B., Ziurys, L. M., & Strom, R. G. 2008

Gabányi, K. É., Marchili, N., Krichbaum, T. P., Britzen, S., Fuhrmann, L., Witzel, A., Zensus, J. A., Müller, P., Liu, X., Song, H. G., Han, J. L., & Sun, X. H. 2007, A&A

Gabuzda, D. C., Cawthorne, T. V., Roberts, D. H., & Wardle, J. F. C. 1992, ApJ, 388, 40

Gabuzda, D. C., Kochenov, P. Y., & Cawthorne, T. V. 2000a, MNRAS, 319, 1125

Gabuzda, D. C., Kochenov, P. Y., Cawthorne, T. V., & Kollgaard, R. I. 2000b, MNRAS, 313, 627

Gabuzda, D. C., Kochenov, P. Y., Kollgaard, R. I., & Cawthorne, T. V. 2000c, MNRAS, 315, 229

Gabuzda, D. C., Vitrishchak, V. M., Mahmud, M., & O'Sullivan, S. P. 2008, MNRAS, 384, 1003

Genzel, R., Lutz, D., Sturm, E., Egami, E., Kunze, D., Moorwood, A. F. M., Rigopoulou, D., Spoon, H. W. W., Sternberg, A., Tacconi-Garman, L. E., Tacconi, L., & Thatte, N. 1998, ApJ, 498, 579

Ghisellini, G., Padovani, P., Celotti, A., & Maraschi, L. 1993, ApJ, 407, 65

Gómez, J.-L., Marscher, A. P., Alberdi, A., Jorstad, S. G., & Agudo, I. 2001, ApJ, 561, L161

Gopal-Krishna & Wiita, P. J. 1992, A&A, 259, 109

Graham, J. A. 1978, PASP, 90, 237

Hardee, P. E. 2003, ApJ, 597, 798

Hébrard, G., Lemoine, M., Vidal-Madjar, A., Désert, J.-M., Lecavelier des Étangs, A., Ferlet, R., Wood, B. E., Linsky, J. L., Kruk, J. W., Chayer, P., Lacour, S., Blair, W. P., Friedman, S. D., Moos, H. W., Sembach, K. R., Sonneborn, G., Oegerle, W. R., & Jenkins, E. B. 2002, ApJS, 140, 103

Heeschen, D. S. 1984, AJ, 89, 1111

Heeschen, D. S., Krichbaum, T., Schalinski, C. J., & Witzel, A. 1987, AJ

Heeschen, D. S. & Rickett, B. J. 1987, AJ

Helmboldt, J. F., Taylor, G. B., Tremblay, S., Fassnacht, C. D., Walker, R. C., Myers, S. T., Sjouwerman, L. O., Pearson, T. J., Readhead, A. C. S., Weintraub, L., Gehrels, N., Romani, R. W., Healey, S., Michelson, P. F., Blandford, R. D., & Cotter, G. 2007, ApJ, 658, 203

Hoegbom, J. A. 1983, in Indirect Imaging. Measurement and Processing for Indirect Imaging. Proceedings of an International Symposium held in Sydney, Australia, August 30-September 2, 1983. Editor, J.A. Roberts; Publisher, Cambridge University Press, Cambridge, England, New York, NY, 1984. LC # QB51.3.E43 I53 1984. ISBN # 0-521-26282-8. P.247, 1983, 247

Homan, D. C. & Lister, M. L. 2006, AJ, 131, 1262

Homan, D. C. & Wardle, J. F. C. 1999, AJ, 118, 1942

Hughes, P. A., Aller, H. D., & Aller, M. F. 1985, ApJ, 298, 301

—. 1989, ApJ, 341, 54

Jackson, J. D. 1975, Classical electrodynamics (92/12/31, New York: Wiley, 1975, 2nd ed.)

Jauncey, D. L. & Macquart, J.-P. 2001, A&A, 370, L9

Jones, T. W. & Odell, S. L. 1977, ApJ, 214, 522

Jorstad, S. G., Marscher, A. P., Lister, M. L., Stirling, A. M., Cawthorne, T. V., Gear, W. K., Gómez, J. L., Stevens, J. A., Smith, P. S., Forster, J. R., & Robson, E. I. 2005, AJ, 130, 1418

Kauffmann, G. & Haehnelt, M. 2000, MNRAS, 311, 576

Kedziora-Chudczer, L., Jauncey, D. L., Wieringa, M. H., Walker, M. A., Nicolson, G. D., Reynolds, J. E., & Tzioumis, A. K. 1997, ApJ, 490, L9+

Kedziora-Chudczer, L. L., Jauncey, D. L., Wieringa, M. H., Tzioumis, A. K., & Reynolds, J. E. 2001, MNRAS, 325, 1411

Kellermann, K. I., Lister, M. L., Homan, D. C., Vermeulen, R. C., Cohen, M. H., Ros, E., Kadler, M., Zensus, J. A., & Kovalev, Y. Y. 2004, ApJ, 609, 539

Kellermann, K. I. & Pauliny-Toth, I. I. K. 1969, ApJ, 155, L71

Kellermann, K. I., Sramek, R., Schmidt, M., Shaffer, D. B., & Green, R. 1989, AJ, 98, 1195

Klare, J. 2003, PhD thesis, University of Bonn, Germany

Klare, J., Zensus, J. A., Lobanov, A. P., Ros, E., Krichbaum, T. P., & Witzel, A. 2005, in Astronomical Society of the Pacific Conference Series, Vol. 340, Future Directions in High Resolution Astronomy, ed. J. Romney & M. Reid, 40–+

Kochenov, P. Y. & Gabuzda, D. C. 1999, in Astronomical Society of the Pacific Conference Series, Vol. 159, BL Lac Phenomenon, ed. L. O. Takalo & A. Sillanpää, 460–+

Komesaroff, M. M., Roberts, J. A., Milne, D. K., Rayner, P. T., & Cooke, D. J. 1984, MNRAS, 208, 409

Komossa, S., Burwitz, V., Hasinger, G., Predehl, P., Kaastra, J. S., & Ikebe, Y. 2003, ApJ, 582, L15

Königl, A. & Choudhuri, A. R. 1985, ApJ, 289, 188

Kovalev, Y. Y., Lobanov, A. P., Pushkarev, A. B., & Zensus, J. A. 2008, A&A, 483, 759

Kraus, A. 1997, PhD thesis, University of Bonn, Germany

Kraus, A., Krichbaum, T. P., Wegner, R., Witzel, A., Cimò, G., Quirrenbach, A., Britzen, S., Fuhrmann, L., Lobanov, A. P., Naundorf, C. E., Otterbein, K., Peng, B., Risse, M., Ros, E., & Zensus, J. A. 2003, A&A, 401, 161

Kraus, A., Witzel, A., Krichbaum, T. P., Lobanov, A. P., Peng, B., & Ros, E. 1999, A&A, 352, L107

Krichbaum, T. P., Kraus, A., Fuhrmann, L., Cimò, G., & Witzel, A. 2002, Publications of the Astronomical Society of Australia, 19, 14

Kudryavtseva, N., Britzen, S., Witzel, A., Ros, E., Aller, M. F., Aller, H. D., Campbell, R. M., Zensus, J. A., Eckart, A., Roland, J., & Mehta, A. 2006, in Proceedings of the 8th European VLBI Network Symposium

Kühr, H., Pauliny-Toth, I. I. K., Witzel, A., & Schmidt, J. 1981a, AJ

Kühr, H., Witzel, A., Pauliny-Toth, I. I. K., & Nauber, U. 1981b, A&AS

Laing, R. A. 1980, MNRAS, 193, 439

Lampton, M., Margon, B., & Bowyer, S. 1976, ApJ, 208, 177

Leppänen, K. J., Zensus, J. A., & Diamond, P. J. 1995, AJ, 110, 2479

Lesch, H. & Pohl, M. 1992, A&A, 254, 29

Lister, M. L., Aller, H. D., Aller, M. F., Cohen, M. H., Homan, D. C., Kadler, M., Kellermann, K. I., Kovalev, Y. Y., Ros, E., Savolainen, T., Zensus, J. A., & Vermeulen, R. C. 2009, AJ, 137, 3718

Lister, M. L. & Homan, D. C. 2005, AJ, 130, 1389

Lobanov, A. P. 1998, A&A, 330, 79

Lobanov, A. P., Krichbaum, T. P., Witzel, A., Kraus, A., Zensus, J. A., Britzen, S., Otterbein, K., Hummel, C. A., & Johnston, K. 1998, A&A, 340, L60

Lobanov, A. P. & Roland, J. 2005, A&A, 431, 831

Lovell, J. E. J., Jauncey, D. L., Bignall, H. E., Kedziora-Chudczer, L., Macquart, J.-P., Rickett, B. J., & Tzioumis, A. K. 2003, AJ, 126, 1699

Lovell, J. E. J., Rickett, B. J., Macquart, J.-P., Jauncey, D. L., Bignall, H. E., Kedziora-Chudczer, L., Ojha, R., Pursimo, T., Dutka, M., Senkbeil, C., & Shabala, S. 2008, ApJ, 689, 108

Macquart, J.-P. 2003, New Astronomy Review, 47, 609

Macquart, J.-P., de Bruyn, A. G., & Dennett-Thorpe, J. 2003, in Astronomical Society of the Pacific Conference Series, Vol. 290, Active Galactic Nuclei: From Central Engine to Host Galaxy, ed. S. Collin, F. Combes, & I. Shlosman, 349–+

Marchili, N. 2009, PhD thesis, AA(Max-Planck-Institut fuer Radioastronomie ¡EMAIL¿marchili@mpifr-bonn.mpg.de¡/EMAIL¿)

Marcowith, A., Henri, G., & Pelletier, G. 1995, MNRAS, 277, 681

Marcowith, A., Henri, G., & Renaud, N. 1998, A&A, 331, L57

Marscher, A. P. 1978, ApJ, 219, 392

—. 1983, ApJ, 264, 296

Marscher, A. P. 1992, in American Institute of Physics Conference Series, Vol. 254, American Institute of Physics Conference Series, ed. S. S. Holt, S. G. Neff, & C. M. Urry, 377–385

Marscher, A. P. & Gear, W. K. 1985, ApJ, 298, 114

Marscher, A. P., Marchenko-Jorstad, S. G., Mattox, J. R., Wehrle, A. E., & Aller, M. F. 2000, in Astrophysical Phenomena Revealed by Space VLBI, ed. H. Hirabayashi, P. G. Edwards, & D. W. Murphy, 39–46

Matthews, T. A. & Sandage, A. R. 1963, ApJ, 138, 30

McHardy, I. 1988, Memorie della Societa Astronomica Italiana, 59, 239

Melrose, D. B. 1991, ARA&A, 29, 31

Murphy, D. W., Browne, I. W. A., & Perley, R. A. 1993, MNRAS, 264, 298

Muxlow, T. W. B., Pelletier, G., & Roland, J. 1988, A&A, 206, 237

Narayan, R. 1992, Philosophical Transactions of the Royal Society of London, 341, 151

Ott, M., Witzel, A., Quirrenbach, A., Krichbaum, T. P., Standke, K. J., Schalinski, C. J., & Hummel, C. A. 1994, A&A, 284, 331

Otterbein, K., Krichbaum, T. P., Kraus, A., Witzel, A., Hummel, C. A., & Zensus, J. A. 1998, in Astronomical Society of the Pacific Conference Series, Vol. 144, IAU Colloq. 164: Radio Emission from Galactic and Extragalactic Compact Sources, ed. J. A. Zensus, G. B. Taylor, & J. M. Wrobel, 73–+

Pearson, T. J. & Readhead, A. C. S. 1984, ARA&A, 22, 97

Pearson, T. J. & Zensus, J. A. 1987, in Superluminal Radio Sources, ed. J. A. Zensus & T. J. Pearson, 1–11

Pelletier, G. & Roland, J. 1989, A&A, 224, 24

Pelletier, G. & Roland, J. 1990, in Parsec-scale radio jets, ed. J. A. Zensus & T. J. Pearson, 323–+

Pelletier, G. & Sol, H. 1992, MNRAS, 254, 635

Pelletier, G., Sol, H., & Asseo, E. 1988, Phys. Rev. A, 38, 2552

Pen, U.-L. 1999, ApJS, 120, 49

Penrose, R. 1969, Nuovo Cimento Rivista Serie, 1, 252

Perucho, M., Lobanov, A. P., Martí, J.-M., & Hardee, P. E. 2006, A&A, 456, 493

Peterson, B. M. 1997, An Introduction to Active Galactic Nuclei (An introduction to active galactic nuclei, Publisher: Cambridge, New York Cambridge University Press, 1997 Physical description xvi, 238 p. ISBN 0521473489)

Pollack, L. K., Taylor, G. B., & Zavala, R. T. 2003, ApJ, 589, 733

Qian, S., Kraus, A., Zhang, X., Krichbaum, T. P., Witzel, A., & Zensus, J. A. 2002, Chinese Journal of Astronony and Astrophysics, 2, 325

Qian, S., Witzel, A., Krichbaum, T., Quirrenbach, A., Hummel, C. A., & Zensus, J. A. 1992, Chinese Astronomy and Astrophysics, 16, 137

Qian, S.-J., Krichbaum, T. P., Gao, L., Zhang, X.-Z., Witzel, A., & Zensus, J. A. 2007, Chinese Journal of Astronomy and Astrophysics, 7, 215

Qian, S. J., Krichbaum, T. P., Zensus, J. A., Steffen, W., & Witzel, A. 1996a, A&A, 308, 395

Qian, S.-J., Krichbaum, T. P., Zhang, X.-Z., Fuhrmann, L., Cimò, G., Kraus, A., Beckert, T., Britzen, S., Witzel, A., & Zensus, J. A. 2006, Chinese Journal of Astronomy and Astrophysics, 6, 1

Qian, S. J., Quirrenbach, A., Witzel, A., Krichbaum, T. P., Hummel, C. A., & Zensus, J. A. 1991, A&A, 241, 15

Qian, S. J., Witzel, A., Kraus, A., Krichbaum, T. P., & Britzen, S. 1996b, in Astronomical Society of the Pacific Conference Series, Vol. 100, Energy Transport in Radio Galaxies and Quasars, ed. P. E. Hardee, A. H. Bridle, & J. A. Zensus, 55–+

Quirrenbach, A., Kraus, A., Witzel, A., Zensus, J. A., Peng, B., Risse, M., Krichbaum, T. P., Wegner, R., & Naundorf, C. E. 2000, A&AS, 141, 221

Quirrenbach, A., Witzel, A., Kirchbaum, T. P., Hummel, C. A., Wegner, R., Schalinski, C. J., Ott, M., Alberdi, A., & Rioja, M. 1992, A&A, 258, 279

Quirrenbach, A., Witzel, A., Krichbaum, T., Hummel, C. A., & Alberdi, A. 1989a, Nature, 337, 442

Quirrenbach, A., Witzel, A., Qian, S. J., Krichbaum, T., Hummel, C. A., & Alberdi, A. 1989b, A&A, 226, L1

Quirrenbach, A., Witzel, A., Wagner, S., Sanchez-Pons, F., Krichbaum, T. P., Wegner, R., Anton, K., Erkens, U., Haehnelt, M., Zensus, J. A., & Johnston, K. J. 1991, ApJ, 372, L71

Rayner, D. P., Norris, R. P., & Sault, R. J. 2000, MNRAS, 319, 484

Readhead, A. C. S. 1994, ApJ, 426, 51

Rees, M. J. 1967, MNRAS, 135, 345

Reuter, H.-P. & Klein, U. 1996, A&A, 313, 768

Rickett, B., Kedziora-Chudczer, L., & Jauncey, D. L. 2002a, Publications of the Astronomical Society of Australia, 19, 106

Rickett, B. J. 2001, Ap&SS, 278, 5

Rickett, B. J., Kedziora-Chudczer, L., & Jauncey, D. L. 2002b, ApJ, 581, 103

Rickett, B. J., Quirrenbach, A., Wegner, R., Krichbaum, T. P., & Witzel, A. 1995, A&A, 293, 479

Robertson, B., Bullock, J. S., Cox, T. J., Di Matteo, T., Hernquist, L., Springel, V., & Yoshida, N. 2006, ApJ, 645, 986

Roland, J., Britzen, S., Kudryavtseva, N. A., Witzel, A., & Karouzos, M. 2008, A&A, 483, 125

Roland, J. & Hermsen, W. 1995, A&A, 297, L9

Roland, J. & Hetem, A. 1996, Determination of the physical parameters in the Cygnus A hot spots (Cygnus A – Study of a Radio Galaxy), 126–+

Roland, J., Pelletier, G., & Muxlow, T. W. B. 1988, A&A, 207, 16

Roland, J., Teyssier, R., & Roos, N. 1994, A&A, 290, 357

Romero, G. E., Combi, J. A., & Colomb, F. R. 1994, A&A, 288, 731

Rybicki, G. B. & Lightman, A. P. 1979, Radiative processes in astrophysics (New York, Wiley-Interscience, 1979. 393 p.)

Ryle, M. & Hewish, A. 1960, MNRAS, 120, 220

Sánchez, S. F., Christensen, L., Becker, T., Kelz, A., Jahnke, K., Benn, C. R., García-Lorenzo, B., & Roth, M. M. 2004, Astronomische Nachrichten, 325, 112

Sanders, D. B. & Mirabel, I. F. 1996, ARA&A, 34, 749

Sanders, D. B., Soifer, B. T., Elias, J. H., Madore, B. F., Matthews, K., Neugebauer, G., & Scoville, N. Z. 1988a, ApJ

Sanders, D. B., Soifer, B. T., Elias, J. H., Neugebauer, G., & Matthews, K. 1988b, ApJ

Savolainen, T., Wiik, K., Valtaoja, E., & Tornikoski, M. 2006, A&A, 446, 71

Scheuer, P. A. G. & Readhead, A. C. S. 1979, Nature, 277, 182

Schmitt, H. R., Pringle, J. E., Clarke, C. J., & Kinney, A. L. 2002, ApJ, 575, 150

Schweizer, F. 1986, Science, 231, 227

Shepherd, M. C., Pearson, T. J., & Taylor, G. B. 1994, in Bulletin of the American Astronomical Society, Vol. 26, Bulletin of the American Astronomical Society, 987–989

Sholomitsky, G. B. 1965, Informational Bulletin on Variable Stars, 83, 1

Simonetti, J. H. 1991, A&A, 250, L1

Simonetti, J. H., Cordes, J. M., & Heeschen, D. S. 1985, ApJ, 296, 46

Skibo, J. G., Dermer, C. D., & Schlickeiser, R. 1997, ApJ, 483, 56

Sol, H., Pelletier, G., & Asseo, E. 1989, MNRAS, 237, 411

Spergel, D. N., Verde, L., Peiris, H. V., Komatsu, E., Nolta, M. R., Bennett, C. L., Halpern, M., Hinshaw, G., Jarosik, N., Kogut, A., Limon, M., Meyer, S. S., Page, L., Tucker, G. S., Weiland, J. L., Wollack, E., & Wright, E. L. 2003, ApJS, 148, 175

Standke, K. J., Quirrenbach, A., Krichbaum, T. P., Witzel, A., Otterbein, K., Alef, W., Eckart, A., Alberdi, A., Marcaide, J. M., Ros, E., Lesch, H., Steffen, W., Kraus, A., & Zensus, J. A. 1996, A&A, 306, 27

Steffen, W., Zensus, J. A., Krichbaum, T. P., Witzel, A., & Qian, S. J. 1995, A&A, 302, 335

Stirling, A. M., Cawthorne, T. V., Stevens, J. A., Jorstad, S. G., Marscher, A. P., Lister, M. L., Gómez, J. L., Smith, P. S., Agudo, I., Gabuzda, D. C., Robson, E. I., & Gear, W. K. 2003, MNRAS, 341, 405

Tateyama, C. E. & Kingham, K. A. 2004, ApJ, 608, 149

Taylor, G. B. 1998, ApJ, 506, 637

—. 2000, ApJ, 533, 95

Taylor, G. B., Carilli, C. L., & Perley, R. A., eds. 1999, Astronomical Society of the Pacific Conference Series, Vol. 180, Synthesis Imaging in Radio Astronomy II

Thompson, A. R., Moran, J. M., & Swenson, Jr., G. W. 2001, Interferometry and Synthesis in Radio Astronomy, 2nd Edition (Interferometry and synthesis in radio astronomy by A. Richard Thompson, James M. Moran, and George W. Swenson, Jr. 2nd ed. New York : Wiley, c2001.xxiii, 692 p. : ill. ; 25 cm. ”A Wiley-Interscience publication.” Includes bibliographical references and indexes. ISBN : 0471254924)

Tingay, S. J., Jauncey, D. L., Reynolds, J. E., Tzioumis, A. K., King, E. A., Preston, R. A., Jones, D. L., Murphy, D. W., Meier, D. L., van Ommen, T. D., McCulloch, P. M., Ellingsen, S. P., Costa, M. E., Edwards, P. G., Lovell, J. E. J., Nicolson, G. D., Quick, J. F. H., Kemball, A. J., Migenes, V., Harbison, P., Jones, P. A., White, G. L., Gough, R. G., Ferris, R. H., Sinclair, M. W., & Clay, R. W. 1998, AJ, 115, 960

Turlo, Z., Forkert, T., Sieber, W., & Wilson, W. 1985, A&A, 142, 181

Tyul'Bashev, S. A. 2005, Astronomy Reports, 49, 967

Urry, C. 2004, in Astronomical Society of the Pacific Conference Series, Vol. 311, AGN Physics with the Sloan Digital Sky Survey, ed. G. T. Richards & P. B. Hall, 49–+

Urry, C. M. & Padovani, P. 1995, PASP, 107, 803

Valtonen, M. J., Lehto, H. J., Nilsson, K., Heidt, J., Takalo, L. O., Sillanpää, A., Villforth, C., Kidger, M., Poyner, G., Pursimo, T., Zola, S., Wu, J.-H., Zhou, X., Sadakane, K., Drozdz, M., Koziel, D., Marchev, D., Ogloza, W., Porowski, C., Siwak, M., Stachowski, G., Winiarski, M., Hentunen, V.-P., Nissinen, M., Liakos, A., & Dogru, S. 2008, Nature, 452, 851

Volonteri, M., Haardt, F., Madau, P., & Sesana, A. 2004, in Astrophysics and Space Science Library, Vol. 301, Astrophysics and Space Science Library, ed. M. Plionis, 227–+

Wagner, S. J. 1992, in Gravitational Lenses, Proceedings of a Conference Held in Hambu rg, Germany, 9-13 September 1991. Edited by Rainer Kayser, Thomas Schramm, and Lars Nieser. Springer-Verlag Berlin Heidelberg New York. Also Lecture Notes in Physics, volume 406, 1992, p.189, 189–+

Wagner, S. J. & Witzel, A. 1995, ARA&A, 33, 163

Wagner, S. J., Witzel, A., Heidt, J., Krichbaum, T. P., Qian, S. J., Quirrenbach, A., Wegner, R., Aller, H., Aller, M., Anton, K., Appenzeller, I., Eckart, A., Kraus, A., Naundorf, C., Kneer, R., Steffen, W., & Zensus, J. A. 1996, AJ, 111, 2187

Wagner, S. J., Witzel, A., Krichbaum, T. P., Wegner, R., Quirrenbach, A., Anton, K., Erkens, U., Khanna, R., & Zensus, A. 1993, A&A, 271, 344

Walker, M. A. 1998, in ASP Conf. Ser. 144: IAU Colloq. 164: Radio Emission from Galact ic and Extragalactic Compact Sources, 285–+

Wardle, J. F. C. & Homan, D. C. 2003, Ap&SS, 288, 143

Weatherall, J. C. & Benford, G. 1991, ApJ, 378, 543

Weiler, K. W. & de Pater, I. 1983, ApJS, 52, 293

Wen, Z. L., Liu, F. S., & Han, J. L. 2008, ArXiv e-prints

Williams, R. K. 1995, Phys. Rev. D, 51, 5387

—. 2004, ApJ, 611, 952

Willott, C. J., Delorme, P., Omont, A., Bergeron, J., Delfosse, X., Forveille, T., Albert, L., Reylé, C., Hill, G. J., Gully-Santiago, M., Vinten, P., Crampton, D., Hutchings, J. B., Schade, D., Simard, L., Sawicki, M., Beelen, A., & Cox, P. 2007, AJ, 134, 2435

Witzel, A., Heeschen, D. S., Schalinski, C., & Krichbaum, T. 1986, Mitteilungen der Astronomischen Gesellschaft Hamburg, 65, 239

Zensus, J. A. & Pearson, T. J., eds. 1987, Superluminal radio sources; Proceedings of the Workshop, Pasadena, CA, Oct. 28-30, 1986

Appendix D

Acknowledgements

Was lange währt... Zum Schluß möchte ich mich bei all denen bedanken, die mir während der zurückliegenden Jahre zur Seite gestanden haben, sei es in fachlicher oder auch in persönlicher Hinsicht.

Ich möchte zunächst den Herren Prof. Dr. J. A. Zensus und Dr. A. Witzel dafür danken, dass sie es mir ermöglicht haben, in der VLBI-Gruppe des Max-Planck-Instituts für Radioastronomie meine Dissertation anzufertigen.

Des Weiteren danke ich den Herren Prof. Dr. Ulrich Klein und Priv.-Doz. Dr. Walter Huchtmeier für die freundliche Übernahme des Referats bzw. Koreferats über die vorliegende Arbeit. Ich möchte auch den Herren Prof. Dr. Ian Brock und Priv.-Doz. Dr. Axel Nothnagel dafür danken, dass sie sich bereit erklärt haben, in meinem Promotionsausschuß mitzuwirken.

Meinem Betreuer Dr. Thomas Krichbaum, der mich auch schon durch meine Diplomarbeit begleitet hat, danke ich für die Bereitstellung der Daten, die Grundlage für diese Arbeit waren sowie für die zahlreichen Anregungen und interessanten Diskussionen, die zum Gelingen der Dissertation beigetragen haben. Nicht zuletzt bin ich dankbar, dass er einen so langen Geduldsfaden hat...

Nun folgt eine ganze Reihe von Personen, bei denen ich mich bedanken möchte, sei es wegen ihrer fachlichen Unterstützung oder auch einfach nur für ihre Gegenwart und viele interessante und inspirierende Gespräche, die wir geführt haben. Die Liste erhebt keinen Anspruch auf Vollständigkeit und man möge mir verzeihen, wenn ich den ein oder anderen hier vergessen haben sollte. Als da wären: Dr. Emmanouil Angelakis (thanks dude!), Dr. Alex Kraus, Dr. Violette Impellizzeri (Violettaaa!), Dr. Walter Alef, Dr. Richard Porcas, Dr. Lars ”Larsi” Fuhrmann, Dr. Nicola Marchili (especially for providing access to the IDV data of the Urumqi observations), Dr. Nadia Kudryavtseva, Dr. Uwe Bach, the members of the ”Big Ban(g)d” (it was nice as long as it lasted!) und natürlich danke ich den derzeitigen und auch ehemaligen Kollegen aus der VLBI-Gruppe im Allgemeinen für das angenehme

Arbeitsklima. Herrn Prof. Jacques Roland danke ich besonders herzlich für seine Unterstützung und die gute Zusammenarbeit beim Binary Black Hole Model, merci bien! Ein besonderer Dank auch an meine Kollegen vom Institut für Geodäsie und Geoinformation der Universität Bonn, die mich so freundlich in ihre Mitte aufgenommen haben, besonders seien hier Arno Mueskens, Alessandra Bertarini und Dr. Axel Nothnagel genannt; und nicht zu vergessen natürlich die Kollegen aus der Korrelator-Gruppe.

This research has made use of data from the MOJAVE database that is maintained by the MOJAVE team (Lister et al., 2009, AJ, 137, 3718). This work is also based on observations with the 100-m telescope of the MPIfR (Max-Planck-Institut für Radioastronomie) at Effelsberg. This research has made use of data from the University of Michigan Radio Astronomy Observatory which has been supported by the University of Michigan and by a series of grants from the National Science Foundation, most recently AST-0607523. Special thanks to Margo Aller for providing data that helped me in the determination of the EVPA correction. This research has also made use of the United States Naval Observatory (USNO) Radio Reference Frame Image Database (RRFID). I would like to thank in particular Alan Fey for the provision of two additional 24 GHz VLBI epochs used in the kinematic analysis.

Last but not least danke ich meiner Familie für ihre fortwährende Unterstützung und dafür, dass sie in den letzten Jahren so geduldig darauf gewartet hat, dass ich endlich fertig werde. Was blieb ihnen auch anderes übrig :-D ...